

https://dspace.org/

Petrogenesis of the late Archean Singertât Alkaline Igneous Complex, North Atlantic Craton, South-East Greenland

Naidoo, Arantxa

2019

https://hdl.handle.net/10539/29541

Downloaded from a DSpace repository. https://dspace.org/

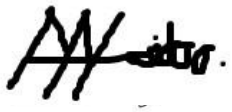
WITS UNIVERSITY

Petrogenesis of the Late Archean Singertât Alkaline Igneous Complex, North Atlantic Craton, South-East Greenland.

Ms. Arantxa Naidoo (681023)
Supervisors: Dr. Grant Bybee (Wits Univ.) and Prof. Sebastian Tappe (Univ. Johannesburg)

Declaration

I Arantxa Naidoo, student number 681023 declare that this dissertation is my own work. It is being submitted at the Faculty of Science, University of the Witwatersrand, Johannesburg for the Degree of Master of Science (Geology). It has not been submitted before for any degree or examination at any other institution.



_____

(Signature of candidate)

24 day of October 2019 at University of The Witwatersrand.

Abstract

The Singertât Complex forms part of the Skjoldungen Alkaline Igneous Province (SAIP, 2760-2690 Ma) located in SE Greenland. It was emplaced into the southern part of the SAIP in a sequence of small, sheet-like intrusions during the Late Archean and was thought until recently to be post-tectonic with previous work suggesting an age of 2680-2660 Ma. The complex consists of a variety of silica undersaturated (nepheline-bearing) alkaline rocks, which occur as modally layered, horizontal sheets cut by minor late-stage nepheline syenite pegmatites and carbonatites. This project aims to understand the petrogenesis of the Singertât Complex, including investigating magmatic processes and crystal cargo dynamics from mantle source to final emplacement in the upper crust. Crucial questions include whether the complex is constructed from single or multiple magma batches, whether those batches were emplaced as crystal-poor liquids or as crystal mushes and what type/s of crystallization processes operated? Detailed petrographic analysis indicates that the Singertât Complex is composed primarily of nepheline-bearing lithologies such as urtite (>70% nepheline), ijolite (70-30% nepheline) and melteigite (<30% nepheline). These alkaline silicate rock types are either equigranular or porphyritic and the main mineral phases include nepheline, orthoclase, microcline, anti-perthite, aegerine-augite, biotite, minor primary carbonate and in some samples sodalite, with accessory magnetite, apatite and zircon. Poikilitic growth relationships suggest that mafic minerals crystallized first followed by nepheline, which appears to have crystallized from the remaining interstitial liquid. Anti-perthite commonly exhibits anastomosing exsolution textures, indicating supersolvus crystallization temperatures above 600 ºC, followed by slow cooling. Both gradational transitions and sharp contacts between rock types are observed. Where sharp boundaries occur, crystal truncation suggests that the pre-existing unit has been chemically or thermally eroded, perhaps as a result of sheet emplacement.

Petrographic and geochemical evidence obtained has found that the syenitic gneiss which forms part of the Singertât Complex is actually a nepheline syenite as nepheline crystal were identified during petrographic investigation and confirmed during EPMA analysis. Major element results obtained from EPMA analysis also demonstrate that the nepheline populations found in the syenitic gneisses are similar to the population found in the nepheline-bearing alkaline rocks. This evidence could mean that if the syenitic gneisses have not undergone fenitization then the syenitic gneisses are not host rocks as previously thought but are actually part of the Singertât Complex itself.

Major element compositions of the nepheline-bearing alkaline rocks show that while nepheline crystal populations in gradationally layered samples are similar (i.e. from the same magma batch), nepheline populations in samples with sharp contacts are different (i.e. from several discrete magma batches). Petrographic studies and EPMA indicated that the aegerine-augite crystals of the nepheline-bearing rocks were compositionally zoned and many of the aegerine-augite crystals in some samples depict a large crystal size variation with some crystals being as large as 1 cm and others < 1mm within the same rock. This compositional zonation and large variation in

crystal size may provide evidence that these aegerine-augite crystals were entrained in a magma which replenished the Singertât magma chamber promoting crystallization as a crystal-rich slurry. Further evidence to support this can be observed in some of the nepheline-bearing alkaline sample, where we observe flow textures with smaller crystals aegerine-augite and nepheline that are aligned around larger crystals. Flow textures are formed from eddie currents, where already crystallized, larger, primocrysts disrupt interstitial liquid flow, causing alignment of the smaller crystals during nucleation. Therefore, it would appear that the Singertât Complex formed as a result of multiple replenishments of crystal-rich magma. Major element analysis also shows that the Singertât is barely peralkaline and is in fact more metaluminous due the results obtained from the alkalinity index. The majority of the samples appear to fall into the category of miaskitic, as they fall within the peraluminous and metaluminous fields on the peralkalinity index and also due to indicator minerals such as zircon present in many of the rock types.

New $^{206}Pb/^{238}U$ zircon age determinations show that the nepheline-bearing pegmatites range from 2785 ± 10 Ma to 2753.4 ± 5.8 Ma, one dated carbonatite returns an age of 2750 ± 11 Ma, a representative ijolite sample is dated at 2771 ± 32 Ma and a representative melteigite sample produces an age of 2774 ± 12 Ma. Not only does this prove that the Singertât Complex is older than previously thought but places the formation of the Singertât Complex outside the Singertât Stage and at the beginning of the Skjoldungen orogeny. These ages also demonstrate that the Singertât Complex may be the oldest alkaline complex in the world. The evidence presented above suggests that the small alkaline Singertât Complex formed during Late Archean orogenesis from multiple batches of crystal-rich magma with subsequent *in-situ* crystallization as the primary processes involved in layer formation.

Acknowledgements

Dr. Grant Bybee at The University of the Witwatersrand is gratefully acknowledged for his consistent guidance, patience and supervision throughout the entire process of this project. Professor Sebastian Tappe at the University of Johannesburg is also acknowledged for his support, supervision and guidance of the project as well as providing the samples for this research project. Dr. Christian Reinke (UJ) and Henriette Ueckermann are acknowledged for their instruction and assistance throughout all EPMA, XRF and LA-ICPMS work performed respectively at UJ. Professor Allan Wilson and Marlin Patchappa are acknowledged for conducting XRF and ICP-MS analyses, as well as Caiphas Majola for the polishing of thin sections at the University of the Witwatersrand and Joe Aphane for his instruction and assistance throughout the all mineral separation work at the Earth Lab at Wits. I would also like to acknowledge both The University of the Witwatersrand and the University of Johannesburg for the use of crushing, milling and mineral separation labs in the preparation stages of the project. This project would not have been possible without the financial support from African Rainbow Minerals (ARM) and the University of the Witwatersrand. Finally, I would like to thank my family, friends and colleagues for their continued support throughout the duration of this project.

Contents

List of Tables 5
List of Figures 6
1. Introduction 11
1.1 Location and Sampling *12*
1.2 Geological setting *15*
2. Literature Review 18
2.1 Alkaline igneous rocks *18*
2.2. Peralkaline rocks versus metaluminous rocks *19*
2.3 Development of igneous layering *21*
3. Aims and Objectives 24
4. Hypothesis 24
5. Methodology 25
5.1 Electron probe microanalysis (EPMA): *25*
5.2 Whole-rock analyses *25*
6. Results 31
6.1 Petrography *31*
6.2 Mineral Chemistry *46*
6.4 Geochronology *70*
7. Discussion 79
7.1 New geological data emerging from the Singertât Complex *79*
7.2 Evolution of the Singertât Complex *84*
8. Conclusion 91
9. References 93
10. Appendices 99

List of Tables

Table 1: Results of the CRMS that were analyzed as unknowns at the Earth Laboratory in the University if the Witwatersrand with the Singertât samples

Table 2: Results for artificial multi-element standards BCR2 and BHVO-2, which were run with the Singertât samples.

Table 3: EPMA results for sodalite in sample 542217B

Table 4: Major element concentrations in wt% of the nepheline-bearing rocks, pegmatites, carbonatites and syenitic gneisses from the Singertât Complex.

Table 5: REE concentrations in ppm of the nepheline-bearing rocks, pegmatites, carbonatites and syenitic gneisses from the Singertât Complex.

Table 6: Trace elements and trace element ratios used for open magma systems according to Rollinson, 1993.

Table 7: Trace element ratios La/Sm, Gd/Yb and La/Yb for the Singertât Complex. All values are normalized to chondritic reference value using Anderson and Grevasse (1989).

Table 8: Ages determined using U-Pb analyses on zircons located in the nepheline-bearing rocks, pegmatites and carbonatite (including inherited zircons, excluding one sample that contained large amounts of common lead). For detailed analyses see Appendix X.

Table 9: Ages of other alkaline igneous complexes in the world.

List of Figures

Figure 1.1: Schematic geological map showing the lithologies that make up the North Atlantic Craton (NAC). The inset shown on the bottom right of the geological map, shows the location of the SAIP and NAC in southern Greenland (Kolb et al., 2013).

Figure 1.2: A geological map of the Singertât Complex of the SAIP by Nielson and Rosing, 1990. The map indicates sample localities for a selection of alkaline rocks (green dots) and the syenitic gneisses (red dots) that were sampled on the 2012 expedition.

Figure 1.3: Schematic geological map showing the extent of the North Atlantic Craton (NAC). The red box shows the location of the SAIP on the NAC. (Bagas et al., 2013).

Figure 1.4: Schematic of the Skjoldungen Arc during the Skjoldungen Orogen taken from Bagas et al. (2013).

Figure 1.5: Synoptic sketch by Bagas et al. (2013), which depicts a proposed Late Archean to Early Proterozoic evolution of the NAC in southeast Greenland. The Singertât Complex intruded at approximately 2664 +4/-2 Ma (Nielson and Rosing, 1990 and Kolb et al., 2012a) and is indicated by the red circles

Figure 2.1: Ternary diagram showing how different feldspathoids relate compositionally and the different alkali feldspars (in molar proportions). Optical features of each feldspathoid is present. TS=thin section. Taken from Gill (2010).

Figure 2.2: Generalized IUGS nomenclature for coarse-grained alkali rocks, based on the silica undersaturated portion of the QAPF diagram (bottom left). The main diagram shows the modal nomenclature applied to rocks, in which nepheline is the dominant Foid. The rock types seen at the top of the diagram with < 10% nepheline are said to be "nepheline-bearing" or "foid bearing" rocks. f = foidolite, fmd = foid monzanite, fg = foid gabbro, P = feldspar >5% An, A = feldspar < 5% An. Taken from Gill (2010).

Figure 2.3: Ternary plot of peraluminous, metaluminous and peralkaline rocks, determined from whole rock $Na_2O + K_2O$, Al_2O and CaO content (in molar proportions; Gill, 2010).

Figure 2.4: Predictions of the geometry of igneous layering within potholes owing to crystal settling (a) and in situ crystallization (b). Settling of crystals from flowing/convecting melt will form layered rocks that are discordant with respect to pothole margins. In contrast, in situ crystallization should result in layering that follows the outlines of pothole margins, (Latypov et al., 2015).

Figure 5.1: Fume cupboard set up for heavy liquid separation using Tetrabromethane (TBE) at the Earth Laboratory in the University of the Witwatersrand.

Figure 5.2: a) Photomicrograph of the zircon grains in sample 542206 as they were being picked, grains are 0.5 mm or less. Schematic maps showing the position of each sample on its respective grain mount, as well as the rock type of each sample.

Figure 5.3: Concordia plots for the secondary standards that were measured while analyzing the Singertât Complex zircon samples a) CDQGNG b) Mud Tank.

Figure 6.1: Ternary diagram used to classify the Singertât rock samples based on the modal abundances obtained during petrographic analyses. M = melteigites, I = ijolites, U = urtites and S = syenitic gneisses.

Figure 6.2: a) Urtite from the Singertât Complex, SE Greenland. The green mineral is clinopyroxene while the grey mineral is nepheline and the white mineral is alkali feldspar (Sample 525988). b) Ijolite from the Singertât Complex, SE Greenland. The black-green mineral is clinopyroxene, while the grey-brown mineral is nepheline and the white mineral is alkali feldspar (Sample 542214). c) Melteigite from the Singertât Complex, SE Greenland. The black-green mineral is clinopyroxene, while the grey-brown mineral is nepheline and the white mineral is alkali feldspar (Sample 542203).

Figure 6.3: Photomicrographs of urtite sample 525988 showing the nepheline, anti-perthite and small percentage of clinopyroxene present in the sample. a) ppl, b) xpl.

Figure 6.4: Photomicrographs of Ijolite samples 542214 a) full thin section scan in ppl, b) thin sections scan in xpl, c) anti-perthite present in the ijolite samples in ppl, d) anti-perthite present in the ijolite samples in xpl.

Figure 6.5: Photomicrographs of Melteigite sample 542215 a) full thin section scan in ppl, b) thin sections scan in xpl, c) anti-perthite present in the ijolite samples in ppl, d) anti-perthite present in the ijolite samples in xpl

Figure 6.6: The layering seen between the nepheline-bearing alkaline rocks show in samples a)542205 which depicts a gradational change (dashed white line) between melteigite and ijolite and b) 542219, which depicts a sharp change (white line) from syenitic gneiss to melteigite to ijolite.

Figure 6.7: Photomicrographs of a layered nepheline-bearing rock sample 542216BII, which shows a gradational contact (indicated by the dashed white line) between an urtite and a melteigite layer. a) full thin section scans in ppl, b) thin sections scan in xpl.

Figure 6.8: Photomicrographs of a layered nepheline-bearing rock sample 542219AII, which shows a sharp contact between a syenitic gneiss and a melteigite layer (indicated by the white line), with a melteigite vein cross cutting the syenitic gneiss. a) full thin section scans in ppl, b) thin sections scan in xpl.

Figure 6.9: Photomicrographs of a layered nepheline-bearing rock sample 542219BII, which shows a gradational contact between an ijolite and a melteigite layer. In this sample there is little nepheline, however sodalite appears to be the dominant feldspathoid present and flow textures are observed in this sample, a) full thin section scan in ppl, b) thin sections scan in xpl c) depicts a truncated boundary seen in sample 542219CII.

Figure 6.10: Hand samples of a)525969 and b) 542206 which depicts pegmatitic nepheline (pale brown-grey), feldspars (white) and biotite (dark brown – black).

Figure 6.11: Photomicrographs of the pegmatite samples a) a zircon crystal in the sample 542206 in ppl, b) a zircon crystal in the sample 542206 in xpl, c) macrocrystic nepheline and anti-perthite in sample 542206 in ppl, d) pegmatitic nepheline and anti-perthite in sample 542206 in xpl, e) anti-perthite texture seen in sample 525969 in xpl, d) pegmatitic biotite crystals in sample 525969 in xpl.

Figure 6.12: Hand samples of a)525972, b)542232 and c) 542249 which depicts a carbonatite breccia (contains fragments of nepheline-bearing rocks and pegmatite), a carbonatite containing almost 100% calcite and a carbonatite containing high Ti-garnet respectively.

Figure 6.13: Photomicrographs of carbonatite sample 542249, which shows a garnet and clinopyroxene surrounded by a large amount of calcite. a) full thin section scans in ppl, b) nepheline xenocryst in carbonatite breccia in ppl and c) rounded fragments of ijolite in a carbonatite breccia in xpl.

Figure 6.14: Hand samples of a)542217, b)525981 and c) 525989 which depicts syenitic gneisses showing the typical gneissic texture (alignment of aegerine-augite and biotite grains).

Figure 6.15: Photomicrographs of syenitic gneiss sample 542217B a) full thin section scan in ppl, b) thin sections scan in xpl, c) anti-perthite present in the ijolite samples in ppl, d) anti-perthite present in the ijolite samples in xpl.

Figure 6.16: Variation diagrams depicting variations in mineral compositions for the layered sample 542205 which depicts gradational transitions from ijolite to melteigite and back to ijolite again. The blue dots represent analyses that were taken across the ijolite-melteigite boundary, while the black dots were analyses taken in the melteigite layer only.

Figure 6.17: Variation diagrams depicting variations in mineral compositions for the layered sample 542216 using samples 542216 BI and CII which transitions from ijolite to melteigite and melteigite to urtite respectively. The blue squares represent analyses from the ijolite layer and the blue dots represent analyses taken in the melteigite layer in samples 542216 CII. The black squares represent analyses from the urtite layer and the blue dots represent analyses taken in the melteigite layer in samples 542216 BI.

Figure 6.18: Variation diagrams depicting variations in mineral compositions for the layered sample 542219 using thin sections 542216 AII, CII and DII which transitions from syenitic gneiss to melteigite and then to ijolite. The black dots represent analyses from the syenitic gneiss layer, the blue dots represent analyses taken across the melteigite-ijolite transition and the red dots represent analyses from the ijolite layer.

Figure 6.19: Variation diagrams depicting variations in mineral compositions for the layered sample 542205 which depicts the core- rim data for aegerine-augite.

Figure 6.20: Variation diagrams depicting variations in mineral compositions for the layered samples 542216BI and 542216CII, which depicts the core- rim data for aegerine-augite.

Figure 6.21: Variation diagrams depicting variations in mineral compositions for the layered sample 542219 which depicts the aegerine augite crystals in the syenitic gneiss, a vein of aegerine-augite within the syenitic gneiss, melteigite and ijolite.

Figure 6.22: A ternary diagram representing the EPMA results for the clinopyroxene crystals found in the nepheline-bearing alkaline rocks of the Singertât Complex.

Figure 6.23: BSE taken of the EPMA image, which shows the sodalite that was analyzed in sample 542217B.

Figure 6.24: BSE image showing the anti-perthite that was analyzed in sample 542219. The dark grey lamellae are the orthoclase, while the lighter grey is the albite host.

Figure 6.25: Ternary diagram for all the samples that were analyzed using EPMA. The results seen are the averages taken for each sample and the orthoclase lamellae and albite host results are joined by tie-line for each sample.

Figure 6.26: Major element concentrations in wt% of the nepheline-bearing rocks, pegmatites, carbonatites and syenitic gneisses from the Singertât Complex.

Figure 6.27: Major element ratios of alkalis to alumina plotted for the nepheline-bearing rocks, pegmatites, carbonatites and syenitic gneisses from the Singertât Complex.

Figure 6.28: REE plots for different rock types that make up the Singertât Complex. The samples were normalized to chondrite (Anderson and Grevasse, 1988).

Figure 6.29: Trace element bivariate plot of Ce/Yb vs Sm, comparing the Singertât rocks as well as the alkaline rocks of Loucna-Oberwiesenthal. a) All Singertât rock types, b) Singertât nepheline-bearing alkaline rocks.

Figure 6.30: CL images depicting laser spot locations of the magmatic zircons in the pegmatite.

Figure 6.31: CL images depicting laser spot analyses of the magmatic zircons in the ijolite sample 525971.

Figure 6.32: CL images depicting the laser spots of the magmatic zircons in the carbonatite breccia sample 525972.

Figure 6.33: CL images depicting the laser spots of the magmatic zircons in the melteigite sample 542204.

Figure 6.34: CL images depicting the laser spots of the magmatic zircons in the pegmatite sample 542206.

Figure 6.35: Concordia plots for the nepheline-bearing rocks, pegmatites and a carbonatite used to determine $^{207}Pb/^{206}Pb$ ages.

Figure 7.1: Geological timeline depicting the ages of the zircons analyzed in this study placing the timing of the Singertat Complex emplacement in the early stages of the Skjoldungen Orogen (Kolb et al., 2013). Note that no error bar was provided for the Blichert-Toft et al., 1995 age, seen as the gray triangle.

Figure 7.2: A geological map of the Singertât Complex of the SAIP by Nielson and Rosing, 1990. The map indicates sample localities for a selection of alkaline rocks (green dots) and the syenitic gneisses (red dots) that were sampled on the 2012 expedition as well as the ages determined for the sample indicated using red circles.

Figure 7.3: Whole-rock data in molecular proportions of the Singertât Complex in Comparison to the rocks from the Gardar Province, the Kola Peninsula and the Tamazeght complex plotted on an AI vs ASI diagram using the definitions by Frost & Frost (2008). They gray fields indicate the composition of important fractionating mineral phases (Marks et al., 2011).

Figure 7.4: Photomicrograph (d) shows a truncated boundary as a result of thermal erosion with in-situ crystallization of nepheline and anti-perthite along the boundary

Figure 7.5: Predictions of the geometry of igneous layering within potholes owing to crystal settling (a) and in situ crystallization (b). Settling of crystals from flowing/convecting melt will form layered rocks that are discordant with respect to pothole margins. In contrast, in situ crystallization should result in layering that follows the outlines of pothole margins, (Latypov et al., 2015).

Figure 7.6: Depicting the compositionally different populations of nepheline across sharp boundaries in between and ijolite and a melteigite and a melteigite and urtite.

Figure 7.7: Variation diagrams depicting variations in mineral compositions for the layered sample 542205 which depicts variation form the core- rim data for aegerine-augite.

Figure 7.8: Sample 542219 depicting flow textures in a nepheline-bearing rock, which may have formed due to new magma being emplaced in a magma chamber resulting in convection currents which formed the flow textures.

Figure 7.9: Melteigite depicting orthoculamte texture seen in the nepheline-bearing rocks of the Singertât Complex. We observe cumulate aegerine-augite with intercumulus nepheline.

Figure 7.10: REE plots for the nepheline-bearing alkaline rocks of the Singertât Complex. The samples were normalized to chondrite (Anderson and Grevasse, 1988)

1. Introduction

The main focus of this project is the peralkaline Singertât Complex, which forms part of the Skjoldungen Alkaline Igneous Province (SAIP) of SE Greenland. The Singertât Complex comprises a variety of silica undersaturated alkaline rocks (e.g., urtites, ijolites and melteigites), which occur as modally layered sheets with minor late-stage foyaitic pegmatite and carbonatitic rocks. Preliminary geochemical and geochronological research has been conducted on the SAIP, suggesting that the province may have formed due to arc magmatism in the Late Archean (2720-2650 Ma)(Blichert-Toft *et al.*, 1995 and Kolb *et al.*, 2013). However, very little investigation of the Singertât Complex has been completed, even though it is unique, and possibly the oldest example of a peralkaline intrusion (Blichert-Toft, Arndt and Ludden, 1996). Peralkaline complexes can be economically important due to the fact that the layered rocks are associated with multi-element ore deposits, often containing high concentrations of rare earth elements and phosphorus, as well as other critical metals such as tantalum, niobium and uranium. Furthermore, the formation of layering in ijolite complexes is poorly understood, as is the case in layered mafic intrusions such as the Bushveld Complex (South Africa). Due to recent uplift and erosion, in addition to previous glacial coverage of the passive East Greenland continental margin, the Singertât Complex has experienced little to none of the pervasive alteration usually associated with peralkaline complexes, making it an ideal candidate for an in-depth investigation of the mineralogy and petrology of economically important peralkaline magmatic systems. It should be noted that compositionally similar intrusive complexes are typically highly overprinted or metasomatized (e.g., Phalaborwa and Pilanesberg), which hampers our understanding of the origin of peralkaline rocks and associated mineralization. Although the Singertât Complex is very well preserved, barely any geochemical and geochronological research has been conducted on this intrusive body due to its remote location and harsh climatic conditions in SE Greenland. Therefore, the aim of this project is to understand the origin and

evolution of the magma(s) that formed the Singertât Complex. This will include understanding of the processes that the magma may have experienced from the mantle source to final emplacement at crustal level, magma and crystal dynamics, as well as the evolution of crystal cargo in the system

1.1 Location and Sampling

The Skjoldungen Province of SE Greenland (Figure 1.1) is made up of numerous peralkaline intrusions (~3000 km²), which were emplaced into a well-defined NW-SE-trending tract (Rosing *et al.*, 1988). The Singertât Complex (~8 km²; Figure 1.2) represents one of these peralkaline intrusions and was emplaced into tonalitic gneiss, amphibolite and quartz syenite of the southern part of the SAIP as a sheet-like intrusion in the Late Archean at ca. 2664 + 4/-2 Ma (Blichert-Toft *et al*., 1995; Nielsen and Rosing, 1990; Kolb, 2010). Extensive sampling of the Singertât Complex took place in 2012 by Prof. Sebastian Tappe in collaboration with the Geological Survey of Denmark and Greenland, with samples currently curated at the University of Johannesburg. Fifty-one samples were selected for this project (Figure 1.2) and include a suite of nepheline-bearing, felsic to mafic lithologies plus several carbonatites, pegmatites and syenitic gneisses. The nepheline-bearing rocks make up the majority of the complex and are cross-cut by the pegmatitic rocks, while the carbonatite breccias cross-cuts the nepheline-bearing rocks as well as the pegmatitic rocks. The syenitic gneiss surrounds the entire complex

and is said to be the host rock intruded by the Singertât Complex (Figure 1.2) (Blichert-Toft et al., 1995; Kolb, 2010).

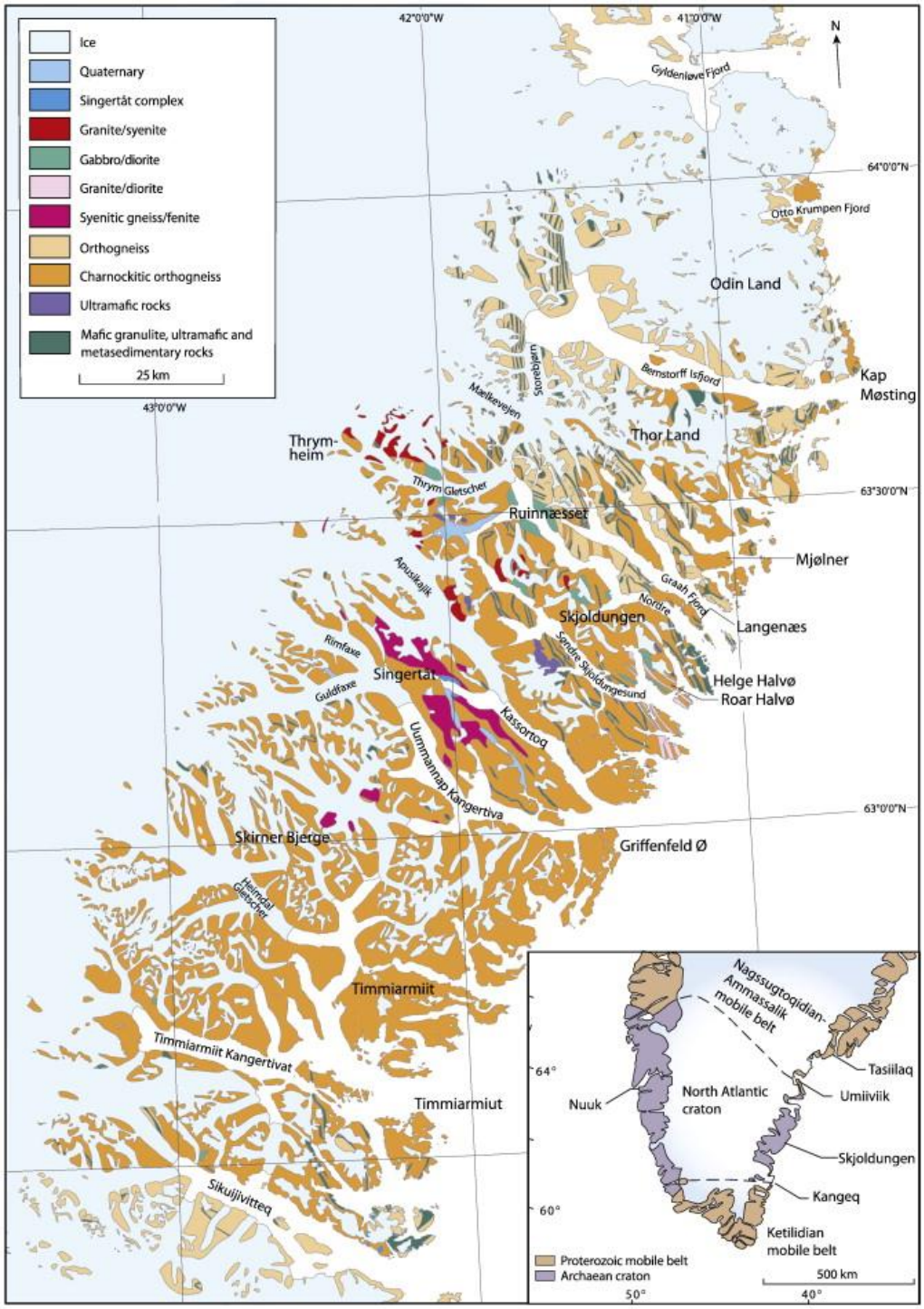
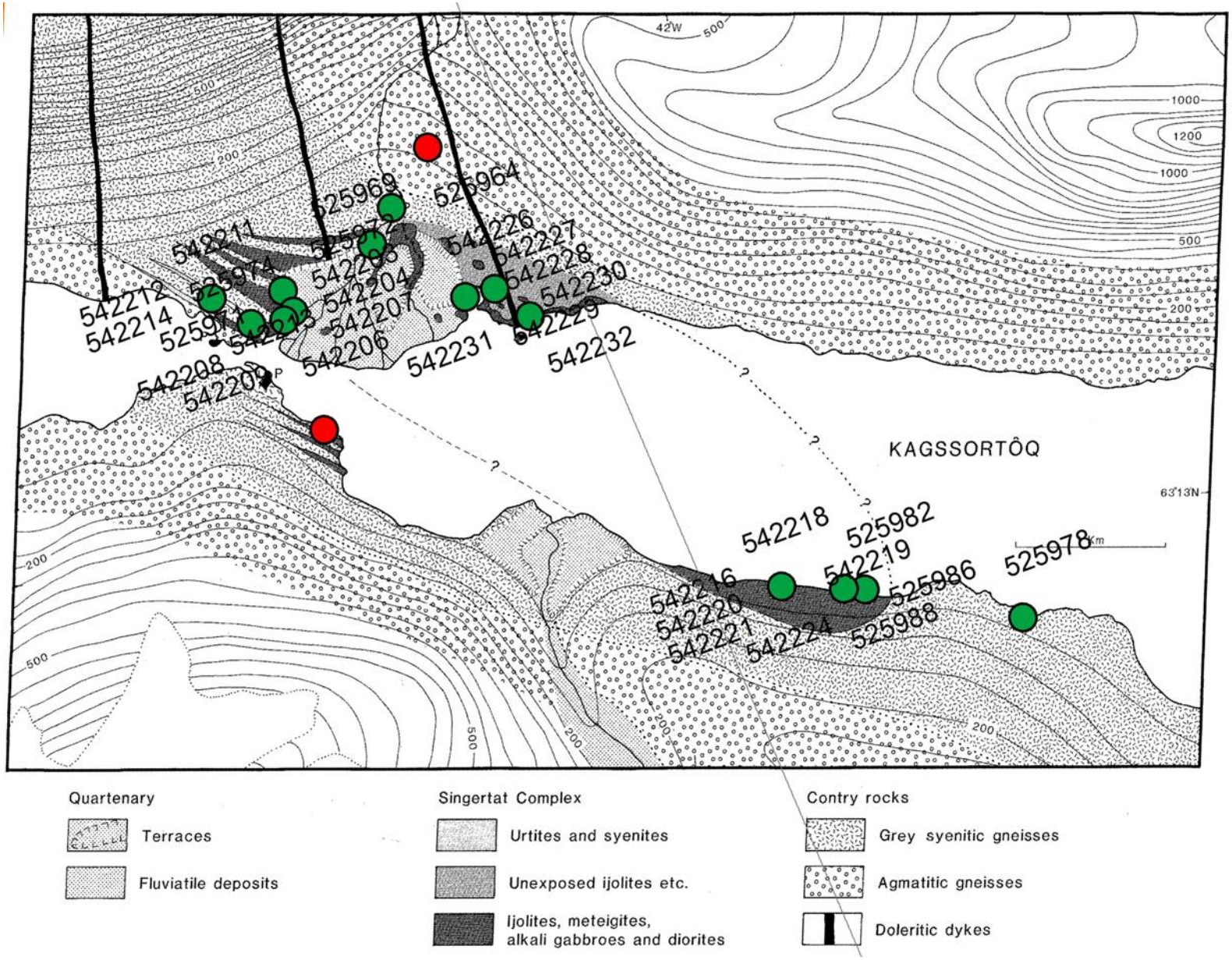


Figure 1.1: Schematic geological map showing the lithologies that make up the North Atlantic Craton (NAC). The inset shown on the bottom right of the geological map, shows the location of the SAIP and NAC in southern Greenland (Kolb et al., 2013).



<u>Figure 1.2:</u> A geological map of the Singertât Complex of the SAIP by Nielson and Rosing, 1990. The map indicates sample localities for a selection of alkaline rocks (green dots) and the syenitic gneisses (red dots) that were sampled on the 2012 expedition.

1.2 Geological setting

The Archean rocks of southern Greenland extend over ~ 500 km on the eastern coast and ~ 700 km on the western coast, forming part of the North Atlantic Craton (NAC; Figure 1.3). The NAC assembled during the Late Archean due the subduction and collision of Early Archean microcontinents (Windley and Garde, 2009). According to Tappe *et al*. (2011), the growth and stabilization of the NAC in the Late Archean was due to tectonic stacking of heterogeneous oceanic lithosphere accompanied by voluminous tonalite–trondhjemite–granodiorite (TTG) magmatism along active margins.

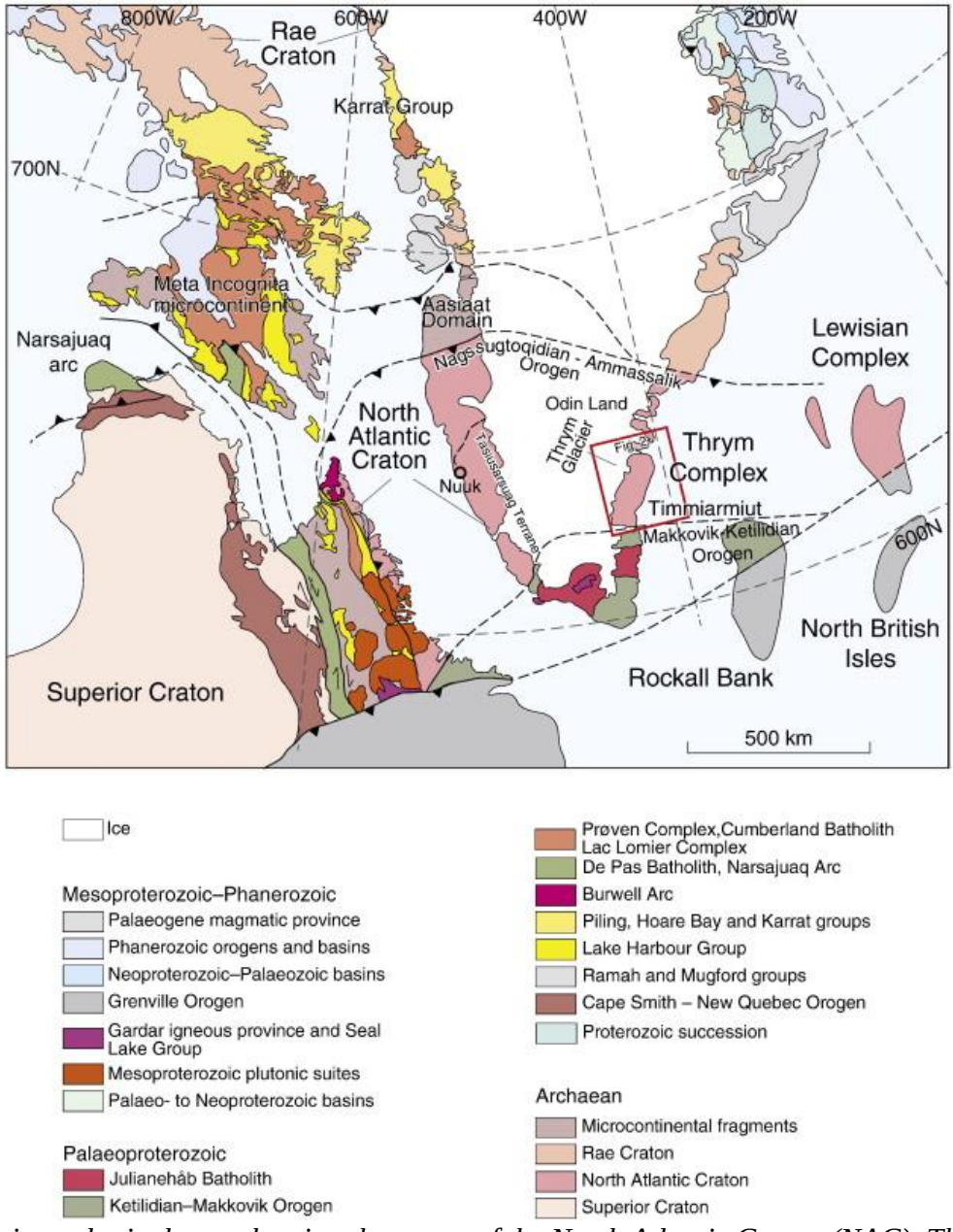
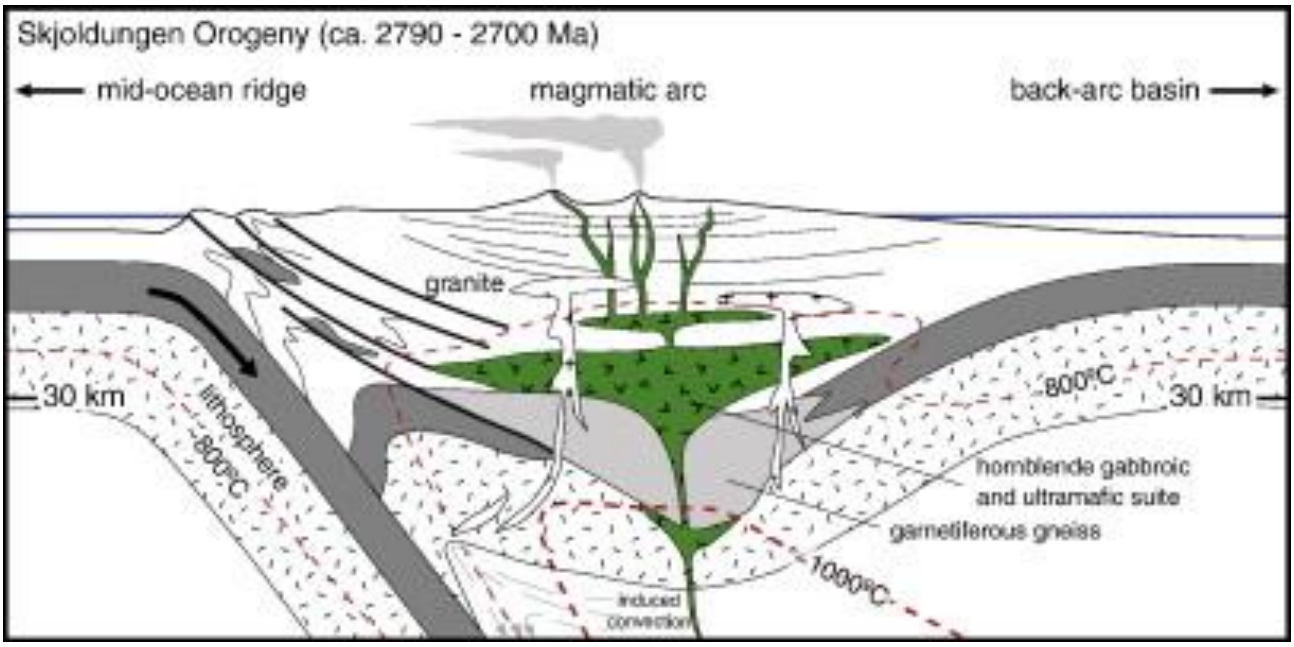
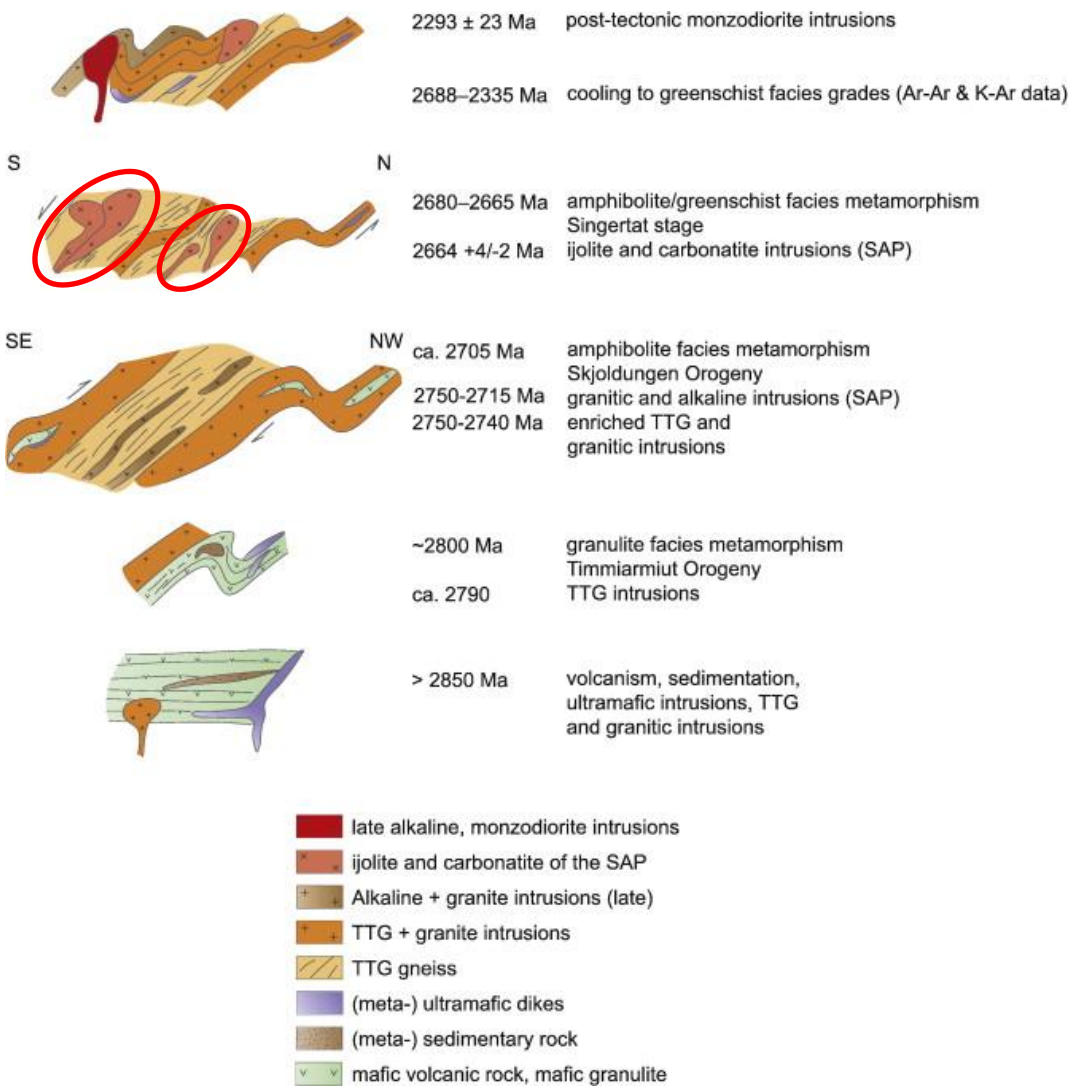


Figure 1.3: Schematic geological map showing the extent of the North Atlantic Craton (NAC). The red box shows the location of the SAIP on the NAC. (Bagas et al., 2013).

The SAIP is located within the NAC and is exposed on the eastern coast of southern Greenland. The ~ 2.76 – 2.68 Ga Skjoldungen Orogeny, was accompanied by granulite facies peak metamorphism and complex calc-alkaline to alkaline and carbonatitic magmatism (Kolb *et al.*, 2015; Blichert-Toft *et al*., 1995). The basement in southeast Greenland, which was intruded by the SAIP, is said to be older than 2865 Ma and possibly as old as 3450 Ma (Kolb *et al*., 2013). At ~ 2.7 Ga the Skjoldungen Arc was formed (Kolb, 2010; Kolb *et al*., 2013), the orogen was exhumed to greenschist-facies relatively quickly, the deformation associated with the orogeny resulted in isoclinal folding and shearing of the surrounding Mesoarchean rocks of the Thrym Complex (Kolb *et al*., 2013b; Berger *et al*., 2014). These shear zones would serve as conduits for upwelling magma coming off the subducting slab in the Skjoldungen arc (Figure 1.4). Magmatism, due to the formation of the Skjoldungen Arc, began at ~ 2.75 Ga (Figure 1.4) with the emplacement of quartz-monzodiorite to syenite and ultramafic intrusions (Kolb *et al*., 2015; Bagas *et al.*, 2013). The shear zones, which are a result of the deformation caused by orogeny, are said to be associated with the ~2.72-2.70 Ga alkaline rocks, which include hornblende-pyroxenite, hornblendite, hornblende-norite, diorite, leucogabbro, monzonite, monzodiorite and syenite (Blichert-Toft *et al*., 1995). At ~ 2.68 Ga, orogen-normal extension, known as the Singertât Stage of deformation, resulted in alkaline-carbonate magmatism (i.e. nephelinite and carbonatite magmas), which formed the intrusive Singertât Complex (Figure 1.5) (Kolb *et al*., 2013b; Kolb *et al*., 2015).



<u>Figure 1.4</u>: Schematic of the Skjoldungen Arc during the Skjoldungen Orogen taken from Bagas et al. (2013).



<u>Figure 1.5:</u> Synoptic sketch by Bagas et al. (2013), which depicts a proposed Late Archean to Early Proterozoic evolution of the NAC in southeast Greenland. The Singertât Complex intruded at approximately 2664 +4/-2 Ma (Nielson and Rosing, 1990 and Kolb et al., 2012a) and is indicated by the red circles.

2. Literature Review

2.1 Alkaline igneous rocks

According to Gill (2010), the alkaline igneous rock category encompasses a wide spectrum of rock types, from ultramafic to felsic. The fascination with these rocks relates to their composition and mineral assemblages which are characterized by:

- A deficiency in SiO_2, resulting in the crystallization of various feldspathoids in place of feldspar species (Figure 2.1).
- Mineral families such as pyroxene and amphibole often appear in alkali rocks. These minerals include sodic clinopyroxenes such as aegerine-augite and riebeckite, a sodic amphibole.
- High concentrations of incompatible elements in alkaline magmas which results in (at least in evolved peralkaline rocks) rare accessory minerals, such as eudialyte and arfvedsonite.

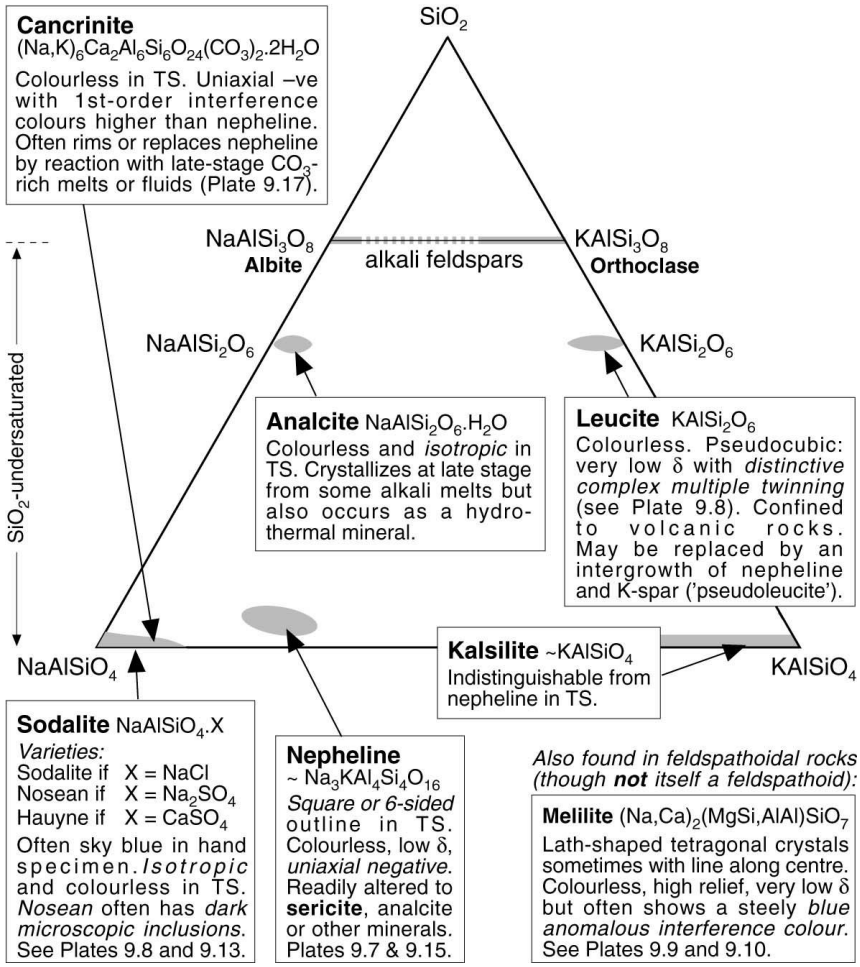


Figure 2.1: Ternary diagram showing how different feldspathoids relate compositionally and the different alkali feldspars (in molar proportions). Optical features of each feldspathoid is present. TS=thin section. Taken from Gill (2010).

The nepheline-bearing rocks (Figure 2.2), according to Gill (2010), are classified into two categories. The first being nephelinite, which refers to a volcanic rock consisting essentially of nepheline and pyroxene. The second being nephilinolite, which refers to a plutonic rock in which nepheline is the abundant feldspathoid. Therefore, to avoid unusual and cumbersome terms, nepheline-bearing rocks in this study will be referred to as urtite, ijolite and melteigite, on the basis of mafic mineral content in the rock. Urtite is the more felsic of the three rock types with over 70% nepheline, ijolite is an intermediate rock type with between 30% - 70% nepheline and melteigite is the more mafic rock type with between 10% - 30% nepheline (Le Maitre, 2002). Gill (2010) refers to melteigite, urtite and ijolite as variations of nephelinitic magmas intruded at depth.

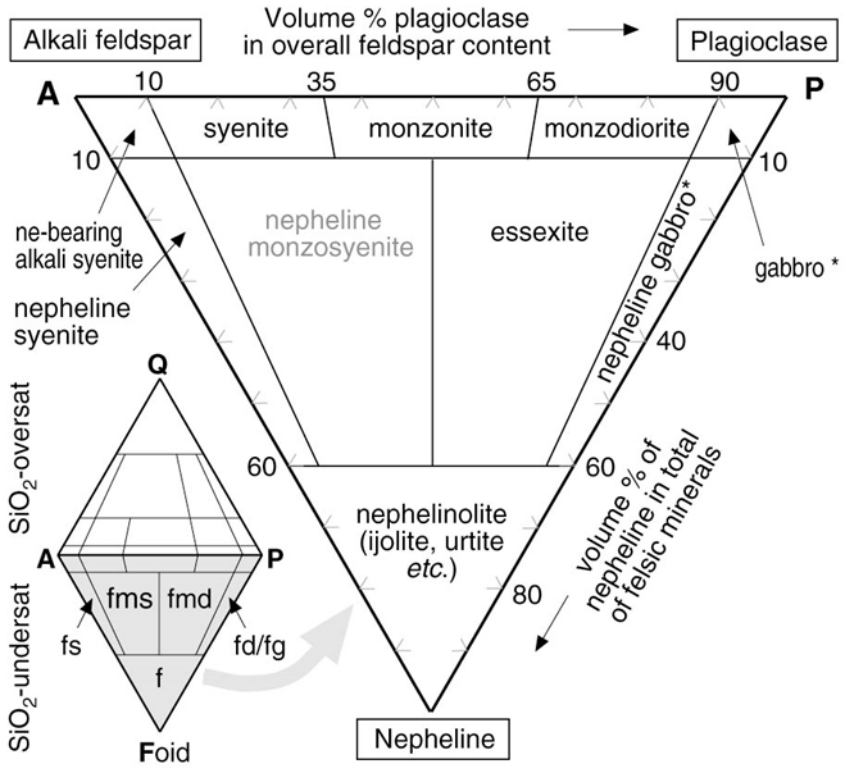


Figure 2.2: Generalized IUGS nomenclature for coarse-grained alkali rocks, based on the silica undersaturated portion of the QAPF diagram (bottom left). The main diagram shows the modal nomenclature applied to rocks, in which nepheline is the dominant Foid. The rock types seen at the top of the diagram with < 10% nepheline are said to be "nepheline-bearing" or "foid bearing" rocks. f = foidolite, fmd = foid monzanite, fg = foid gabbro, P = feldspar >5% An, A = feldspar < 5% An. Taken from Gill (2010)

2.2. Peralkaline rocks versus metaluminous rocks

According to Gill (2010) and Le Maitre *et al.* (2002), peralkaline is a chemical term for rocks in which the molecular amounts of $Na_2O + K_2O > Al_2O$. In contrast, rocks in which the molecular amounts of $Na_2O + K_2O < Al_2O$, are considered to be metaluminous (Figure 2.3). According to Marks et al. (2011), peraluminous nepheline syenites are a rare occurrence as nepheline syenites are usually either metaluminous or peralkaline.

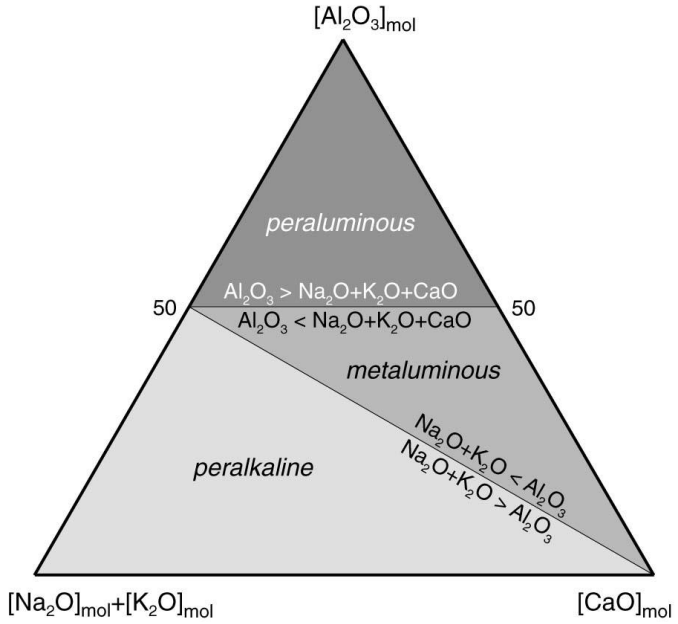


Figure 2.3: Ternary plot of peraluminous, metaluminous and peralkaline rocks, determined from whole rock $Na_2O + K_2O$, Al_2O and CaO content (in molar proportions; Gill, 2010).

Peralkaline rocks may be divided into two categories, agpaitic and miaskitic, which can be defined as follows (Le Maitre, 2002):

- Agpaitic is a general term to characterize nepheline syenites, these rocks generally have high contents of Na, Fe, Cl and Zr with low Mg and Ca. Agpaitic rocks are restricted to nepheline syenites which contain Zr and Ti minerals i.e. eudialyte and zircon. For agpaitic rocks the molecular ratio $(Na_2O + K_2O) / Al_2O_3 > 1$.
- Miaskitic is said to be a leucocratic variety of biotite-nepheline monzosyenite, with oligoclase and perthite orthoclase. For miaskitic rocks the molecular ratio is also $(Na_2O + K_2O) / Al_2O_3 < 1$. The Singertât Complex is said to be a miaskitic peralkaline complex (Blichert-Toft *et al*., 1995).

According to Marks and Markl, (2017), peralkaline rocks are rich in the following:

- High ion lithophile elements (LILE i.e. Li, Na, K, Rb and Cs)
- Halogens (F, Cl, Br and I),
- Rare earth elements
- High field strength elements (HFSEs i.e. Zr, Hf, Nb, Ta and U)

It is due to this extreme enrichment of alkalis, HFSEs, halogens and REEs during the differentiation of peralkaline magmas that the precipitation of a substantial amount of rare minerals including F-bearing phases (e.g. villiaumite) and Cl-minerals (e.g. sodalite) may result. Peralkaline magmatic systems appear to be Cl-rich

compared to metaluminous systems, because in peralkaline systems, Cl partitions into the melt phase rather than into coexisting fluids. Hence, degassing of Cl in metaluminous systems is much larger than in peralkaline varieties (Marks and Markl, 2017; Bacon et al., 1992). The Cl in many peralkaline rocks partition into what is known as early-magmatic sodalite-group minerals (SGMs). These SGMs can be subdivided into Cl-rich (sodalite *sensu stricto*) and S-rich (haüyne and nosean). This is important because SGMs are often sulfate-rich in miaskitic rocks, while Cl-rich in agpaitic rocks (Mark and Markl, 2017; Parat et al., 2011; Krumrei et al., 2007). Marks et al. (2011) also state that sodalite present in nepheline syenites, syenitic gneisses or nepheline-rich rocks may indicate a transition from miaskitic to agpaitic.

According to Marks et al. (2011), the mineralogical transition from miaskitic to agpaitic depends on variations in the chemical potentials of Na_2O, K_2O and CaO in the melt. These then define two evolutionary paths for agpaitic rocks; the first being the Ca-depleted trend (e.g. Gardar Province) and the second being the high-Ca trend (e.g. Kola Peninsula). The Ca-depleted trend forms from basaltic parental melts due to fractionation of plagioclase prior to the formation of the peralkaline plutonic rocks. While high-Ca trends can only form if the plagioclase fractionation did not occur in the early fractionation history of the precursor melts, which were most likely nephlinitic in composition.

2.3 Development of igneous layering

The layering observed in peraluminous to peralkaline intrusions is common throughout geological history (Naslund and McBirney, 1996). The layering observed in these intrusions is said to represent processes in fossilized magma chambers and can, therefore, aid in the understanding of magma origin and evolution (O'Driscoll *et al*., 2014). The formation of these layers is said to occur at the cumulus stage through processes such as gravity settling, in-situ crystallization, gain or loss of volatiles, pressure changes, magma replenishments and assimilation (Irvine, 1987; Spandler *et al*., 2005; Mondal and Mathez, 2007).

Magma chambers that experience multiple injections of crystal-rich magma (entrained crystal cargos), may result in the formation of primary igneous layering (Hunt, 2015). The microphenocrysts entrained in these magmas are likely to have nucleated in a plumbing system below the main chamber (i.e. a lower magma chamber or staging magma chamber), where they were incorporated into the magma as suspended load and injected into the upper magma chamber (Eales, 2000). Development of stratiform layers on the magma chamber floor would form as a result of settling of these crystals from suspension or injection as crystal-rich slurries. Repeated replenishment events would result in cyclicity of the layering (Hunt, 2015; Mondal and Mathez, 2007). However, development of primary igneous layering may also occur due to convection currents and thermal gradients (Marsh, 2013). Double-diffusive convection cells are said to account for primary igneous layering and occur in magma bodies in

which variation in composition exists (Hunt, 2015; Hupert and Sparks, 1984). Thermal gradients present within a magma chamber allow for crystal nucleation at thermal boundaries. This nucleation is a result of the lowering of the liquidus temperature as a response to cooling at the thermal boundary. The crystals that nucleate at the thermal boundary may be transported away by convection currents and will either dissolve or continue to grow (which may result in the formation of a crystal mush) (Marsh, 2013; Hunt, 2015).

According to Marsh (2013), the processes responsible for the formation of layering in large igneous intrusions is undoubtedly due to injections of crystal-rich slurries in the magma system. Marsh (2013) argues that layers form as a result of repetition of emplaced magmas carrying phenocrysts with appropriate composition. Marsh (2013) notes that layering may be formed from crystal-rich slurries in the following scenarios:

- Layering in granular avalanches: this occurs when crystals with significantly different angles of repose and shape are poured together and form a conical heap. The coarser grains roll down the bed of fine particles much easier than finer particles run down a heap of coarse particles. The fine particles sieve through and fill the interstices among the larger particles. The heap then grows in size and an avalanche occurs and the grains reaching the base of the pile form a slope with a distinct break or kink in its profile, which runs back up slope to form a layer. The layering produced in this process is reversely graded, coarse over fine.
- Kinetic sieving in granular flows: in poorly sorted granular flows, particles become sorted by size. This depicts an upward migration of large particles in a finer medium due to kinetic sieving.
- Layering and segregation in slurry sedimentation: a large contrast in size allows small particles to sieve through the matrix of larger grains, even when the larger grains are at maximum packing. Small grains plug the matrix and collect at specific horizons, spread horizontally, separating the larger grains and forming an extensive layer. The higher the density contrast between the size classes, the better the layering or segregation. In experiments with metallic copper grains as the small particles and leucite as the larger particles, the copper forms unusually sharp and distinct layers strikingly similar to the Dwars River chromite seams in Bushveld anorthosite.

However, Latypov *et al*. (2015) state that it is improbable for repeated recharge of magma that invariably contained phenocrysts with just the right compositions to mimic fractional crystallization of a single parent magma. Latypov *et al*. (2015) therefore propose that layering in igneous intrusions is more likely a result of internal processes occurring within the main magma chamber, such as *in-situ* crystallization or gravity settling as seen in Figure 2.4, which shows layer formation in potholes of the Merensky Reef in the Bushveld Complex. While Latypov (2015) does not denounce the fact that magma replenishments may hold crystals in suspension, he says it is improbable that each layer in a layered intrusion formed as a result of a single pulse of crystal rich magma which does not undergo some sort of in-situ crystallization. Evidence for this is cryptic layering which is

ignored by March (2013), as this presents an obstacle the acceptance of external crystal slurries as essential components in the development of layered cumulates.

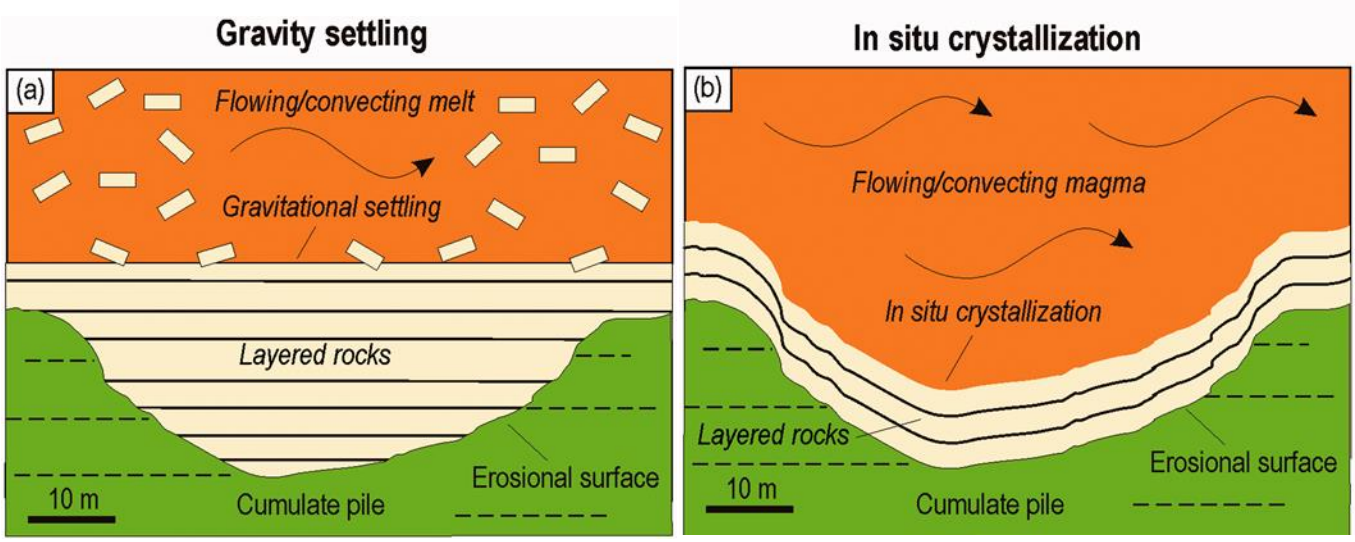


Figure 2.4: Predictions of the geometry of igneous layering within potholes owing to crystal settling (a) and in situ crystallization (b). Settling of crystals from flowing/convecting melt will form layered rocks that are discordant with respect to pothole margins. In contrast, in situ crystallization should result in layering that follows the outlines of pothole margins, (Latypov et al., 2015).

3. Aims and Objectives

The overarching aim of this project is to understand the origin and evolution of the magmas that formed the Singertât Complex. An understanding of the origin and evolution or petrogenesis of the magma(s) includes assessing the processes that the magma may have experienced from the mantle source to final emplacement at upper crustal level, magma and crystal dynamics, as well as the evolution of the crystal cargo in the system.

The main objectives that will assist in achieving these aims include:

- Understanding whether the complex is constructed from multiple batches of magma, or a single pulse.
- Determining whether those magma batches were mushes (crystal-bearing) or were emplaced mainly as crystal-poor liquids.
- Determining the processes of crystallization, such as gravity settling or in-situ crystallization that operated in the magma chamber and assessing the layering mechanism in these alkaline rocks.
- Determine if any relationship exists between the "host" syenitic gneisses and the alkaline rocks of the Singertât Complex.
- Determine and better constrain the age of the Singertât Complex using U/Pb geochronology.

4. Hypothesis

We propose that the Singertât Complex operated as an open-magma system, whereby the main magma chamber experienced multiple magma injections of crystal-bearing liquid. We also propose that while the magma chamber may have experienced repeated replenishment events of crystal slurries, the dominant crystallization processes occurring within the magma chamber is in-situ crystallization. This may account for the compositional and textural variation, as well as the sharp layer boundaries seen in the layered nepheline-bearing intrusive rocks. We further propose that the syenitic gneisses are not host rocks, but rather that the syenitic gneisses formed with the at the same time as the other rocks which make up the Singertât Complex.

5. Methodology

5.1 Electron probe microanalysis (EPMA):

Electron probe microanalysis was performed at the Spectrum analytical facilities of the University of Johannesburg, using the Cameca SX-100 instrument operating at 20 kV with a beam current of 20 nA. SiO_2, Na_2O, CaO, K_2O, MgO, Al_2O_3, TiO_2, MnO, Cr_2O_3 and (total Fe as) FeO. All elements were measured by analyzing the cations on their Kα lines. Electron microprobe analysis was performed on the clinopyroxene, nephelines and feldspars from 12 Singertât samples. The 12 samples were all carbon coated at the University of Johannesburg

5.2 Whole-rock analyses

Of the 51 samples selected for this project, 26 representative samples were analyzed for whole rock major and trace element compositions. The 26 samples were coarsely crushed by hand using a hammer and steel plate at the University of the Witwatersrand. Samples were then milled to a powder using the carbide steel swing mill at the University of Johannesburg.

5.2.1 Major element analyses

Major element (SiO_2, Al_2O_3, CaO, Na_2O, K_2O, Fe_2O_3, MgO, TiO_2, MnO, P_2O_5, NiO, Cr_2O_3, SO_3) compositions of 20 samples were determined by X-Ray Fluorescence (XRF) using the Panalytical PW2404 spectrometer, located in the Earth Laboratory at the University of the Witwatersrand. The powdered samples were prepared into fusion disks, using a Spectroflux 105 flux, according to the following method provided by the Earth Laboratory at the University of the Witwatersrand:

Samples were first dried in a furnace at 1020 °C.

- Approximately 1.75g of Spectroflux 105 was added into each Pt crucible. The sample was then ignited at 1020^{o}C for 40 minutes after which the samples were removed from the furnace and allowed to cool in a desiccator.
- Using the Pt crucible ID and LOI dishes ID number to match the samples. Approximately 0.34g of the pre-ignited sample is measured into each corresponding Pt crucible. Samples are ignited at 1020^{o}C for 50 minutes after which remove samples from the furnace and allow to cool in a desiccator.
- Fusion beads were individually poured and pressed on the hot plate.
- The beads were allowed to on the hot plate after which the hot plate was switched off to allow to anneal overnight. The samples were then ready to be analyzed.

The results for the CRMs measured can be found in Table 1.

Table 1: Results of the CRMS that were analyzed as unknowns at the Earth Laboratory in the University of the Witwatersrand with the Singertât samples.

	SiO_2	Al_2O_3	Fe_2O_3	FeO	MnO	MgO	CaO	Na_2O	K_2O	TiO_2	P_2O_5	Cr_2O_3	NiO	TOTAL	LOI
NIM-P	51.15	4.3	1.28	10.39	0.22	25.44	2.63	0.34	0.09	0.189	0.03	3.5535	0.0772	99.69	-0.23
NIM-D	38.9	0.32	1.71	13.85	0.22	43.83	0.3	0.01	0.01	0.0251	0.01	0.4013	0.2649	99.85	-0.51
W2	53.06	15.59	1.1	8.88	0.17	6.48	10.96	2.24	0.63	1.0706	0.13	0.0287	0.0114	100.35	0.19
NIM-S	63.84	17.4	0.14	1.13	0.01	0.46	0.69	0.37	15.4	0.048	0.12	0.0168	0.0001	99.61	0.42
GSP2	67.34	15.12	0.5	4.01	0.04	0.97	2.13	2.85	5.46	0.6722	0.29	0.0127	0.0031	99.41	0.87
BCR2	55.05	13.77	1.4	11.31	0.19	3.66	7.18	3.21	1.81	2.2823	0.36	0.0194	0.0007	100.24	0.1
NIM-N	53.31	16.81	0.91	7.33	0.18	7.61	11.55	2.45	0.25	0.1975	0.02	0.0186	0.0152	100.65	0.04
NIM-G	76.57	12.32	0.2	1.6	0.02	0.04	0.8	3.35	5.09	0.097	0.01	0.0156	-0.0014	100.12	0.73
PCC1	43.9	0.73	0.87	7.01	0.13	45.72	0.59	0.06	0.01	0.0139	0.01	0.4076	0.33	99.77	5.09
BHVO2	50.2	13.76	1.25	10.12	0.17	7.32	11.45	2.22	0.52	2.7408	0.27	0.0541	0.0155	100.09	-0.48
AGV2	60.55	17.31	0.68	5.53	0.1	1.82	5.3	4.29	2.94	1.047	0.48	0.0135	0.0023	100.05	1.8
G2	69.72	15.48	0.27	2.17	0.03	0.77	1.96	4.1	4.53	0.4868	0.14	0.0101	-0.0004	99.67	0.64
DTS1	41.02	0.25	0.87	7.06	0.12	50.17	0.16	0.08	0	0.0064	0.01	0.5733	0.3131	100.64	-0.02
G2	69.73	15.48	0.27	2.16	0.03	0.76	1.95	4.11	4.52	0.4851	0.14	0.0104	-0.0021	99.65	0.64
For CRMs 10% of total Fe allocated as Fe3+															

Major element (SiO_2, Al_2O_3, CaO, Na_2O, K_2O, Fe_2O_3, MgO, TiO_2, MnO, P_2O_5, NiO, Cr_2O_3, SO_3, BaO, V_2O_5) compositions of the 6 carbonatite samples were determined by XRF using the wavelength-dispersive XRF spectrometer Malvern Panalytical MagiX PRO located in the analytical facilities (Spectrum) of the University of Johannesburg because this facility has more experience analyzing carbonatites and yields some of the best results for these rock types . The powdered samples were prepared into fusion discs using the following method provided by the Spectrum at the University of Johannesburg:

Samples were first dried in a furnace at 105 °C.

- 1 g of the dried material was used to determine the loss on ignition (LOI) after about 30 min at 930 °C.
- 0.7 g of the dried material was mixed with 0.5 g $LiNO_3$ and 5.9 g of a lithium borate flux, fused for 19 minutes in a Pt–5 % Au crucible at 1050 °C and then cast to form a glass disc on cooling. An electric fusion machine called TheOx from Claisse.
- The lithium borate flux consisted of 49.75 mass % $Li_2B_4O_7$, 49.75 mass % $LiBO_2$ and 0.50 mass % LiBr.
- The LOI measurements and fusions were done in an air atmosphere.
- Borate fusion discs of BE-N, JSy-1, SARM 2 and SARM 16 together with the unknowns. The measurements of the RMs were used for a drift correction.

The XRF major element method had been calibrated with mixtures of pure chemicals (essentially oxides) and with certified reference materials (RMs) using a fundamental parameters model. This allows for all combinations of elements within the range of the calibration from about 0.05 mass % up to:

- 3 mass % Cr2O3.
- 20 mass % for Na_2O, SO_3, K_2O, V_2O_5, NiO and BaO.
- 40 mass % P_2O_5.
- 50 mass % for MgO and TiO_2.
- 65 mass % MnO.
- 90 mass % CaO.
- 95 mass % Fe_2O_3.
- 100 mass % for Al_2O_3 and SiO_2.

5.2.2 Trace element analyses

Trace elements were analyzed for the same 26 samples by inductively-coupled plasma mass spectroscopy (ICP-MS) using a Perkin-Elmer ELAN DRC in the Earth Laboratory at the University of the Witwatersrand. The analytical procedure is described as follows:

50 mg of sample powder is dissolved in a 2:1 HF/HNO_3 mixture and is placed into the microwave digester at 190°C and 450 PSI, for 40 minutes.

- Samples are then evaporated on the hot plate at 70°C until all the liquid has evaporated.
- 2 ml of HNO_3 is then added, the beakers are capped and placed on a hot plate at 60°C for 24 hours.
- After 24 hours the cap is removed and the beakers are placed on a hot plate at 70°C until all the liquid has evaporated.
- 2ml of HNO_3 is added to the sample and left to evaporate.
- Once all the liquid is evaporated 300 µl of HNO_3 is added and the sample is ready to be analyzed using ICP-MS.

Standardization was USGS against artificial multi-element standards BCR-2 and BHVO-2, results can be seen in Table 2.

Table 2: Results for artificial multi-element standards BHVO-2, which were run with the Singertât samples.

	This study			Published values			
	Run 1	Run 2	Run 3	1	2	3	4
La	12.00	12.02	15.14	15.2	15	14.8	15.25
Ce	31.51	32.11	36.59	37.5	38	38.8	37.84
Pr	4.25	4.33	4.94	5.29			5.351
Nd	19.44	19.62	23.35	24.5	25	24.6	24.39
Sm	4.81	4.85	5.63	6.07	6.2	6	6.03
Eu	1.68	1.69	1.89	2.07		2.01	2.036
Gd	5.01	4.95	5.86	6.24	6.3		6.229

Tb	0.79	0.77	0.84	0.936	0.9	0.88	
Dy	4.15	4.11	4.84	5.31			5.3
Ho	0.76	0.74	0.89	0.972	1.04		
Er	2.05	2.04	2.25	2.54			2.547
Tm	0.26	0.25	0.29	0.341			
Yb	1.53	1.53	1.93	2	2	1.89	1.955
Lu	0.22	0.21	0.25	0.274	0.28	0.275	0.2709

1 = Raczek *et al.* (2001); 2 = Wilson (1997); 3 = Ila & Frey (2000); 4 = Kent *et al.* (2004)

5.2.3 Zircon Mineral Separation

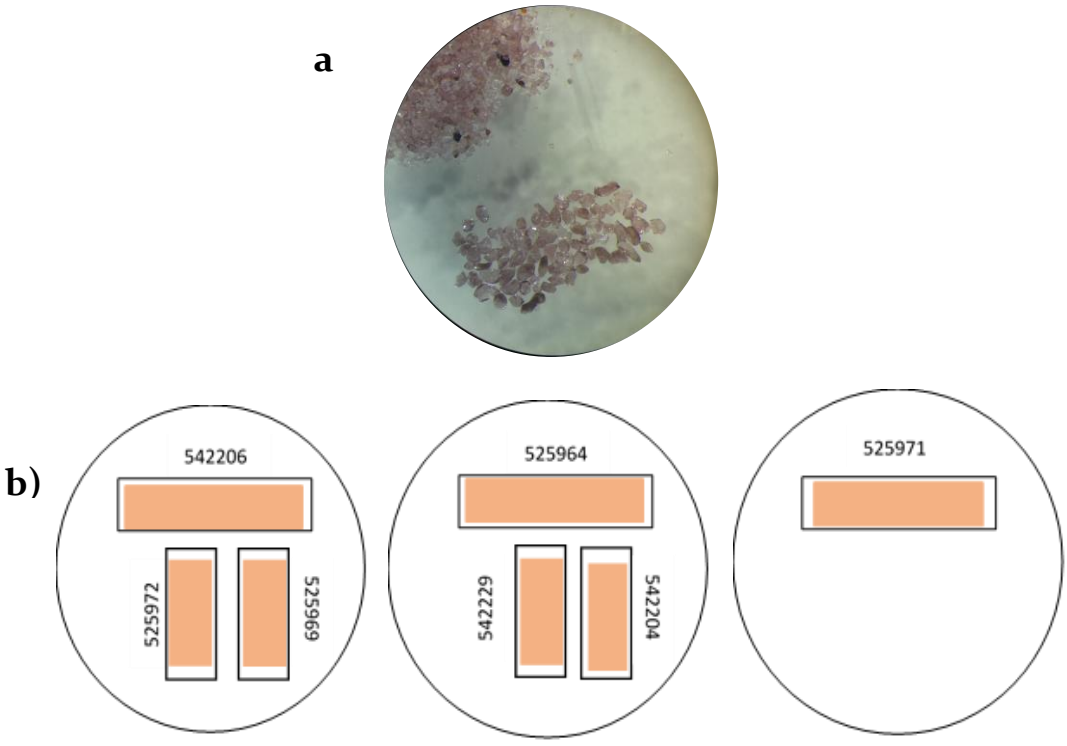
10 representative samples were chosen taken to the University of Pretoria to undergo mineral liberation using the Selfrag, to ensure preservation of the zircons during the separation process. The comminuted samples were then sieved down to ≤ 0.5 mm and underwent mineral separation at the Earth Laboratory at the University of the Witwatersrand. The following procedure was used for mineral separation using heavy liquids:

- Each sample was poured onto a clean sheet of white paper and a hand magnet was used to remove magnetic minerals. Remaining non-magnetic minerals were then processed through heavy liquid separation.
- Tetrabromoethane (TBE), which has a density of 2.96 g/cm^3, was used as the heavy liquid media. The TBE was poured into the separating funnel after which the sample was added. The sample was then stirred using a plastic rod to insure all the heavy minerals would sink to the bottom of the funnel while the light minerals floated to the top (Figure 5.1).
- The tap at the bottom of the funnel was then opened to allow for the heavy minerals to be separated out onto the filter paper which was placed on a second funnel directly below the separation funnel (Figure 5.1). The heavy minerals were the placed in beaker with some ethanol and the beakers were placed in a water bath for 5 minutes to evaporate in TBE that remained in the sample. The samples were then placed in an oven to dry.
- Once the samples were dry they were placed in a magnetic separator where variable current was used to separate out any remaining magnetic minerals. These magnetic minerals were also placed in vials and kept and the non-magnetic minerals were placed in separate vials for zircon picking later on.

The vials of non-magnetic minerals were then taken to the University of Johannesburg for zircon picking. Out of the 10 samples that underwent mineral separation only 7 samples were found to contain zircons. These zircons were first picked and arranged on double-sided tape before being mounted in epoxy resin and later analyzed using the LA-ICPMS at the (Spectrum) of the University of Johannesburg (Figure 5.2).



Figure 5.1: Fume cupboard set up for heavy liquid separation using Tetrabromethane (TBE) at the Earth Laboratory in the University of the Witwatersrand.



Pegmatites Carbonatite	Ijolite	Melteigite	
-525964 525972	-525971	-542204	-

Figure 5.2: a) Photomicrograph of the zircon grains in sample 542206 as they were being picked, grains are 0.5 mm or less. Schematic maps showing the position of each sample on its respective grain mount, as well as the rock type of each sample.

5.2.4 U-Pb zircon dating

U-Pb dating was performed on the Resolution ASI laser ablation system, which is connected to a Nu Plasma II MC-ICP-MS instrument in the Department of Geology at the University of Johannesburg. The zircon U-Pb ages were analyzed using a single 50 µm spot size, energy set to 4 mJ, a frequency of 2 Hz and attenuator value of 12.5 %. The energy of the electron beam was 1.9 J/cm^2 and the measurement was measurements were taken over 50 s with a background measurement of 20 s. The calibration standards used were OGC (^{207}Pb/^{206}Pb age = 3465.4 ± 0.6 Ma: Stern *et al.*, 2009), 91500 (^{207}Pb/^{206}Pb age = 1065 ± 1 Ma: Wiedenbeck *et al.*, 1995) and A382 (^{207}Pb/^{206}Pb age = 1877 ± 2 Ma: Huhma *et al.*, 2012). While CDQGNG (^{207}Pb/^{206}Pb age = 1851 ± 2 Ma: Black *et al.*, 2003) and Mud Tank (^{207}Pb/^{206}Pb = 732 ± 5 Ma: Black and Gulson, 1978) were used as secondary standards to ensure the accuracy of results.

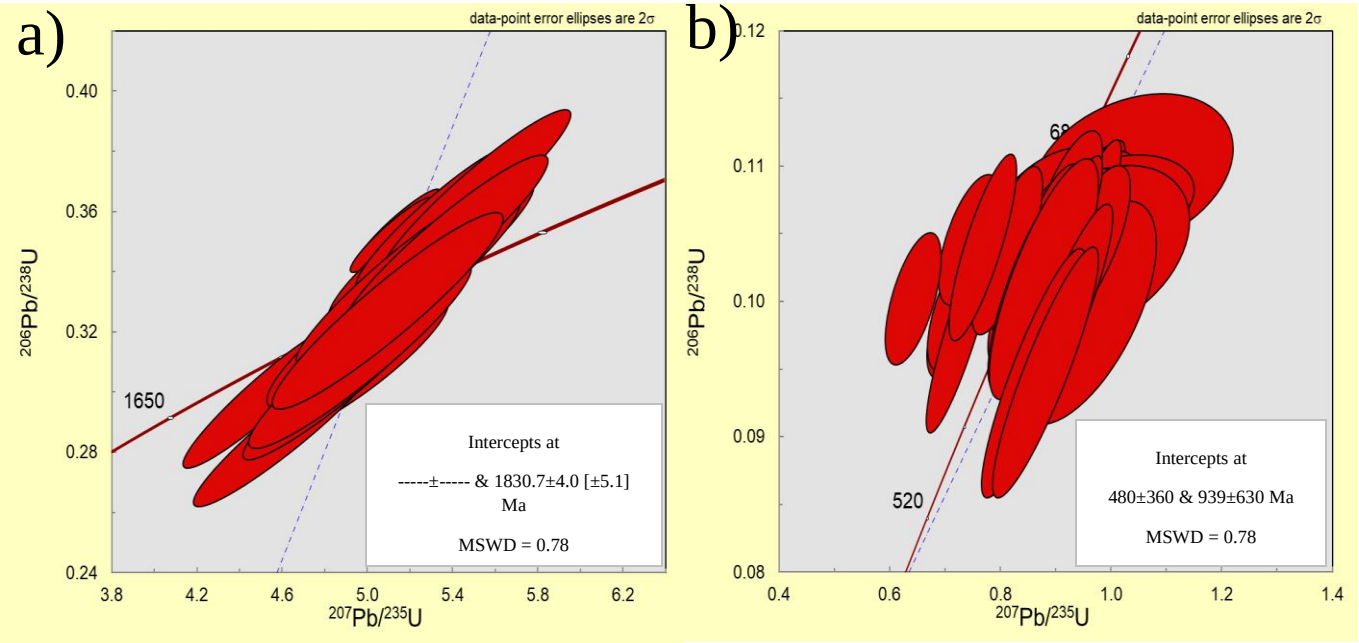


Figure 5.3: Concordia plots for the secondary standards that were measured while analyzing the Singertât Complex zircon samples a) CDQGNG b) Mud Tank.

6. Results

6.1 Petrography

The following section deals with a petrographic description of the main rock types in the study area, namely the nepheline-bearing layered intrusive rocks (urtite, ijolite and melteigite), host syenitic gneisses (Figure 6.1), late-stage carbonatites and peralkaline pegmatites. These rock types have been characterized and classified according to modal abundance analysis and results for the syenitic and nepheline-bearing rocks are shown in Figure 6.1 and Appendix XI. The main focus of this section is to identify mineral assemblages, as well as predominant textures that aid in the fulfilment of the aims and objectives of this study.

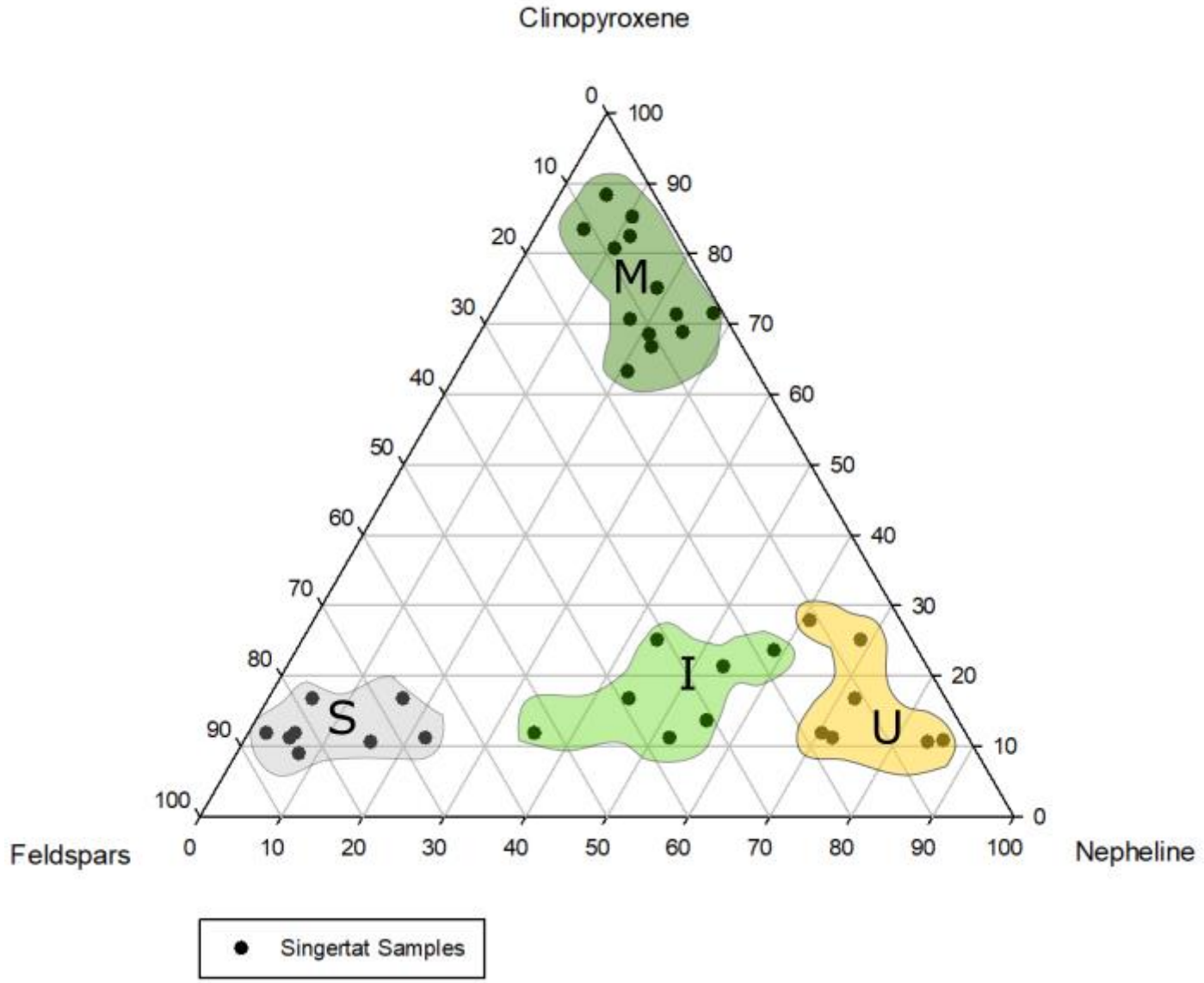


Figure 6.1: Ternary diagram used to classify the Singertât rock samples based on the modal abundances obtained during petrographic analyses. M = melteigites, I = ijolites, U = urtites and S = syenitic gneisses.

6.1.1 Nepheline-bearing rocks

The nepheline-bearing rocks are coarse-grained (1.5 cm – 1 cm grain size) with a urtitic to melteigitic composition and show late-stage intergrowths of albite and K-feldspar i.e. anti-perthite. On the basis of mineral abundances, there are 3 types of nepheline-bearing layered intrusive rocks and urtite contains the highest modal proportions of nepheline (approximately >70%). Ijolite contains between 70-30% nepheline and melteigite contains <30% nepheline with more mafic minerals present such as dark green clinopyroxene (aegerine), dark brown biotite and in some sample's minor amounts of microcline or plagioclase (Figure 6.2). It is noted that all samples contain some form of accessory calcite, magnetite and/or ilmenite. Detailed petrographic descriptions can be found in Appendix XI.

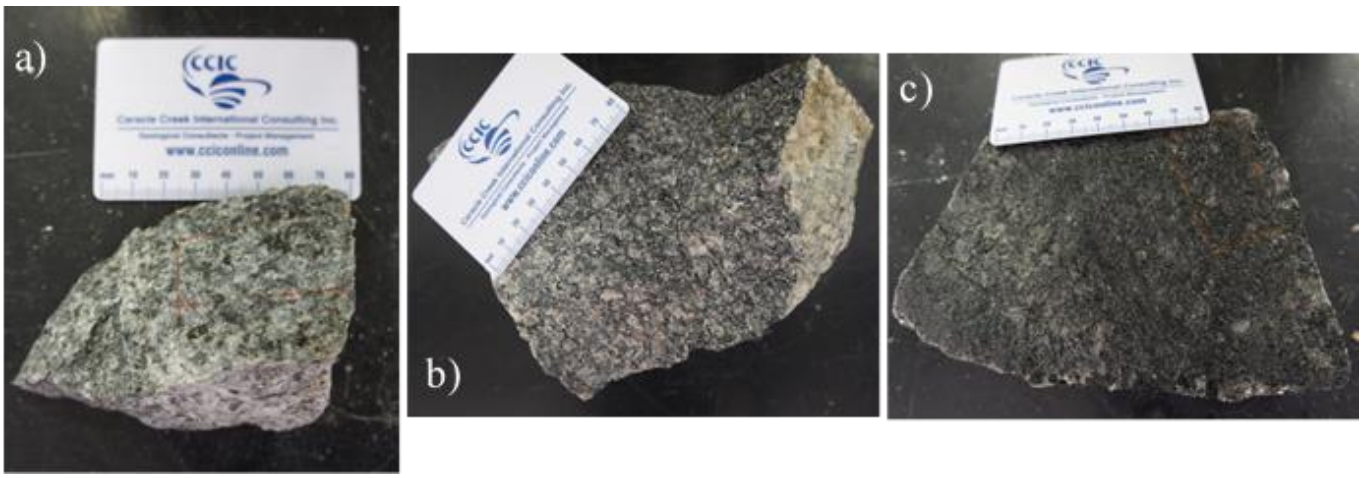


Figure 6.2: a) Urtite from the Singertât Complex, SE Greenland. The green mineral is clinopyroxene while the grey mineral is nepheline and the white mineral is alkali feldspar (Sample 525988). b) Ijolite from the Singertât Complex, SE Greenland. The black-green mineral is clinopyroxene, while the grey-brown mineral is nepheline and the white mineral is alkali feldspar (Sample 542214). c) Melteigite from the Singertât Complex, SE Greenland. The black-green mineral is clinopyroxene, while the grey-brown mineral is nepheline and the white mineral is alkali feldspar (Sample 542203).

Urtite

Predominantly composed of nepheline with very small amounts of aegerine-augite, biotite and minor anti-perthite (Figure 6.3a, b). The nepheline crystals are euhedral to subhedral and range in size from 0.5 mm to >3 mm. The aegerine-augite and biotite are subhedral and range in size from 0.1 mm to 2 mm. Disseminated magnetite does occur as an accessory mineral in this rock type, along with some clay alteration.

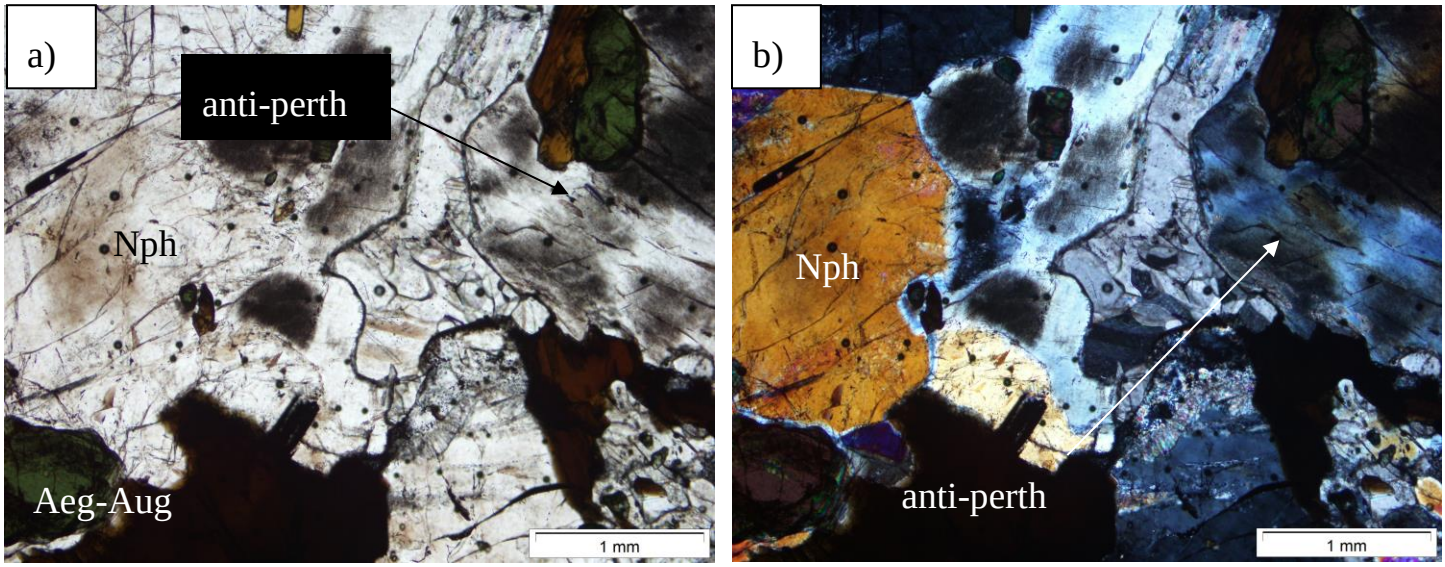


Figure 6.3: Photomicrographs of urtite sample 525988 showing the nepheline, anti-perthite and small percentage of clinopyroxene present in the sample. a) ppl, b) xpl.

Ijolite

The ijolite samples are primarily composed of nepheline, aegerine-augite, biotite, anti-perthite and accessory magnetite, calcite and zircon in certain samples. The nepheline that occurs in these rocks appears to be euhedral to subhedral, while the aegerine-augite is subhedral and biotite crystals are euhedral to subhedral (Figure 6.4a and 6.4b). The anti-perthite ranges between 5% and 15% and is interstitial, likely representing the last major mineral that crystallized (Figure 6.4c and 6.4d). The anti-perthite is seen as orthoclase lamellae that have been exsolved from an albite host. The volumetric proportions of lamellae to host crystal vary from sample to sample, with some anti-perthites containing 60% host and 40% lamellae and 80% host to 20% lamellae in other samples. Minor disseminated magnetite and pyrite occur in the ijolites.

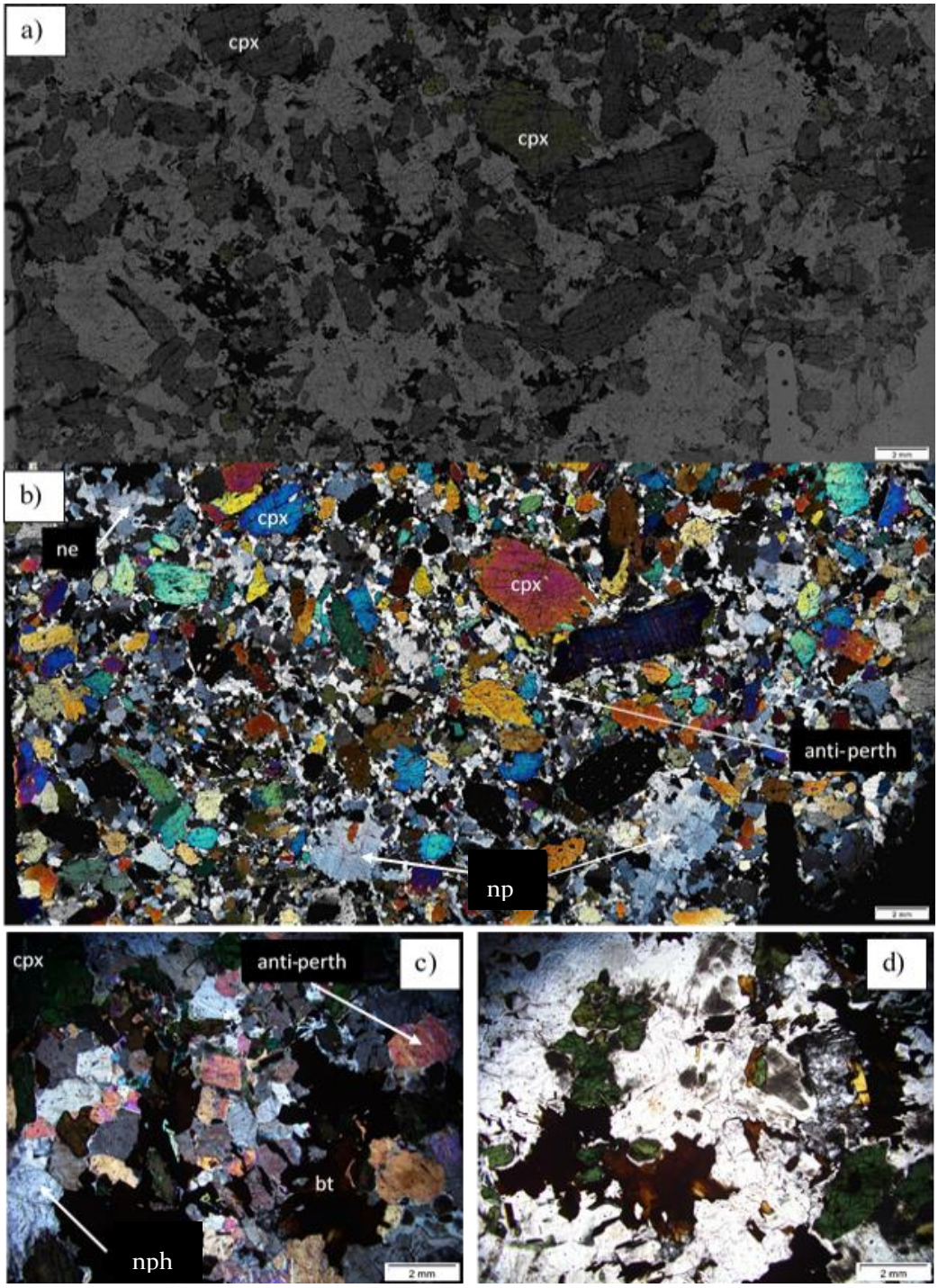
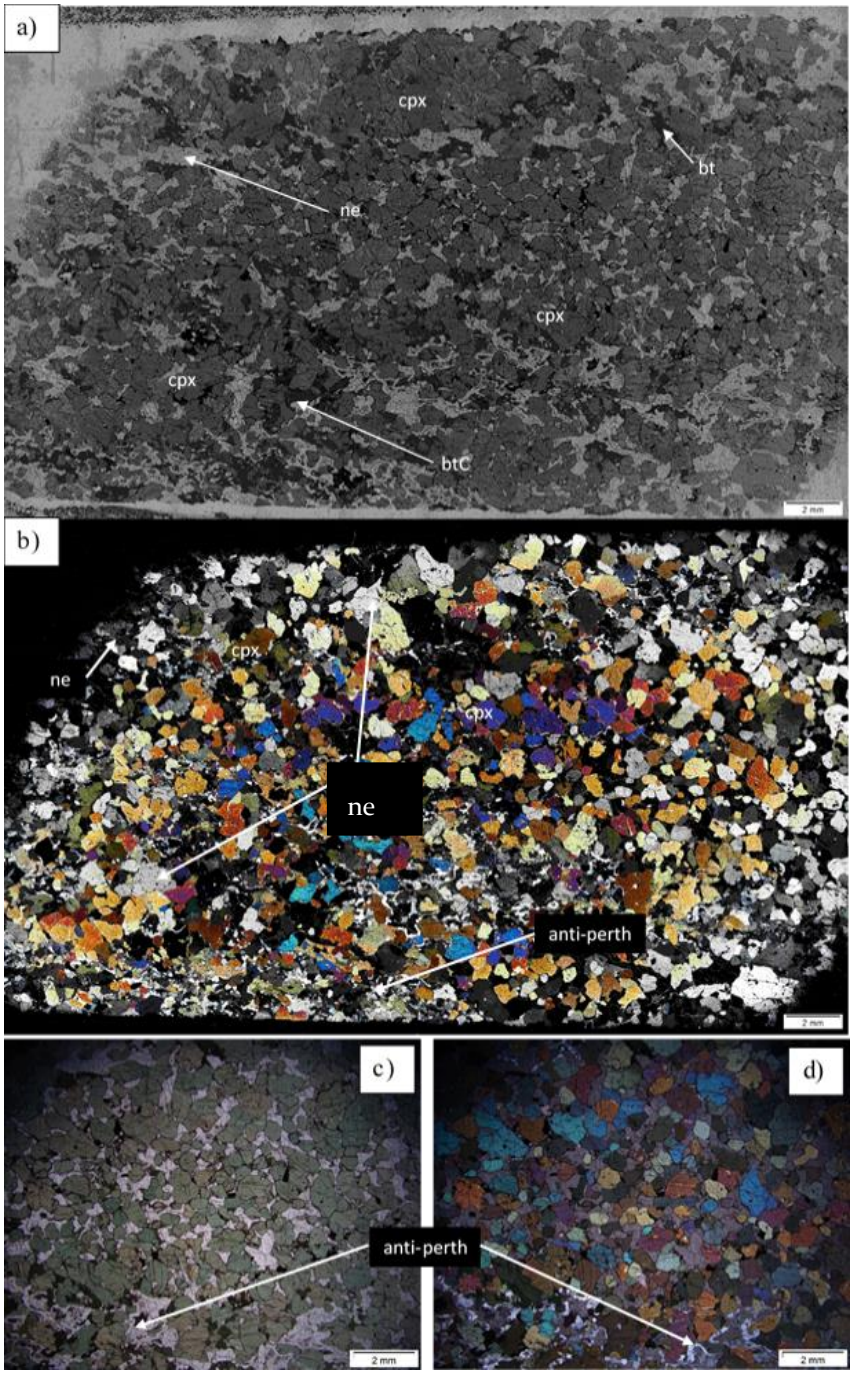


Figure 6.4: Photomicrographs of Ijolite samples 542214 a) full thin section scan in ppl, b) thin sections scan in xpl, c) anti-perthite present in the ijolite samples in ppl, d) anti-perthite present in the ijolite samples in xpl.

Melteigite

The melteigites are composed of predominantly aegerine-augite with subordinate biotite, nepheline and anti-perthite, samples also contain accessory magnetite, calcite and in some cases zircon. The nepheline that occurs in these rocks appears to be subhedral to anhedral, while the aegerine-augite and biotite crystals are euhedral to subhedral (Figure 6.5a and 6.5b). The anti-perthite is interstitial at approximately 5% (Figure 6.5c and 6.5d). The

anti-perthite is seen as orthoclase lamellae that have been exsolved from an albite host. Disseminated magnetite and pyrite occurs in the melteigites.



<u>Figure 6.5</u>: Photomicrographs of Melteigite sample 542215 a) full thin section scan in ppl, b) thin sections scan in xpl, c) anti-perthite present in the ijolite samples in ppl, d) anti-perthite present in the ijolite samples in xpl

Layered nepheline-bearing intrusive rocks and the host syenitic gneisses

The layered Singertât samples consist of the urtite, ijolite, melteigite, which intrude weakly foliated syenitic gneisses. The samples either have a gradational contact between different rock types (Figure 6.6a, 6.7a and 6.7b) or sharp contacts (Figure 6.6c, 6.8a and 6.8b). The samples that contain sharp contacts seem to have truncated grain boundaries (Figure 6.6b). In layered sample 542219, looking at the layers in 542219AII we observe that sodalite occurs with nepheline in one rock layer and in this sample and nepheline is the dominant feldspathoid (Figure 6.7b). However, when looking at the layers in sample 542219BII we observe that there less than 30 % nepheline and sodalite is the dominant feldspathoid in this particular layer (Figure 6.9a and 6.9b).

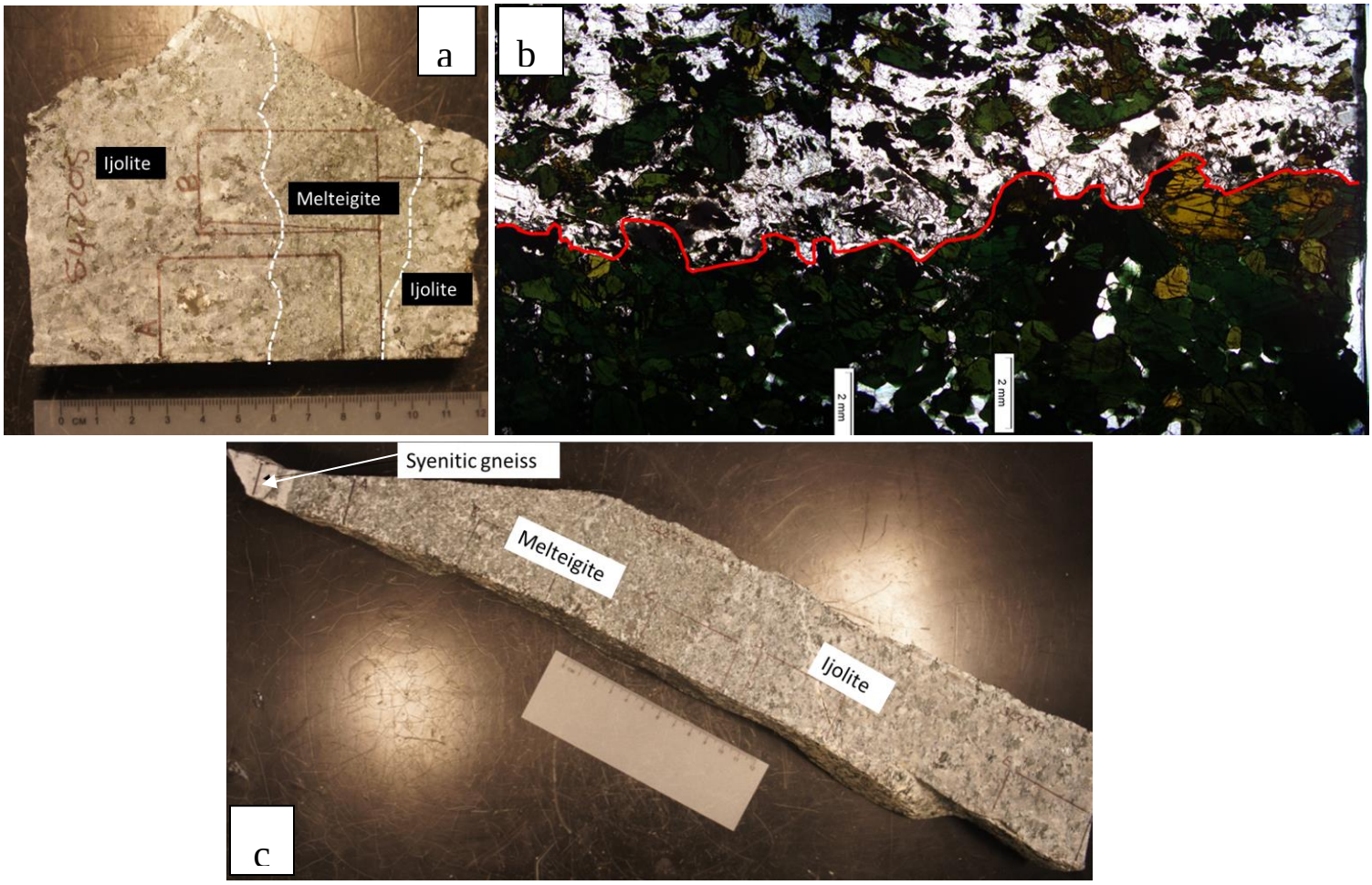


Figure 6.6: The layering seen between the nepheline-bearing alkaline rocks show in samples a)542205 which depicts a gradational change (dashed white line) between melteigite and ijolite and b) 542219, which depicts a sharp change (white line) from syenitic gneiss to melteigite to ijolite.

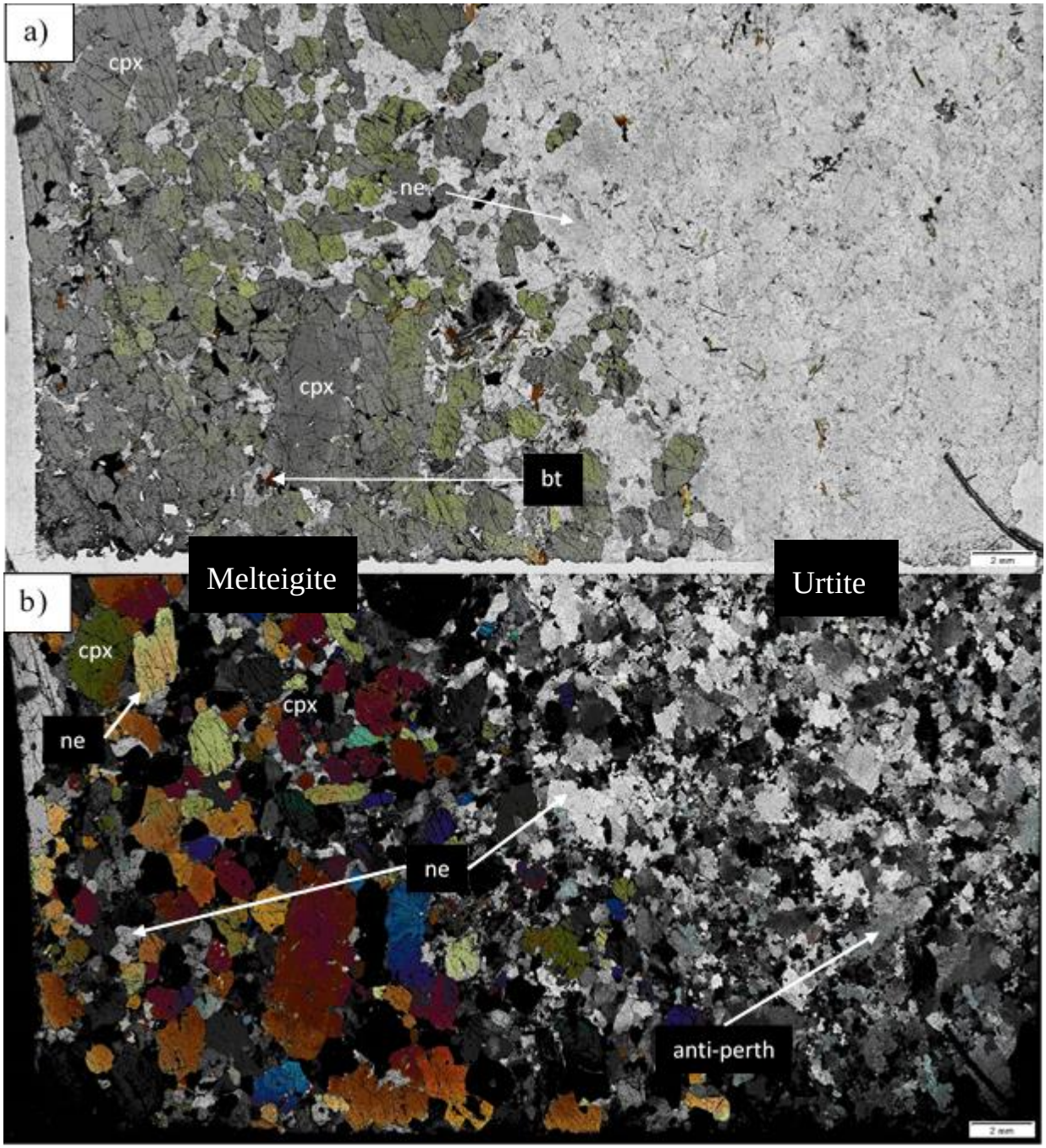


Figure 6.7: Photomicrographs of a layered nepheline-bearing rock sample 542216BII, which shows a gradational contact (indicated by the dashed white line) between an urtite and a melteigite layer. a) full thin section scans in ppl, b) thin sections scan in xpl.

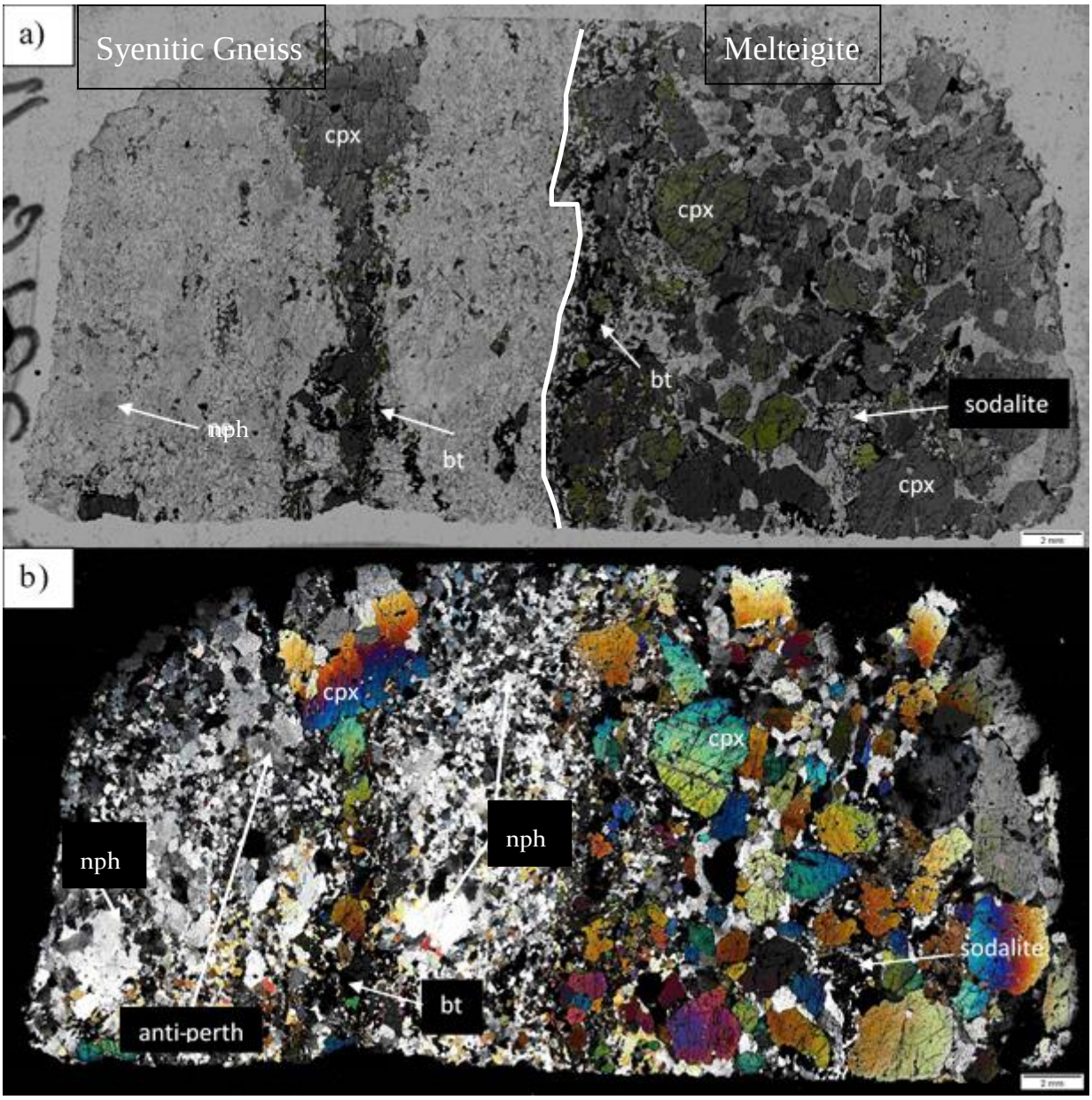


Figure 6.8: Photomicrographs of a layered nepheline-bearing rock sample 542219AII, which shows a sharp contact between a syenitic gneiss and a melteigite layer (indicated by the white line), with a melteigite vein cross cutting the syenitic gneiss. a) full thin section scans in ppl, b) thin sections scan in xpl.

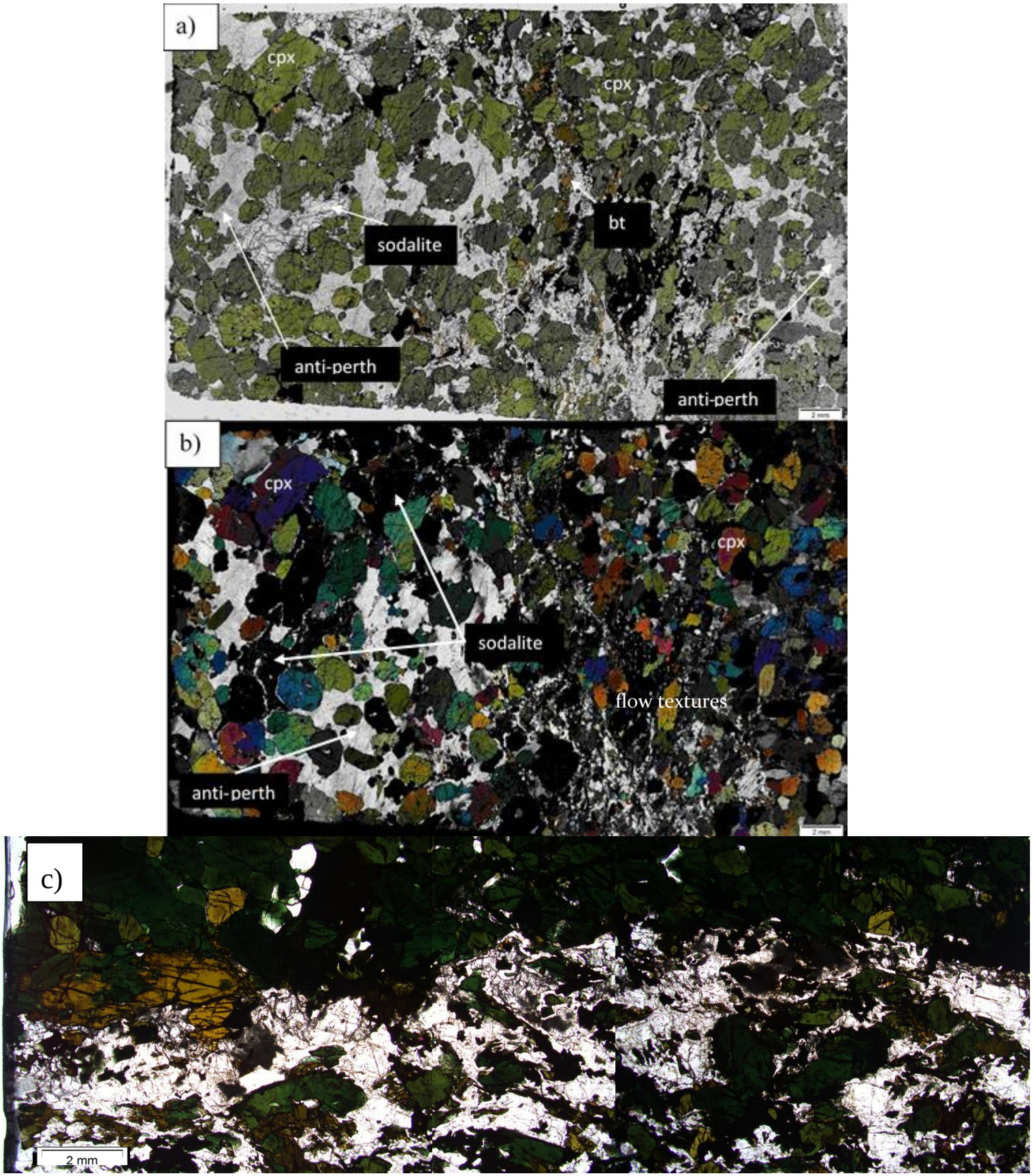


Figure 6.9: Photomicrographs of a layered nepheline-bearing rock sample 542219BII, which shows a gradational contact between an ijolite and a melteigite layer. In this sample there is little nepheline, however sodalite appears to be the dominant feldspathoid present and flow textures are observed in this sample, a) full thin section scan in ppl, b) thin sections scan in xpl c) depicts a truncated boundary seen in sample 542219CII.

Peralkaline pegmatites

The pegmatites are primarily composed of nepheline, orthoclase and biotite with all samples containing accessory magnetite, zircon and apatite. All minerals are euhedral and the crystals range in size from 1 cm to >5 cm (Figure 6.10, 6.11a-6.10f). Disseminated magnetite is present in all the samples and the zircon crystals ranging from 0.1 mm to 4 mm (Figure 6.11a and 6.11b).

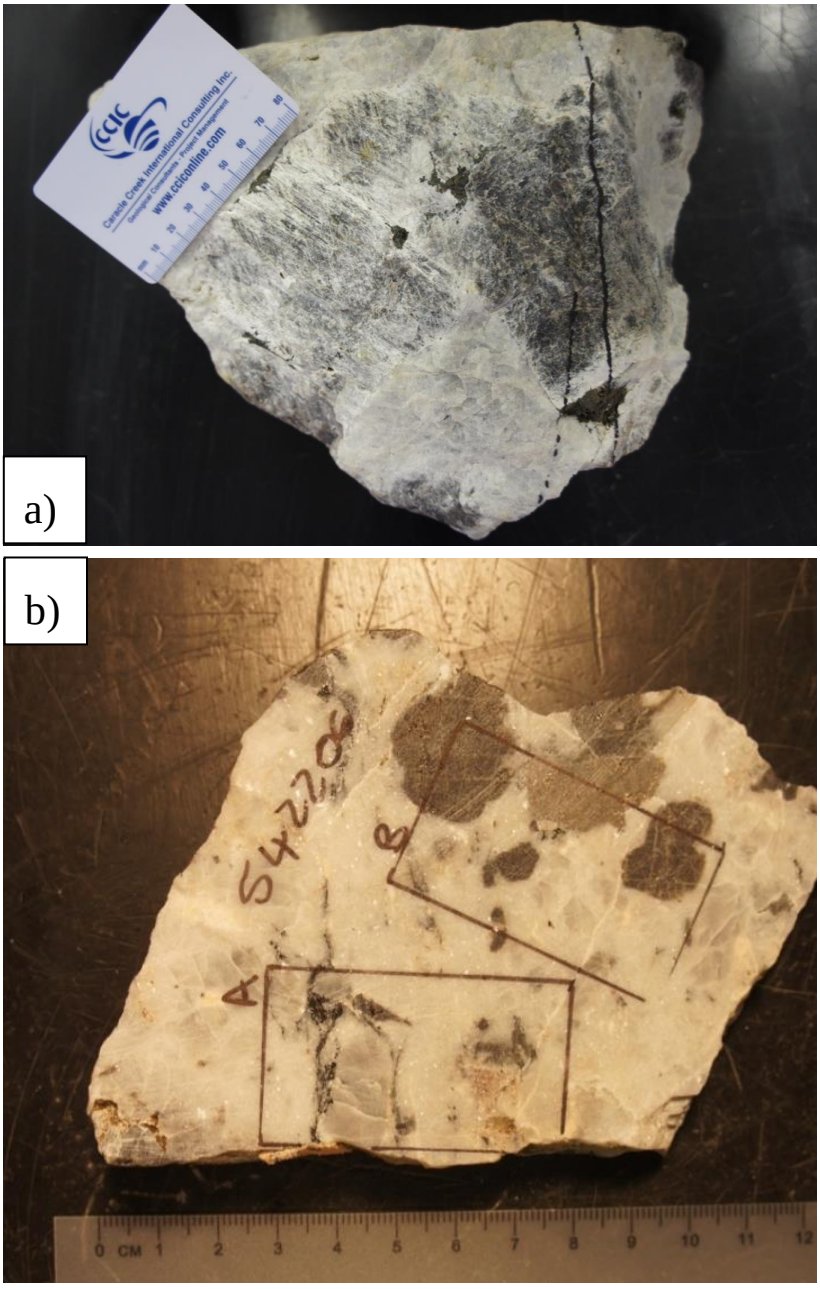
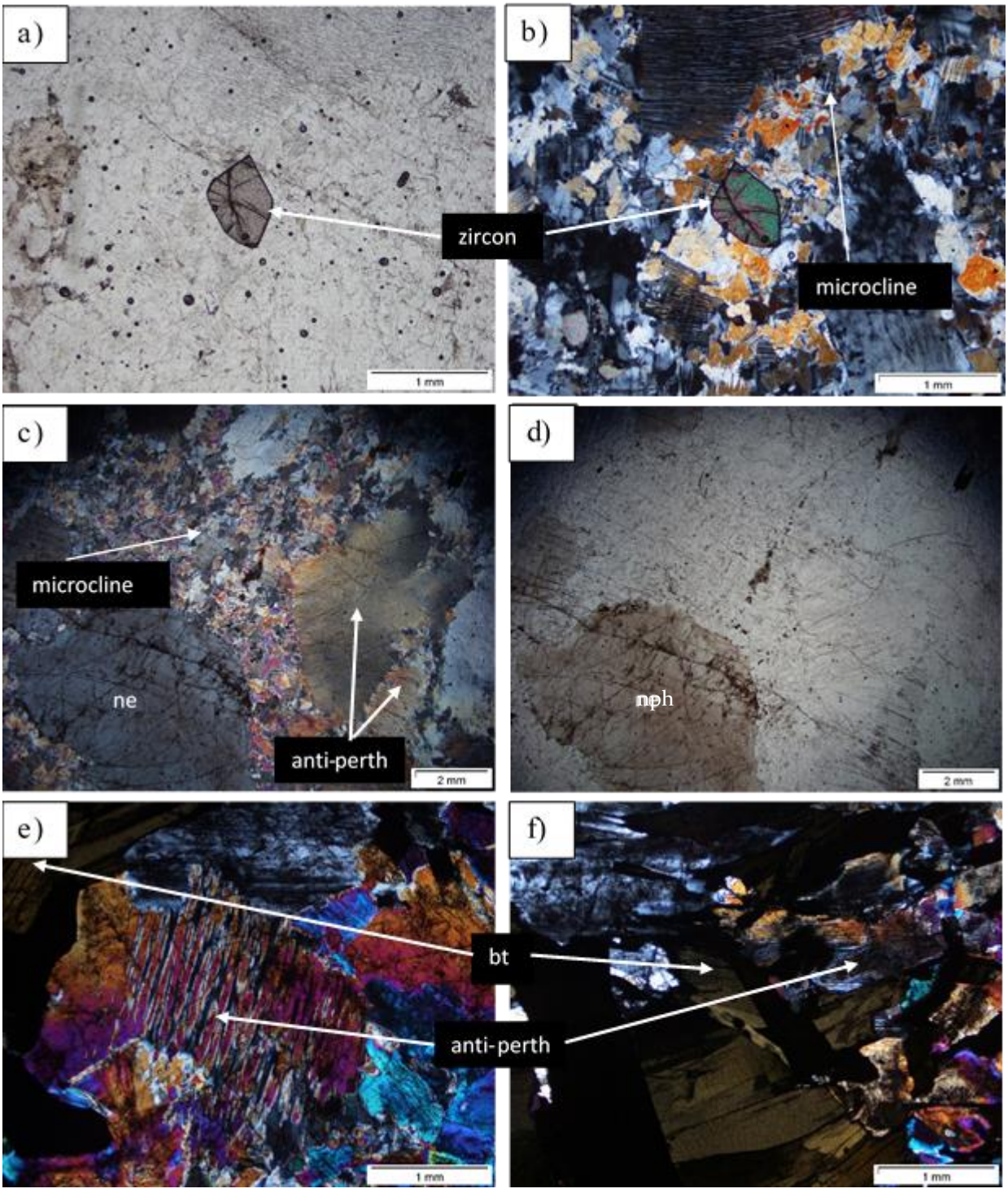


Figure 6.10: Hand samples of a)525969 and b) 542206 which depicts pegmatitic nepheline (pale brown-grey), feldspars (white) and biotite (dark brown – black).



<u>Figure 6.11</u>: Photomicrographs of the pegmatite samples a) a zircon crystal in the sample 542206 in ppl, b) a zircon crystal in the sample 542206 in xpl, c) macrocrystic nepheline and anti-perthite in sample 542206 in ppl, d) pegmatitic nepheline and anti-perthite in sample 542206 in xpl, e) anti-perthite texture seen in sample 525969 in xpl, d) pegmatitic biotite crystals in sample 525969 in xpl.

Carbonatites

The Singertât Complex contains two types of the carbonatitic occurrence. The first type of carbonatite is composed predominately of calcite and in places contains garnet and aegerine-augite (Figure 6.12b and 6.12c). The second is a carbonatitic breccia, which contains fragments of the nepheline-bearing layered silicate rocks (Figure 6.12 a), as well as larger nepheline and orthoclase crystals from the pegmatites (Figure 6.13b and 6.13c). The calcite present in these samples has perfect cleavage and is euhedral to subhedral. The garnet in these samples has a high-Ti content due to the unusual orange-red color and is euhedral to subhedral, as is the aegerine-augite in these particular carbonatites. The carbonatites contain little or no magnetite, however, there is still some accessory apatite and zircon present. (Figure 6.13a and 6.13b).

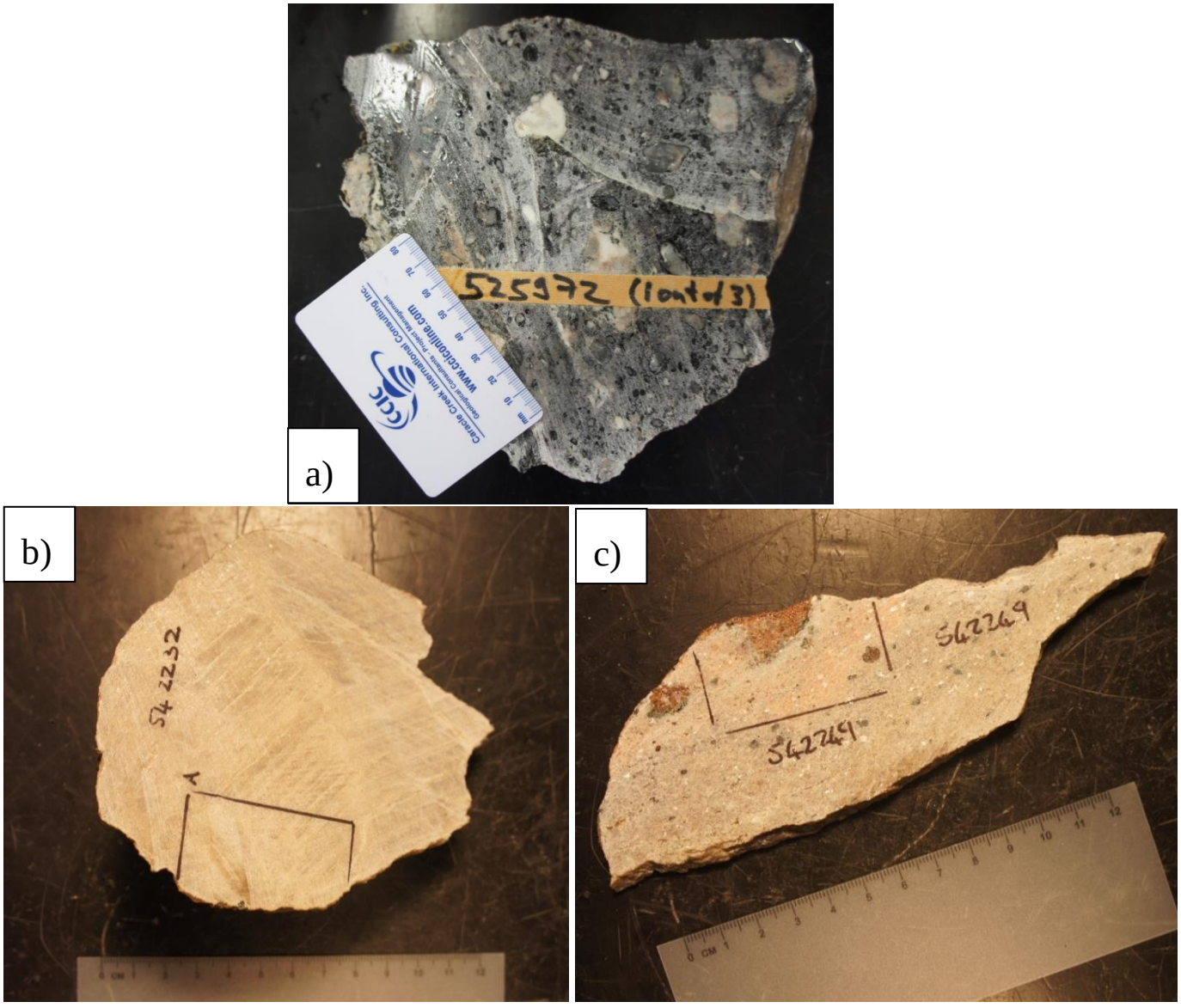
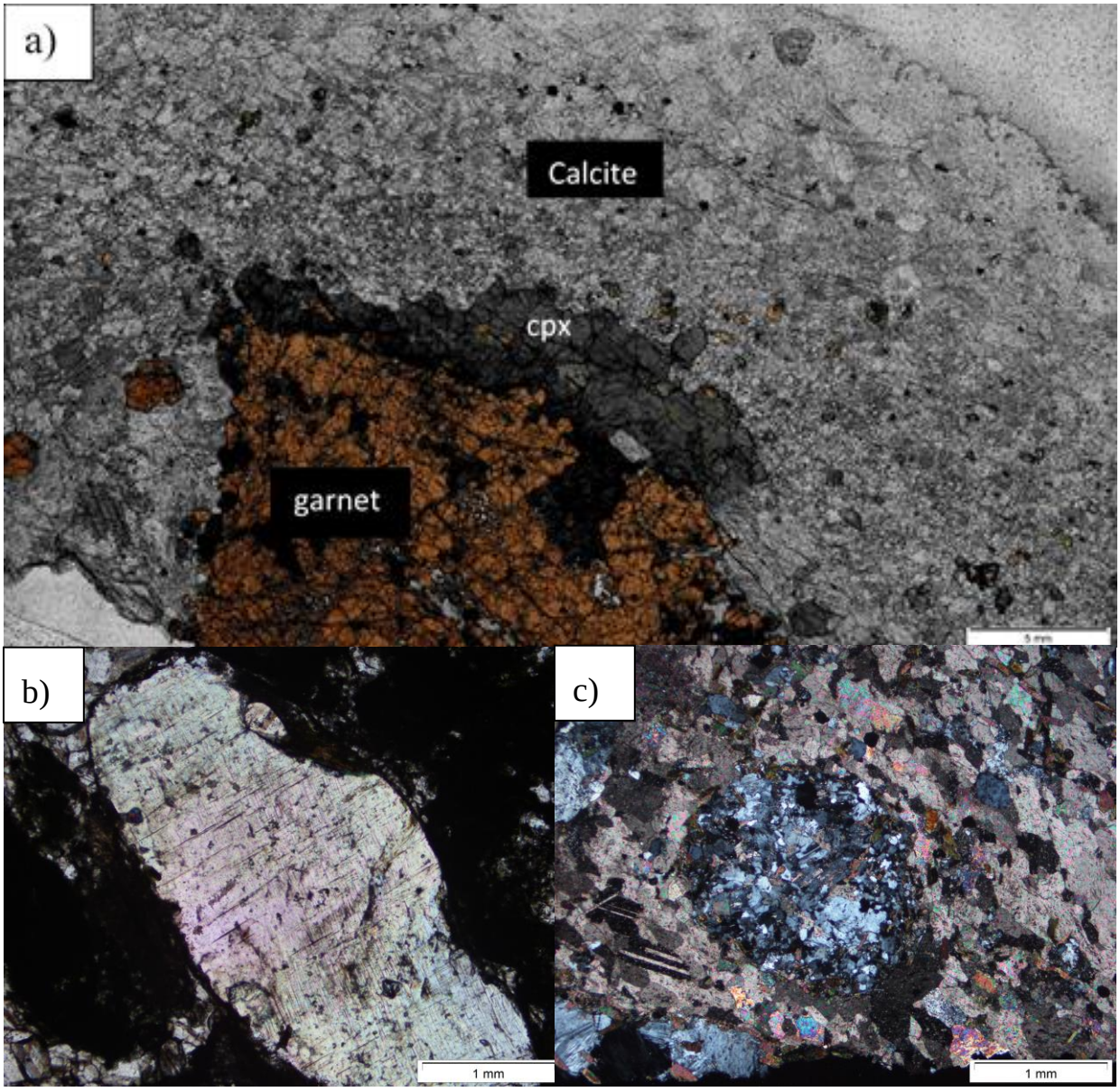


Figure 6.12: Hand samples of a)525972, b)542232 and c) 542249 which depicts a carbonatite breccia (contains fragments of nepheline-bearing rocks and pegmatite), a carbonatite containing almost 100% calcite and a carbonatite containing high Ti-garnet respectively.

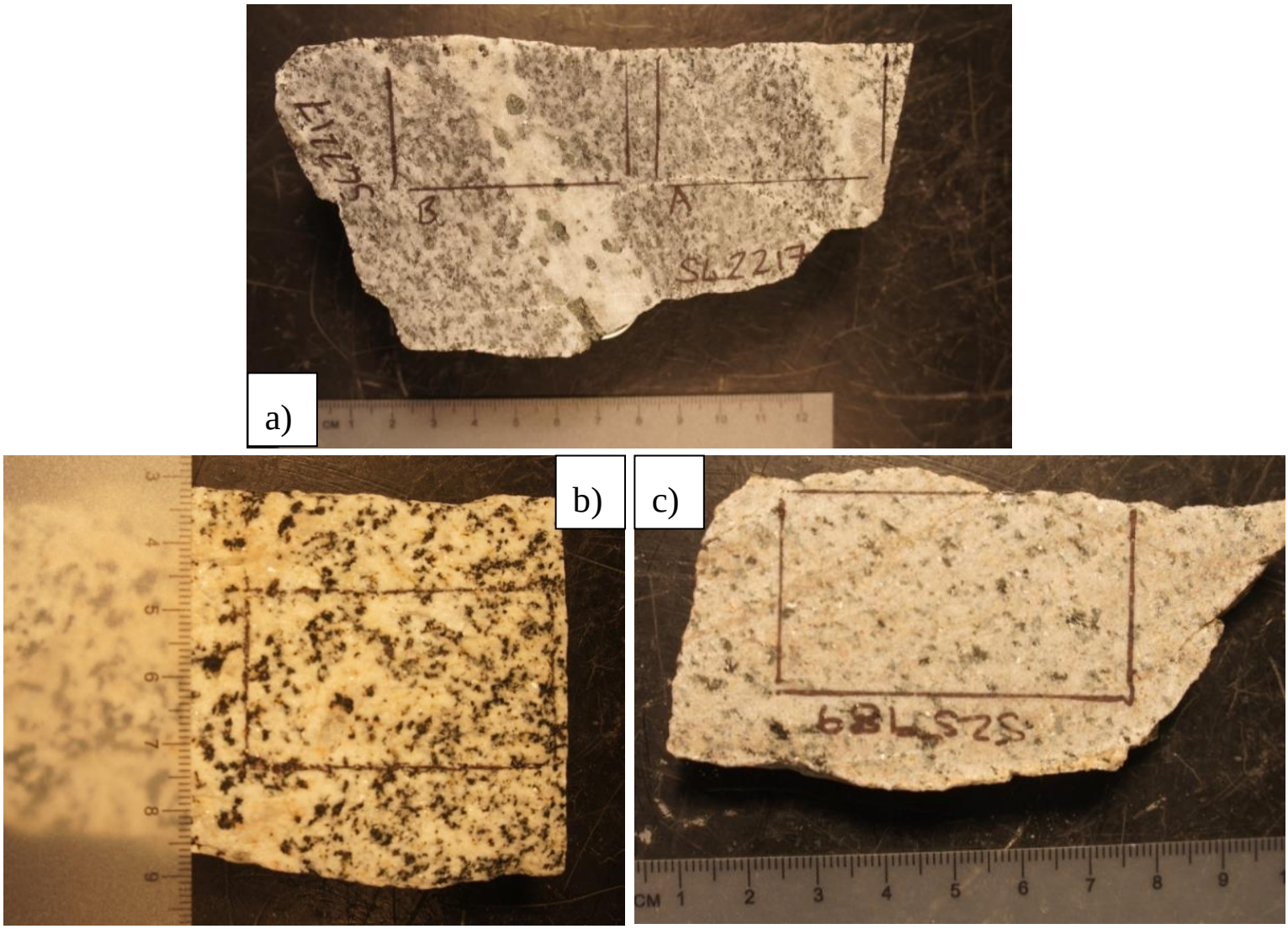


<u>Figure 6.13</u>: Photomicrographs of carbonatite sample 542249, which shows a garnet and clinopyroxene surrounded by a large amount of calcite. a) full thin section scans in ppl, b) nepheline xenocryst in carbonatite breccia in ppl and c) rounded fragments of ijolite in a carbonatite breccia in xpl.

<u>Grey Syenitic Gneisses</u>

These rocks are primarily composed of anti-perthite with aegerine-augite, biotite and small amounts of nepheline with all samples containing accessory magnetite and apatite (Figure 6.14). The clinopyroxenes are euhedral to

subhedral, nepheline and anti-perthite are subhedral, while the biotite is anhedral (Figure 6.15a and 6.15b). Disseminated magnetite is present in all the samples and the zircon crystals range from 0.1 mm to 0.5 mm



<u>Figure 6.14</u>: Hand samples of a)542217, b)525981 and c) 525989 which depicts syenitic gneisses showing the typical gneissic texture (alignment of aegerine-augite and biotite grains).

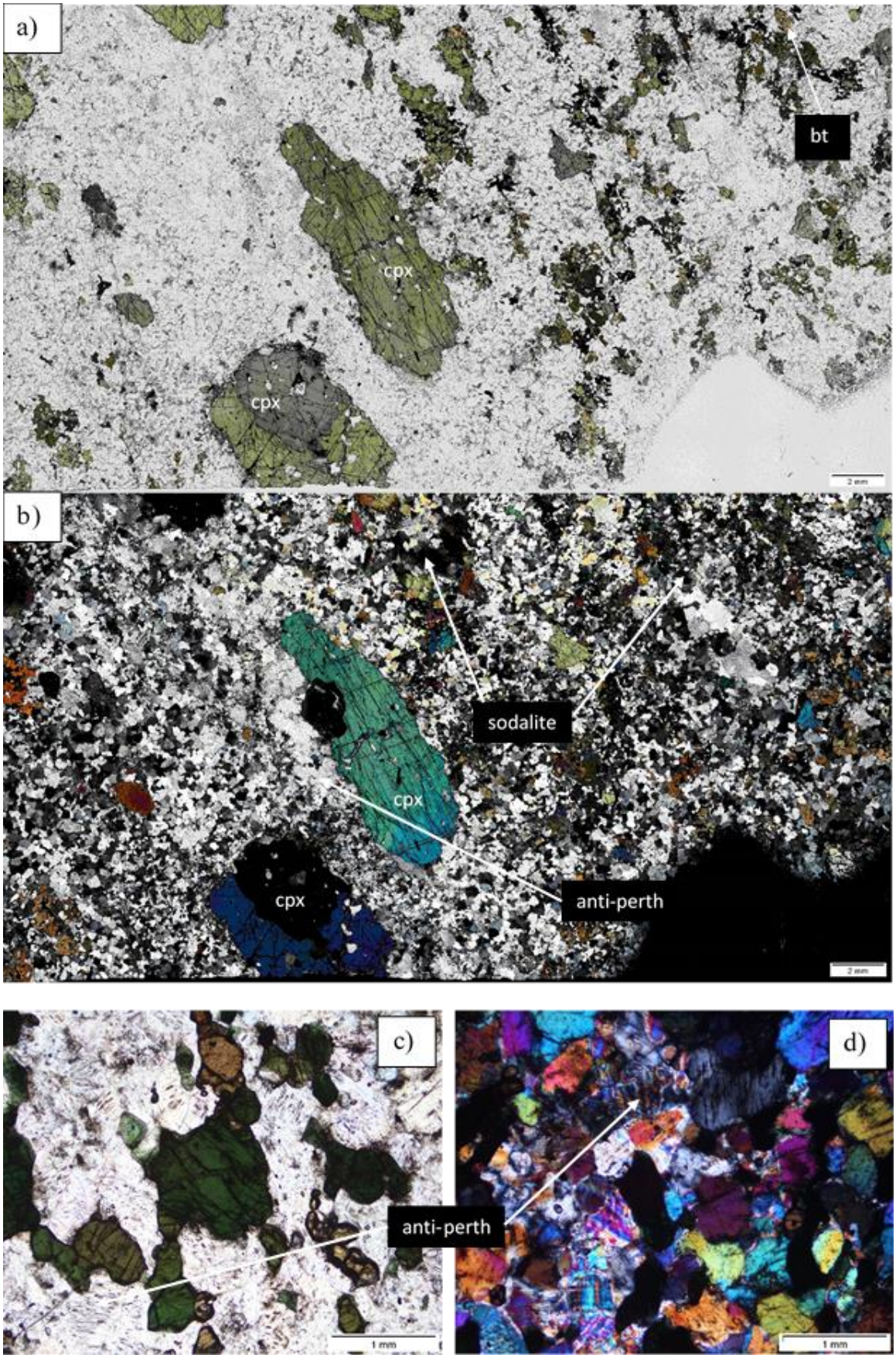


Figure 6.15: Photomicrographs of syenitic gneiss sample 542217B a) full thin section scan in ppl, b) thin sections scan in xpl, c) anti-perthite present in the ijolite samples in ppl, d) anti-perthite present in the ijolite samples in xpl.

6.2 Mineral Chemistry

The aim of this section is to determine whether the minerals observed in different layers are compositionally similar or not. This aids in determining if the minerals crystallized from the same melt or not and ultimately whether the Singertât Complex was formed from a single magma or multiple batches of magma. For the detailed mineral chemistry results refer to Appendix I-IX.

Nepheline

Due to the formula for nepheline being $(Na, K)AlSiO_4$, variation diagrams containing each component were plotted in Figures 6.16, 6.17 and 6.18. These plots are meant to depict variation between nepheline crystals found in the different layered nepheline-bearing rock types. Sample 542205 shows an ijolite gradationally transitioning into melteigite and back to ijolite again. Nepheline from both rock types generally appear to plot in a cluster, with the exceptions of a few outliers (Figure 6.16). The general clustering of data could suggest that the melteigite and the ijolite in this particular sample crystallized from the same melt.

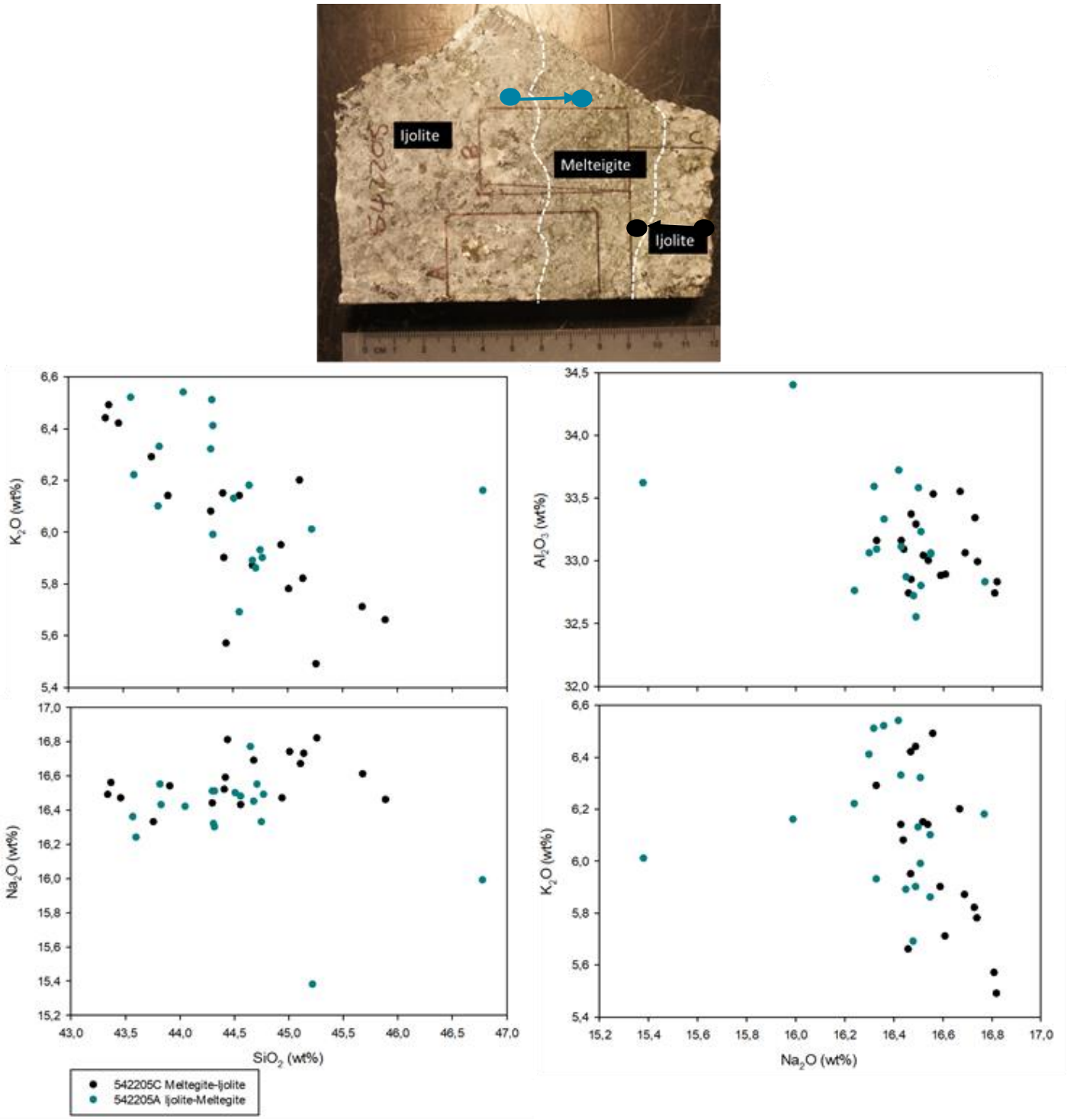


Figure 6.16: Variation diagrams depicting variations in mineral compositions for the layered sample 542205 which depicts gradational transitions from ijolite to melteigite and back to ijolite again. The blue dots represent analyses that were taken across the ijolite-melteigite boundary, while the black dots were analyses taken in the melteigite layer only.

For sample 542216, two thin sections were analyzed, sample 542216 BI shows a sharp transition from urtite to melteigite, while sample 542216 CII shows a gradational transition from ijolite to melteigite. Referring to Figure 6.17 it appears that there are different populations of nepheline in each rock type. The nephelines in sample 542216BII are higher in SiO_2, K_2O and Al_2O_3, while in sample 542216 CII the ijolite has higher amounts of Na_2O. It is observed that in both samples 542216BII and 542216CII the nepheline population in the melteigites contain more sodium compared to the ijolite and urtite, this may be due to the fact that these particular nepheline crystals were crystalizing with the aegerine-augite. Therefore, both minerals would be competing for sodium in the magma, this would leave less sodium in the residual liquid from which the nepheline populations in the ijolite and urtite may have crystallized from. While this is likely for sample 542216CII, where we observe some overlap between the two populations of nepheline, seen in plots where Na_2O vs K_2O and Al_2O_3 (Figure 6.17).

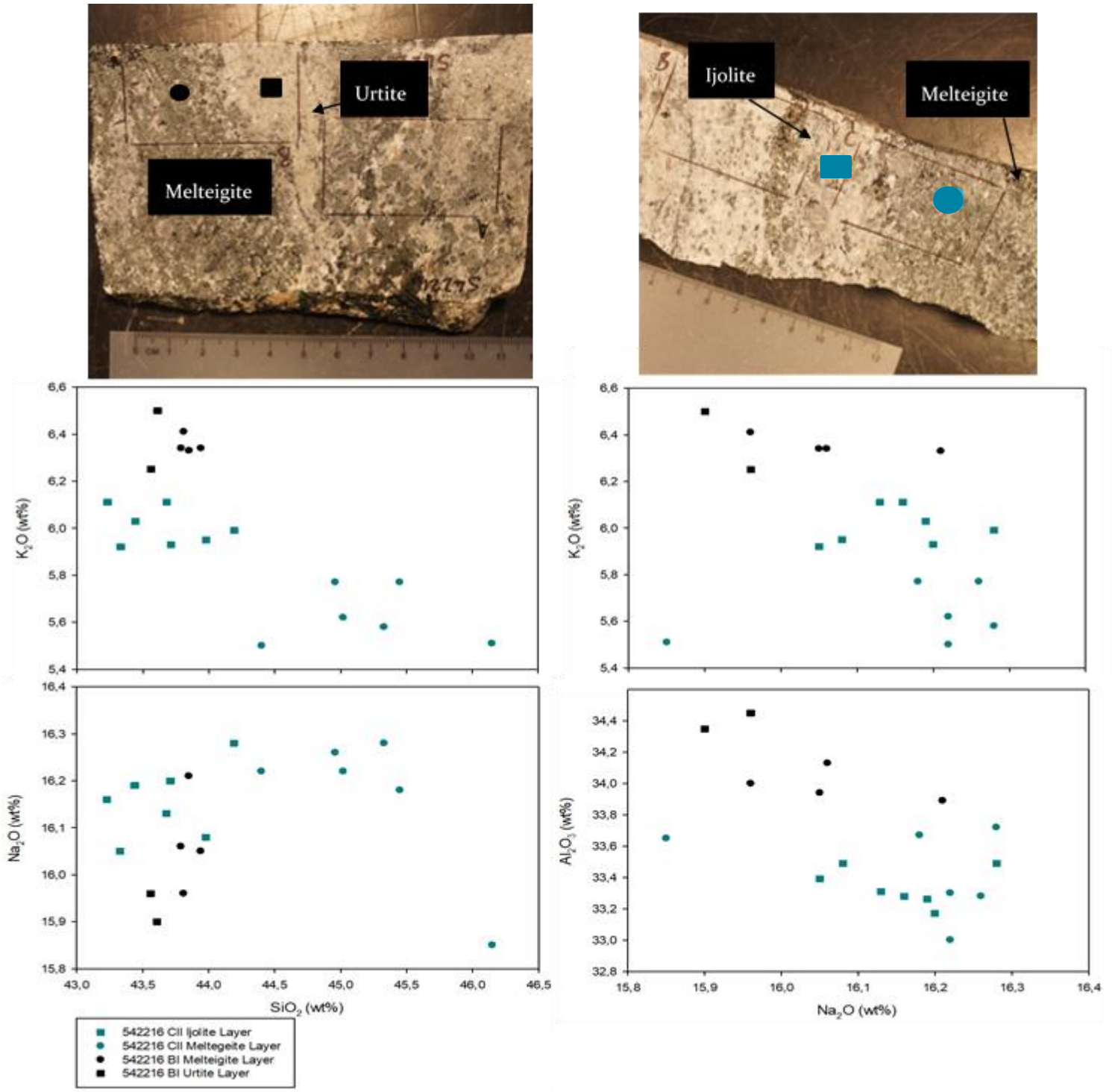


Figure 6.17: Variation diagrams depicting variations in mineral compositions for the layered sample 542216 using samples 542216 BI and CII which transitions from ijolite to melteigite and melteigite to urtite respectively. The blue squares represent analyses from the ijolite layer and the blue dots represent analyses taken in the melteigite layer in samples 542216 CII. The black squares represent analyses from the urtite layer and the blue dots represent analyses taken in the melteigite layer in samples 542216 BI.

For sample 542219 three thin sections were analyzed, sample 542219 AII shows sharp transition from syenitic gneiss to melteigite, sample 542219 CII shows a sharp transition from ijolite to melteigite and finally sample

542219 DII shows a gradational transition from ijolite to melteigite. According to Figure 6.18 the nepheline populations which in the syenitic gneiss and melteigite appear to be similar in composition, as the results for these two rock types tend to cluster together. However, the population of nepheline occurring in the ijolite layer appears to compositionally different from the populations in the syenitic gneiss and melteigite layers. The nepheline occurring in the ijolite has the highest percentage and range of silica (43.9 – 45.6 wt% SiO_2), while the nepheline in the melteigite and syenitic gneiss samples have a similar silica percentage and range from 43.0 – 44.2 wt% SiO_2. The syenitic gneiss and melteigite have higher percentages of Al_2O_3 and K_2O, but lower Na_2O with respect to the ijolite.

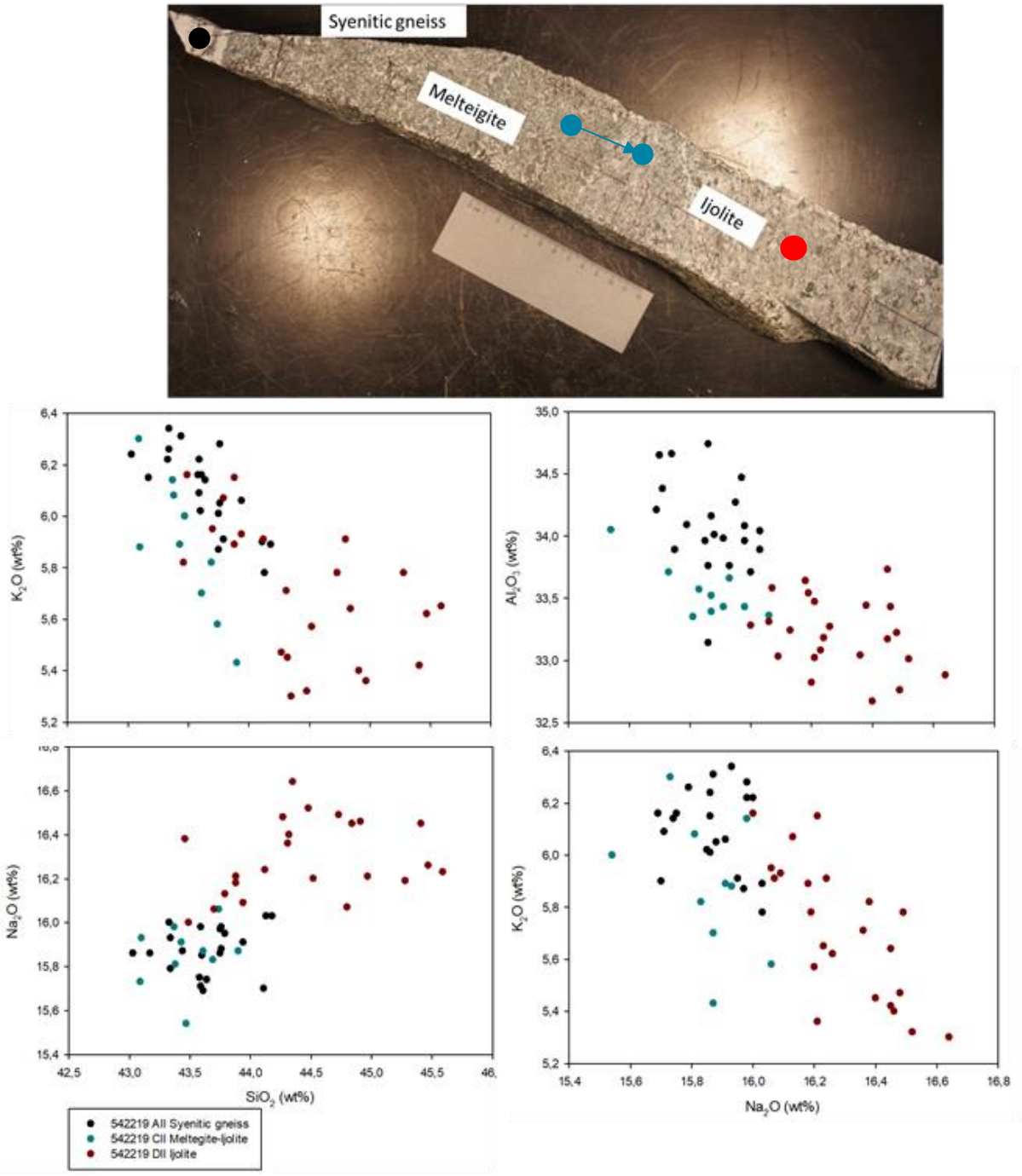


Figure 6.18: Variation diagrams depicting variations in mineral compositions for the layered sample 542219 using thin sections 542219 AII, CII and DII which transitions from syenitic gneiss to melteigite and then to ijolite. The black dots represent analyses from the syenitic gneiss layer, the blue dots represent analyses taken across the melteigite-ijolite transition and the red dots represent analyses from the ijolite layer.

Aegerine- Augite

For samples 542205 and 542216 it was noted that some of the clinopyroxene crystals appeared to be zoned, therefore core and rim readings were taken (Figure 6.19 and 6.20). It was further noted that the populations of clinopyroxenes on either side of the gradational boudary in sample 542205 were similar in composition. However

in sample 542216, sample 542216 CII's clinopyroxenes are compositionally different from the clinopyroxenes in sample 542216 BI.

Referring to Figure 6.19, it appears that sample 542205 does show some compositional zoning as we see seperate clusters of core and rim data. The rims appear to be more alkaline in composition due to the higher amounts of Na_2O (~ 4.05 -4.35 wt%) in comparison with the core which appears to have higher concentration of CaO (~.18.1 – 18.4 wt%), i.e. more diopside-rich. The rims also have a higher Al_2O_3 content, but lower SiO_2, TiO_2 and MgO and similar amounts of FeO and Fe_2O_3. This can similarly be seen in sample 542216 CII, which also shows a gradational change from ijolite to melteigite (Figure 6.20).

For sample 542216 BI (Figure 6.20), we observe very little variation from core to rim in the melteigite and urtite layers. The cores and rims seem to have similar concentrations of all the major elements, however, some of the rims seem to have a slightly higher magnesium and alumina content compared to the rest of the data (~ 9.55 -9.65 wt% MgO and ~ 4.3 – 4.5 wt% Al_2O_3). The populations of clinopyroxene appears to differ from sample

Referring to Figure 6.21 for the layered sample 542219, which transitions from syenitic gneiss to melteigite to ijolite. A vein of meleigitic composition was analyzed and plotted, this vein is seen cross-cutting the syenitic gneiss. The sample shows that while the clinopyroxene populations found in the syenitic gneiss are different, the clinopyroxes found in the vein and the melteigite are compositionally similar with respect to the major elements compositons. The clinopyroxene in the ijolitic layer appears to be compositionally different from the vein (similar to the nepheline data mentioned before). The ijolitc layer appears to have a higher percentage of MgO, SiO_2 and CaO. This shows that the clinopyroxene found in the ijolitic layer may be more augite-rich in composition compared with the clinopyroxenes in the syenitic gneiss, vein and melteigite layers. It also appears that the amount of Na_2O present in the aegerine-augite crystals, ocurring in the ijolite layer, begins to decrease this may be due to nepheline beginning to crystalize. The vein which appears to be melteigitic in composition is appears to be chemically different from the actual melteigite layer regarding TiO_2 and MgO . The vein has a higher percentage of TiO_2, but a lower percentage of MgO with respect to the melteigite layer percentage of TiO_2, but a lower percentage of MgO with respect to the melteigite layer. Therefore while vein is melteigtic in composition it is not part of the melteigite layer we observe in sample 542219.

Referring to Appendices III, V and VIII we observe that the samples have characterstic alkali clinopyroxene such as higher Fe^{3+} vs Fe^{2+} in all the clinopyroxenes that were analyzed. The pyroxenes also have mol%, 24% - 30% acmite (aegerine) with considerable amounts of Jadeite. The pyroxenes also appeat to have elevated Ca-tschermark values and excess alumina.

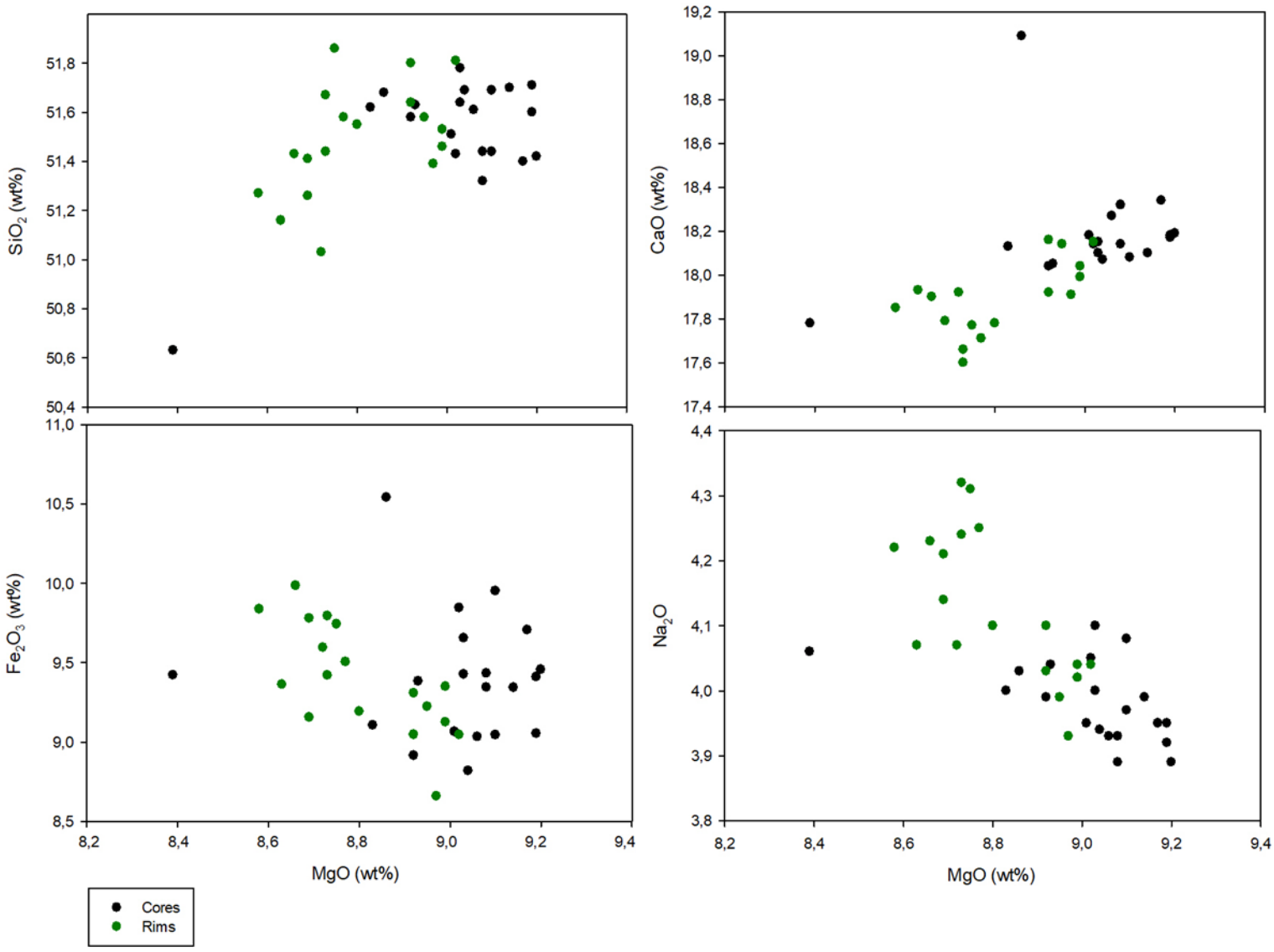
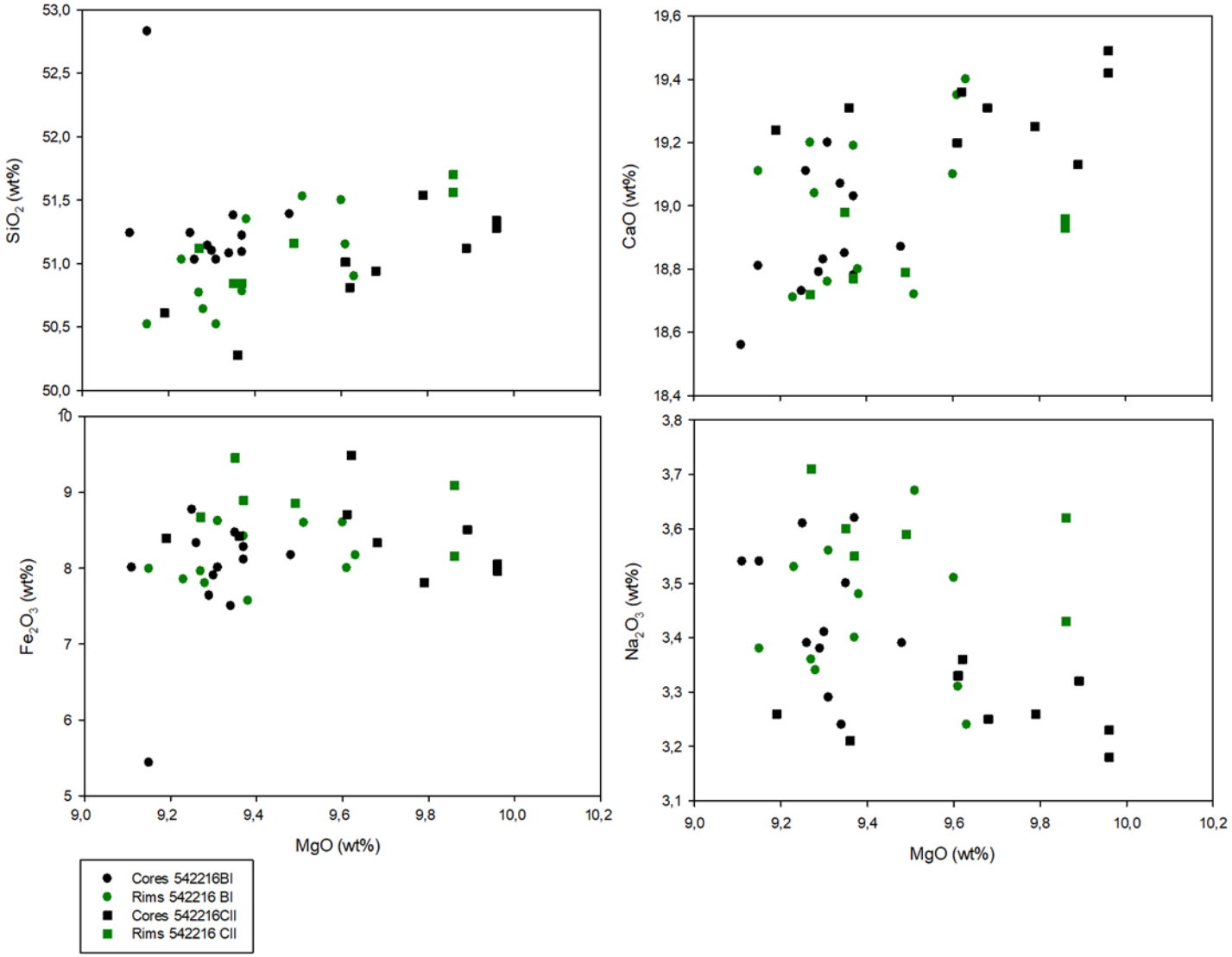
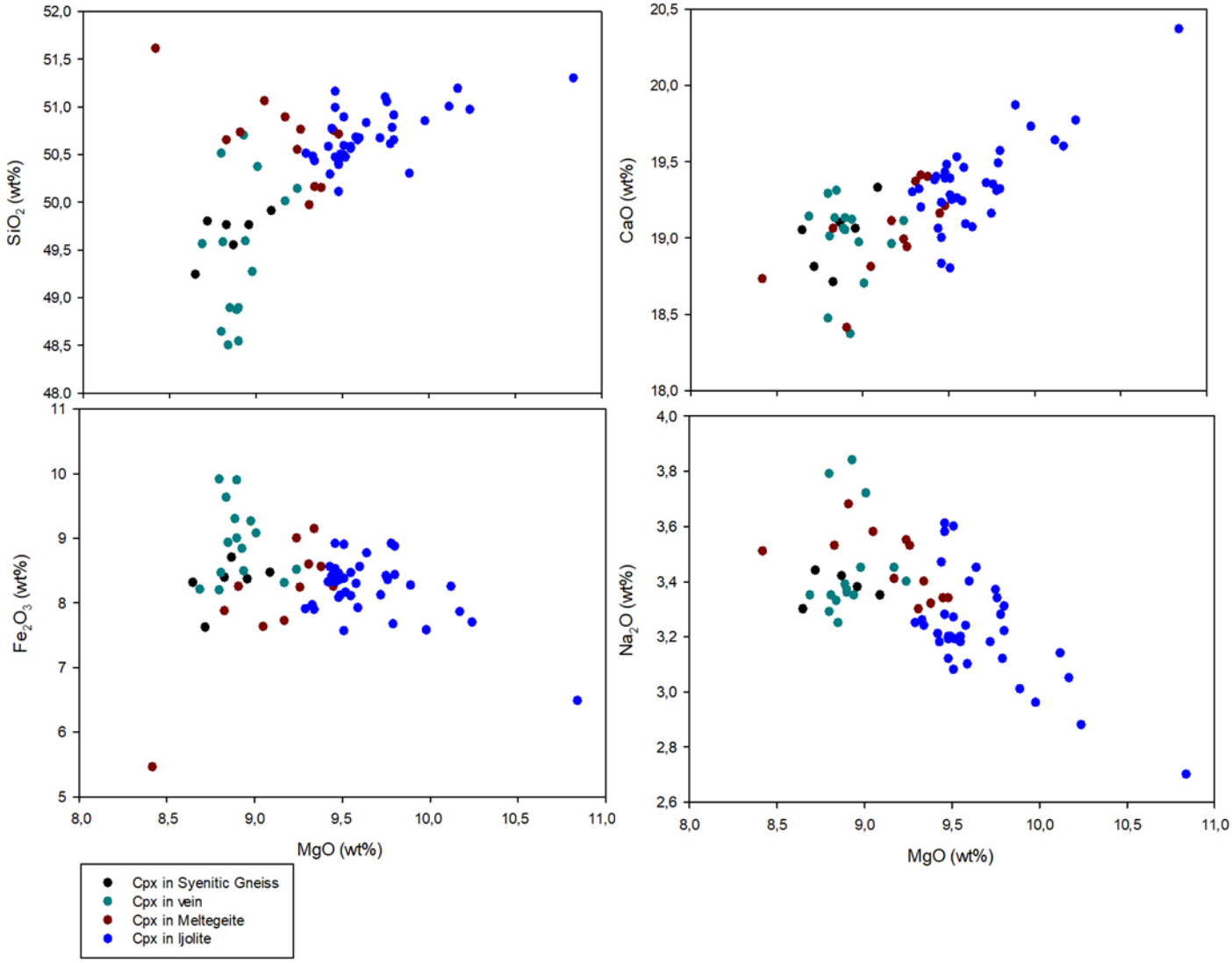


Figure 6.19: Variation diagrams depicting variations in mineral compositions for the layered sample 542205 which depicts the core- rim data for aegerine-augite.



<u>Figure 6.20</u>: Variation diagrams depicting variations in mineral compositions for the layered samples 542216BI and 542216CII, which depicts the core- rim data for aegerine-augite.



<u>Figure 6.21</u>: Variation diagrams depicting variations in mineral compositions for the layered sample 542219 which depicts the aegerine augite crystals in the syenitic gneiss, a vein of aegerine-augite within the syenitic gneiss, melteigite and ijolite.

Referring to Figure 6.19, it appears that sample 542205 does show some compositional zoning as we a see seperate clusters of core and rim data. The rims appear to be more alkaline in composition due to the higher amounts of Na_2O (~ 4.05 -4.35 wt%) in comparison with the core which appears to have higher concentration of CaO (~.18.1 – 18.4 wt%), i.e. more diopside-rich. The rims also have a higher Al_2O_3 content, but lower SiO_2, TiO_2 and MgO and similar amounts of FeO and Fe_2O_3. This can similarly be seen in sample 542216 CII, which also shows a gradational change from ijolite to melteigite (Figure 6.20).

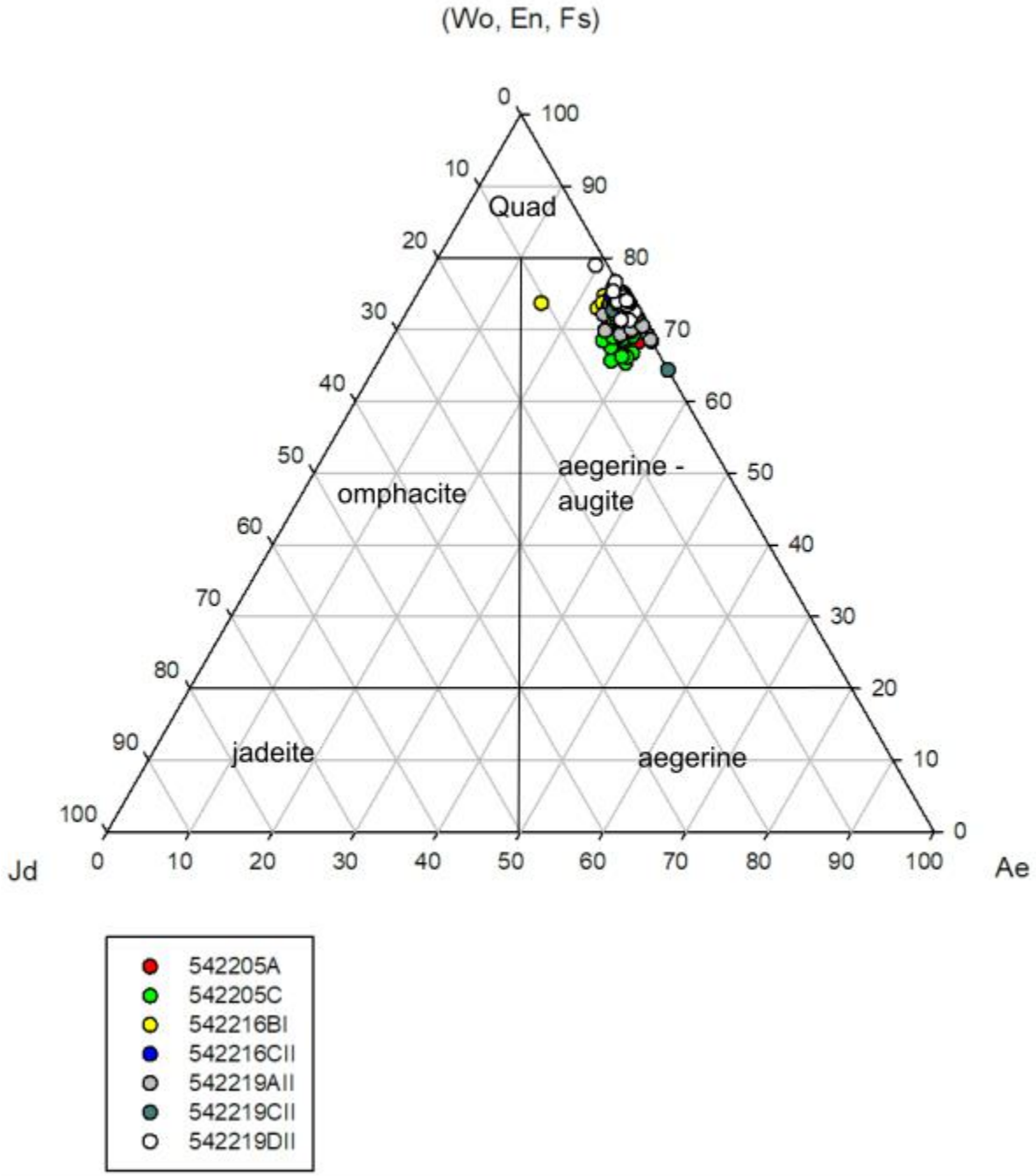


Figure 6.22: A ternary diagram representing the EPMA results for the clinopyroxene crystals found in the nepheline-bearing alkaline rocks of the Singertât Complex.

Sodalite

Sodalite was identified using EPMA in the syenitic gneiss sample (542217B) and petrographically the sodalite appeared isotropic. It was observed as the medium gray BSE reflectance seen in Figure 6.23. The results obtained can be seen in Table 3. The total weight does not add up to 100 wt% due the fact that spectrometers were not calibrated to measure chlorine and fluorine.

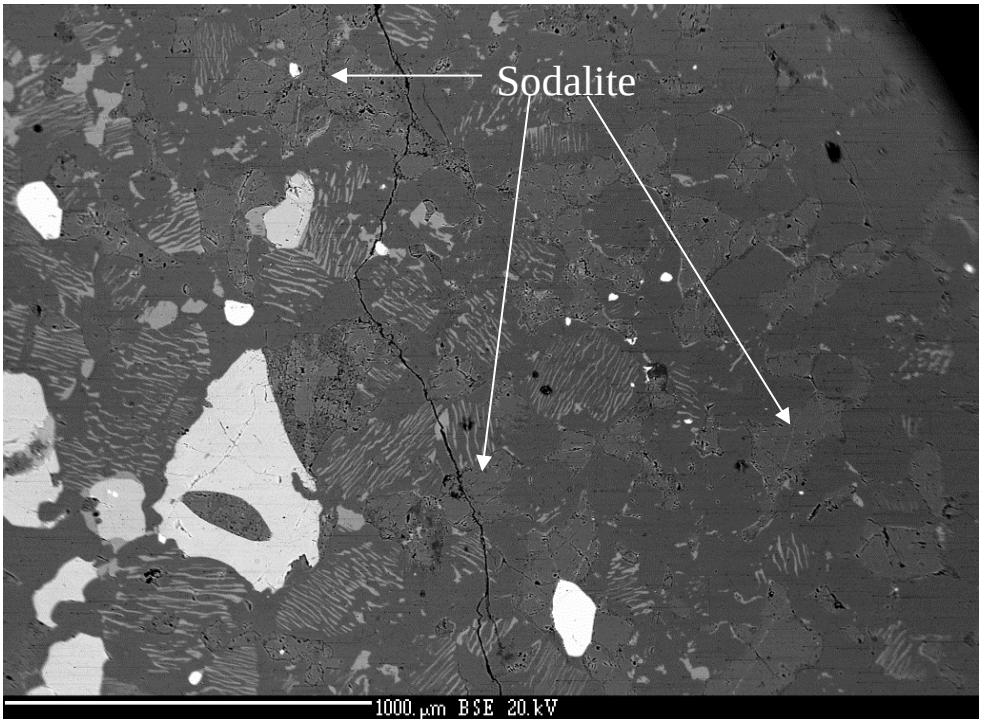


Figure 6.23: BSE taken of the EPMA image, which shows the sodalite that was analyzed in sample 542217B.

Table 3: EPMA results for sodalite in sample 542217B

Major elements (wt%)	Na_2O	MgO	SiO_2	K_2O	CaO	TiO_2	FeO	MnO	Cr_2O_3	NiO	Al_2O_3	Total
542217B	8.85	0	34.7	0.15	5.65	0	0.01	0	0	0.01	24.85	74.22
	8.44	0	34.42	0.2	5.62	0	0	0	0	0.01	24.69	73.36
	8.52	0.01	35.6	0.47	5.76	0	0	0	0	0.01	27.02	77.4
	9.1	0	35.25	0.15	5.64	0	0	0	0	0	27.48	77.63
	9.03	0	34.71	0.17	5.53	0	0.07	0	0	0.01	27.34	76.85
	8.93	0	34.86	0.16	5.63	0.01	0.04	0	0	0	25.95	75.57
	8.74	0	34.9	0.15	6	0.01	0	0.01	0	0	27.34	77.14
	8.68	0	34.63	0.16	5.71	0	0.02	0	0	0	24.56	73.75
	8.41	0.01	35.01	0.26	5.74	0	0.02	0	0	0	25.51	74.96
	8.66	0.01	34.45	0.16	5.76	0	0.01	0.01	0.01	0	25.85	74.91
	8.78	0	34.72	0.17	5.69	0	0	0	0	0	28.23	77.59
	8.88	0	34.72	0.16	5.64	0.01	0	0	0	0	25.16	74.58
	9.11	0	35.31	0.15	5.76	0.02	0.02	0	0.01	0	28.77	79.15
	8.64	0.02	34.87	0.14	5.52	0	0	0.01	0	0	26.56	75.76
	8.66	0	35.09	0.2	5.66	0	0	0	0	0	27.72	77.34
	8.89	0	34.49	0.13	5.52	0	0	0	0	0	25.68	74.73
	9.21	0	34.74	0.12	5.71	0.01	0	0	0	0	25.88	75.68
	9.67	0.01	35.18	0.15	5.79	0	0	0	0	0	26.93	77.74
	9.16	0.01	34.82	0.14	5.87	0	0	0	0	0	27.04	77.05
	9.12	0	34.38	0.13	5.91	0	0	0	0	0.01	25.6	75.14
	8.75	0	34.76	0.17	5.99	0.01	0	0	0	0.01	27.05	76.74
	9.05	0	34.61	0.16	5.95	0	0.01	0	0	0	28.79	78.57
	9.06	0	34.74	0.15	5.85	0	0	0	0	0.01	27.27	77.08
	8.86	0	34.79	0.18	5.99	0	0	0	0	0	28.24	78.07
	9.06	0	34.63	0.15	5.86	0	0	0	0.01	0	28.24	77.95
	16.63	0	34.8	0.2	6.79	0.03	0.02	0.01	0.01	0	28.65	87.14

Anti-perthite

The anti-perthite is present in all the samples and appears as dark grey orthoclase lamellae occurring as anastomosing textures with a light grey albite host (Figure 6.24). The anti-perthites were analyzed using EMPA to determine the crystals mineral composition, averages for each major element were plotted for each sample on Figure 6.24. Referring to Figure 6.25, we can see the anti-perthite is made up orthoclase and albite, however there is an anorthite component to the anti-perthites in each sample.

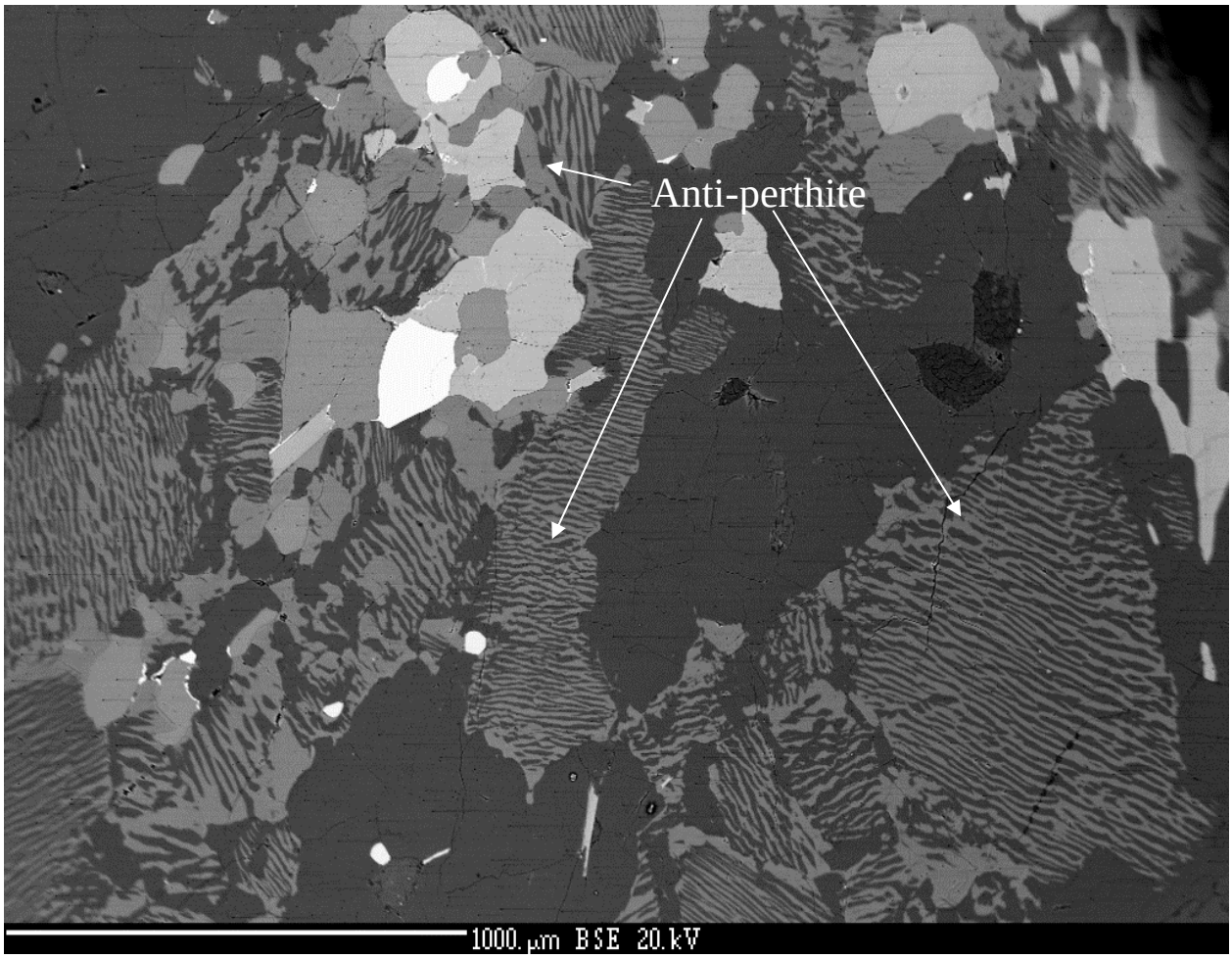
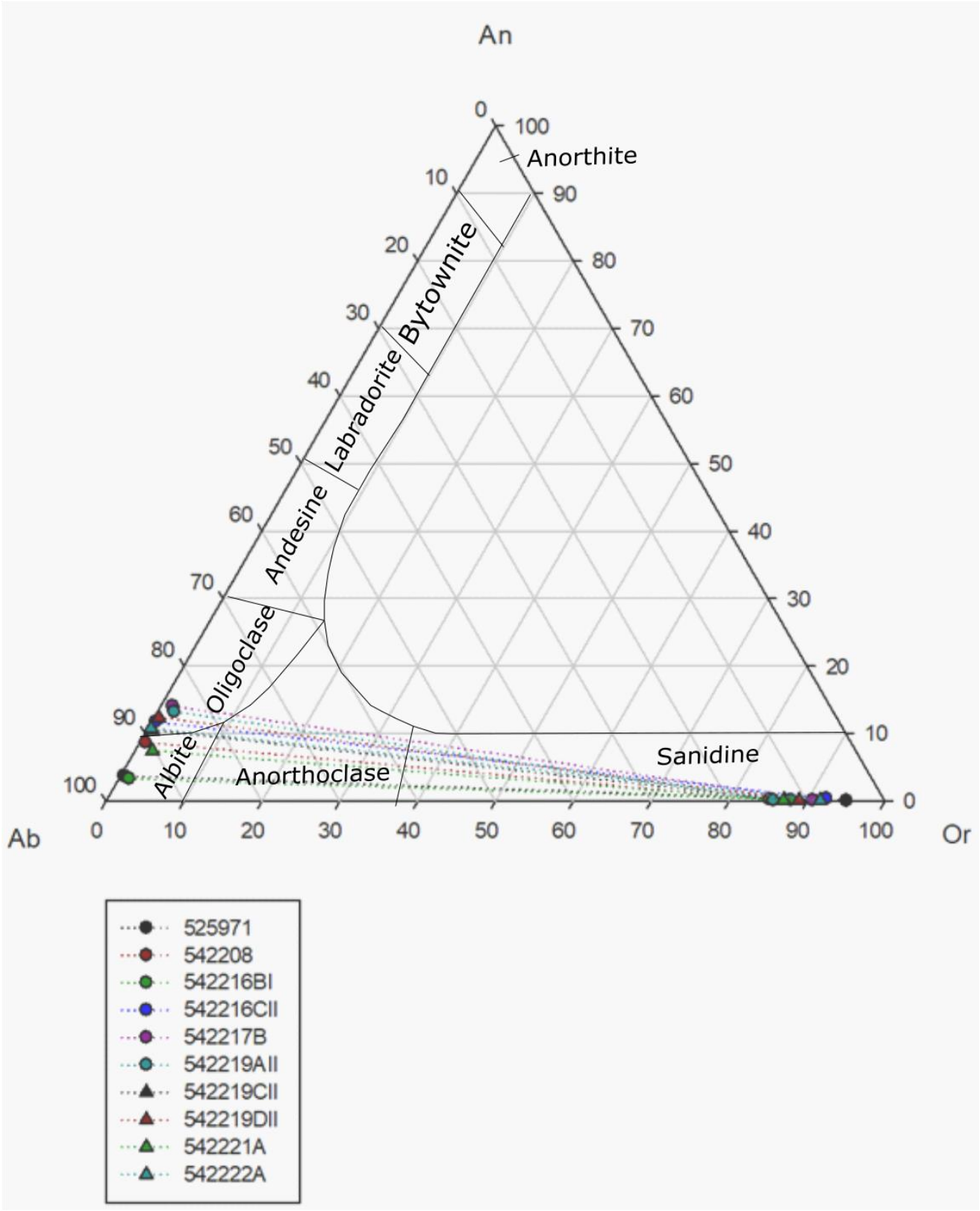


Figure 6.24: BSE image showing the anti-perthite that was analyzed in sample 542219. The dark grey lamellae are the orthoclase, while the lighter grey is the albite host.



<u>Figure 6.25</u>: Ternary diagram for all the samples that were analyzed using EPMA. The results seen are the averages taken for each sample and the orthoclase lamellae and albite host results are joined by tie-line for each sample.

6.3 Whole-Rock Chemistry

The whole rock data in this section will be used to compare the layered rock types which make up the Singertât Complex, as well as to similar complexes around the world. The major element geochemistry will also be used to better characterize the Singertât Complex.

6.3.1 Major Element Chemistry

Bulk rock major element data for the Singertât Complex samples are presented in Table 3 and Figure 6.26. These major element data will allow us to see variation between the different rock types which make up the Complex.

The silica contents of the rocks show quite a wide range of values with the carbonatites having the lowest SiO_2 compositions (0.53 – 41.52 wt%), similar to the ijolites, while melteigites and urtite samples have a lower silica content (47.3 -49.4 wt%, 46.2 – 48.3 wt% and 47.2 wt% respectively), compared to the pegmatites and the syenitic gneisses (53.4 – 58 wt% and 56.5 – 62.7 wt% respectively). With regards to the alumina content of the rocks, there is some overlap between the samples, but the alumina content does range significantly between the samples. The ijolites appear to have the widest range for Al_2O_3, between 10.27 – 25.28 wt%, while the carbonatites have the lowest Al_2O_3 content ranging from 0.16 – 14.52 wt%, probably due to the lack of nepheline and albite (anti-perthite). The melteigites appear to have the lowest alumina content amongst the nepheline-bearing rock - this is due to the low modal percentage of nepheline and albite in these rocks.

All the samples have relatively low Fe contents, the pegmatites having the lowest Fe content with the exception of one outlier, which has an FeO content of 9.11 wt%. The melteigite samples show the highest FeO content (6.13 – 10 wt%), due to the presence of magnetite in the samples. The rest of the samples have a fairly constricted range for FeO content.

The magnesium content is quite low in the pegmatites and syenitic gneisses (0.08 – 0.51 wt% and 1.19 – 1.68 wt% respectively), with the pegmatites having the lowest MgO content. From the nepheline-bearing rocks, the melteigites have highest magnesium content ranging from 5.21 – 7.75 wt% as it is the most mafic rock type.

The carbonatites have the highest CaO content (12.81 – 52.76 wt%) due to the large amounts of calcite present in the samples. The pegmatites have the lowest CaO content from all the samples (0.72 – 1.69 wt%). The ijolite and melteigite rock types have some overlap with regards to CaO content, which has values ranging from 3.66 – 13.88 wt% and 8.94 – 11.55 wt% respectively. The sodium content for all the samples largely overlaps and the range is relatively small ranging between 5.6 – 12.01 wt%. The potassium content for the rocks are similar as well, however one of the carbonatites has a very low potassium content of 0.07 wt%.

Table 4: Major element concentrations in wt% of the nepheline-bearing rocks, pegmatites, carbonatites and syenitic gneisses from the Singertât Complex.

Sample ID	Rock Type	SiO2	Al2O3	FeO	MnO	MgO	CaO	Na2O	K2O	TiO2	P2O5	Cr2O3	NiO	LOI	Total
525964	Pegmatite	53.42	19.92	9.11	0.07	0.51	1.69	5.60	6.37	0.86	0.03	0.01	0.00	2.11	99.70
525969	Pegmatite	53.41	26.44	0.69	0.01	0.18	1.52	10.74	5.31	0.05	0.02	0.01	0.00	2.35	100.72
525983	Pegmatite	58.07	23.75	0.69	0.01	0.14	0.72	9.71	5.65	0.06	0.03	0.01	0.00	1.21	100.06
542206	Pegmatite	57.27	24.94	1.60	0.01	0.08	0.73	10.95	5.48	0.06	0.01	0.01	0.00	-0.72	100.44
525972*	Carbonatite	20.18	7.33	1.95	0.12	1.41	34.69	2.31	2.23	0.23	0.96	-	-	27.38	98.80
542229*	Carbonatite	41.52	14.50	6.10	0.10	4.20	12.81	6.36	3.29	0.40	1.15	-	-	8.62	99.51
542230*	Carbonatite	-	-	1.43	0.56	1.26	52.76	-	-	-	-	-	-	42.82	98.88
542262*	Carbonatite	0.53	0.16	2.06	0.16	3.30	51.31	-	-	-	-	-	-	42.95	100.46
542263*	Carbonatite	15.23	1.51	1.92	0.11	5.21	44.88	-	0.07	0.09	-	-	-	30.90	99.92
525980	Syenitic Gneiss	58.76	19.75	2.06	0.05	1.2	5.49	6.79	2.63	0.62	0.34	0.01	-	0.94	98.9
525981	Syenitic Gneiss	59.51	17.5	3.13	0.05	1.68	5.86	6.08	3.74	0.62	0.37	0.01	-	0.52	99.46
525989	Syenitic Gneiss	62.71	17.24	2.9	0.05	1.34	4.61	4.57	3.94	0.6	0.34	0.01	-	0.65	99.33
542210	Syenitic Gneiss	62.74	17.05	2.32	0.04	1.19	2.76	6.99	4.73	0.3	0.12	0.01	-	0.92	99.46
542223	Syenitic Gneiss	56.61	18.56	2.81	0.05	1.32	6.76	6.26	2.87	0.73	0.32	0.01	-	2.57	99.22
525988	Urtite	47.23	24.78	2.91	0.06	2.08	4.52	11.5	3.14	0.23	0.03	0.01	-	3.16	100
525971	Ijolite	47.85	25.28	3.12	0.04	2.05	3.66	12.01	4.17	0.2	0.02	0.01	-	1.62	100.41
525982	Ijolite	47.48	21.81	4.38	0.08	4.34	5.7	9.8	3.71	0.64	0.07	0.02	-	1.36	99.93
525987	Ijolite	49.49	10.27	7.75	0.15	7.57	13.88	5.89	1.31	0.63	0.02	0.02	-	2.03	99.97
542212	Ijolite	45.48	23.35	5.52	0.09	3.98	5.44	9.75	3.62	0.79	0.02	0.01	-	1.67	100.41
542214	Ijolite	49.49	17.21	6.5	0.11	4.81	9.04	8.07	2.32	0.55	0.02	0.01	-	1.01	99.94
542224	Ijolite	47.38	16.07	6.89	0.13	5.28	11.41	7.2	1.44	0.63	0.24	0.02	-	2.03	99.56
525974	Melteigite	48.31	14.03	7.83	0.13	6.26	11.55	7.66	2.2	0.56	0.02	0.02	-	0.72	100.25
525984	Melteigite	47.25	14.9	7.2	0.12	7.75	11.01	6.41	2.85	0.98	0.02	0.03	-	1.21	100.62
525986	Melteigite	47.74	15.77	6.13	0.12	6.56	11.23	7.69	2.41	0.69	0.01	0.04	0.01	1.19	100.34
542203	Melteigite	46.8	17.86	7.14	0.11	5.21	8.94	8.94	2.96	0.77	0.02	0.01	-	0.59	100.24
542204	Melteigite	46.26	15.44	10.00	0.13	5.66	11.03	7.87	2.35	0.73	-	-	-	0.28	100.56

Major element data determined at the University of the Witwatersrand as well as the University of Johannesburg

* = XRF results determined at the University of Johannesburg

(-) =below detection limit

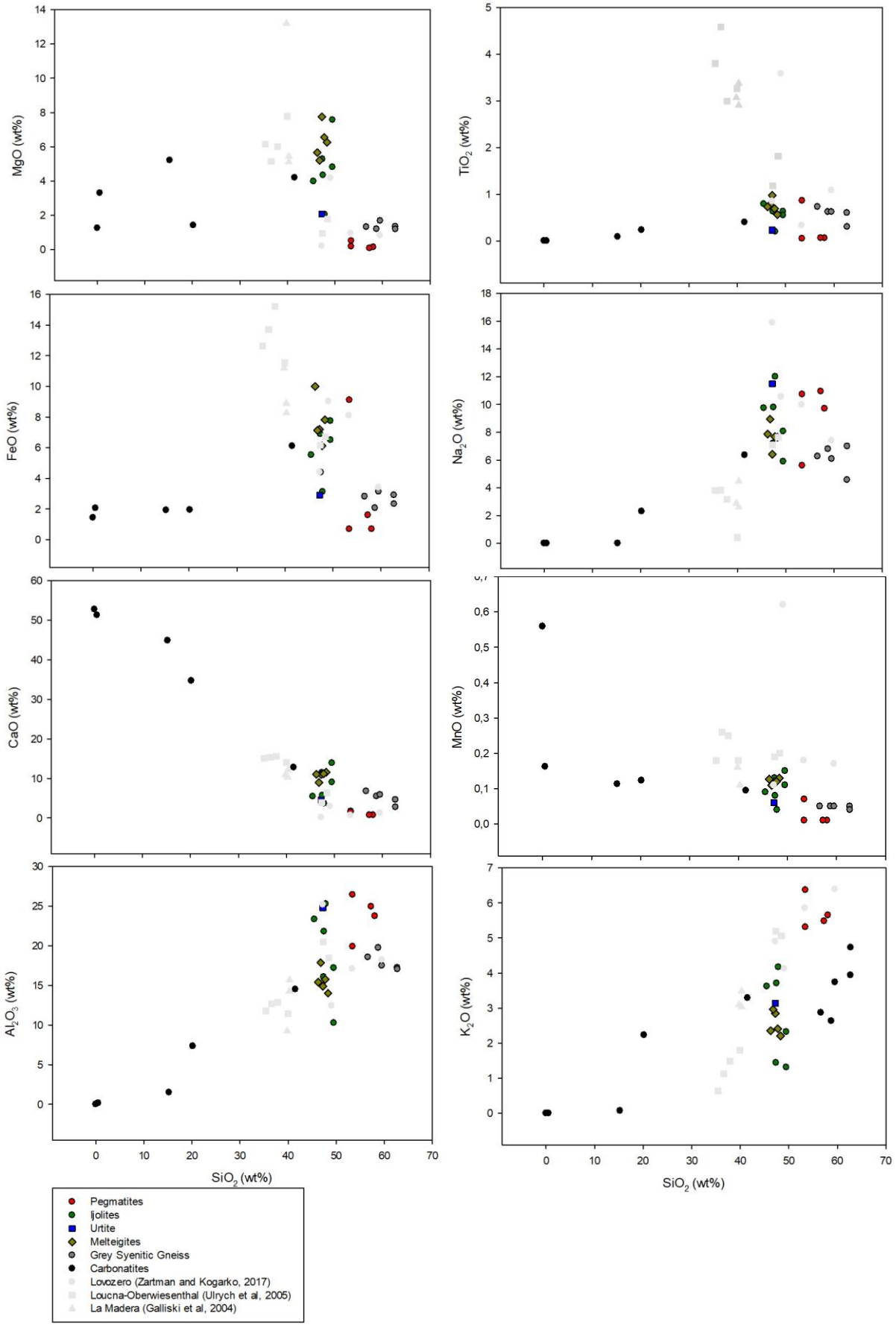
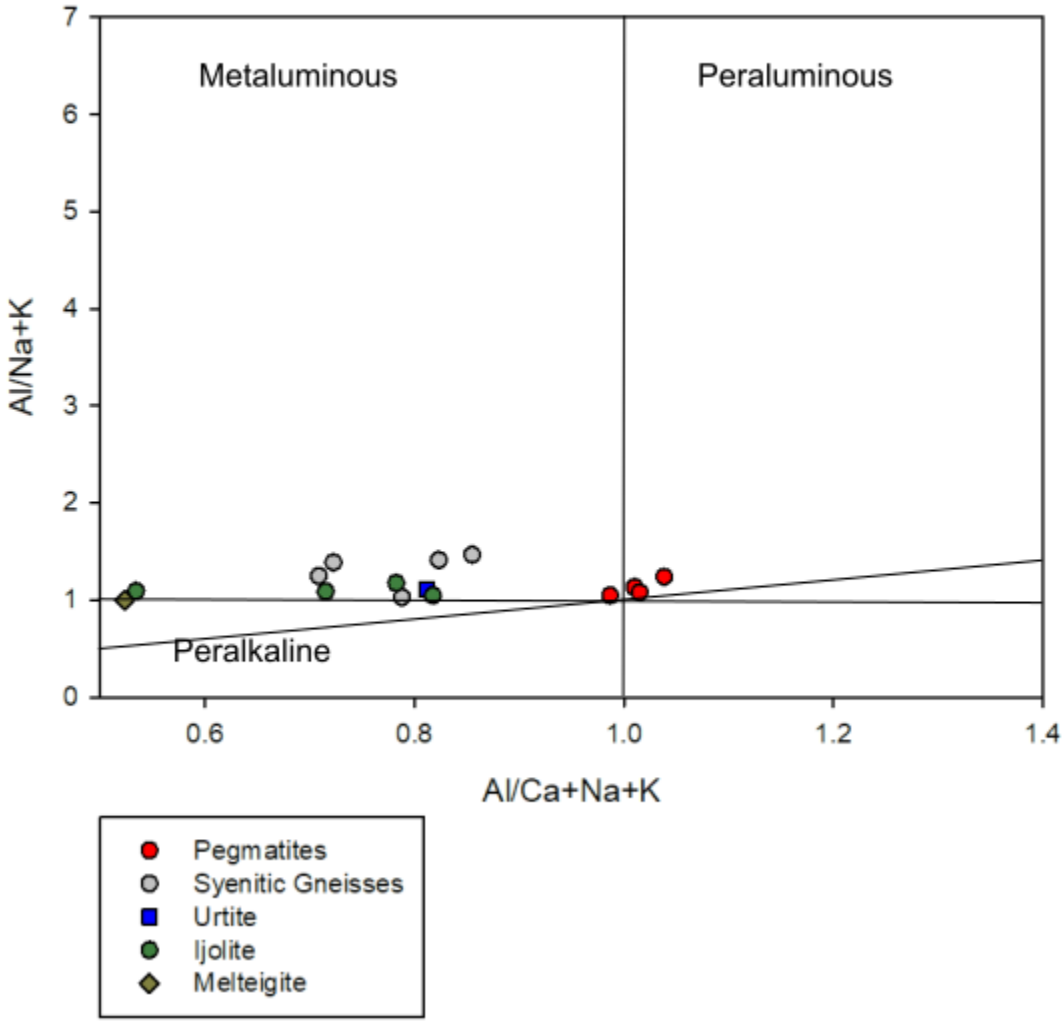


Figure 6.26 : Major element concentrations in wt% of the nepheline-bearing rocks, pegmatites, carbonatites and syenitic gneisses from the Singertât Complex.

Referring to Figure 6.27 below it would appear that the syenitic gneisses, the nepheline bearing rock samples and one of the pegmatite rock samples are metaluminous as they have $Al_2O_3/Na_2O+K_2O>1$ and $Al_2O_3/CaO+Na_2O+K_2O <1$. While the remaining pegmatite samples plot within the peraluminous field. It also appears that a few of the samples plot along the metaluminous-peralkaline boundary.



<u>Figure 6.27</u>: Major element ratios of alkalis to alumina plotted for the nepheline-bearing rocks, pegmatites, carbonatites and syenitic gneisses from the Singertât Complex (Shand, 1943).

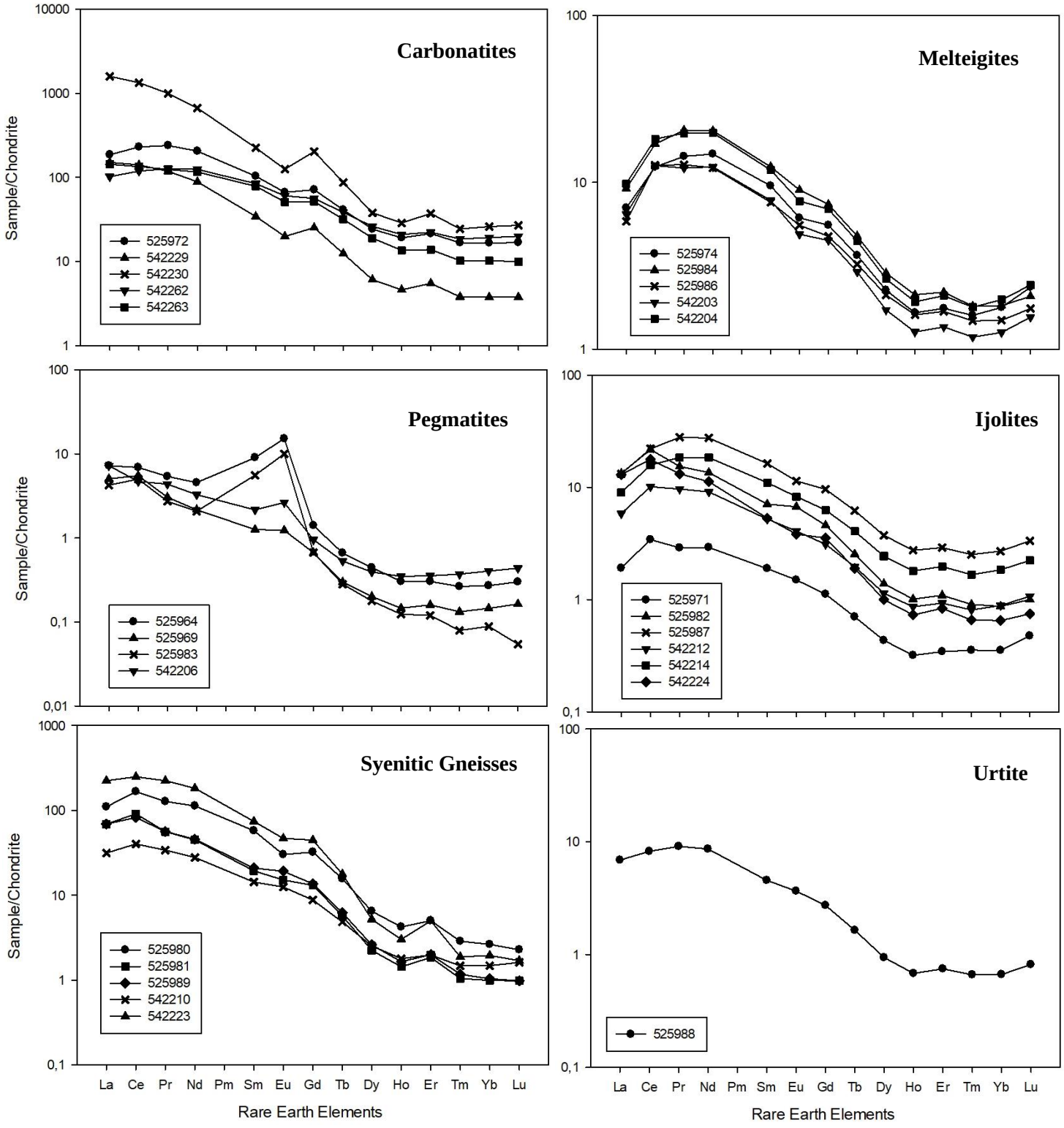
6.3.2 Trace Element Chemistry

Selected Rare earth Element (REE) bulk rock trace element data for the Singertât Complex samples are presented in Table 4 and Figure 6.28. This major element data will allow us to see variation between the different rock types which make up the Complex. All the rock types were normalized to chondritic reference value using Anderson and Grevasse (1989). The REE plots generally have an unusual "S" shape which appears to occur mainly in the nepheline-bearing rock samples. It is noted the "S" shape does flatten out from melteigite to urtite.

The ijolite, urtite, syenitic gneiss and pegmatite samples appear to be enriched in Light Rare Earth Elements (LREE) relative to chondrite and depleted in Heavy Rare Earth Elements (HREE), however the carbonatites and melteigites appears to be enriched in both LREE and HREE relative to chondrite. The carbonatites appear to be the most enriched in REES as these rocks are an order of magnitude more enriched with respect to the other rock types.

While the pegmatites all have positive Eu anomalies which is most likely due the large amounts of microcline in the sample. Samples 525983 and 525964 have quite large Eu anomalies. Samples 525983 and 542206 show a Ce anomaly which could represent the presence of monazite being in the sample. The syenitic gneiss samples appear to be enriched in REES with respect to the nepheline-bearing rocks. This is not typical of a host rock and this may serve as further evidence to suggest the syenitic gneiss is an intrusion that forms part if the Singertât Complex.

Sample ID	Rock type	La	Ce	Pr	Nd	Pm	Sm	Eu	Gd	Tb	Dy	Ho	Er	Tm	Yb	Lu
Anders and Grevesse (1989) in ppm	Chondrite	0.45	1.14	0.17	0.83	-	0.26	0.10	0.33	0.06	0.39	0.09	0.25	0.04	0.25	0.04
525964	Pegmatite	7.25	6.91	5.40	4.56	-	9.03	15.25	1.41	0.66	0.44	0.30	0.30	0.26	0.27	0.30
525969	Pegmatite	5.06	5.51	3.06	2.17	-	1.26	1.23	0.67	0.30	0.20	0.15	0.16	0.13	0.15	0.16
525983	Pegmatite	4.25	5.03	2.74	2.08	-	5.59	10.01	0.67	0.28	0.18	0.12	0.12	0.08	0.09	0.05
542206	Pegmatite	7.24	4.70	4.37	3.28	-	2.16	2.64	0.95	0.53	0.39	0.35	0.35	0.37	0.40	0.44
525972	Carbonatite	186.23	230.23	239.78	205.41	-	103.41	66.55	71.39	41.09	24.19	19.07	21.39	16.69	16.55	16.78
542229	Carbonatite	150.89	141.07	118.01	88.84	-	34.31	19.77	25.22	12.42	6.06	4.60	5.49	3.79	3.75	3.76
542230	Carbonatite	1593.48	1340.12	997.73	668.14	-	225.22	125.44	202.78	87.43	37.80	28.68	37.14	24.38	25.95	26.81
542262	Carbonatite	102.07	118.59	127.22	124.68	-	84.49	60.29	56.14	38.32	26.09	20.91	22.19	18.50	19.18	19.89
542263	Carbonatite	143.17	134.53	124.50	116.08	-	78.57	50.91	51.43	31.77	18.88	13.57	13.80	10.22	10.21	9.95
525980	Syenitic Gneiss	110.12	166.76	127.42	113.09	-	57.66	30.16	32.26	15.66	6.49	4.23	5.01	2.87	2.64	2.28
525981	Syenitic Gneiss	69.07	91.10	56.25	44.89	-	19.40	15.14	13.09	5.72	2.24	1.43	1.85	1.04	0.99	0.98
525989	Syenitic Gneiss	69.10	82.46	56.55	45.81	-	20.92	19.21	13.66	6.24	2.60	1.65	2.00	1.17	1.04	0.98
542210	Syenitic Gneiss	31.46	40.32	34.04	27.92	-	14.33	12.51	8.81	4.85	2.53	1.79	1.98	1.47	1.48	1.61
542223	Syenitic Gneiss	224.29	249.52	223.92	182.42	-	74.15	46.80	44.67	17.80	5.19	3.01	4.98	1.87	1.95	1.69
525988	Urtite	6.89	8.24	9.11	8.63	-	4.55	3.66	2.73	1.64	0.94	0.68	0.75	0.66	0.67	0.82
525971	Ijolite	1.91	3.44	2.90	2.93	-	1.89	1.50	1.12	0.70	0.43	0.32	0.34	0.35	0.35	0.48
525982	Ijolite	13.35	21.84	15.44	13.60	-	7.11	6.74	4.61	2.55	1.39	1.01	1.09	0.91	0.87	1.00
525987	Ijolite	13.28	22.14	28.04	27.62	-	16.38	11.43	9.66	6.23	3.75	2.76	2.91	2.53	2.71	3.35
542212	Ijolite	5.85	10.17	9.71	9.14	-	5.24	4.09	3.12	1.97	1.14	0.86	0.93	0.81	0.89	1.07
542214	Ijolite	9.03	15.86	18.54	18.49	-	11.06	8.30	6.30	4.08	2.45	1.80	1.97	1.67	1.85	2.24
542224	Ijolite	13.07	17.79	13.26	11.27	-	5.35	3.84	3.55	1.90	1.00	0.73	0.84	0.66	0.65	0.75
525974	Melteigite	7.02	12.37	14.32	14.79	-	9.53	6.12	5.54	3.65	2.25	1.65	1.76	1.59	1.78	2.35
525984	Melteigite	9.17	16.99	20.53	20.39	-	12.39	9.01	7.36	4.76	2.86	2.12	2.19	1.81	1.82	2.08
525986	Melteigite	5.83	12.69	12.77	12.23	-	7.59	5.52	4.75	3.23	2.11	1.61	1.68	1.48	1.49	1.75
542203	Melteigite	6.44	12.60	12.19	12.37	-	7.80	4.88	4.49	2.90	1.72	1.27	1.36	1.18	1.26	1.55
542204	Melteigite	9.83	18.18	19.70	19.79	-	11.85	7.71	6.90	4.45	2.63	1.92	2.09	1.78	1.98	2.42



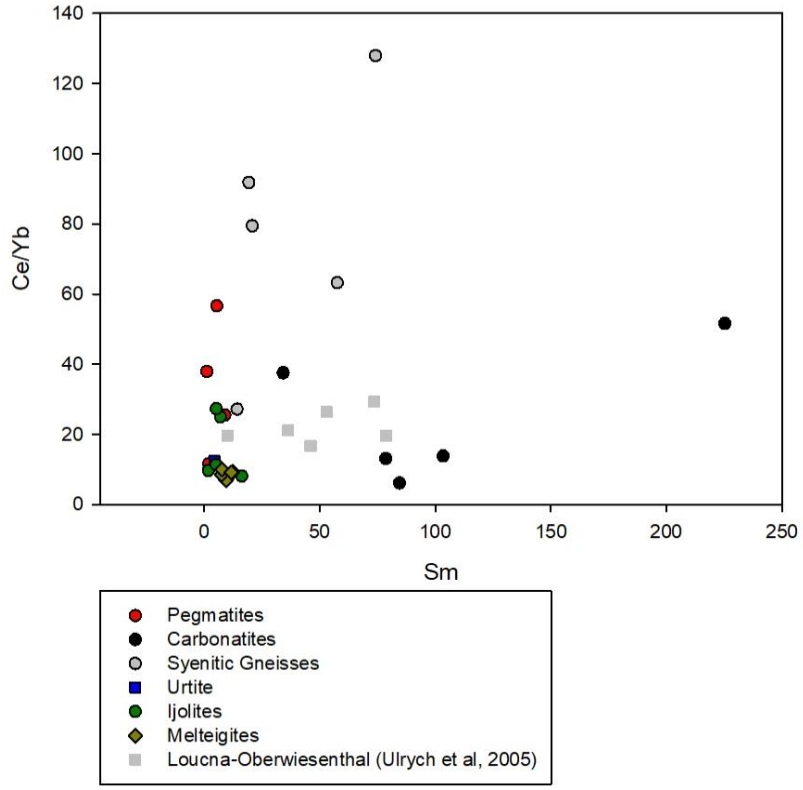
<u>Figure 6.28</u>: REE plots for different rock types that make up the Singertât Complex. The samples were normalized to chondrite (Anderson and Grevasse, 1988)

Referring to Figure 6.29 the rock types do not cluster together but rather plot sparsely. However, while many of the syenitic gneiss samples tend to plot away from the rest of the rock types (with a high Ce/Yb ratio) one of the syenitic gneiss samples plots with the alkaline bearing rocks. The pegmatites seem to form a linear trend which has a high Ce/Yb ratios (Table 6), which then decreases and plots closer to the nepheline-bearing alkaline rocks. The carbonatites tend to plot on their own without much relationship to the other rock types.

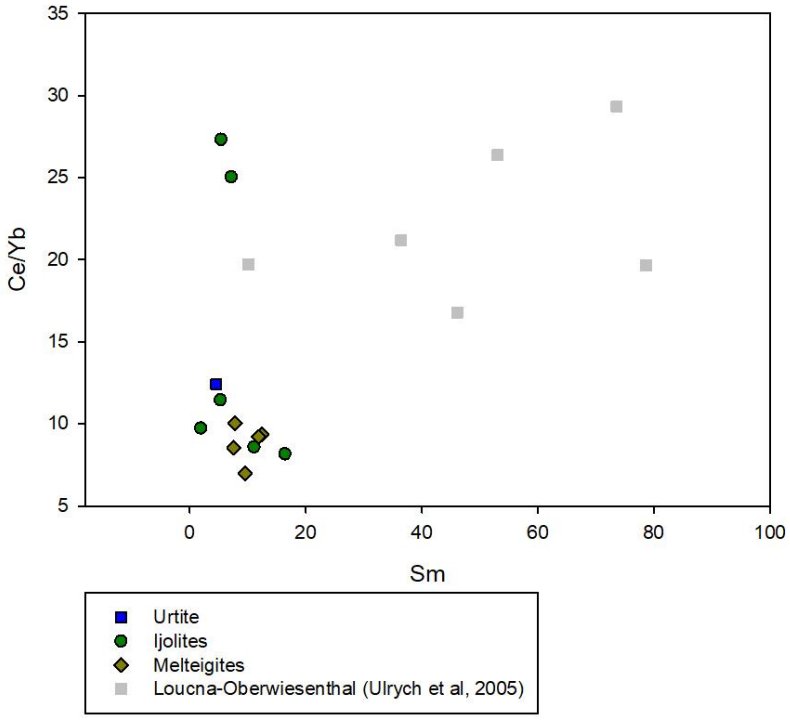
Table 6: Trace elements and trace element ratios used for open magma systems according to Rollinson, 1993. All values are normalized to chondritic reference value using Anderson and Grevasse (1989)

	Ce/Yb	Ce	Yb	Sm
Pegmatites				
525964	25.56452	6.909331	0.27027	9.031758
525969	37.95848	5.512324	0.14522	1.258714
525983	56.63848	5.026408	0.088745	5.588691
542206	11.66177	4.704225	0.403388	2.164988
ijolite				
525971	9.741126	3.437839	0.35292	1.891227
525982	25.05044	21.83553	0.871663	7.11366
525987	8.162796	22.13541	2.711743	16.38278
542212	11.45691	10.16978	0.887655	5.236936
542214	8.591881	15.85903	1.845816	11.05746
542224	27.32815	17.79119	0.651021	5.346472
Urtite				
525988	12.39205	8.242237	0.665123	4.554084
Meleigites				
525974	6.961447	12.37189	1.777201	9.527216
525984	9.340252	16.9922	1.819245	12.39303
525986	8.531457	12.6879	1.487191	7.590573
542203	10.02125	12.60311	1.257638	7.796272
542204	9.197707	18.17885	1.976455	11.85175
Carbonatites				
525972	13.90876	230.233	16.55309	103.408
542229	37.57063	141.0733	3.754882	34.30562
542230	51.63533	1340.116	25.95348	225.2211
542262	6.182008	118.5889	19.18291	84.49215
542263	13.17951	134.5275	10.20732	78.57462
Syenitic Gneisses				
525980	63.27068	166.7556	2.635591	57.6638
525981	91.82858	91.09623	0.992025	19.40214
525989	79.4796	82.45884	1.037484	20.91629
542210	27.25707	40.32425	1.479405	14.32516
542223	127.9648	249.5172	1.949888	74.14793
Loucna-Oberwiesenthal				
Ijolite	19.71884	66.02113	3.348124	10.06971
Nephilinite	29.33987	247.3592	8.430819	73.58637
Nephilinite	19.64773	222.7113	11.33522	78.62122
Nephilinite	26.36847	153.169	5.808794	53.05964
Nephilinite	16.78629	132.0423	7.866075	46.0883
Nephilinite	21.18834	205.9859	9.721662	36.40589

a)



b)



<u>Figure 6.29:</u> Trace element bivariate plot of Ce/Yb vs Sm which have been normalized to chondritic reference value using Anderson and Grevasse (1989), comparing the Singertât rocks as well as the alkaline rocks of Loucna-Oberwiesenthal. a) All Singertât rock types, b) Singertât nepheline-bearing alkaline rocks.

Table 7 shows the calculated trace element ratios $(La/Sm)_N$, $(Gd/Yb)_N$ and $(La/Yb)_N$. $(La/Yb)_N$ determines the degree of fractionation between LREEs and HREEs during geochemical processes (Aubert et al., 2001; Yusoff et al., 2013), while $(La/Sm)_N$, $(Gd/Yb)_N$ show the degree of fractionation between LREEs and MREEs (Middle Rare Earth Elements) and between MREEs and HREEs, respectively (Yusoff et al., 2013).

These ratios in the pegmatites have ranges for $(La/ Yb)_N$ from 1.80 to 34.86, for $(Gd/Yb)_N$ from 1.33 to 7.54 and for $(La/Sm)_N$ from 0.76 to 4.02. The greatest fractionation occurred between LREEs and HREEs with moderate fractionation between MREEs and HREEs and LREEs and MREEs. The carbonatites have ranges for $(La/ Yb)_N$ from 5.03 to 61.40, for $(Gd/Yb)_N$ from 2.92 to 7.81 and for $(La/Sm)_N$ from 1.21 to 7.07. The greatest fractionation occurred between LREEs and HREEs with moderate fractionation between LREEs and MREEs and MREEs and HREEs. The syenitic gneisses have ranges for $(La/ Yb)_N$ from 21.26 to 115.02, for $(Gd/Yb)_N$ from 5.95 to 22.91 and for (La/Sm)n from 1.91 to 3.56. The greatest fractionation occurred between LREEs and HREEs and the MREEs and HREEs with relatively minor fractionation between LREEs and MREEs. The ijolites have ranges for $(La/ Yb)_N$ from 4.89 to 20.08, for $(Gd/Yb)_N$ from 3.16 to 5.45 and for $(La/Sm)_N$ from 0.81 to 2.44. The greatest fractionation occurred between LREEs and HREEs with relatively minor fractionation between MREEs and HREEs and LREEs and MREEs. The melteigites have ranges for $(La/ Yb)_N$ from 3.92 to 5.04, for $(Gd/Yb)_N$ from 3.11 to 4.05 and for $(La/Sm)_N$ from 0.82 to 0.73. The greatest fractionation occurred between LREEs and HREEs with relatively minor fractionation between MREEs and HREEs and LREEs and MREEs.

Table 7: Trace element ratios La/Sm, Gd/Yb and La/Yb for the Singertât Complex. All values are normalized to chondritic reference value using Anderson and Grevasse (1989).

Sample ID	Rock type	La/Sm	Gd/Yb	La/Yb
Anders and Grevesse (1989) in ppm	Chondrite	1.727343145	1.331181928	1.799112545
525964	Pegmatite	0.802598859	5.213636364	26.82085202
525969	Pegmatite	4.022184201	4.611607744	34.86286746
525983	Pegmatite	0.761066102	7.546267218	47.9276702
542206	Pegmatite	3.344087376	2.366318182	17.94773767
525972	Carbonatite	1.80091444	4.312605458	11.25040325
542229	Carbonatite	4.39847373	6.717227126	40.18565638
542230	Carbonatite	7.075199008	7.813288258	61.39770885
542262	Carbonatite	1.208011466	2.926691458	5.320750058
542263	Carbonatite	1.82209564	5.038756477	14.02625625
525980	Syenitic Gneiss	1.909753684	12.24100569	41.78328683
525981	Syenitic Gneiss	3.560117173	13.19392938	69.62919241
525989	Syenitic Gneiss	3.303658669	13.16952876	66.60369698
542210	Syenitic Gneiss	2.196130954	5.954313523	21.26526207
542223	Syenitic Gneiss	3.024838656	22.90984541	115.024802

525988	Urtite	1.512667732	4.103997506	10.35720728
525971	Ijolite	1.010163712	3.166575464	5.41326148
525982	Ijolite	1.876728511	5.285825834	15.31602909
525987	Ijolite	0.810881174	3.560889012	4.898872435
542212	Ijolite	1.117352126	3.514907893	6.592093511
542214	Ijolite	0.816942894	3.413909243	4.893939758
542224	Ijolite	2.445355057	5.453383305	20.08234886
525974	Melteigite	0.736936514	3.116248939	3.950567655
525984	Melteigite	0.740094313	4.047730171	5.04165892
525986	Melteigite	0.768402345	3.1912906	3.921900754
542203	Melteigite	0.826315835	3.566362129	5.122443896
542204	Melteigite	0.829644277	3.493182197	4.97493663

6.4 Geochronology

6.4.1 Zircon morphology and texture

The zircon crytsals present in the Singertât Complex appear to be magmatic in origin. They are angular to blocky in shape and range in size from 100 μm – 400 μm in the pegmatite samples (Figure 6.30 a and b, 6.34), 100 μm – 200 μm in the ijolite sample (Figure 6.31), 100 μm – 150 μm in the melteigite sample (Figure 6.33), and 100 μm – 200 μm in the carbonatite breccia samples (Figure 6.32). Zircon colour varies from pink to orange-brown. Zircon grains appear to have no noticeable radiation damage (i.e., metamictization). The zircons have patchy zoning; however, the cores seem to be fairly homogenous. LA-MC-ICPMS U/Pb age determinations were performed on 6 samples. All of the samples that were analyzed continued low-U zircons with values ranging from 21 -53 ppm for pegmatite sample 525964, 11 – 60 ppm in pegmatite sample 525969, 22 – 141 ppm in pegmatite sample 542206, 69 -174 ppm in carbonatite sample 525972, 24 -72 ppm in ijolite sample 525971 and 6 – 67 ppm in melteigite sample 542204.The results for each sample are shown as Concordia diagrams in Figure 6.35, which were created in Isoplot (Ludwig, 2003). All U/Pb data in the Concordia diagrams are regressed and anchored to zero as some recent Pb-loss appears to have occurred. The samples were not common lead correct, however looking the 206/204 results in Appendix X, the ratios are quite high which may serve as evidence that these zircons do not contain significant amounts of common lead.

Referring to Table 8 and Figure 6.35 the ijolite sample 525971 had 21 spots analyzed from 16 zircons. In this sample one of the grains appears to be inherited and 5 spots yielded a $^{206}Pb/^{238}U$ age of 3094 ± 300 Ma, which were excluded from the regression. The remainder of the other analyses yielded a $^{206}Pb/^{238}U$ age of 2771 ± 9.9 Ma. The Concordia plot calculated from these 21 analyses shows that the zircons in this sample are discordant, which may be a result of recent Pb loss. Melteigite sample 542204 had 26 spots analyzed from 9 zircons, which yielded a $^{206}Pb/^{238}U$ age of 2774 ± 5.8 Ma. The Concordia plot calculated from these 26 analyses shows that the zircons in this sample are discordant, which may be a result of recent lead loss. Pegmatite sample 525964 had 18 spots analyzed from 7 zircons, which yielded an $^{206}Pb/^{238}U$ age of 2785 ± 10 Ma. The Concordia plot calculated

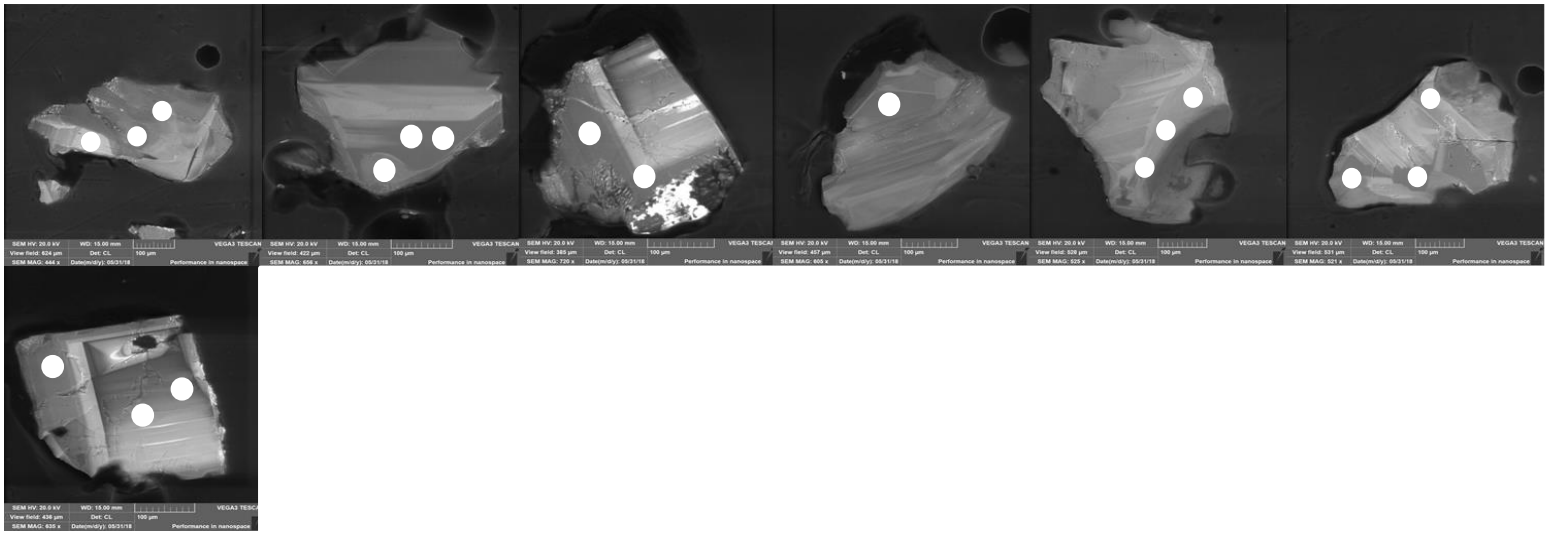
from these 18 analyses shows that the zircons in this sample are discordant, which may be a result of recent lead loss. Pegmatite sample 525969 had 19 spots analyzed from 7 zircons, which yielded a $^{206}Pb/^{238}U$ age of 2771 ± 32 Ma. The Concordia plot calculated from these 19 analyses shows that the zircons in this sample are discordant, which may be a result of recent lead loss. Pegmatite sample 542206 had 61 spots analyzed from 20 zircons, which yielded a $^{206}Pb/^{238}U$ age of 2753 ± 5.8 Ma. The Concordia plot calculated from these 61 analyses shows that the zircons in this sample are discordant, which may be a result of recent lead loss. Carbonatite sample 525972 had 47 spots analyzed from 19 zircons. In this sample one of the grains appears to be inherited, with 5 spots yielding an age of 2837 ± 120 Ma these spots were excluded from the regression seen below, while the other analyses yielded an age of 2750 ± 11 Ma. The Concordia plot calculated from these 47 analyses shows that the zircons in this sample are discordant, which may be a result of recent lead loss.

Table 8: Ages determined using U-Pb analyses on zircons located in the nepheline-bearing rocks, pegmatites and carbonatite (including inherited zircons, excluding one sample that contained large amounts of common lead). For detailed analyses see Appendix X.

Sample	Rock Type	Pb 207/206 age (Ma)	Number of analyses
CDQNGNG	Standard	1824 ± 11	63
Mud Tank	Standard	720 ± 35	62
525964	Pegmatite	2785 ± 10	18
525969	Pegmatite	2771 ± 9.9	19
542206	Pegmatite	2753.4 ± 5.8	61
525971	Ijolite	2771 ± 32	21
525971*	Ijolite	3094 ± 300	5
542204	Melteigite	2774 ± 12	26
525972	Carbonatite	2750 ± 11	47
525972*	Carbonatite	2837 ± 120	4

* - Ages for inherites zircons found in sample

a)



b

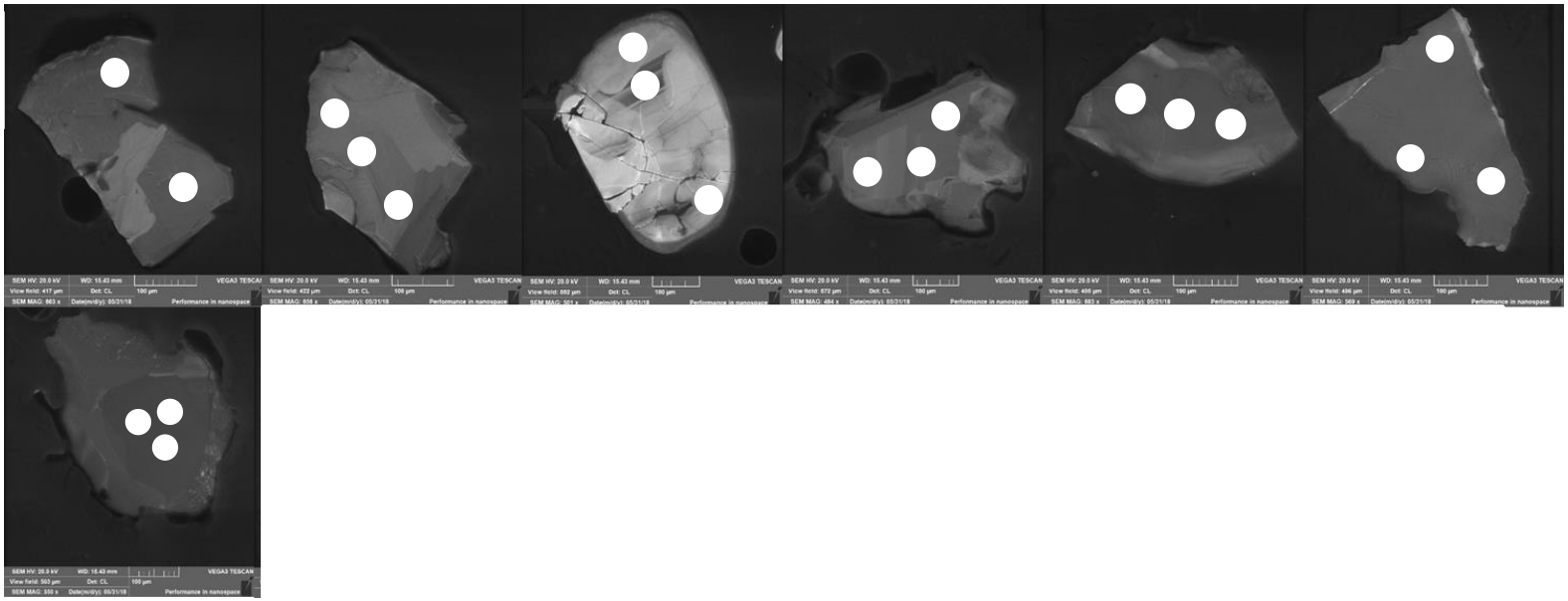


Figure 6.30: CL images depicting laser spot locations of the magmatic zircons in the

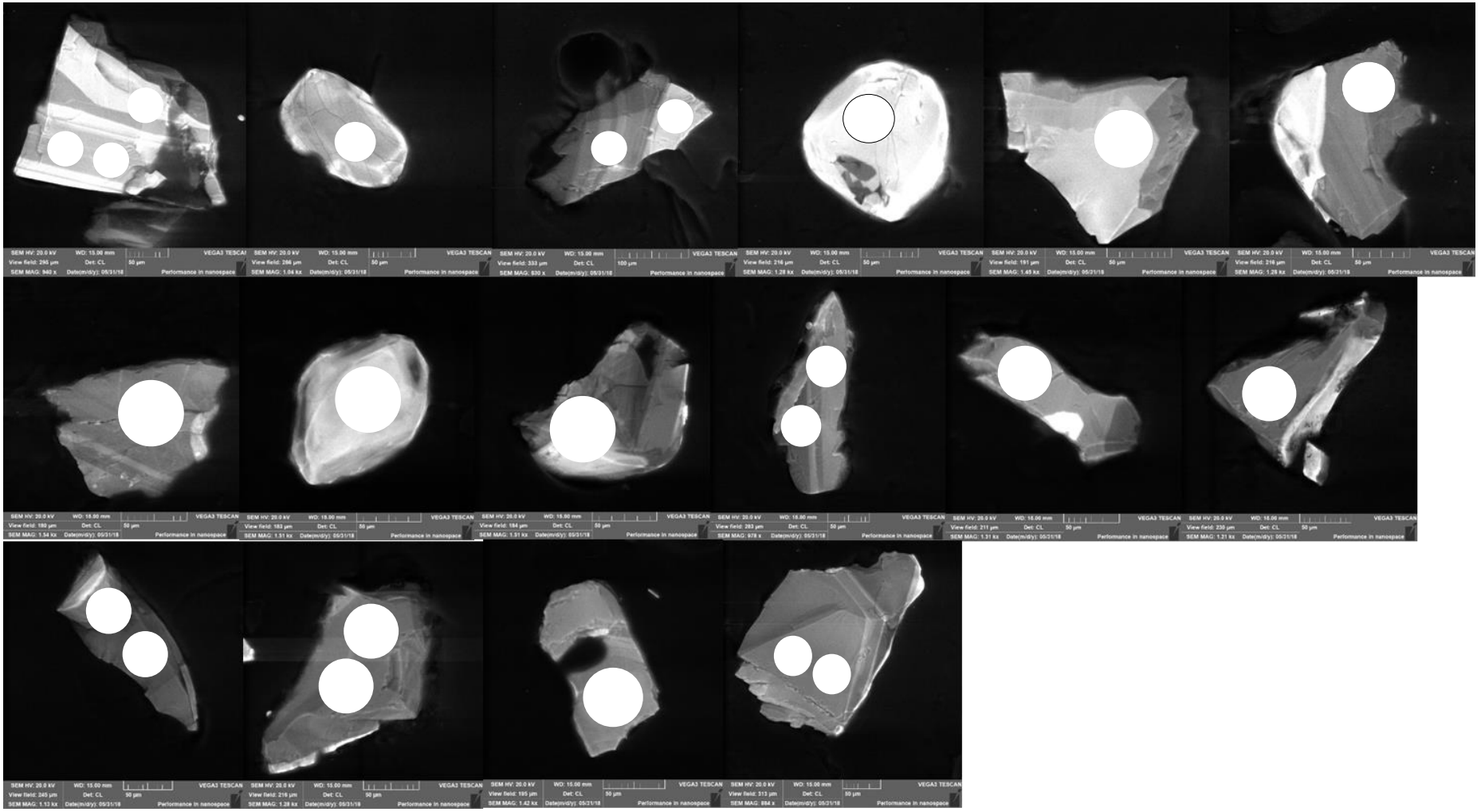


Figure 6.31: CL images depicting laser spot analyses of the magmatic zircons in the ijolite sample 525971

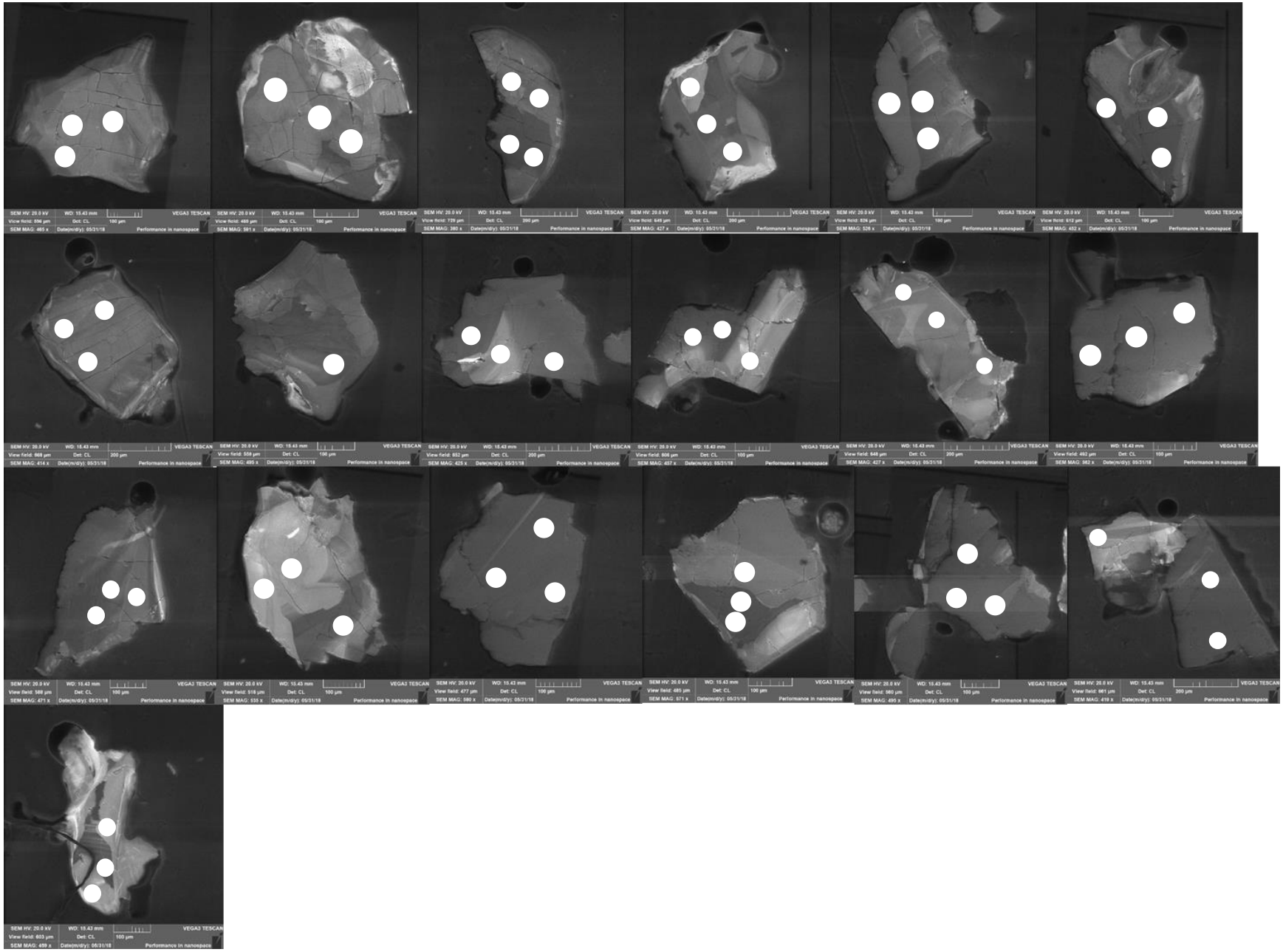


Figure 6.32: CL images depicting the laser spots of the magmatic zircons in the carbonatite breccia sample 525972

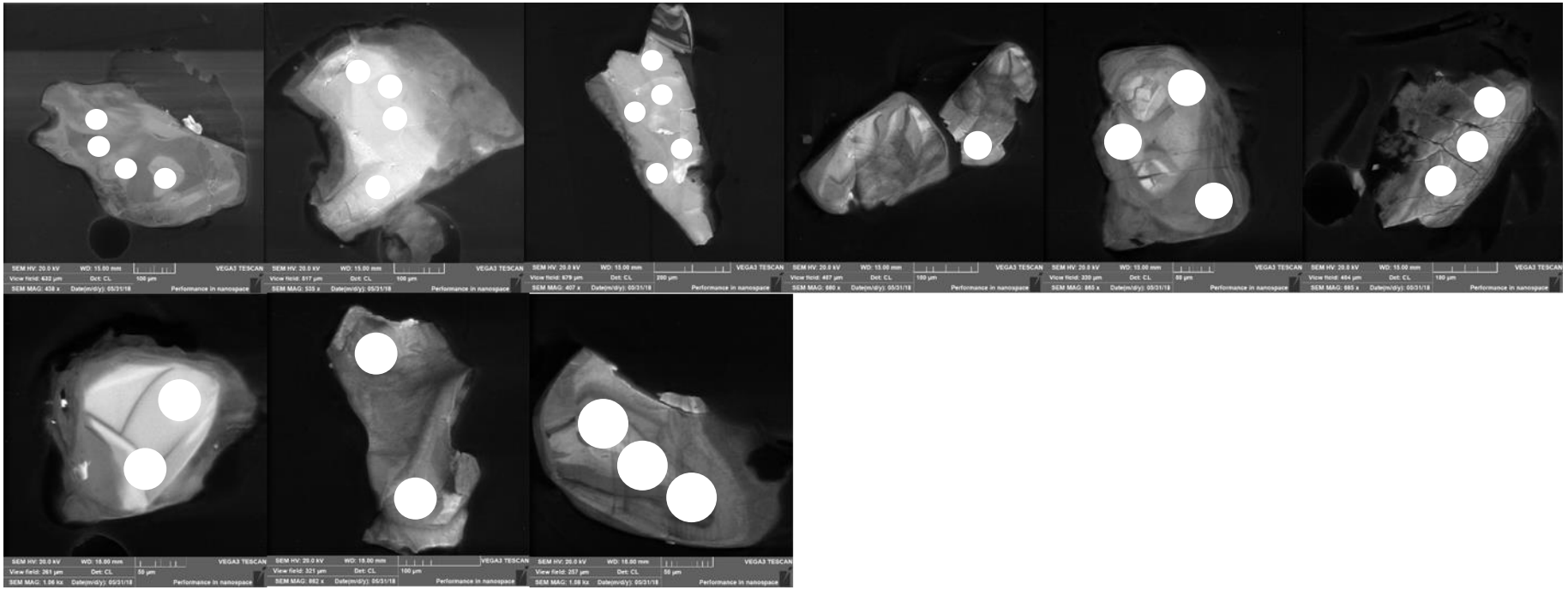


Figure 6.33: CL images depicting the laser spots of the magmatic zircons in the melteigite sample 542204.

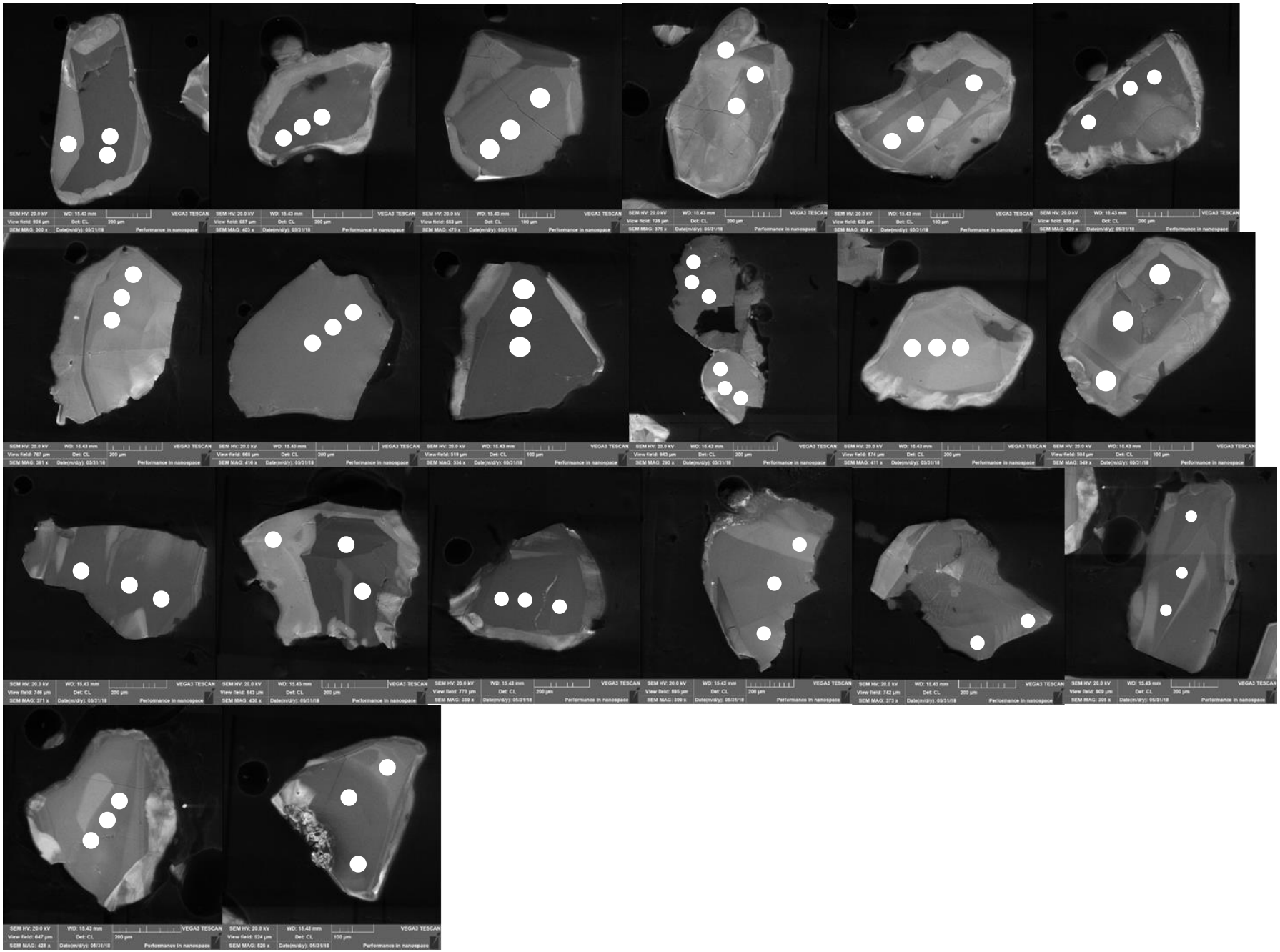
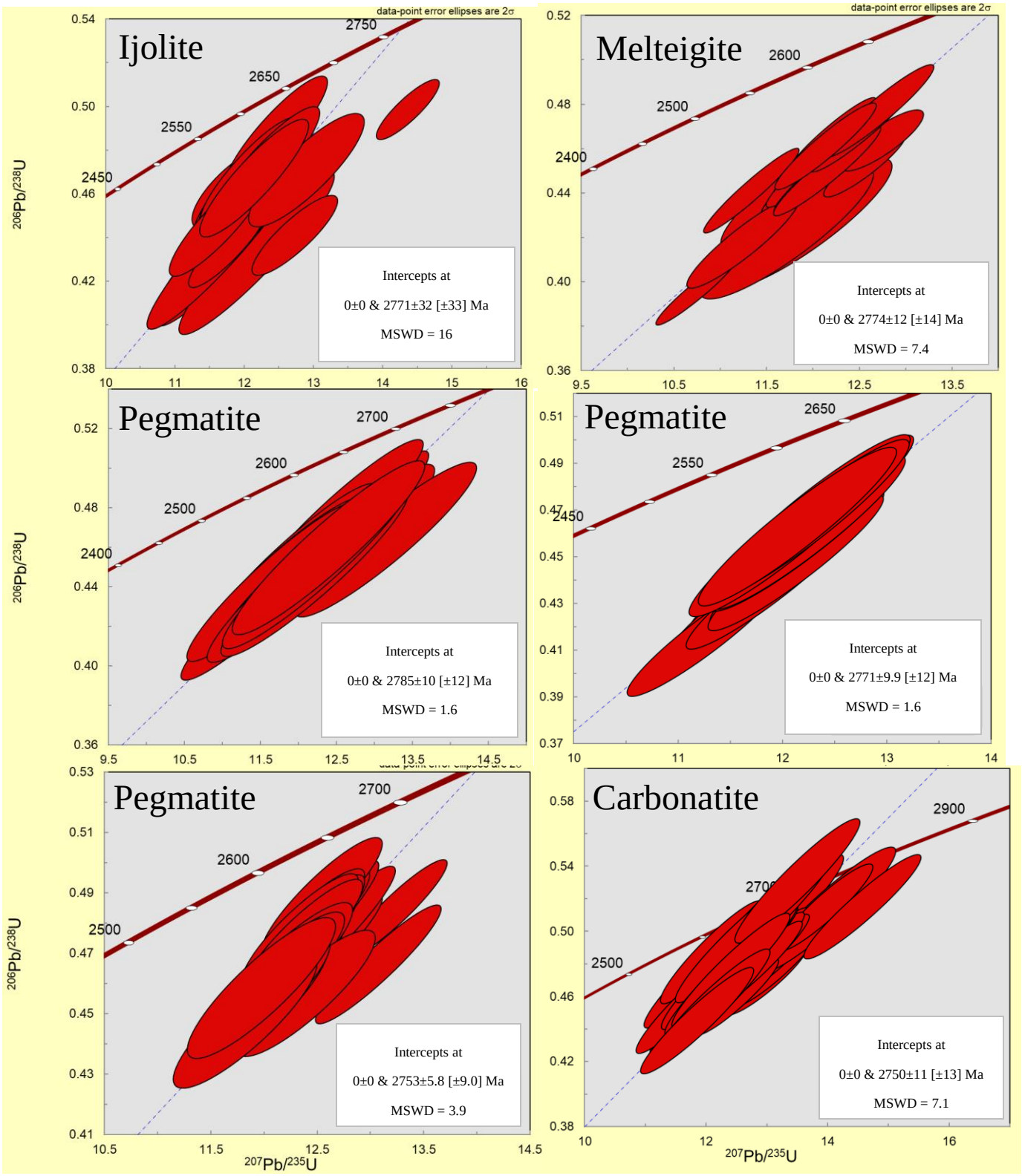


Figure 6.34: CL images depicting the laser spots of the magmatic zircons in the pegmatite sample 542206.



<u>Figure 6.35</u>: Concordia plots for the nepheline-bearing rocks, pegmatites and a carbonatite used to determine $^{207}Pb/^{206}Pb$ ages.

7. Discussion

7.1 New geological data emerging from the Singertât Complex

7.1.1 The Singertât syenitic gneiss should be reclassified as a nepheline syenite

The syenitic gneisses found in the study area were previously thought to be an older host rock to the alkaline Singertât Complex, however the petrographic and geochemical evidence found in this study shows that this may not be the case. The first line of evidence supporting this is the presence of nepheline in these "gneisses", suggesting a more accurate description may be nepheline syenite. The occurrence of nepheline would make the syenite silica undersaturated and likely to formed with the other alkaline rock types that make up the Singertât Complex. Secondly, while the contacts which occur between the syenitic gneisses and the nepheline bearing alkaline rocks are generally sharp (Figure 6.8, Chapter 6.1), this is most likely because the syenitic gneiss and nepheline-bearing alkaline rocks were a part of a separate pulses of magma forming the Singertât Complex. However, across this sharp boundary the populations of nepheline in the syenitic gneiss are chemically similar to those which occur in the melteigite (Figure 6.18). This could serve as further evidence that the syenitic gneiss are actually part of the Singertât Complex and not the host rock. However, an alternative explanation for this relationship is described by Brøgger (1921) and Anderson (1989), and may be explained by the process of fenitization, whereby due to metasomatic processes a rock may be depleted in silica, while introducing alkalis. The resultant rock would be a silica undersaturated, peralkaline gneiss with aegerine-augite as a characteristic mineral. This process of fenitization is observed in the Fen Complex, Norway and also may be a possible explanation for the silica-undersaturated syenitic gneiss seen in the Singertât Complex. Testing of this hypothesis requires new geochronology data for the syenitic gneisses, which is beyond the scope of this thesis.

7.1.2 The Singertât Complex is older than previously stated

According to Blichert-Toft *et al*. (1995) at ~ 2.68 Ga the Singertât Stage occurred during the formation of the SAIP in the Late Archean. This age was determined from a single zircon found in a carbonatite sample, which is one of the youngest rocks that form part the Singertât Complex, as it cross cuts all the other rocks types in the Singertât Complex. This age would place the intrusion of the Singertât Complex after the formation of the Skjoldungen Orogeny (2.79 -2.7 Ga), thereby classifying it as post-orogenic event. However, the results obtained using U/Pb zircon geochronology in this study demonstrates that the Singertât Complex is older than previously stated. The nepheline-bearing pegmatite ages range from 2785 ± 10 Ma to 2753.4 ± 5.8 Ma, one dated carbonatite returns an age of 2750 ± 11 Ma, a representative ijolite sample is dated at 2771 ± 32 Ma and a representative melteigite sample produces an age of 2774 ± 12 Ma (Figure 7.1 and Figure 7.2). A few analyzed zircon grains were much older than the orogen (3094 ± 300 Ma and 2837 ± 120 Ma) found in the previously mentioned samples and are likely to be inherited from the older, surrounding, >2850 Ma TTG host rocks (Kolb *et al*., 2013). The ages obtained in this study provide evidence that the Singertât Complex was formed in the Archean, making this

possibly one of the oldest alkaline igneous complexes in the world, as it even older than the Nechalacho Layered Alkaline Suite in Canada (Table 9). Figure 7.1 depicts that the ages found for the rock types of the Singertât Complex fall within the early formation of the SAIP, which is much earlier than previously stated by literature (Kolb *et al*., 2013 and Blichert-Toft *et al*., 1995) which is shown as the gray triangle in Figure 7.1 below.

Table 9: Ages of other alkaline igneous complexes in the world.

Name of the Alkaline Intrusion	Age	Reference
Nechalacho Layered Alkaline Suite, Canada	2.1 Ga	Sheard *et al*., 2012
Pilanesberg Complex, South Africa	1370 Ma	Elburg & Cawthorn, 2017
Khibina & Lovozero Complexes, Russia	371 - 362 Ma	Kramm *et al*., 1993
Tamazeght Complex, Morocco	44 – 35 Ma	Marks *et al*., 2009
Illimaussaq, Greenland	1160 ± 2Ma	Waight *et al*., 2002

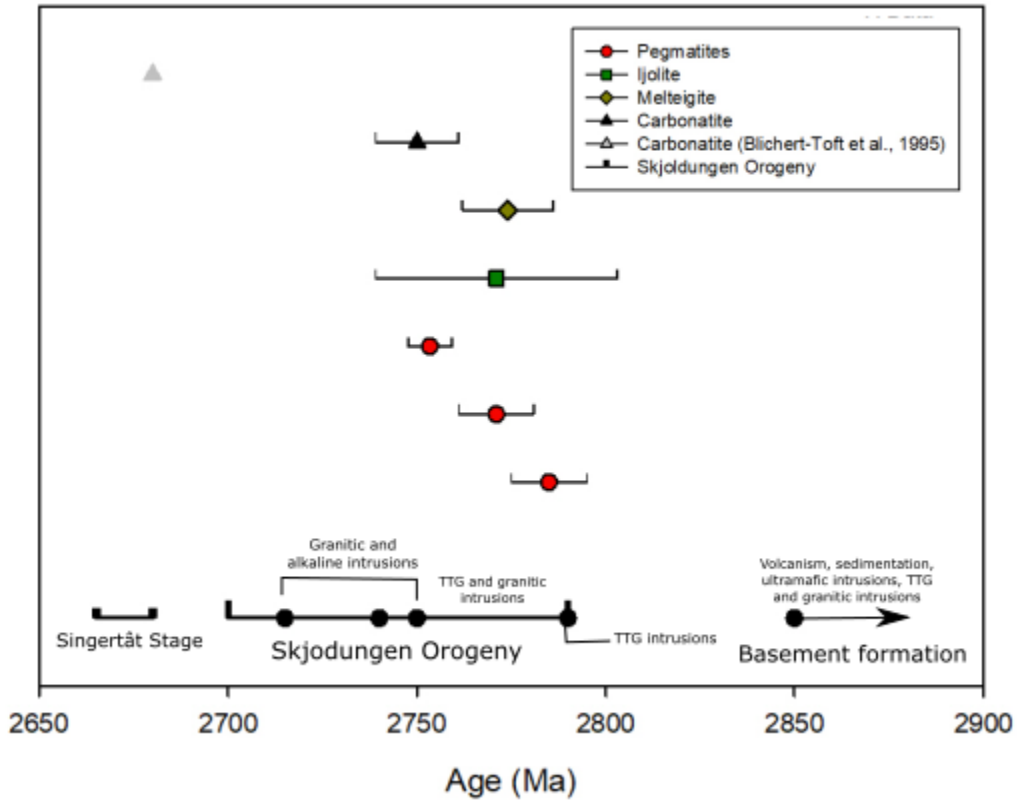
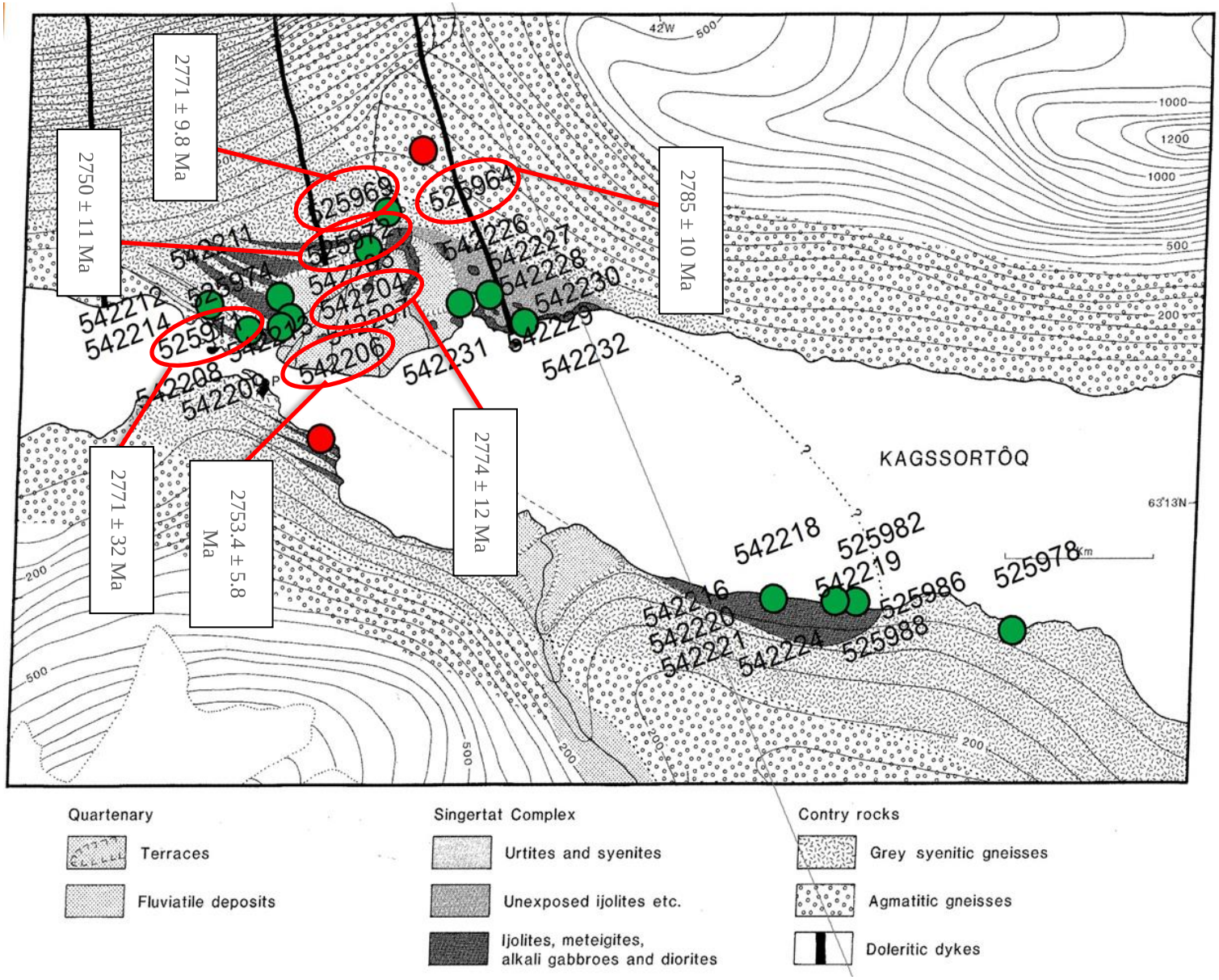


Figure 7.1: Geological timeline depicting the ages of the zircons analyzed in this study placing the timing of the Singertat Complex emplacement in the early stages of the Skjoldungen Orogen (Kolb et al., 2013). Note that no error bar was provided for the Blichert-Toft et al., 1995 age, seen as the gray triangle.



<u>Figure 7.2:</u> A geological map of the Singertât Complex of the SAIP by Nielson and Rosing, 1990. The map indicates sample localities for a selection of alkaline rocks (green dots) and the syenitic gneisses (red dots) that were sampled on the 2012 expedition as well as the ages determined for the sample indicated using red circles.

7.4.2 Comparing Singertât to other alkaline intrusives – a miaskitic to agpaitic transition?

Alkaline igneous rocks can be sub-divided into either peralkaline, metaluminous and peraluminous depending on the geochemistry, whereby peralkaline is a chemical term for rocks in which the molecular amounts of $Na_2O + K_2O > Al_2O$, metaluminous where $Na_2O + K_2O < Al_2O$ and peraluminous where the amount of alkalis equals the alumina. According Marks & Markl (2017), peralkaline and metaluminous rocks can also be further sub-divided into miaskitic and agpaitic rocks depending on which mineral assemblages HFSE's partition into. Literature states that a HFSE-rich mineral in miaskitic rocks is zircon and titanite, while in agpaitic rocks these HFSE mineral are most likely eudialyte, aenigmatite and astrophyllite. The syenitic gneisses, which appear to be agpaitic due to the lack of zircon or titanite in these samples, can further be sub-divided into Ca-depleted and high-Ca agpaites. This classification is based on whether the precursor melt has experienced a large amount of plagioclase fractionation (Marks *et al*., 2011). Depending on whether the agpaite is Ca-depleted or high-Ca, the parental melts would be nephelinitic or basaltic in composition respectively (Marks *et al*., 2009 and Frost & Frost, 2008). There is a chance that in alkaline complexes there can be a transition between miaskitic and agpaitic rock types i.e. both are present in the same alkaline complex. An indicator mineral for this change according to Marks et al. (2011) is sodalite in nepheline syenites, syenitic gneisses or nepheline-rich rocks. Geochemically the AI (alkalinity index) and ASI (aluminium saturation index) values would need to be calculated for each rock type and the plotted to determine the high fractionating mineral in the rock types.

The presence of sodalite (Chapter 6.2, Figure 6.23) in some of the samples may indicate a transition from miaskitic to agpaitic, however according to Edgar (1974), sodalite in itself is not an indication that a rock is agpaitic. Literature also states that zircon is a HFSE-rich mineral found in miaskitic rocks as discussed in Chapter 6.1 and observed in Chapter 6.4. While there is no zircon present in any of the syenitic gneisses and many of the ijolites and melteigites, which could be evidence the rocks are likely agpaitic. However, these rock samples plot predominantly as metaluminous and not peralkaline compositions in Figure 6.28 (Chapter 6.3) and Figure 7.3 below. Furthermore, other than the presence of sodalite in some of the samples there were no other diagnostic agpaitic minerals present in any of the samples. Figure 7.3 shows a trend between the nepheline-bearing alkaline rocks whereby the melteigites which have more aegerine-augite fractionation plot closer to the left of the graph. The urtite which has the least amount of aegerine-augite trend more towards the right and the ijolites plot in middle. Similarly, the ijolites and melteigites in Figure 7.3 plot both in the peralkaline and the metaluminous field, this also observed in Figure 6.27. The pegmatites plot in the peraluminous field and have experienced fractionation of plagioclase, this correlates with the trace element results (Chapter 6.24, Figure 6.28) as the pegmatites were the only rock types with positive Eu anomalies. Finally, the carbonatites all seem to plot within the aegerine-augite fractionation field, while one of the samples plot with the other rock types, this is most likely due to the garnet present in this sample. Therefore, looking at the results depicted in Figure 7.3 it appears that the rocks of the Singertât Complex are more metaluminous and barely peralkaline.

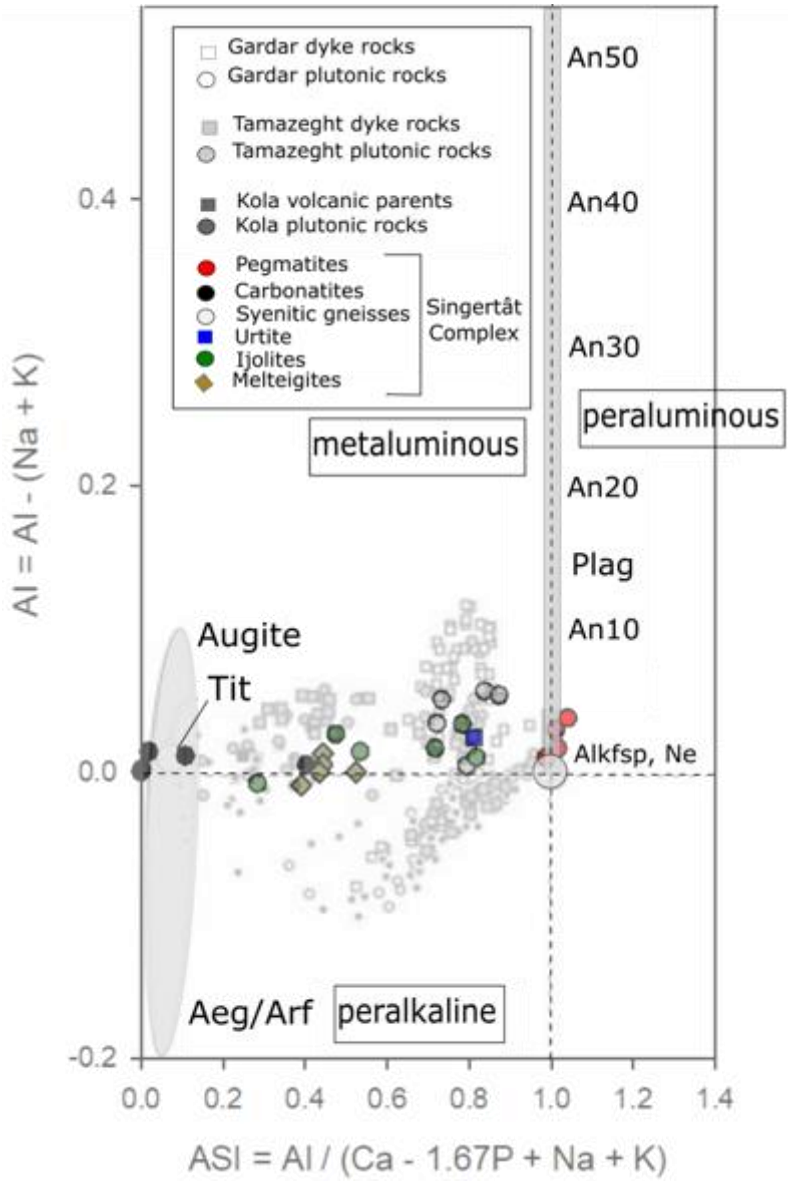


Figure 7.3: Whole-rock data in molecular proportions of the Singertât Complex in Comparison to the rocks from the Gardar Province, the Kola Peninsula and the Tamazeght complex plotted on an AI vs ASI diagram using the definitions by Frost & Frost (2008). They gray fields indicate the composition of important fractionating mineral phases (Marks et al., 2011).

However, transitions between miaskitic and agpaitic do occur and there are many examples of alkaline igneous complexes that have this occurrence. In the Pilanesberg, South Africa the transition may have occurred during the final alteration stages where minerals assemblages may be transformed into miaskitic assemblages and vice versa (Mitchell & Liferovich, 2006). In the Langesundfjord region, Norway and Gardiner Complex, East Greenland the agpaitic assmeblages are restricted to the pegmatites within the miaskitic rocks (Marks et al., 2009). In Tamazeght, Morocco the transition occurred locally during the late-magmatic or hydrothermal stage where miaskitic rocks were transformed to agpaitic (Salvi *et al*., 2000 and Marks & Markl, 2003). Referring to Figure

7.3 we observe that like the Singertât the Tamazeght plutonic rocks also plots as more metaluminous than peralkaline and there is a transition from miaskitic to agpaitic in this Complex. However, unlike the Tamazeght plutonic rocks, the Singertât Complex does not have any of the diagnostic mineralogy to be agpaitic other than the presence of sodalite, which may be late stage hydrothermal.

7.2 Evolution of the Singertât Complex

7.2.1 Assessing magmatic processes operating in the Singertât Complex

There are many processes that could result in the formation of layering in intrusive bodies. Many of these processes are said to occur at the cumulus stage through processes such as gravity settling, in-situ crystallization, gain or loss of volatiles, pressure changes, magma replenishments and assimilation (Irvine, 1987; Spandler *et al*.,2005; Mondal and Mathez, 2007). An open magma chamber may experience multiple injections of crystal-rich magma (entrained crystal cargos), which may result in the formation of primary igneous layering (Maier *et al*., 2013). The microphenocrysts entrained in these magmas are likely to have nucleated in a plumbing system below the main chamber (i.e. a lower magma chamber or staging magma chamber), where they were incorporated into the magma as suspended load and injected into the upper magma chamber (Eales, 2000). Development of stratiform layers on the magma chamber floor would form as a result of settling of these crystals from suspension or injection as crystal-rich slurries. Repeated replenishment events would result in cyclicity of the layering (Hunt, 2015; Mondal and Mathez, 2007). However, development of primary igneous layering may also occur due to convection currents and thermal gradients (Marsh, 2013). Thermal gradients present within a magma chamber allow for crystal nucleation at thermal boundaries. This nucleation is a result of the lowering of the liquidus temperature as a response to cooling at the thermal boundary. The crystals that nucleate at the thermal boundary may be transported away by convection currents and will either dissolve or continue to grow (which may result in the formation of a crystal mush) (Marsh, 2013; Hunt, 2015). While a closed magma chamber with no replenishment may most likely form layering due to fractional crystallization, these crystals may sink due to gravity settling (or float) and form layers within the closed chamber. However, in-situ crystallization occurring on the roof, floor or in melt suspension in the magma chamber is another important mechanism that may be responsible for layering development (Latypov et al., 2015)

Various textural and geochemical data from the Singertât Complex presented in this work provide evidence that the layering in this alkaline intrusion may have formed in an open magma system with replenishments of crystal rich slurries. Petrographic studies of the aegerine-augite show that many of the samples contained zoned aegerine-augite crystals, formed because the aegerine-augite may have formed at lower depths and were subsequently transported into the main magma chamber. These crystals would have continued to crystallize in a compositionally different melt. This compositional variation between core and rim can be seen in Figure 6.19 and

6.20, where a distinct chemical difference between the cores and rims of the nepheline-bearing rock types is observed. However, the zoning may have also formed due to crystals which were crystallizing as cumulates in a closed magma system, these crystals may have formed due to fractional crystallization, which may explain why the rims are more sodic than the cores of the clinopyroxene crystals. Therefore, the rims would have been crystallizing in an environment with less CaO as the residual magma would have been depleted in CaO as a result of the formation of the clinopyroxene cores. Referring to the petrographic evidence, the layered samples in the Singertât Complex contain both sharp and gradational contacts between different rock types (Figure 6.8). The sharp boundaries appear to have experienced chemical erosion (a hotter melt chemically eroding a cooler one) as we observe truncated boundaries (Figure 6.9 and Figure 7.4) at these contacts, providing further evidence that the complex formed in an open magma system due to multiple replenishments. Referring to the Figure 7.5 by Latypov *et al*., 2015, he refers to the in-situ crystallization vs. gravity settling in potholes, these potholes form as a result of thermal erosion in the Merensky Reef of the Bushveld Complex. These potholes are good indicators to depict whether in-situ crystallization or gravity settling is the method for crystal formation. While in Singertât this is seen in a smaller scale looking at Figure 7.4 we can see that the crystals forming close to the truncation have crystallized by trending with the shape of the thermally eroded boundary. Samples which depict a gradational transition between rock types such as ijolite and melteigite appear to have larger euhedral crystals concentrated in what could be considered the "lower" half of the sample while smaller crystals more subhedral to anhedral crystal are concentrated in the "upper" half of a sample. This layer formation may have been a result of gravity settling occurring in these pulses of magma.

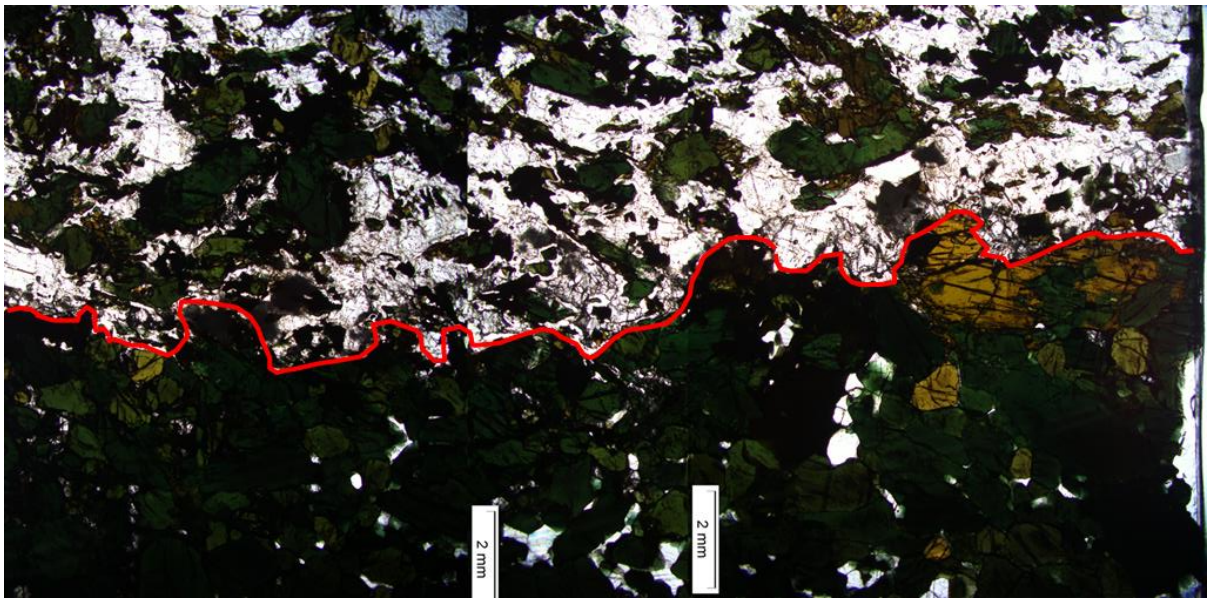


Figure 7.4: Photomicrograph showing a truncated boundary as a result of thermal erosion with in-situ crystallization of nepheline and anti-perthite along the boundary

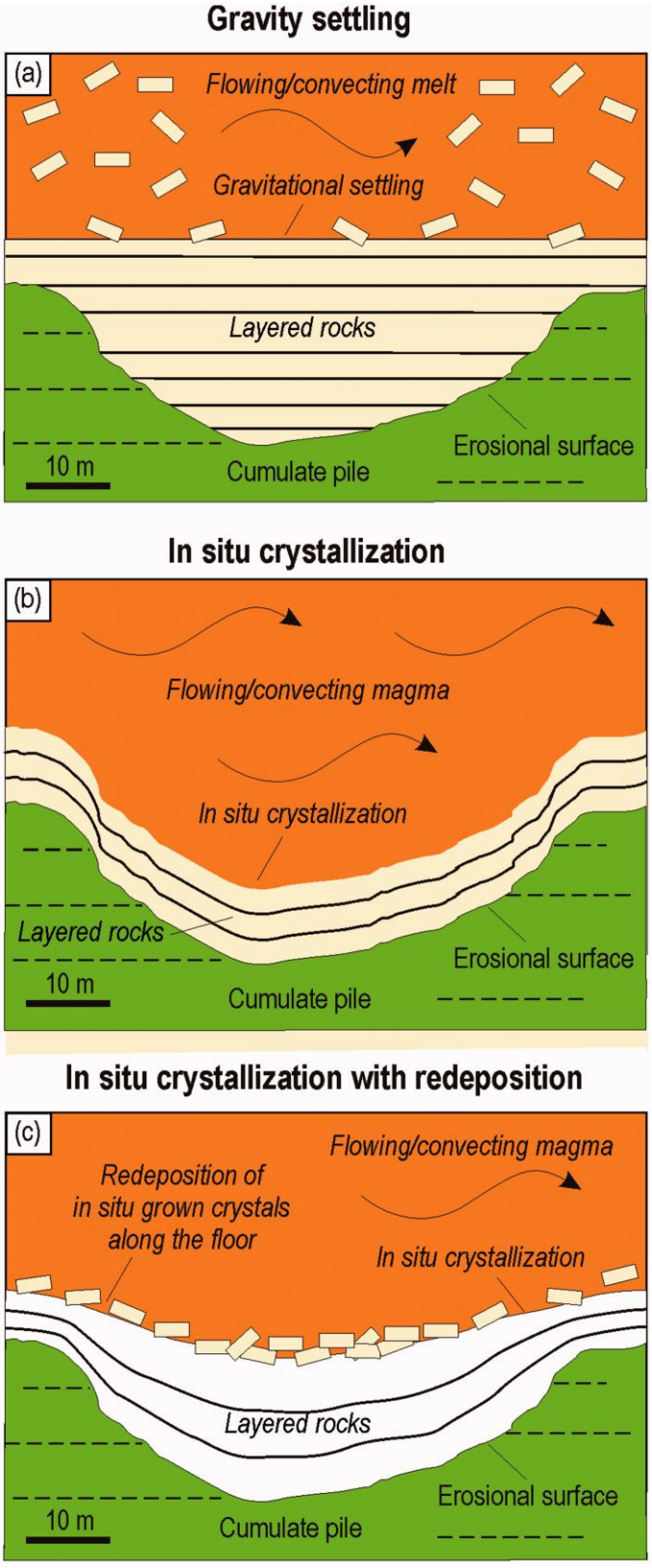


Figure 7.5: Predictions of the geometry of igneous layering within potholes owing to crystal settling (a) and in situ crystallization (b). Settling of crystals from flowing/convecting melt will form layered rocks that are discordant with respect to pothole margins. In contrast, in situ crystallization should result in layering that follows the outlines of pothole margins, (Latypov et al., 2015).

The geochemical evidence further supports that the Singertât was formed from multiple intrusions as we observe compositionally different populations across sharp boundaries as seen in Figure 6.17 and 6.18, where we observe differences in nepheline and aegerine-augite crystals across these sharp boundaries (Figure 7.6). While across the gradational boundaries the populations are chemically similar (Figure 6.37). This is similar to what is seen in the the Khibina & Lovozero Complexes where we observe different populations of the same mineral across sharp boundaries, which may have formed as a result of emplacement of cargoes of crystal-rich mush sourced from a lower magma chamber,(Féménias *et al*., 2005). The Singertât in this way is dissimilar to the Tamzeght Complex in Morocco, as the layering in this complex was formed due to fractional crystallization of a single batch of magma (Salvi et al., 2000).

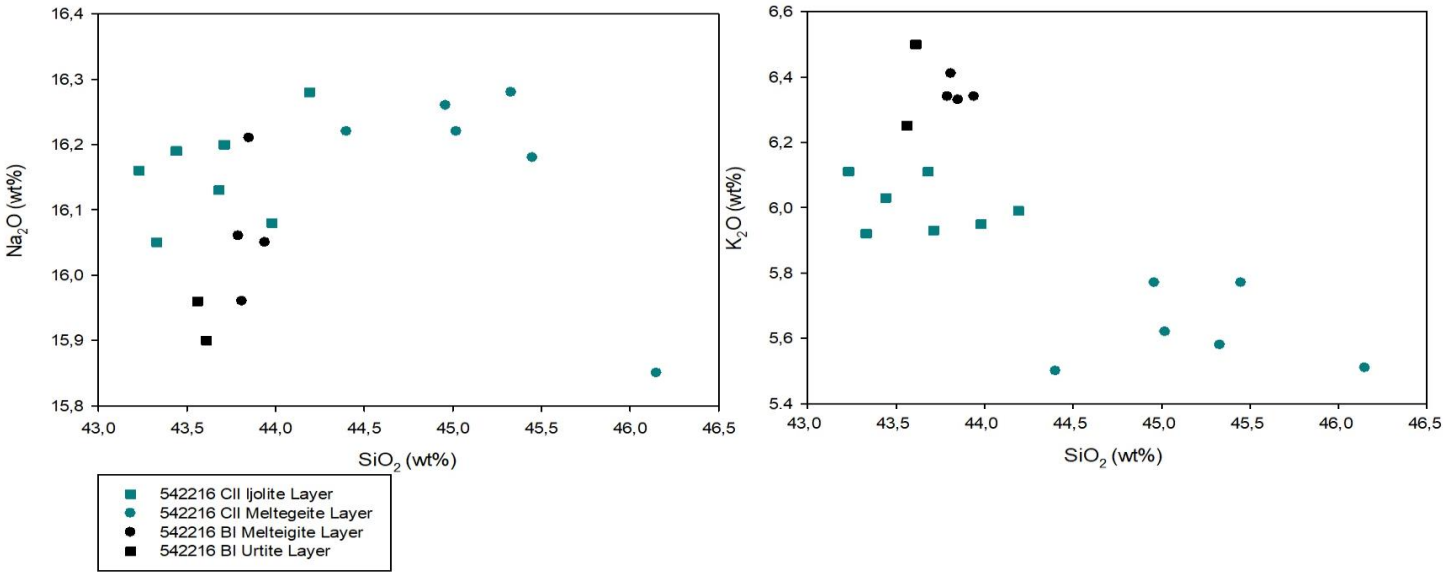


Figure 7.6: Depicting the compositionally different populations of nepheline across sharp boundaries in between and ijolite and a melteigite and a melteigite and urtite.

We also observe that some of the nepheline-bearing rocks have zoned aegerine-augite crystals as previously mentioned these zoned were analyzed using EMPA and it can be seen in Figure 7.7 that the cores and rims of these crystals are chemically different. This provides could be seen as evidence that the Singertât Complex was formed form multiple intrusion and that the magma replenishing the magma chamber was a crystal-rich magma or slurry. However as mentioned before, because the change in composition is a more gradational rather than abrupt step-like chnages it may also be evidence that the aegerine-augite crystals formed due to fractional crystallization.

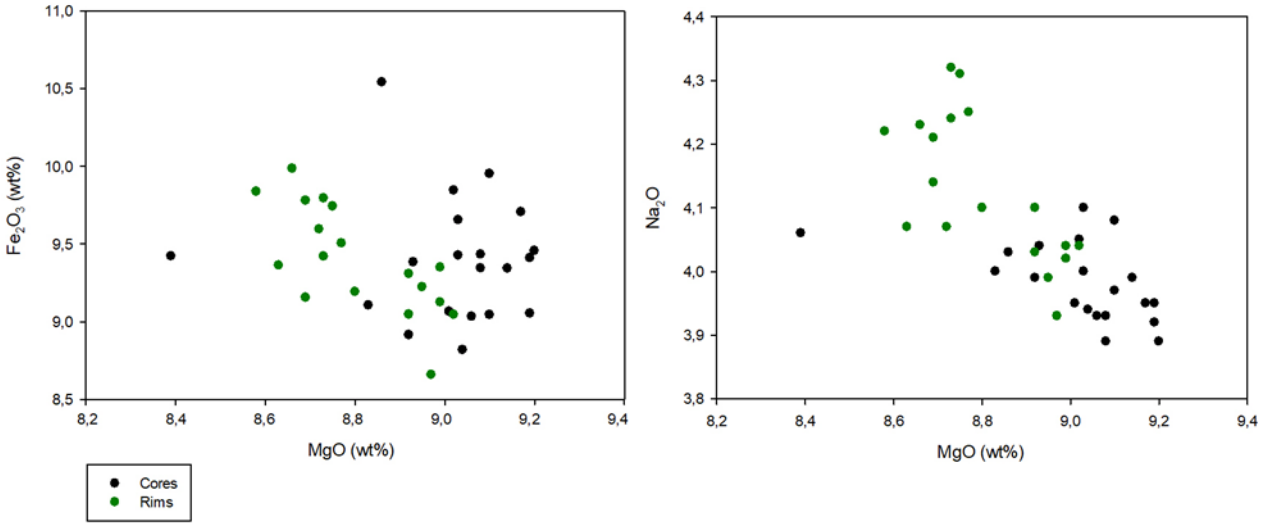


Figure 7.7: Variation diagrams for the layered sample 542205 which depicts variation form the core- rim data for aegerine-augite

The presence of flow textures in some of the samples (Figure 7.8) suggests that magma mixing occurred in the magma chamber, this provided further evidence that the Singertât Complex formed in an open magma system and according Marsh (2013) these thermal convection currents are likely to from when a crystal mush is replenishing a magma chamber. As we would have needed a hot magma to replenish the chamber as magma in the chamber was cooling, this would have resulted in the formation of convection currents which would result in the movement of crystals and therefore the formation of the flow textures observed. Therefore, the evidence suggests that the Singertât Complex formed as a result of multiple replenishments of crystal-rich magma.

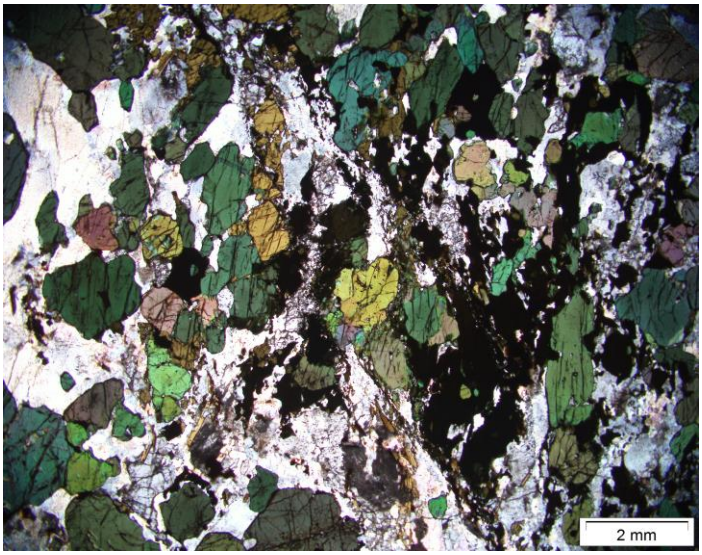


Figure 7.8: Sample 542219 depicting flow textures in a nepheline-bearing rock, which may have formed due to new magma being emplaced in a magma chamber resulting in convection currents which formed the flow textures.

Comparing the rocks of the Singertat complex to other alkaline igneous intrusions globally, we observe out of the 3 intrusions the Singertât Complex is similar to the Lovozero alkaline intrusion. The nepheline-bearing rocks plotted for the Lovozero generally cluster with the nepheline-bearing rocks in all of the plots seen in Figure 6.26. While the nepheline-bearing rocks plotted for La Madera and Loucna-Oberwiesenthal do not appear to cluster with Singertât nepheline-bearing rocks. However, La Madera and Loucna-Oberwiesenthal are similar to the Singertât rocks with respect to their CaO and Al_2O_3 compositions. Similarly, the trace elements plotted in Figure 6.29 show that the nephelinite rocks of Loucna-Oberwiesenthal do not plot with the Singertât Complex nepheline-bearing rocks, however the ijolite sample from Loucna-Oberwiesenthal is similar to the nepheline-bearing alkaline rocks of Singertât.

7.2.2 The Singertât Complex may have formed by accumulations of crystals (i.e. may be cumulus)

Nepheline bearing rocks appear to be orthocumulate in texture as many of the samples appear to have large crystals of either cumulus aegerine-augite and/or nepheline with intercumulus anti-perthite, biotite and in some sample calcite (Figure 7.9). This cumulus texture is also present in the rocks of Lovozero (Zartman and Kogarko, 2017). The trace element graphs also depict a strange bell/S-shaped REE patterns for the nepheline-bearing alkaline rocks. This does not reflect normal mantle-derived magma composition, but rather the cumulate nature of these rocks (Figure 7.10). This "S-shaped" curve is usually associated with cumulus aegerine-augite as the lightest REE's are incompatible in clinopyroxene (Philpotts & Ague, 2009), while the remainder of the REE's are partitioned into the aegerine-augite crystals. This is why the "S-shape" is more prominent when looking at the REE plot for the melteigite (more aegerine-augite) and less prominent for the urtite (less aegerine-augite) (Figure 7.10).

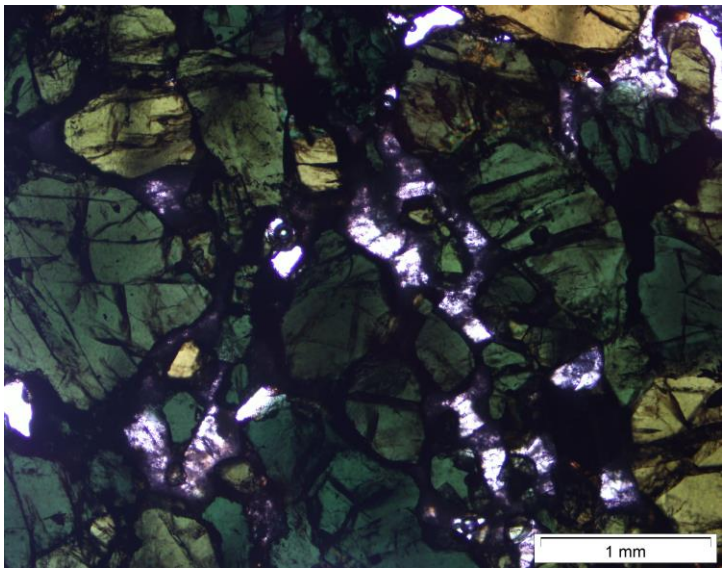
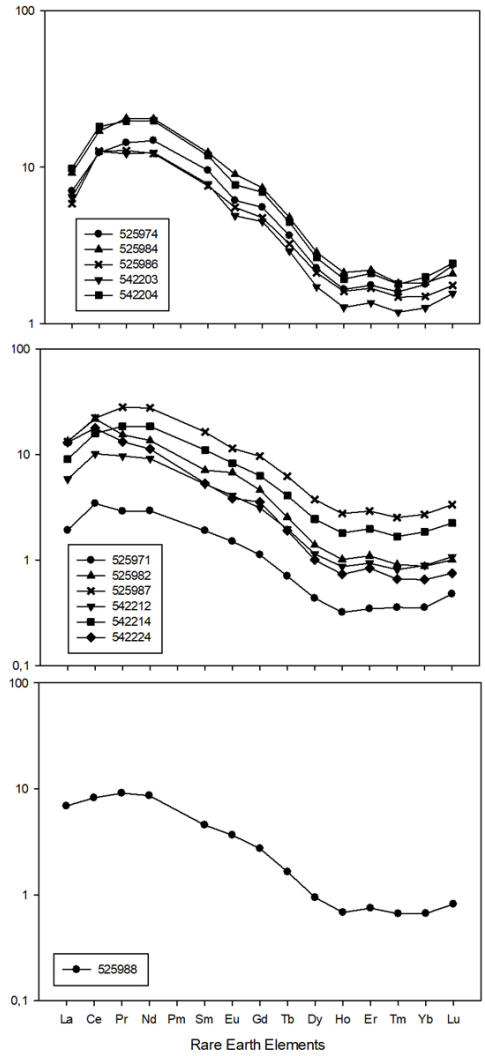


Figure 7.9: Melteigite depicting orthoculamte texture seen in the nepheline-bearing rocks of the Singertât Complex. We observe cumulate aegerine-augite with intercumulus nepheline.



<u>Figure 7.10</u>: REE plots for the nepheline-bearing alkaline rocks of the Singertât Complex. The samples were normalized to chondrite (Anderson and Grevasse, 1988)

8. Conclusion

We conclude that the Singertât Complex is an alkaline igneous complex with a stronger metaluminous signature than peralkaline signature. The rock types making up the Singertât Complex are nepheline-bearing alkaline igneous rocks (urtite, ijolite and melteigite), pegmatites, carbonatites and syenitic gneisses. These syenitic gneisses were found through petrographic and geochemical analyses to contain nepheline and should therefore be referred to as nepheline syenites. We further conclude that while there is evidence to support these nepheline syenites form part of the Singertât Complex and are not host rocks as previously stated, using the evidence from EPMA analyses we observed that the nepheline populations in the syenitic gneiss are compositionally similar to that of a melteigite it is in contact with. However, we acknowledge that the process of fenitization may have occurred and altered these rocks due to metasomatic process, thereby depleting the rocks in silica while enriching the rock with alkalis.

We also conclude that the alkaline rocks of the Singertât Complex are miaskitic, as we have the nepheline-bearing alkaline rocks, pegmatites and carbonatites rocks which contain abundant zircon as the HFSE mineral into which titanium can partition. However, the nepheline syenites contains no zircon, and the presence of sodalite in some of the sample may serve as evidence for a transition between miaskitic and agpaitic. Sodalite alone cannot be a diagnostic characteristic of an agpaitic rock. Furthermore, is would appear that the rocks of the Singertat Complex are actually more metaluminous and peraluminous, rather than peralkaline as previously thought.

We further conclude the Singertât Complex formed by multiple intrusions of crystal-rich magma, with evidence for this coming from thermal erosion observed at sharp boundaries between the nepheline-bearing alkaline rock types. We also observe that the populations of crystals are compositionally different across these sharp boundaries. Some of the samples even show evidence of flow textures which form as a result of flow and convection currents in a magma chamber. These currents in turn form as a result of magma mixing. The evidence that the magma replenishing the chamber is crystal-rich is that the aegerine-augite crystals in many of the sample have compositional zoning, meaning they would have started to crystallize in a deeper magma chamber and were emplaced in the new magma chamber and continued to crystallize with a different composition due to the surrounding melt. We believe that the method of crystallization that formed the Singertât Complex is in-situ crystallization, evidence observed at thermally eroded boundaries show crystals were crystallizing along the boundary as they retain the shape of these microscopic “potholes”, this would not be seen if the layering had formed due to gravity settling. We also think that the Singertât Complex may be made up of cumulates as we observe nepheline bearing rocks appear to be orthocumulate in texture as many of the samples appear to have large crystals of either cumulus, euhedral aegerine-augite and/or nepheline with intercumulus, anhedral to subhedral anti-perthite, biotite and in cerrtain samples we observe minor subhedral calcite. Further evidence that

the rocks may be cumulate is the unusual S-shaped REE pattern that were found using trace element analyses, which is usually associated with cumulus aegerine -augite.

Finally, we conclude that the Singertât Complex is older than stated by previous literature, which placed the complex after the Skjoldungen Orogeny at ~ 2.68 Ga in what is known as the Singertât Stage. However, the results obtained using U/Pb zircon geochronology in this study demonstrates that the Singertât Complex is older than previously stated. The nepheline-bearing pegmatite ages range from 2785 ± 10 Ma to 2753.4 ± 5.8 Ma, one dated carbonatite returns an age of 2750 ± 11 Ma, a representative ijolite sample is dated at 2771 ± 32 Ma and a representative melteigite sample produces an age of 2774 ± 12 Ma. These ages place the Singertât Complex in the early formation of the Skjoldungen Orogeny rather than being post-orogenic.

9. References

Anders, E. & Grevasse, N., 1988. Abundances of the elements: Meteoritic and solar. *Geochemica et Cosmochimca Acta, 53,* 197-214

Andersen, T., 1989, Carbonatite-related contact metasomatism in the Fen Complex, Norway: effects and petrogenetic implications: *Mineralogical Magazine*. 53, no. 4, p. 395-414.

Aubert, D. Stille, P. & Probst, A., 2001. REE fractionation during granite weathering and removal by waters and suspended loads: Sr and Nd isotopic evidence. *Geochimica et Cosmochimica Acta 65*, 387–406

Bacon, C.R., Newman, S., Stolper, E., 1992. Water, CO2, Cl, and F in melt inclusions in phenocrysts from three Holocene explosive eruptions, Crater lake, Oregon. *Am. Mineral. 77*, 1021‑1030.

Bagas, L., Naeraa, T., Kolb, J., Reno, B. L. & Fiorentini, M. L. 2013. Partial melting of the Archean Thrym Complex of southeastern Greenland. *Lithos,* 160-161, 164-182.

Berger, A., Kokfelt, T. F. & Kolb, J. 2014. Exhumation rates in the Archean from pressure-time paths: example from the Skjoldungen Orogen (SE Greenland). *Precambrian Research, 255,* 774-790.

Black, L. P., Kamo, S. L., Williams, I. S., Mundil, R., Davis, D. W., Korsch, R. J. & Foudoulis, C. (2003). The application of SHRIMP to Phanerozoic geochronology; a critical appraisal of four zircon standards. *Chemical Geology 200*, 171-188.

Blichert-Toft, J., Arndt, N. T., Ludden, J. N., 1996.Precambrian alkaline magmatism. *Lithos, 37*, 97-111.

Blichert-Toft, J., Rosing, M. T., Lescher, C. E., Chauvel, C., 1995. Geochemical constraints on the origin of the Late Archean Skjoldungen alkaline igneous Province, SE Greenland. *Journal of Petrology, 36*, 515-561.

BMR Journal of Australian Geology & Geophysics, 3, 1978, 227-232 227 The age of the Mud Tank Carbonatite, Strangways Range, Northern Territory L. P_ Black and B. L. Gulson

Brøgger, W. C. (1921) Die Eruptivgesteine des Kristianiagebietes, IV. Dos Fengebiet in Telemark, Norwegen. Vit. Selsk. Skr., I Mat. Nat. Klasse 1920, 1, Kristiania, 494 pp.

Cawthorn, R. (2015). The geometry and emplacement of the Pilanesberg Complex, South Africa. Geological Magazine. 152. 1-11.

Eales, H. V. (2000). Implications of the chromium budget of the Western Limb of the Bushveld Complex. *South African Journal of Geology, 103*, 141-150.

Earth Element Analysis of Geochemical Reference Materials NIST SRM 6 10, NIST SRM 6 12, NIST SRM 6 14, BHVO-2G, BHVO-2, BCR-2G, JB-2, WS-E, W-2, AGV-1 and AGV-2. *Geostandards and Geoanalytical Research, 28(3)*, 417-429.

Edgar, A. D. (1974). On the Use of the Term `Agpaitic'. *Mineralogical Magazine, vol. 39*, 729-73

Elburg, M. & Cawthorn, G., R. (2017). Source and evolution of the alkaline Pilanesberg Complex, South Africa. *Chemical Geology. 455*.

Féménias, O., Coussaert, N., Brassinnes, S. and Demaiffe, D. (2005). Emplacement processes and cooling history of layered cyclic unit II-7 from the Lovozero alkaline massif (Kola Peninsula, Russia). *Lithos. 83*. 371-393.

Frost, B. R. & Frost, C. D. (2008). A geochemical classification for feldspathic igneous rocks. *Journal of Petrology 49*, 1955-1969.

Gill, R. 2010. Igneous Rocks and Processes a practical guide. Wiley-Blackwell.

Huhma, H., Mänttäri, I., Peltonen, P., Kontinen, A., Halkoaho, T., Hanski, E., Hokkanen, T., Hölttä, P., Juopperi, H. & Konnunaho, J. (2012). The age of the Archaean greenstone belts in Finland. Geological Survey of Finland, *Special Paper 54*, 74-175.

Hunt, H. J. 2015. Magma Chamber Dynamics in the Peralkaline Magmas of the Kakortokite Series, South Greenland. Unpublished Thesis, U. of St. Andrews, Scotland.

Hupert, H. E., Sparks, R. S. J. 1984. Double-diffusive convection due to crystallization in magmas. *Annual Review of Earth and Planetary Sciences, 12*, 11-37.

Ila, P., & Frey, F. A. (2000). Trace element analysis of USGS standards AGV2, BCR2, BHVO2, DTS2 and GSP2 by INAA. *Journal of Radioanalytical and Nuclear Chemistry, 244(3)*, 599-602.

Irvine, T. N. (1987). Processes involved in the formation and development of layered igneous rocks. In: Parsons, I. (ed.) *Origins of Igneous Layering. Dordrecht: D. Reidel Publishing*, 649-656.

Jerram, D. A., Higgins, M. D. 2007. 3D Analysis of Rock Textures: Quantifying Igneous Microstructures. *Elements, 3*, 239-245.

Johannsen, A. 1938. A Descriptive Petrography of the Igneous Rocks. U. of Chicago Press, Chicago.

Kent, A. J., Jacobsen, B., Peate, D. W., Waight, T. E., & Baker, J. A. (2004). Isotope Dilution MC-ICP-MS Rare.

Kolb, J. 2010. Geology of the South-East Greenland Archean Craton. *Geological Survey of Denmark and Greenland*. Fact sheet No. 23.

Kolb, J., Kokfelt, T. F., Dziggel, A., 2012. Geodynamic setting and deformation history of an Archean terrane at mid-crustal level: the Tiasiusaruaq terrane of southern West Greenland. *Precambrian Res*. 212-213, 34-56.

Kolb, J., Bagas, L. & Fiorentini, M., L. 2015. Metallogeny of the North Atlantic Craton in Greenland. *Mineralogical Magazine, 79(4),* 815-855.

Kolb, J., Thrane, K. & Bagas, L. (2013b). Field relationships of high –grade Neo- to Mesoarchean rocks of South-East Greenland: Tectono-metamorphic and magmatic evolution. *Gondwana Research, 23,* 471-491.

Kramm, Ulrich & Kogarko, Lia & Kononova, V.A. & Vartiainen, H. (1993). The Kola Alkaline Province of the CIS and Finland: Precise Rb・Sr ages define 380–360 Ma age range for all magmatism. Lithos. 30. 33-44.

Krumrei, T.V., Pernicka, E., Kaliwoda, M., Markl, G., 2007. Volatiles in a peralkaline system: abiogenic hydrocarbons and F-Cl-Br systematics in the naujaite of the Ilímaussaq intrusion, South Greenland. *Lithos 95*, 298‑314.

Latypov, R. Morse, T., Robins, B., Wilson, R., Cawthorn, G., Tegner, C., Holness, M., Lesher, C., Barnes, S., O'Driscoll, B., Vekster, I., Higgins, M., Wilson, A., Namur, O., Chistyakova, S., Naslund, R., Thy, P. 2015. A fundamental dispute of "On some fundamentals of igneous petrology" by Bruce Marsh, *Contributions to Mineralogy and Petrology*, *166*, 665-690. *Springer, 169*, 20.

Latypov, R., Chistyakova, S., Page, A., Hornsey, R., 2015. Field Evidence for the In-Situ Crystallization of the Merensky Reef. *Journal of Petrology 56, 2341-2372*. https://doi.org/10.1093/petrology/egv023

Le Maitre, R. W., Bateman, P., Dudek, A., Keller, J., Lameyre, J., Le Bas, M. J., Sabine, P. A., Schmid., Sørensen, H., Streckeisen, A., Woolley, A. R., Zanettin, B. 1989. A Classification of Igneous Rocks and Glossary of Terms. *Blackwell Scientific Publications*.

Le Maitre, R. W., Streckeisen, A., Zanettin, Le Bas, M. J., Bonin, B., B., Bateman, P., Bellieni, G., Dudek, A., Efremova, S., Keller, J., Lameyre, J., Sabine, P. A., Schmid., Sørensen, H., Woolley, A. R. 2002. A Classification of Igneous Rocks and Glossary of Terms. 2nd Edition. *Cambridge University Press.*

Maier, W. D., Barnes, S. J. and Groves, D. I. (2013). The Bushveld Complex, South Africa: formation of platinum-palladium, chrome- and vanadium-rich layers via hydrodynamic sorting of a mobilized cumulate slurry in a large, relatively slowly cooling magma chamber. *Mineralium Deposita, 48,* 1-56.

Marks, M. A. W. & Markl, G. (2003). Ilimaussaq ‘‘en miniature’’: closed-system fractionation in an agpaitic dike rock from the Gardar Province, South Greenland. Mineralogical Magazine 67, 893^919

Marks, M. A. W., & Neukirchen, F., & Vennemann, T & Markl, G. (2009). Textural, chemical, and isotopic effects of late-magmatic carbonatitic fluids in the carbonatite–syenite Tamazeght complex, High Atlas Mountains, Morocco. Mineralogy and Petrology. 97. 23-42.

Marks, Michael & Hettmann, Kai & Schilling, Julian & Ronald Frost, B & Markl, Gregor. (2011). The Mineralogical Diversity of Alkaline Igneous Rocks: Critical Factors for the Transition from Miaskitic to Agpaitic Phase Assemblages. *Journal of Petrology*. *52*. 10.1093/petrology/egq086.

Marsh, B. D. 2013. On some fundamentals of igneous petrology. *Contributions to Mineralogy and Petrology, 166,* 665-690.

Mitchell, R. H. & Liferovich, R. P. (2006). Subsolidus deuteric/hydrothermal alteration of eudialyte in lujavrite from the Pilansberg alkaline complex, south Africa. Lithos *91*, 353-372

Mondal, S. K. and Mathez, E. A. (2007). Origin of the UG2 chromitite layer, Bushveld Complex. *Journal of Petrology, 48,* 495-510.

Naslund, H. R. and Mcbirney, A. R. (1996). Mechanisms of the Formation of Igneous Layering. In: Cawthorn, R. G. (ed.) Layered intrusions: Developments in Petrology. Amsterdam: Elsevier Science B. V.

Nielsen, T. F. D. & Rosing, M. T., 1990. The Archaean Skjoldungen alkaline province, South-East Greenland. *Geological Survey of Greenland Internal Report, 148,* 93-100.

O'Driscoll, B. Butcher, A. R. and Latypov, R. (2014). New insights into precious metal enrichment on the Isle of Rum, Scotland. *Geology Today, 30.*

Parat, F., Holtz, F., Streck, M.J., 2011. Sulfur-bearing magmatic accessory minerals. *Rev. Mineral. Geochem. 73,* 285‑314.

Phillpotts, A. R., & Ague, J. J. (2009). *Principles of Igneous and Metamorphic Petrology* (2nd ed.). Cambridge: Cambridge University Press, pp. 667.

Raczek, I., Stoll, B., Hofmann, A. W., & Jochum, K. P. (2001). High-Precision Trace Element Data for the USGS Reference Materials BCR-1, BCR-2, BHVO-1, BHVO-2, AGV-1, AGV-2, DTS-1, DTS-2, GSP-1 and GSP-2 by ID-TIMS and MIC-SSMS. *Geostandards Newsletter, 25,* 77-86.

Rollinson, H.R. (1993) Using Geochemical Data: Evolution, Presentation, Interpretation. Longman Scientific and Technical, England.

Rosing, M. T., Nielsen, T. F. D. & Vasudcv, V. N., 1988. An alkaline igneous province in the Skjoldungen area, South-East Greenland. *Geological Survey of Greenland Internal Report, 145,* 55—66.

SACS (SOUTH AFRICA COMMITTEE FOR STRATIGRAPHY) (1980) Stratigraphy of South Africa Handbook 9. Part 1: Lithostratigraphy of the Republic of South Africa, South West Africa/Namibia and the Republics of Bophuthatswana, Transkei and Venda. Geological Survey South Africa, Pretoria.

Salvi, S., Fontan, F. & Monchoux, P. (2000). Hydrothermal mobilization of high field strength elements in alkaline igneous systems: Evidence from the Tamazeght Complex, (Morocco). *Economic Geology 95,* 559-576.

Shand, S.J., 1943. The eruptive rocks: 2nd edition, John Wiley, New York, 444 p.

Sheard, E. R., & Williams-Jones, A. E., Heiligmann, M., Pederson, C & Trueman, D. L. (2012). Controls on the Concentration of Zirconium, Niobium, and the Rare Earth Elements in the Thor Lake Rare Metal Deposit, Northwest Territories, Canada. Economic Geology. 107. 81-104.

Spandler, C. Mavrgenes, J. & Arculus, R. (2005). Origin of chromitites in layered intrusions: Evidence from chromitite-hosted melt inclusions form the Stillwater Complex. *Geology, 33,* 893-896.

Tappe, S., Smart, K. A., Pearson, D. G., Steenfelt, A. & Simoetti, A. 2011. Craton formation of the Late Archean subduction zones revealed by Greenland eclogites. *Geology, 39,* 1103-1106.

Thrane, K., Kolb, J., Stensgaard, B. M., 2011. Geology of the Archean and Paleoproterozoic parts of unexplored South-East Greenland. *Geological Survey of Denmark and Greenland*, www.geus.dk.

Yusoff, Z.M., Ngwenya, B.T. & Parsons, I., 2013. Mobility and fractionation or REE during deep weathering of geochemically contrasting granites in a tropical setting, Malaysia. *Chemical Geology* 349–350, 71–86.

Waight, T., Baker, J., & Willigers, B. (2002). Rb isotope dilution analyses by MC-ICPMS using Zr to correct for mass fractionation: Towards improved Rb-Sr geochronology? Chemical Geology. 186. 99-116.

Wiedenbeck, M., Alle, P., Corfu, F., Griffin, W., Meier, M., Oberli, F. v., Quadt, A.v., Roddick, J. & Spiegel, W. (1995). Three natural zircon standards for U-Th-Pb, Lu- Hf, trace element and REE analyses. *Geostandards and Geoanalytical Research 19,* 1-23.

Wilson, S. A. (1997). *Data compilation for USGS reference material BHVO-2, Hawaiian Basalt.* U.S. Geological Survey Open-File Report.

Windley, B. F. & Garde, A. A. 2009. Arc-generated blocks with crustal sections in the North Atlantic craton of West Greenland: Crustal growth in the Archean with modern analogues. *Earth-Science Reviews, 93,* 1-30.

Zartman, R.E. & Kogarko, L.N. 2017. Lead isotopic evidence for interaction between plume and lower crust during emplacement of peralkaline Lovozero rocks and related rare-metal deposits, East Fennoscandia, Kola Peninsula, Russia. *Contributions to Mineralogy and Petrology*, *172*, Issue 5, article id.32, 14 pp

10. Appendices

Appendix I: Nepheline EMPA data for sample 542205

542205C																	
DataSet	89 / 1 .	90 / 1 .	91 / 1 .	92 / 1 .	106 / 1 .	107 / 1 .	108 / 1 .	109 / 1 .	141 / 1 .	142 / 1 .	156 / 1 .	157 / 1 .	158 / 1 .	167 / 1 .	168 / 1 .	169 / 1 .	170 / 1 .
Name	1	2	3	4	5	6	7	8	9	10	1	2	3	4	5	6	7
SiO_2	44.94	44.42	45.14	44.68	44.44	45.26	45.68	45.01	43.91	44.56	44.41	45.11	45.89	43.37	43.76	43.34	43.46
TiO_2	0	0	0	0.01	0	0	0.01	0	0	0.02	0	0	0	0	0	0.01	0
Al_2O_3	32.85	32.88	33.34	33.06	32.74	32.83	32.89	32.99	33	33.16	33.04	33.55	32.74	33.53	33.16	33.29	33.37
Fe_2O_3	0.033339	0.033339	0.044452	0.033339	0.033339	0.033339	0.211147	0.055565	0.055565	0.066678	0.055565	0.088904	0.022226	0.044452	0.033339	0.033339	0.022226
FeO	0	0	0	0	0	0	0	0	0	0	0	0	0	0	0	0	0
FeO_T	0.03	0.03	0.04	0.03	0.03	0.03	0.19	0.05	0.05	0.06	0.05	0.08	0.02	0.04	0.03	0.03	0.02
MnO	0	0.01	0.02	0	0.01	0	0	0.01	0.01	0	0	0	0	0	0	0	0
MgO	0.01	0.01	0	0.01	0.01	0.01	0	0	0	0	0	0	0	0	0.01	0.01	0
CaO	0.41	0.3	0.32	0.31	0.38	0.35	0.36	0.35	0.32	0.32	0.3	0.28	0.28	0.35	0.33	0.33	0.33
Na_2O	16.47	16.59	16.73	16.69	16.81	16.82	16.61	16.74	16.54	16.43	16.52	16.67	16.46	16.56	16.33	16.49	16.47
K_2O	5.95	5.9	5.82	5.87	5.57	5.49	5.71	5.78	6.14	6.14	6.15	6.2	5.66	6.49	6.29	6.44	6.42
P_2O_5																	
Cr_2O_3	0	0	0	0.01	0.01	0	0	0	0	0	0	0	0	0	0	0	0
NiO	0	0	0	0	0	0	0.01	0.02	0	0	0	0	0.01	0	0	0	0.01
ZnO																	
BaO																	
Total	100.66	100.14	101.41	100.67	100	100.79	101.46	100.95	99.97	100.69	100.47	101.89	101.06	100.34	99.91	99.94	100.08
Sample 542205A																	
Point	13/1	14/1	15/1	16/1	17/1	18/1	19/1	20/1	21/1	41/1	42/1	43/1	44/1	45/1	72/1	73/1	77/1
SiO_2	44.75	44.56	43.60	46.78	44.51	45.22	44.32	44.71	44.32	43.83	43.82	43.57	44.65	44.77	44.30	44.05	44.31
TiO_2	0.00	0.00	0.01	0.00	0.00	0.00	0.00	0.00	0.00	0.00	0.00	0.00	0.01	0.00	0.01	0.00	0.00
Al_2O_3	33.09	32.72	32.76	34.40	33.58	33.22	33.06	33.06	32.80	33.11	33.05	33.33	32.83	32.55	33.23	33.72	33.59
Fe_2O_3	0.09	0.02	0.04	0.02	0.04	0.12	0.07	0.03	0.04	0.03	0.01	0.02	0.06	0.03	0.02	0.01	0.09
FeO	0.00	0.00	0.00	0.00	0.00	0.00	0.00	0.00	0.00	0.00	0.00	0.00	0.00	0.00	0.00	0.00	0.00
FeO_T	0.08	0.02	0.04	0.02	0.04	0.11	0.06	0.03	0.04	0.03	0.01	0.02	0.05	0.03	0.02	0.01	0.08
MnO	0.00	0.00	0.01	0.00	0.00	0.01	0.00	0.00	0.00	0.00	0.00	0.02	0.01	0.00	0.00	0.00	0.00
MgO	0.01	0.01	0.01	0.00	0.00	0.01	0.00	0.02	0.01	0.00	0.01	0.00	0.01	0.01	0.00	0.00	0.00
CaO	0.39	0.39	0.37	0.73	0.32	1.10	0.33	0.35	0.33	0.33	0.33	0.30	0.33	0.33	0.28	0.29	0.20
Na_2O	16.33	16.48	16.24	15.99	16.50	15.38	16.30	16.55	16.51	16.43	16.55	16.36	16.77	16.49	16.51	16.42	16.32
K_2O	5.93	5.69	6.22	6.16	6.13	6.01	6.41	5.86	5.99	6.33	6.10	6.52	6.18	5.90	6.32	6.54	6.51
P_2O_5																	
Cr_2O_3	0.00	0.00	0.01	0.00	0.00	0.01	0.00	0.01	0.00	0.00	0.00	0.02	0.00	0.00	0.00	0.01	0.00
NiO	0.00	0.01	0.01	0.00	0.00	0.00	0.00	0.01	0.00	0.00	0.00	0.00	0.02	0.00	0.01	0.00	0.00
ZnO																	
BaO																	
Total	100.58	99.88	99.28	104.08	101.08	101.07	100.48	100.6	100	100.06	99.87	100.14	100.86	100.08	100.68	101.04	101.01

Appendix II: Anti-perthite EMPA data for sample 542205

542205C										
Point	93/1	94/1	104/1	105/1	138/1	139/1	154/1	155/1	165/1	166/1
SiO2	68.42	66.57	66.97	67.75	67.2	66.78	66.97	66.61	67.88	66.26
TiO2	0.01	0	0.02	0	0	0.01	0	0	0.01	0
Al2O3	21.08	20.76	20.71	20.91	21.1	20.72	21.15	20.97	21.07	20.8
Fe2O3	0	0.033339	0.066678	0.088904	0.088904	0.055565	0	0.11113	0.122243	0.188921
FeO	0.05	0	0	0	0	0	0.06	0	0	0
FeOT	0.05	0.03	0.06	0.08	0.08	0.05	0.06	0.1	0.11	0.17
MnO	0.01	0	0	0	0	0.01	0	0	0	0.01
MgO	0	0.01	0	0	0	0	0	0	0.01	0.01
CaO	1.8	1.97	1.85	1.79	1.88	1.8	1.84	1.91	1.81	2.02
Na2O	10.95	10.84	10.96	11.04	10.91	10.96	10.44	10.98	11.1	10.84
K2O	0.05	0.04	0.05	0.07	0.05	0.09	0.08	0.08	0.07	0.08
P2O5										
Cr2O3	0.01	0	0.02	0	0	0.01	0	0	0	0.01
NiO	0	0	0	0	0	0	0	0	0	0.01
ZnO										
BaO										
Total	102.38	100.22	100.64	101.64	101.22	100.43	100.54	100.65	102.06	100.21
Structural formula per 8 O										
Si	2.930824	2.917722	2.922928	2.926594	2.915532	2.921284	2.91929	2.910039	2.921522	2.909311
Al	1.064234	1.072389	1.065314	1.064552	1.078923	1.068259	1.086593	1.079736	1.068788	1.07637
Ti	0.000322	0	0.000656	0	0	0.000329	0	0	0.000324	0
Fe2+T	0.001791	0.0011	0.00219	0.00289	0.002903	0.001829	0.002187	0.003654	0.003959	0.006242
Mn	0.000363	0	0	0	0	0.000371	0	0	0	0.000372
Mg	0	0.000653	0	0	0	0	0	0	0.000642	0.000654
Ca	0.082611	0.092511	0.086511	0.082845	0.087391	0.084365	0.085936	0.089403	0.083466	0.095028
Na	0.909433	0.92118	0.927467	0.924639	0.917748	0.929582	0.882363	0.930062	0.926276	0.922822
K	0.002732	0.002236	0.002784	0.003857	0.002767	0.005022	0.004449	0.004458	0.003843	0.004481
P	0	0	0	0	0	0	0	0	0	0
Cr	0.000339	0	0.00069	0	0	0.000346	0	0	0	0.000347
Ni	0	0	0	0	0	0	0	0	0	0.000353
Zn	0	0	0	0	0	0	0	0	0	0
Ba	0	0	0	0	0	0	0	0	0	0
Total	4.99265	5.007792	5.008539	5.005378	5.005264	5.011387	4.980819	5.017353	5.00882	5.015982
An	8.304524	9.10605	8.508474	8.191616	8.670568	8.27942	8.834371	8.731453	8.234688	9.295223
Ab	91.42083	90.67381	91.21774	91.42698	91.05488	91.22771	90.70831	90.83313	91.38614	90.26648
Or	0.27465	0.220136	0.273789	0.381401	0.274553	0.492875	0.457314	0.435422	0.379169	0.438294
	100	100	100	100	100	100	100	100	100	100
An content	8.327395	9.12614	8.531833	8.222978	8.694439	8.320429	8.874957	8.769637	8.26603	9.336143

542205A								
Point	47/1	48/1	57/1	58/1	59/1	70/1	71/1	79/1
SiO2	67.43	67.96	68.13	67.81	68.16	69.82	68.09	68.68
TiO2	0	0	0	0.02	0	0	0	0
Al2O3	20.92	21.26	21.15	21.08	21.59	21.34	21.5	21.45
Fe2O3	0.077791	0	0	0	0	0	0	0
FeO	0	0.15	0.11	0.11	0.16	0.04	0.1	0.04
FeOT	0.07	0.15	0.11	0.11	0.16	0.04	0.1	0.04
MnO	0	0.01	0	0	0	0.01	0	0.01
MgO	0	0	0	0.02	0	0	0	0
CaO	1.95	2	2	2	1.96	1.86	1.46	1.89
Na2O	10.98	10.49	10.8	10.84	10.92	11.12	10.7	10.62
K2O	0.08	0.08	0.07	0.05	0.05	0.04	0.36	0.05
P2O5								
Cr2O3	0	0	0	0	0	0.02	0	0
NiO	0	0.01	0.01	0	0.02	0.01	0.03	0
ZnO								
BaO								
Total	101.43	101.96	102.27	101.93	102.86	104.26	102.24	102.74
Structural formula per 8 O								
Si	2.920831	2.92285	2.923909	2.920924	2.910389	2.936102	2.921316	2.927613
Al	1.068008	1.077646	1.069783	1.07018	1.08651	1.057658	1.08716	1.077632
Ti	0	0	0	0.000648	0	0	0	0
Fe2+T	0.002536	0.005395	0.003948	0.003963	0.005713	0.001407	0.003588	0.001426
Mn	0	0.000364	0	0	0	0.000356	0	0.000361
Mg	0	0	0	0.001284	0	0	0	0
Ca	0.0905	0.09216	0.091964	0.092303	0.089668	0.083804	0.067113	0.086319
Na	0.922159	0.87474	0.898668	0.905328	0.904054	0.906664	0.89008	0.877724
K	0.00442	0.004389	0.003832	0.002747	0.002723	0.002146	0.019703	0.002719
P	0	0	0	0	0	0	0	0
Cr	0	0	0	0	0	0.000665	0	0
Ni	0	0.000346	0.000345	0	0.000687	0.000338	0.001035	0
Zn	0	0	0	0	0	0	0	0
Ba	0	0	0	0	0	0	0	0
Total	5.008454	4.977891	4.992449	4.997376	4.999745	4.989141	4.989995	4.973793
An	8.898039	9.488466	9.247571	9.226848	8.998816	8.442778	6.870067	8.928674
Ab	90.66733	90.05965	90.36707	90.49851	90.72787	91.34105	91.11307	90.7901
Or	0.434627	0.45188	0.385356	0.274638	0.273317	0.216172	2.016868	0.28123
	100	100	100	100	100	100	100	100
An content	8.936882	9.531537	9.283345	9.252258	9.023478	8.461068	7.011479	8.953855

Appendix III: Clinopyroxene EMPA data for sample 542205

542205A CPX																				
Point	1/1	2/1	3/1	4/1	5/1	6/1	7/1	8/1	22/1	23/1	24/1	25/1	26/1	27/1	28/1	29/1	30/1	31/1	33/1	34/1
Mineral	cpx	cpx	cpx	cpx	cpx	cpx	cpx	cpx	cpx	cpx	cpx	cpx	cpx	cpx	cpx	cpx	cpx	cpx	cpx	cpx
SiO2	51.63	51.78	51.64	51.68	51.44	51.55	51.41	51.27	50.63	51.7	51.44	51.86	51.26	51.39	51.69	51.71	51.16	51.03	51.58	51.44
TiO2	0.72	0.64	0.71	0.72	0.58	0.62	0.51	0.55	0.65	0.71	0.64	0.57	0.6	0.69	0.76	0.67	0.59	0.55	0.71	0.69
Al2O3	3.6	3.69	3.58	3.52	4.34	4.1	4.21	4.41	4.58	3.53	3.58	4.47	4.15	3.74	3.52	3.63	3.81	3.93	3.64	3.62
Cr2O3	0	0	0	0	0	0	0	0	0.01	0	0.01	0	0	0	0.01	0	0.01	0	0.01	0
FeO	12.83	12.66	12.77	12.8	12.48	12.78	12.62	12.73	12.84	12.66	12.66	12.71	12.41	12.5	12.69	12.71	12.72	12.55	12.63	12.57
MnO	0.18	0.21	0.2	0.19	0.19	0.2	0.21	0.19	0.2	0.2	0.22	0.2	0.18	0.2	0.2	0.2	0.18	0.19	0.19	0.2
NiO	0.04	0.01	0	0	0	0.01	0.1	0	0	0.02	0.01	0	0	0	0	0	0	0	0	0.01
MgO	8.93	9.03	9.03	8.86	8.73	8.8	8.69	8.58	8.39	9.14	9.08	8.75	8.69	8.97	9.04	9.19	8.63	8.72	8.92	9.1
CaO	18.05	18.1	18.15	19.09	17.6	17.78	17.79	17.85	17.78	18.1	18.14	17.77	17.79	17.91	18.07	18.18	17.93	17.92	18.04	18.08
Na2O	4.04	4.1	4	4.03	4.32	4.1	4.21	4.22	4.06	3.99	3.93	4.31	4.14	3.93	3.94	3.95	4.07	4.07	3.99	4.08
K2O	0	0	0	0	0.01	0	0	0	0	0	0.01	0.01	0	0	0	0	0	0.01	0	0
BaO																				
SrO																				
Total reported	100.02	100.22	100.08	100.89	99.69	99.94	99.75	99.8	99.14	100.05	99.72	100.65	99.22	99.33	99.92	100.24	99.1	98.97	99.71	99.79
Result: cations per formula unit																				
Si	1.9155	1.9144	1.9143	1.9015	1.9078	1.9122	1.9086	1.9026	1.8952	1.9162	1.9134	1.9065	1.9131	1.9189	1.9202	1.9129	1.9150	1.9106	1.9193	1.9094
Ti	0.0201	0.0178	0.0198	0.0199	0.0162	0.0173	0.0142	0.0154	0.0183	0.0198	0.0179	0.0158	0.0168	0.0194	0.0212	0.0186	0.0166	0.0155	0.0199	0.0193
Al	0.1574	0.1608	0.1564	0.1526	0.1897	0.1792	0.1842	0.1929	0.2020	0.1542	0.1569	0.1937	0.1825	0.1646	0.1541	0.1583	0.1681	0.1734	0.1596	0.1584
Cr	0.0000	0.0000	0.0000	0.0000	0.0000	0.0000	0.0000	0.0000	0.0003	0.0000	0.0003	0.0000	0.0000	0.0000	0.0003	0.0000	0.0003	0.0000	0.0003	0.0000
Fe	0.3981	0.3914	0.3959	0.3939	0.3871	0.3965	0.3918	0.3951	0.4019	0.3924	0.3938	0.3908	0.3873	0.3903	0.3942	0.3932	0.3982	0.3930	0.3930	0.3902
Mn	0.0057	0.0066	0.0063	0.0059	0.0060	0.0063	0.0066	0.0060	0.0063	0.0063	0.0069	0.0062	0.0057	0.0063	0.0063	0.0063	0.0057	0.0060	0.0060	0.0063
Ni	0.0012	0.0003	0.0000	0.0000	0.0000	0.0003	0.0030	0.0000	0.0000	0.0006	0.0003	0.0000	0.0000	0.0000	0.0000	0.0000	0.0000	0.0000	0.0000	0.0003
Mg	0.4939	0.4977	0.4990	0.4860	0.4827	0.4866	0.4809	0.4747	0.4682	0.5050	0.5035	0.4795	0.4835	0.4993	0.5006	0.5068	0.4816	0.4867	0.4948	0.5035
Ca	0.7175	0.7170	0.7209	0.7526	0.6994	0.7067	0.7076	0.7098	0.7131	0.7188	0.7230	0.6999	0.7114	0.7166	0.7192	0.7206	0.7191	0.7189	0.7192	0.7191
Na	0.2906	0.2939	0.2875	0.2875	0.3106	0.2949	0.3030	0.3036	0.2947	0.2867	0.2834	0.3072	0.2996	0.2845	0.2838	0.2833	0.2954	0.2954	0.2879	0.2936
K	0.0000	0.0000	0.0000	0.0000	0.0005	0.0000	0.0000	0.0000	0.0000	0.0000	0.0005	0.0005	0.0000	0.0000	0.0000	0.0000	0.0000	0.0005	0.0000	0.0000
Sum of Cations	4.0000	4.0000	4.0000	4.0000	4.0000	4.0000	4.0000	4.0000	4.0000	4.0000	4.0000	4.0000	4.0000	4.0000	4.0000	4.0000	4.0000	4.0000	4.0000	4.0000
Total Charge balance	11.7380	11.7314	11.7370	11.7081	11.7266	11.7434	11.7268	11.7252	11.7346	11.7394	11.7360	11.7304	11.7429	11.7567	11.7535	11.7380	11.7363	11.7297	11.7504	11.7220
free	0.2620	0.2686	0.2630	0.2919	0.2734	0.2566	0.2732	0.2748	0.2654	0.2606	0.2640	0.2696	0.2571	0.2433	0.2465	0.2620	0.2637	0.2703	0.2496	0.2780
Fe3	0.2620	0.2686	0.2630	0.2919	0.2734	0.2566	0.2732	0.2748	0.2654	0.2606	0.2640	0.2696	0.2571	0.2433	0.2465	0.2620	0.2637	0.2703	0.2496	0.2780
Fe2	0.1361	0.1228	0.1329	0.1020	0.1137	0.1399	0.1186	0.1203	0.1365	0.1318	0.1298	0.1212	0.1302	0.1470	0.1477	0.1313	0.1345	0.1226	0.1434	0.1122
Mg-#T	55.3717	55.9757	55.7624	55.2350	55.4954	55.1056	55.1061	54.5757	53.8062	56.2738	56.1117	55.1006	55.5209	56.1248	55.9446	56.3111	54.7392	55.3289	55.7320	56.3414
Result: components																				
En	0.2470	0.2489	0.2495	0.2430	0.2413	0.2433	0.2405	0.2373	0.2341	0.2525	0.2518	0.2398	0.2417	0.2497	0.2503	0.2534	0.2408	0.2434	0.2474	0.2518
Fs	0.0681	0.0614	0.0664	0.0510	0.0569	0.0699	0.0593	0.0602	0.0683	0.0659	0.0649	0.0606	0.0651	0.0735	0.0739	0.0656	0.0672	0.0613	0.0717	0.0561
Wo	0.3266	0.3246	0.3275	0.3370	0.3117	0.3181	0.3152	0.3139	0.3133	0.3274	0.3271	0.3111	0.3207	0.3274	0.3303	0.3261	0.3254	0.3225	0.3292	0.3238
Tschermak	0.0443	0.0500	0.0462	0.0586	0.0598	0.0532	0.0630	0.0666	0.0679	0.0442	0.0505	0.0620	0.0532	0.0423	0.0370	0.0498	0.0515	0.0584	0.0407	0.0521
Mn-Px	0.0028	0.0033	0.0031	0.0030	0.0030	0.0031	0.0033	0.0030	0.0032	0.0031	0.0035	0.0031	0.0028	0.0032	0.0031	0.0031	0.0029	0.0030	0.0030	0.0031
Ni-Px	0.0006	0.0001	0.0000	0.0000	0.0000	0.0001	0.0015	0.0000	0.0000	0.0003	0.0001	0.0000	0.0000	0.0000	0.0000	0.0000	0.0000	0.0000	0.0000	0.0001
Cr-Ts	0.0000	0.0000	0.0000	0.0000	0.0000	0.0000	0.0000	0.0000	0.0003	0.0000	0.0003	0.0000	0.0000	0.0000	0.0003	0.0000	0.0003	0.0000	0.0003	0.0000
CaTiTs	0.0201	0.0178	0.0198	0.0199	0.0162	0.0173	0.0142	0.0154	0.0183	0.0198	0.0179	0.0158	0.0168	0.0194	0.0212	0.0186	0.0166	0.0155	0.0199	0.0193
Jadeite	0.0286	0.0253	0.0245	0.0000	0.0373	0.0383	0.0298	0.0289	0.0293	0.0262	0.0194	0.0376	0.0424	0.0412	0.0372	0.0214	0.0317	0.0251	0.0382	0.0156
Acmite	0.2620	0.2686	0.2630	0.2919	0.2734	0.2566	0.2732	0.2748	0.2654	0.2606	0.2640	0.2696	0.2571	0.2433	0.2465	0.2620	0.2637	0.2703	0.2496	0.2780
Esseneite	0.0000	0.0000	0.0000	0.0000	0.0000	0.0000	0.0000	0.0000	0.0000	0.0000	0.0000	0.0000	0.0000	0.0000	0.0000	0.0000	0.0000	0.0000	0.0000	0.0000
K-Cpx	0.0000	0.0000	0.0000	0.0000	0.0005	0.0000	0.0000	0.0000	0.0000	0.0000	0.0005	0.0005	0.0000	0.0000	0.0000	0.0000	0.0000	0.0005	0.0000	0.0000
Total	1.0000	1.0000	1.0000	1.0044	1.0000	1.0000	1.0000	1.0000	1.0000	1.0000	1.0000	1.0000	1.0000	1.0000	1.0000	1.0000	1.0000	1.0000	1.0000	1.0000
Triangular Plotting Coordinates																				
En	0.3849	0.3920	0.3878	0.3851	0.3957	0.3854	0.3910	0.3882	0.3802	0.3910	0.3910	0.3921	0.3852	0.3837	0.3825	0.3928	0.3802	0.3880	0.3816	0.3986
Fs	0.1061	0.0967	0.1033	0.0808	0.0932	0.1108	0.0964	0.0984	0.1109	0.1021	0.1008	0.0991	0.1037	0.1130	0.1128	0.1017	0.1061	0.0978	0.1106	0.0888
Wo	0.5090	0.5113	0.5089	0.5341	0.5111	0.5038	0.5126	0.5134	0.5089	0.5069	0.5082	0.5088	0.5110	0.5033	0.5047	0.5055	0.5137	0.5142	0.5078	0.5126
x	0.4164	0.4069	0.4131	0.4017	0.4027	0.4188	0.4073	0.4100	0.4218	0.4105	0.4098	0.4082	0.4148	0.4210	0.4217	0.4093	0.4192	0.4098	0.4209	0.3985
y	0.5090	0.5113	0.5089	0.5341	0.5111	0.5038	0.5126	0.5134	0.5089	0.5069	0.5082	0.5088	0.5110	0.5033	0.5047	0.5055	0.5137	0.5142	0.5078	0.5126
Tschermak	0.0443	0.0500	0.0462	0.0586	0.0598	0.0532	0.0630	0.0666	0.0682	0.0442	0.0508	0.0620	0.0532	0.0423	0.0373	0.0498	0.0517	0.0584	0.0410	0.0521
Tschermak	0.0644	0.0678	0.0660	0.0785	0.0760	0.0705	0.0772	0.0820	0.0865	0.0640	0.0687	0.0778	0.0700	0.0617	0.0586	0.0685	0.0684	0.0739	0.0608	0.0714
Tschermak(%)	6.4390	6.7760	6.5952	7.8530	7.5984	7.0476	7.7205	8.1999	8.6546	6.4018	6.8679	7.7780	7.0047	6.1683	5.8579	6.8453	6.8360	7.3919	6.0841	7.1373

542205C CPX																				
Point	83/1	84/1	85/1	86/1	87/1	88/1	96/1	97/1	98/1	99/1	100/1	101/1	102/1	103/1	133/1	134/1	135/1	136/1	137/1	150/1
Mineral	cpx	cpx	cpx	cpx	cpx	cpx	cpx	cpx	cpx	cpx	cpx	cpx	cpx	cpx	cpx	cpx	cpx	cpx	cpx	cpx
SiO2	51.63	51.47	51.75	51.87	51.69	51.9	51.46	51.61	51.84	51.97	51.3	51.31	51.83	51.78	51.99	51.15	51.77	52.14	52.1	52.03
TiO2	0.84	0.9	0.89	0.48	0.57	0.46	0.85	0.81	0.6	0.54	0.54	0.54	0.58	0.5	0.73	0.76	0.61	0.52	0.51	0.69
Al2O3	3.55	3.57	3.48	3.4	3.79	4.65	3.62	3.67	3.59	3.88	4.78	4.32	3.97	4.39	3.48	3.5	3.56	3.61	3.97	3.68
Cr2O3	0.01	0.01	0.01	0	0.01	0	0.01	0	0	0	0.01	0	0	0	0	0.01	0	0.01	0	0
FeO	12.77	12.76	12.77	12.83	12.73	12.99	12.68	12.76	12.8	12.8	12.68	12.65	12.62	12.85	12.76	12.78	12.84	12.54	12.51	12.65
MnO	0.21	0.21	0.19	0.2	0.21	0.18	0.19	0.2	0.18	0.18	0.21	0.2	0.19	0.18	0.21	0.21	0.2	0.2	0.18	0.2
NiO	0.02	0.01	0	0	0.02	0	0	0	0.01	0.02	0.01	0	0	0.01	0	0	0	0.02	0	0
MgO	9.07	9.13	9.16	9.01	8.92	8.35	9.13	8.95	8.96	8.92	8.42	8.52	8.65	8.6	9.16	8.98	9.12	9.06	8.88	9.08
CaO	18.16	18.06	18.26	18.12	18	17.37	18.21	18.15	18	17.78	17.45	17.63	17.86	17.58	18.1	18.16	18.22	18.16	17.87	17.98
Na2O	4.02	3.91	3.88	4	4.05	4.44	3.99	3.98	4.04	4.31	4.4	4.32	4.22	4.35	4.01	3.89	3.91	3.95	4.12	4.06
K2O	0.01	0	0	0	0	0	0	0	0	0.01	0	0	0	0	0	0	0	0	0.01	0.01
BaO																				
SrO																				
Total reported	100.29	100.03	100.39	99.91	99.99	100.34	100.14	100.13	100.02	100.41	99.8	99.49	99.92	100.24	100.44	99.44	100.23	100.21	100.15	100.38
Result: cations per formula unit																				
Si	1.9102	1.9105	1.9147	1.9258	1.9168	1.9150	1.9060	1.9134	1.9224	1.9152	1.9014	1.9088	1.9219	1.9120	1.9200	1.9102	1.9169	1.9295	1.9267	1.9213
Ti	0.0234	0.0251	0.0248	0.0134	0.0159	0.0128	0.0237	0.0226	0.0167	0.0150	0.0151	0.0151	0.0162	0.0139	0.0203	0.0213	0.0170	0.0145	0.0142	0.0192
Al	0.1548	0.1562	0.1517	0.1488	0.1656	0.2022	0.1580	0.1604	0.1569	0.1685	0.2088	0.1894	0.1735	0.1910	0.1515	0.1541	0.1554	0.1574	0.1730	0.1602
Cr	0.0003	0.0003	0.0003	0.0000	0.0003	0.0000	0.0003	0.0000	0.0000	0.0000	0.0003	0.0000	0.0000	0.0000	0.0000	0.0003	0.0000	0.0003	0.0000	0.0000
Fe	0.3951	0.3961	0.3951	0.3984	0.3948	0.4008	0.3928	0.3956	0.3970	0.3945	0.3930	0.3936	0.3913	0.3968	0.3941	0.3991	0.3976	0.3881	0.3869	0.3907
Mn	0.0066	0.0066	0.0060	0.0063	0.0066	0.0056	0.0060	0.0063	0.0057	0.0056	0.0066	0.0063	0.0060	0.0056	0.0066	0.0066	0.0063	0.0063	0.0056	0.0063
Ni	0.0006	0.0003	0.0000	0.0000	0.0006	0.0000	0.0000	0.0000	0.0003	0.0006	0.0003	0.0000	0.0000	0.0003	0.0000	0.0000	0.0000	0.0006	0.0000	0.0000
Mg	0.5003	0.5052	0.5052	0.4987	0.4931	0.4593	0.5041	0.4947	0.4953	0.4901	0.4653	0.4725	0.4782	0.4734	0.5043	0.5000	0.5034	0.4998	0.4896	0.4999
Ca	0.7199	0.7183	0.7239	0.7208	0.7152	0.6867	0.7227	0.7210	0.7152	0.7021	0.6930	0.7027	0.7096	0.6955	0.7162	0.7267	0.7228	0.7201	0.7081	0.7114
Na	0.2884	0.2814	0.2783	0.2879	0.2912	0.3176	0.2865	0.2861	0.2905	0.3080	0.3162	0.3116	0.3034	0.3114	0.2871	0.2817	0.2807	0.2834	0.2954	0.2907
K	0.0005	0.0000	0.0000	0.0000	0.0000	0.0000	0.0000	0.0000	0.0000	0.0005	0.0000	0.0000	0.0000	0.0000	0.0000	0.0000	0.0000	0.0000	0.0005	0.0005
Sum of Cations	4.0000	4.0000	4.0000	4.0000	4.0000	4.0000	4.0000	4.0000	4.0000	4.0000	4.0000	4.0000	4.0000	4.0000	4.0000	4.0000	4.0000	4.0000	4.0000	4.0000
Total Charge balance	11.7334	11.7464	11.7526	11.7392	11.7401	11.7400	11.7311	11.7463	11.7447	11.7205	11.7259	11.7256	11.7462	11.7313	11.7449	11.7358	11.7424	11.7623	11.7590	11.7500
free	0.2666	0.2536	0.2474	0.2608	0.2599	0.2600	0.2689	0.2537	0.2553	0.2795	0.2741	0.2744	0.2538	0.2687	0.2551	0.2642	0.2576	0.2377	0.2410	0.2500
Fe3	0.2666	0.2536	0.2474	0.2608	0.2599	0.2600	0.2689	0.2537	0.2553	0.2795	0.2741	0.2744	0.2538	0.2687	0.2551	0.2642	0.2576	0.2377	0.2410	0.2500
Fe2	0.1286	0.1425	0.1477	0.1375	0.1348	0.1408	0.1239	0.1419	0.1417	0.1150	0.1189	0.1192	0.1376	0.1281	0.1390	0.1350	0.1399	0.1504	0.1459	0.1407
Mg-#T	55.8714	56.0532	56.1147	55.5920	55.5373	53.3985	56.2080	55.5621	55.5124	55.4019	54.2064	54.5580	54.9920	54.4008	56.1340	55.6060	55.8721	56.2919	55.8566	56.1312
Result: components																				
En	0.2501	0.2526	0.2526	0.2493	0.2466	0.2296	0.2521	0.2473	0.2477	0.2450	0.2326	0.2363	0.2391	0.2367	0.2521	0.2500	0.2517	0.2499	0.2448	0.2499
Fs	0.0643	0.0712	0.0739	0.0688	0.0674	0.0704	0.0619	0.0709	0.0709	0.0575	0.0595	0.0596	0.0688	0.0641	0.0695	0.0675	0.0700	0.0752	0.0729	0.0703
Wo	0.3268	0.3270	0.3317	0.3300	0.3239	0.3072	0.3262	0.3285	0.3272	0.3161	0.3048	0.3133	0.3238	0.3107	0.3282	0.3291	0.3283	0.3320	0.3245	0.3260
Tschermak	0.0427	0.0389	0.0355	0.0474	0.0512	0.0595	0.0464	0.0414	0.0441	0.0548	0.0682	0.0610	0.0458	0.0603	0.0395	0.0468	0.0492	0.0412	0.0449	0.0403
Mn-Px	0.0033	0.0033	0.0030	0.0031	0.0033	0.0028	0.0030	0.0031	0.0028	0.0028	0.0033	0.0032	0.0030	0.0028	0.0033	0.0033	0.0031	0.0031	0.0028	0.0031
Ni-Px	0.0003	0.0001	0.0000	0.0000	0.0003	0.0000	0.0000	0.0000	0.0001	0.0003	0.0001	0.0000	0.0000	0.0001	0.0000	0.0000	0.0000	0.0003	0.0000	0.0000
Cr-Ts	0.0003	0.0003	0.0003	0.0000	0.0003	0.0000	0.0003	0.0000	0.0000	0.0000	0.0003	0.0000	0.0000	0.0000	0.0000	0.0003	0.0000	0.0003	0.0000	0.0000
CaTiTs	0.0234	0.0251	0.0248	0.0134	0.0159	0.0128	0.0237	0.0226	0.0167	0.0150	0.0151	0.0151	0.0162	0.0139	0.0203	0.0213	0.0170	0.0145	0.0142	0.0192
Jadeite	0.0218	0.0278	0.0309	0.0271	0.0312	0.0576	0.0176	0.0324	0.0352	0.0285	0.0421	0.0372	0.0496	0.0428	0.0320	0.0175	0.0231	0.0457	0.0544	0.0407
Acmite	0.2666	0.2536	0.2474	0.2608	0.2599	0.2600	0.2689	0.2537	0.2553	0.2795	0.2741	0.2744	0.2538	0.2687	0.2551	0.2642	0.2576	0.2377	0.2410	0.2500
Esseneite	0.0000	0.0000	0.0000	0.0000	0.0000	0.0000	0.0000	0.0000	0.0000	0.0000	0.0000	0.0000	0.0000	0.0000	0.0000	0.0000	0.0000	0.0000	0.0000	0.0000
K-Cpx	0.0005	0.0000	0.0000	0.0000	0.0000	0.0000	0.0000	0.0000	0.0000	0.0005	0.0000	0.0000	0.0000	0.0000	0.0000	0.0000	0.0000	0.0000	0.0005	0.0005
Total	1.0000	1.0000	1.0000	1.0000	1.0000	1.0000	1.0000	1.0000	1.0000	1.0000	1.0000	1.0000	1.0000	1.0000	1.0000	1.0000	1.0000	1.0000	1.0000	1.0000
Triangular Plotting Coordinates																				
En	0.3901	0.3882	0.3838	0.3847	0.3865	0.3782	0.3937	0.3824	0.3836	0.3961	0.3898	0.3878	0.3785	0.3871	0.3880	0.3866	0.3872	0.3803	0.3812	0.3868
Fs	0.1003	0.1094	0.1122	0.1061	0.1057	0.1160	0.0967	0.1097	0.1097	0.0929	0.0996	0.0978	0.1089	0.1048	0.1069	0.1044	0.1076	0.1144	0.1136	0.1088
Wo	0.5096	0.5024	0.5039	0.5092	0.5078	0.5059	0.5095	0.5079	0.5067	0.5110	0.5106	0.5143	0.5126	0.5081	0.5051	0.5090	0.5051	0.5053	0.5053	0.5044
x	0.4100	0.4164	0.4205	0.4165	0.4152	0.4260	0.4059	0.4199	0.4192	0.4024	0.4099	0.4099	0.4217	0.4144	0.4151	0.4144	0.4159	0.4239	0.4229	0.4169
y	0.5096	0.5024	0.5039	0.5092	0.5078	0.5059	0.5095	0.5079	0.5067	0.5110	0.5106	0.5143	0.5126	0.5081	0.5051	0.5090	0.5051	0.5053	0.5053	0.5044
Tschermak	0.0430	0.0392	0.0358	0.0474	0.0514	0.0595	0.0467	0.0414	0.0441	0.0548	0.0684	0.0610	0.0458	0.0603	0.0395	0.0471	0.0492	0.0415	0.0449	0.0403
Tschermak	0.0664	0.0644	0.0606	0.0608	0.0673	0.0723	0.0703	0.0640	0.0608	0.0698	0.0835	0.0761	0.0619	0.0741	0.0597	0.0684	0.0662	0.0560	0.0591	0.0595
Tschermak(%)	6.6403	6.4361	6.0557	6.0839	6.7347	7.2283	7.0340	6.4004	6.0845	6.9788	8.3503	7.6094	6.1946	7.4141	5.9736	6.8418	6.6151	5.6004	5.9092	5.9496

Appendix IV: Nepheline EMPA data for sample 542216

	542216BI						542216CII								
Point	58 / 1 .	59 / 1 .	60 / 1 .	61 / 1 .	74 / 1 .	75 / 1 .	221 / 1 .	222 / 1 .	223 / 1 .	239 / 1 .	240 / 1 .	241 / 1 .	256 / 1 .	257 / 1 .	258 / 1 .
SiO2	43.81	43.85	43.79	43.94	43.61	43.56	45.33	44.96	45.45	43.33	43.68	43.71	44.4	45.02	46.15
TiO2	0.01	0	0	0	0	0	0	0.01	0	0	0	0	0	0	0
Al2O3	34	33.89	34.13	33.94	34.35	34.45	33.72	33.28	33.67	33.39	33.31	33.17	33	33.3	33.65
Fe2O3	0.077791	0.011113	0.044452	0.044452	0.033339	0.077791	0.077791	0.088904	0.100017	0.022226	0.066678	0.044452	0.022226	0.022226	0.055565
FeO	0	0	0	0	0	0	0	0	0	0	0	0	0	0	0
FeOT	0.07	0.01	0.04	0.04	0.03	0.07	0.07	0.08	0.09	0.02	0.06	0.04	0.02	0.02	0.05
MnO	0	0	0	0	0	0	0	0.01	0	0.01	0.02	0	0	0	0
MgO	0	0	0.02	0	0.01	0	0.01	0	0	0	0	0	0	0	0.01
CaO	0.42	0.43	0.44	0.42	0.57	0.55	0.76	0.75	0.8	0.73	0.75	0.76	0.73	0.74	0.68
Na2O	15.96	16.21	16.06	16.05	15.9	15.96	16.28	16.26	16.18	16.05	16.13	16.2	16.22	16.22	15.85
K2O	6.41	6.33	6.34	6.34	6.5	6.25	5.58	5.77	5.77	5.92	6.11	5.93	5.5	5.62	5.51
P2O5															
Cr2O3	0	0	0.01	0	0	0.02	0	0.01	0	0.01	0	0	0	0	0
NiO	0.01	0	0	0	0	0.01	0	0	0	0	0	0	0.01	0.01	0
ZnO															
BaO															
Total	100.69	100.72	100.83	100.73	100.97	100.87	101.75	101.13	101.96	99.46	100.06	99.81	99.88	100.93	101.9

Appendix V: Clinopyroxene EMPA data for sample 542216

542216BI CPX																								
Point	1 / 1 .	2 / 1 .	3 / 1 .	4 / 1 .	5 / 1 .	6 / 1 .	7 / 1 .	22 / 1 .	23 / 1 .	24 / 1 .	25 / 1 .	52 / 1 .	53 / 1 .	54 / 1 .	55 / 1 .	56 / 1 .	57 / 1 .	62 / 1 .	63 / 1 .	64 / 1 .	65 / 1 .	66 / 1 .	67 / 1 .	
Mineral	cpx	cpx	cpx	cpx	cpx	cpx	cpx	cpx	cpx	cpx	cpx	cpx	cpx	cpx	cpx	cpx	cpx	cpx	cpx	cpx				
SiO2	51.38	51.24	51.24	51.39	50.52	51.03	51.35	52.83	51.22	51.5	51.53	51.08	51.03	51.03	50.78	50.9	51.15	51.14	51.1	51.09	50.64	50.77	50.52	
TiO2	0.88	0.95	0.9	0.96	1.05	1.09	0.97	1.03	1.04	0.8	0.88	1.01	1.02	1.02	1.1	0.97	1.01	0.94	0.97	0.99	1.06	1.03	1.1	
Al2O3	3.61	3.81	3.7	3.43	4.12	4.33	4.06	4.35	4.15	3.75	3.88	3.8	3.91	3.96	4.47	4.09	4.24	3.57	3.83	3.69	4.28	4.48	4.52	
Cr2O3	0.01	0	0.01	0	0	0	0	0	0	0	0.01	0.01	0	0	0.01	0.01	0	0	0	0	0.01	0	0	
FeO	12.49	12.51	12.58	12.54	11.67	11.98	11.84	11.89	11.82	11.9	11.91	12.35	12.39	12.42	11.94	11.78	11.75	12.28	12.31	12.14	11.76	11.79	11.81	
MnO	0.27	0.27	0.27	0.28	0.27	0.29	0.27	0.27	0.23	0.25	0.28	0.28	0.26	0.27	0.25	0.26	0.25	0.28	0.25	0.26	0.28	0.24	0.28	
NiO	0.01	0.01	0	0.02	0	0	0	0	0	0	0	0	0.01	0	0.01	0	0	0	0.01	0	0	0	0	
MgO	9.35	9.25	9.11	9.48	9.31	9.23	9.38	9.15	9.37	9.6	9.51	9.34	9.31	9.26	9.37	9.63	9.61	9.29	9.3	9.37	9.28	9.27	9.15	
CaO	18.85	18.73	18.56	18.87	18.76	18.71	18.8	18.81	18.78	19.1	18.72	19.07	19.2	19.11	19.19	19.4	19.35	18.79	18.83	19.03	19.04	19.2	19.11	
Na2O	3.5	3.61	3.54	3.39	3.56	3.53	3.48	3.54	3.62	3.51	3.67	3.24	3.29	3.39	3.4	3.24	3.31	3.38	3.41	3.4	3.34	3.36	3.38	
K2O	0.01	0	0	0.01	0.01	0	0.01	0	0.01	0.01	0	0	0.01	0.01	0.01	0	0	0	0	0.01	0.02	0.02	0.01	
BaO																								
SrO																								
Total reported	100.36	100.38	99.91	100.37	99.27	100.19	100.16	101.87	100.24	100.42	100.39	100.18	100.43	100.47	100.53	100.28	100.67	99.67	100.01	99.98	99.71	100.16	99.88	
Result: cations per formula unit																								
Si	1.9044	1.8978	1.9090	1.9063	1.8877	1.8923	1.9039	1.9288	1.8954	1.9025	1.9029	1.9001	1.8928	1.8910	1.8769	1.8860	1.8871	1.9100	1.9012	1.9007	1.8878	1.8835	1.8803	
Ti	0.0245	0.0265	0.0252	0.0268	0.0295	0.0304	0.0271	0.0283	0.0289	0.0222	0.0244	0.0283	0.0285	0.0284	0.0306	0.0270	0.0280	0.0264	0.0271	0.0277	0.0297	0.0287	0.0308	
Al	0.1577	0.1663	0.1625	0.1500	0.1814	0.1892	0.1774	0.1872	0.1810	0.1633	0.1689	0.1666	0.1709	0.1729	0.1947	0.1786	0.1844	0.1571	0.1679	0.1618	0.1880	0.1959	0.1983	
Cr	0.0003	0.0000	0.0003	0.0000	0.0000	0.0000	0.0000	0.0000	0.0000	0.0000	0.0003	0.0003	0.0000	0.0000	0.0003	0.0003	0.0000	0.0000	0.0000	0.0000	0.0003	0.0000	0.0000	
Fe	0.3871	0.3875	0.3920	0.3890	0.3647	0.3715	0.3671	0.3630	0.3658	0.3676	0.3678	0.3842	0.3843	0.3849	0.3691	0.3650	0.3625	0.3836	0.3830	0.3777	0.3666	0.3658	0.3676	
Mn	0.0085	0.0085	0.0085	0.0088	0.0085	0.0091	0.0085	0.0083	0.0072	0.0078	0.0088	0.0088	0.0082	0.0085	0.0078	0.0082	0.0078	0.0089	0.0079	0.0082	0.0088	0.0075	0.0088	
Ni	0.0003	0.0003	0.0000	0.0006	0.0000	0.0000	0.0000	0.0000	0.0000	0.0000	0.0000	0.0000	0.0003	0.0000	0.0003	0.0000	0.0000	0.0000	0.0003	0.0000	0.0000	0.0000	0.0000	
Mg	0.5166	0.5107	0.5060	0.5242	0.5186	0.5102	0.5185	0.4980	0.5169	0.5287	0.5235	0.5180	0.5148	0.5115	0.5163	0.5319	0.5285	0.5173	0.5158	0.5197	0.5157	0.5127	0.5077	
Ca	0.7486	0.7433	0.7409	0.7500	0.7511	0.7434	0.7469	0.7358	0.7446	0.7560	0.7407	0.7601	0.7631	0.7587	0.7600	0.7702	0.7649	0.7519	0.7507	0.7586	0.7605	0.7632	0.7621	
Na	0.2515	0.2592	0.2557	0.2438	0.2579	0.2538	0.2502	0.2506	0.2597	0.2514	0.2628	0.2337	0.2366	0.2436	0.2436	0.2328	0.2368	0.2448	0.2460	0.2452	0.2414	0.2417	0.2439	
K	0.0005	0.0000	0.0000	0.0005	0.0005	0.0000	0.0005	0.0000	0.0005	0.0005	0.0000	0.0000	0.0005	0.0005	0.0005	0.0000	0.0000	0.0000	0.0000	0.0005	0.0010	0.0009	0.0005	
Sum of Cations	4.0000	4.0000	4.0000	4.0000	4.0000	4.0000	4.0000	4.0000	4.0000	4.0000	4.0000	4.0000	4.0000	4.0000	4.0000	4.0000	4.0000	4.0000	4.0000	4.0000	4.0000	4.0000	4.0000	
Total Charge balance	11.7638	11.7555	11.7755	11.7719	11.7576	11.7809	11.7887	11.8507	11.7694	11.7608	11.7610	11.7900	11.7764	11.7677	11.7658	11.7722	11.7778	11.7853	11.7787	11.7728	11.7811	11.7778	11.7761	
free	0.2362	0.2445	0.2245	0.2281	0.2424	0.2191	0.2113	0.1493	0.2306	0.2392	0.2390	0.2100	0.2236	0.2323	0.2342	0.2278	0.2222	0.2147	0.2213	0.2272	0.2189	0.2222	0.2239	
Fe3	0.2362	0.2445	0.2245	0.2281	0.2424	0.2191	0.2113	0.1493	0.2306	0.2392	0.2390	0.2100	0.2236	0.2323	0.2342	0.2278	0.2222	0.2147	0.2213	0.2272	0.2189	0.2222	0.2239	
Fe2	0.1509	0.1430	0.1674	0.1609	0.1222	0.1524	0.1559	0.2137	0.1352	0.1285	0.1288	0.1742	0.1608	0.1526	0.1348	0.1372	0.1403	0.1689	0.1617	0.1505	0.1477	0.1436	0.1437	
Mg-#T	57.1633	56.8606	56.3489	57.4034	58.7136	57.8664	58.5445	57.8380	58.5596	58.9838	58.7353	57.4130	57.2552	57.0641	58.3143	59.3041	59.3154	57.4207	57.3873	57.9099	58.4489	58.3608	58.0025	
Result: components																								
En	0.2583	0.2554	0.2530	0.2621	0.2593	0.2551	0.2592	0.2490	0.2584	0.2643	0.2618	0.2590	0.2574	0.2558	0.2581	0.2660	0.2643	0.2586	0.2579	0.2598	0.2579	0.2563	0.2538	
Fs	0.0755	0.0715	0.0837	0.0804	0.0611	0.0762	0.0779	0.1069	0.0676	0.0642	0.0644	0.0871	0.0804	0.0763	0.0674	0.0686	0.0702	0.0844	0.0809	0.0753	0.0739	0.0718	0.0719	
Wo	0.3387	0.3337	0.3375	0.3415	0.3342	0.3330	0.3389	0.3464	0.3345	0.3404	0.3340	0.3442	0.3422	0.3391	0.3337	0.3416	0.3400	0.3442	0.3395	0.3435	0.3390	0.3377	0.3366	
Tschermak	0.0463	0.0493	0.0403	0.0401	0.0532	0.0469	0.0420	0.0147	0.0467	0.0531	0.0480	0.0431	0.0502	0.0522	0.0617	0.0597	0.0569	0.0371	0.0445	0.0439	0.0524	0.0590	0.0581	
Mn-Px	0.0042	0.0042	0.0043	0.0044	0.0043	0.0046	0.0042	0.0042	0.0036	0.0039	0.0044	0.0044	0.0041	0.0042	0.0039	0.0041	0.0039	0.0044	0.0039	0.0041	0.0044	0.0038	0.0044	
Ni-Px	0.0001	0.0001	0.0000	0.0003	0.0000	0.0000	0.0000	0.0000	0.0000	0.0000	0.0000	0.0000	0.0001	0.0000	0.0001	0.0000	0.0000	0.0000	0.0001	0.0000	0.0000	0.0000	0.0000	
Cr-Ts	0.0003	0.0000	0.0003	0.0000	0.0000	0.0000	0.0000	0.0000	0.0000	0.0000	0.0003	0.0003	0.0000	0.0000	0.0003	0.0003	0.0000	0.0000	0.0000	0.0000	0.0003	0.0000	0.0000	
CaTiTs	0.0245	0.0265	0.0252	0.0268	0.0295	0.0304	0.0271	0.0283	0.0289	0.0222	0.0244	0.0283	0.0285	0.0284	0.0306	0.0270	0.0280	0.0264	0.0271	0.0277	0.0297	0.0287	0.0308	
Jadeite	0.0153	0.0148	0.0312	0.0157	0.0155	0.0346	0.0389	0.1013	0.0291	0.0122	0.0238	0.0237	0.0130	0.0112	0.0094	0.0049	0.0146	0.0301	0.0247	0.0181	0.0225	0.0195	0.0200	
Acmite	0.2362	0.2445	0.2245	0.2281	0.2424	0.2191	0.2113	0.1493	0.2306	0.2392	0.2390	0.2100	0.2236	0.2323	0.2342	0.2278	0.2222	0.2147	0.2213	0.2272	0.2189	0.2222	0.2239	
Esseneite	0.0000	0.0000	0.0000	0.0000	0.0000	0.0000	0.0000	0.0000	0.0000	0.0000	0.0000	0.0000	0.0000	0.0000	0.0000	0.0000	0.0000	0.0000	0.0000	0.0000	0.0000	0.0000	0.0000	
K-Cpx	0.0005	0.0000	0.0000	0.0005	0.0005	0.0000	0.0005	0.0000	0.0005	0.0005	0.0000	0.0000	0.0005	0.0005	0.0005	0.0000	0.0000	0.0000	0.0000	0.0005	0.0010	0.0009	0.0005	
Total	1.0000	1.0000	1.0000	1.0000	1.0000	1.0000	1.0000	1.0000	1.0000	1.0000	1.0000	1.0000	1.0000	1.0000	1.0000	1.0000	1.0000	1.0000	1.0000	1.0000	1.0000	1.0000	1.0000	
Triangular Plotting Coordinates																								
En	0.3841	0.3866	0.3752	0.3832	0.3961	0.3840	0.3834	0.3546	0.3913	0.3952	0.3965	0.3752	0.3786	0.3811	0.3916	0.3933	0.3918	0.3763	0.3802	0.3829	0.3844	0.3850	0.3833	
Fs	0.1122	0.1082	0.1242	0.1176	0.0934	0.1147	0.1153	0.1522	0.1024	0.0960	0.0976	0.1262	0.1182	0.1137	0.1023	0.1015	0.1040	0.1229	0.1192	0.1109	0.1101	0.1078	0.1085	
Wo	0.5037	0.5052	0.5006	0.4993	0.5105	0.5013	0.5013	0.4933	0.5064	0.5088	0.5059	0.4987	0.5032	0.5052	0.5062	0.5052	0.5041	0.5008	0.5005	0.5062	0.5054	0.5072	0.5082	
x	0.4204	0.4167	0.4324	0.4240	0.4025	0.4218	0.4225	0.4605	0.4105	0.4046	0.4048	0.4336	0.4271	0.4229	0.4103	0.4088	0.4112	0.4310	0.4266	0.4203	0.4190	0.4173	0.4187	
y	0.5037	0.5052	0.5006	0.4993	0.5105	0.5013	0.5013	0.4933	0.5064	0.5088	0.5059	0.4987	0.5032	0.5052	0.5062	0.5052	0.5041	0.5008	0.5005	0.5062	0.5054	0.5072	0.5082	
Tschermak	0.0466	0.0493	0.0406	0.0401	0.0532	0.0469	0.0420	0.0147	0.0467	0.0531	0.0482	0.0434	0.0502	0.0522	0.0620	0.0599	0.0569	0.0371	0.0445	0.0439	0.0527	0.0590	0.0581	
Tschermak	0.0711	0.0758	0.0658	0.0669	0.0827	0.0773	0.0690	0.0429	0.0757	0.0753	0.0727	0.0716	0.0787	0.0806	0.0926	0.0870	0.0849	0.0635	0.0716	0.0716	0.0824	0.0877	0.0889	
Tschermak(%)	7.1112	7.5777	6.5790	6.6907	8.2748	7.7295	6.9015	4.2946	7.5686	7.5288	7.2690	7.1621	7.8706	8.0616	9.2562	8.6979	8.4898	6.3545	7.1626	7.1623	8.2447	8.7741	8.8878	

542216CII CPX															
Point	195 / 1 .	196 / 1 .	197 / 1 .	198 / 1 .	199 / 1 .	200 / 1 .	217 / 1 .	227 / 1 .	228 / 1 .	248 / 1 .	249 / 1 .	250 / 1 .	251 / 1 .	263 / 1 .	264 / 1 .
Mineral	cpx	cpx	cpx	cpx	cpx	cpx	cpx	cpx	cpx	cpx	cpx	cpx	cpx	cpx	cpx
SiO2	51.28	51.34	51.12	51.7	51.56	50.84	51.12	50.28	50.94	50.61	50.81	51.16	50.84	51.54	51.01
TiO2	0.73	0.74	0.56	0.49	0.56	0.4	0.47	0.62	0.54	0.98	0.98	0.64	0.6	0.85	0.87
Al2O3	3.66	3.69	4	4.58	4.35	4.71	4.87	5.04	4.36	3.94	3.85	4.52	4.74	3.95	3.68
Cr2O3	0.01	0.01	0	0	0.02	0	0	0	0	0	0	0	0	0	0.01
FeO	11.37	11.49	11.53	11.54	11.47	11.73	11.42	11.7	11.56	12.48	12.38	11.81	11.88	11.88	12.18
MnO	0.24	0.26	0.22	0.23	0.23	0.22	0.22	0.24	0.27	0.29	0.25	0.25	0.24	0.28	0.26
NiO	0	0	0	0.02	0.03	0	0	0.01	0	0	0.01	0.02	0	0	0
MgO	9.96	9.96	9.89	9.86	9.86	9.35	9.27	9.36	9.68	9.19	9.62	9.49	9.37	9.79	9.61
CaO	19.42	19.49	19.13	18.96	18.93	18.98	18.72	19.31	19.31	19.24	19.36	18.79	18.77	19.25	19.2
Na2O	3.23	3.18	3.32	3.62	3.43	3.6	3.71	3.21	3.25	3.26	3.36	3.59	3.55	3.26	3.33
K2O	0	0	0	0	0.01	0.01	0	0	0	0.01	0	0	0	0.01	0
BaO															
SrO															
Total reported	99.9	100.16	99.77	101	100.45	99.84	99.8	99.77	99.91	100	100.62	100.27	99.99	100.81	100.15
Result: cations per formula unit															
Si	1.9031	1.9018	1.8975	1.8910	1.8994	1.8837	1.8930	1.8700	1.8901	1.8863	1.8774	1.8893	1.8833	1.8990	1.8933
Ti	0.0204	0.0206	0.0156	0.0135	0.0155	0.0111	0.0131	0.0173	0.0151	0.0275	0.0272	0.0178	0.0167	0.0236	0.0243
Al	0.1601	0.1611	0.1750	0.1974	0.1889	0.2057	0.2125	0.2209	0.1907	0.1731	0.1677	0.1967	0.2069	0.1715	0.1610
Cr	0.0003	0.0003	0.0000	0.0000	0.0006	0.0000	0.0000	0.0000	0.0000	0.0000	0.0000	0.0000	0.0000	0.0000	0.0003
Fe	0.3529	0.3560	0.3579	0.3530	0.3534	0.3635	0.3537	0.3639	0.3587	0.3890	0.3825	0.3647	0.3680	0.3661	0.3781
Mn	0.0075	0.0082	0.0069	0.0071	0.0072	0.0069	0.0069	0.0076	0.0085	0.0092	0.0078	0.0078	0.0075	0.0087	0.0082
Ni	0.0000	0.0000	0.0000	0.0006	0.0009	0.0000	0.0000	0.0003	0.0000	0.0000	0.0003	0.0006	0.0000	0.0000	0.0000
Mg	0.5510	0.5500	0.5473	0.5376	0.5415	0.5165	0.5117	0.5190	0.5354	0.5106	0.5299	0.5225	0.5175	0.5378	0.5317
Ca	0.7722	0.7736	0.7608	0.7430	0.7472	0.7535	0.7427	0.7695	0.7677	0.7683	0.7665	0.7435	0.7450	0.7600	0.7636
Na	0.2324	0.2284	0.2389	0.2567	0.2450	0.2586	0.2664	0.2315	0.2338	0.2356	0.2407	0.2571	0.2550	0.2329	0.2396
K	0.0000	0.0000	0.0000	0.0000	0.0005	0.0005	0.0000	0.0000	0.0000	0.0005	0.0000	0.0000	0.0000	0.0005	0.0000
Sum of Cations	4.0000	4.0000	4.0000	4.0000	4.0000	4.0000	4.0000	4.0000	4.0000	4.0000	4.0000	4.0000	4.0000	4.0000	4.0000
Total Charge balance	11.7750	11.7779	11.7623	11.7497	11.7739	11.7364	11.7583	11.7642	11.7672	11.7645	11.7362	11.7539	11.7521	11.7833	11.7568
Free	0.2250	0.2221	0.2377	0.2503	0.2261	0.2636	0.2417	0.2358	0.2328	0.2355	0.2638	0.2461	0.2479	0.2167	0.2432
Fe3	0.2250	0.2221	0.2377	0.2503	0.2261	0.2636	0.2417	0.2358	0.2328	0.2355	0.2638	0.2461	0.2479	0.2167	0.2432
Fe2	0.1278	0.1339	0.1203	0.1026	0.1273	0.0998	0.1120	0.1281	0.1259	0.1535	0.1187	0.1186	0.1201	0.1494	0.1348
Mg-#T	60.9609	60.7108	60.4593	60.3660	60.5114	58.6932	59.1335	58.7812	59.8827	56.7598	58.0745	58.8886	58.4367	59.4976	58.4453
Result: components															
En	0.2755	0.2750	0.2736	0.2688	0.2708	0.2582	0.2559	0.2595	0.2677	0.2553	0.2649	0.2612	0.2587	0.2689	0.2659
Fs	0.0639	0.0669	0.0601	0.0513	0.0636	0.0499	0.0560	0.0640	0.0630	0.0768	0.0594	0.0593	0.0601	0.0747	0.0674
Wo	0.3479	0.3480	0.3370	0.3238	0.3311	0.3242	0.3244	0.3284	0.3364	0.3411	0.3355	0.3253	0.3225	0.3413	0.3406
Tschermak	0.0558	0.0566	0.0712	0.0820	0.0690	0.0940	0.0808	0.0953	0.0797	0.0588	0.0681	0.0751	0.0832	0.0539	0.0578
Mn-Px	0.0038	0.0041	0.0035	0.0036	0.0036	0.0035	0.0035	0.0038	0.0042	0.0046	0.0039	0.0039	0.0038	0.0044	0.0041
Ni-Px	0.0000	0.0000	0.0000	0.0003	0.0004	0.0000	0.0000	0.0001	0.0000	0.0000	0.0001	0.0003	0.0000	0.0000	0.0000
Cr-Ts	0.0003	0.0003	0.0000	0.0000	0.0006	0.0000	0.0000	0.0000	0.0000	0.0000	0.0000	0.0000	0.0000	0.0000	0.0003
CaTiTs	0.0204	0.0206	0.0156	0.0135	0.0155	0.0111	0.0131	0.0173	0.0151	0.0275	0.0272	0.0178	0.0167	0.0236	0.0243
Jadeite	0.0074	0.0063	0.0013	0.0064	0.0189	0.0000	0.0247	0.0000	0.0010	0.0001	0.0000	0.0109	0.0070	0.0162	0.0000
Acmite	0.2250	0.2221	0.2377	0.2503	0.2261	0.2636	0.2417	0.2358	0.2328	0.2355	0.2638	0.2461	0.2479	0.2167	0.2432
Esseneite	0.0000	0.0000	0.0000	0.0000	0.0000	0.0000	0.0000	0.0000	0.0000	0.0000	0.0000	0.0000	0.0000	0.0000	0.0000
K-Cpx	0.0000	0.0000	0.0000	0.0000	0.0005	0.0005	0.0000	0.0000	0.0000	0.0005	0.0000	0.0000	0.0000	0.0005	0.0000
Total	1.0000	1.0000	1.0000	1.0000	1.0000	1.0050	1.0000	1.0043	1.0000	1.0000	1.0231	1.0000	1.0000	1.0000	1.0036
Triangular Plotting Coordinates															
En	0.4009	0.3986	0.4080	0.4175	0.4069	0.4084	0.4021	0.3980	0.4013	0.3793	0.4015	0.4045	0.4034	0.3926	0.3946
Fs	0.0930	0.0970	0.0896	0.0797	0.0956	0.0789	0.0880	0.0982	0.0944	0.1140	0.0900	0.0918	0.0936	0.1091	0.1001
Wo	0.5061	0.5044	0.5024	0.5028	0.4975	0.5127	0.5099	0.5038	0.5043	0.5067	0.5085	0.5037	0.5029	0.4983	0.5054
x	0.3996	0.4032	0.3936	0.3823	0.3976	0.3871	0.3960	0.4043	0.4002	0.4242	0.3975	0.3968	0.3985	0.4137	0.4073
y	0.5061	0.5044	0.5024	0.5028	0.4975	0.5127	0.5099	0.5038	0.5043	0.5067	0.5085	0.5037	0.5029	0.4983	0.5054
Tschermak	0.0561	0.0569	0.0712	0.0820	0.0695	0.0940	0.0808	0.0953	0.0797	0.0588	0.0681	0.0751	0.0832	0.0539	0.0581
Tschermak	0.0765	0.0775	0.0869	0.0955	0.0851	0.1051	0.0939	0.1126	0.0948	0.0862	0.0954	0.0929	0.1000	0.0774	0.0824
Tschermak(%)	7.6503	7.7533	8.6853	9.5531	8.5052	10.5118	9.3934	11.2635	9.4813	8.6238	9.5381	9.2896	9.9953	7.7415	8.2430

Appendix VI: Anti-perthite EMPA data for sample 542216

542216BI																					
Point	8 / 1.	9 / 1.	10 / 1.	11 / 1.	12 / 1.	13 / 1.	26 / 1.	27 / 1.	28 / 1.	29 / 1.	30 / 1.	31 / 1.	32 / 1.	33 / 1.	34 / 1.	35 / 1.	46 / 1.	47 / 1.	48 / 1.	49 / 1.	50 / 1.
SiO2	64.18	64.62	64.97	68.79	68.76	68.62	65.34	65.54	70.46	69.14	65.04	64.56	64.39	68.09	68.96	68.87	64.44	63.99	64.39	67.77	66.41
TiO2	0.04	0.02	0.02	0.03	0.01	0.05	0.01	0.02	0.01	0.02	0.04	0	0	0.01	0.02	0	0.02	0.02	0.01	0.02	0.02
Al2O3	18.88	18.73	18.92	20.49	20.84	20.37	18.94	19.12	20.87	20.5	18.68	18.66	18.47	20.21	20.44	20.35	18.68	18.82	18.62	21.26	21.52
Fe2O3	0	0	0	0	0	0	0	0	0	0	0	0	0	0.022226	0	0	0	0	0	0	0
FeO	0.05	0.03	0.03	0.04	0.03	0.04	0.04	0.08	0.03	0.07	0.03	0.02	0.02	0	0.06	0.04	0.02	0.03	0.01	0.04	0.04
FeOT	0.05	0.03	0.03	0.04	0.03	0.04	0.04	0.08	0.03	0.07	0.03	0.02	0.02	0.02	0.06	0.04	0.02	0.03	0.01	0.04	0.04
MnO	0	0.01	0	0	0	0	0	0	0	0	0	0	0	0	0.01	0.02	0	0	0	0	0
MgO	0.01	0.01	0	0.01	0.01	0.01	0.01	0.02	0	0	0.01	0.01	0	0	0.03	0	0	0.01	0	0.01	0
CaO	0.04	0.03	0.03	0.43	0.44	0.43	0.02	0.07	0.4	0.5	0.08	0.03	0.01	0.41	0.46	0.41	0.05	0.01	0.02	1.36	1.9
Na2O	1.19	0.87	1.29	10.64	10.93	10.16	2.3	1.24	10.57	10.96	1.2	0.9	0.9	11.09	11.11	11.09	1.92	0.84	1.52	10.29	10.1
K2O	13.98	15.11	14.48	0.09	0.08	0.09	12.93	14.67	0.15	0.08	14.41	15.16	15.26	1.48	0.06	0.08	13.26	15.13	14.06	0.15	0.1
P2O5																					
Cr2O3	0	0	0	0	0	0	0.01	0	0	0	0	0	0	0	0	0.01	0	0.01	0	0	0.01
NiO	0	0	0	0.01	0.02	0	0.02	0	0.02	0	0	0	0	0	0	0	0	0.01	0	0	0.01
ZnO																					
BaO																					
Total	98.37	99.43	99.74	100.53	101.12	99.77	99.62	100.76	102.51	101.27	99.49	99.34	99.05	101.31	101.15	100.87	98.39	98.87	98.63	100.9	100.11
Structural formula per 8 O																					
Si	2.98568	2.989179	2.987785	2.978919	2.96456	2.987656	2.991193	2.985156	2.988079	2.976615	2.996475	2.990375	2.993741	2.959232	2.974171	2.977843	2.991591	2.979456	2.991685	2.93485	2.905728
Al	1.035155	1.021133	1.025456	1.045767	1.058965	1.045275	1.021892	1.02638	1.043114	1.040176	1.014301	1.01867	1.012097	1.035194	1.038985	1.037041	1.022076	1.032771	1.019616	1.085104	1.109746
Ti	0.001399	0.000696	0.000692	0.000977	0.000324	0.001637	0.000344	0.000685	0.000319	0.000648	0.001386	0	0	0.000327	0.000649	0	0.000698	0.0007	0.000349	0.000651	0.000658
Fe2+T	0.001945	0.001161	0.001154	0.001449	0.001082	0.001456	0.001531	0.003047	0.001064	0.00252	0.001156	0.000775	0.000778	0.000727	0.002164	0.001446	0.000776	0.001168	0.000389	0.001449	0.001464
Mn	0	0.000392	0	0	0	0	0	0	0	0	0	0	0	0	0.000365	0.000732	0	0	0	0	0
Mg	0.000693	0.000689	0	0.000645	0.000643	0.000649	0.000682	0.001358	0	0	0.000687	0.00069	0	0	0.001929	0	0	0.000694	0	0.000645	0
Ca	0.001994	0.001487	0.001478	0.019951	0.020325	0.020059	0.000981	0.003416	0.018175	0.023063	0.003949	0.001489	0.000498	0.019092	0.021256	0.018994	0.002487	0.000499	0.000996	0.063103	0.089071
Na	0.107335	0.078029	0.115021	0.893357	0.913681	0.857677	0.204147	0.109505	0.86911	0.914859	0.107192	0.080827	0.081131	0.934496	0.929037	0.929722	0.172822	0.075832	0.136928	0.864	0.856827
K	0.829619	0.891615	0.849441	0.004972	0.0044	0.004999	0.755078	0.852351	0.008115	0.004394	0.84688	0.895755	0.905062	0.082051	0.003301	0.004413	0.785269	0.898653	0.833318	0.008286	0.005581
P	0	0	0	0	0	0	0	0	0	0	0	0	0	0	0	0	0	0	0	0	0
Cr	0	0	0	0	0	0	0.000362	0	0	0	0	0	0	0	0	0.000342	0	0.000368	0	0	0.000346
Ni	0	0	0	0.000348	0.000693	0	0.000736	0	0.000682	0	0	0	0	0	0	0	0	0.000374	0	0	0.000352
Zn	0	0	0	0	0	0	0	0	0	0	0	0	0	0	0	0	0	0	0	0	0
Ba	0	0	0	0	0	0	0	0	0	0	0	0	0	0	0	0	0	0	0	0	0
Total	4.96382	4.984381	4.981026	4.946385	4.964674	4.919407	4.976948	4.981897	4.928657	4.962275	4.972025	4.988581	4.993307	5.031118	4.971857	4.970533	4.975718	4.990516	4.98328	4.95809	4.969772
An	0.212336	0.153105	0.153027	2.172642	2.165945	2.272373	0.102163	0.353891	2.029804	2.447531	0.412198	0.152221	0.050487	1.843455	2.229073	1.992807	0.258908	0.051167	0.102509	6.746152	9.361321
Ab	11.43139	8.034828	11.90766	97.28594	97.36519	97.16136	21.26076	11.34443	97.06394	97.08622	11.18887	8.263888	8.222558	90.23377	97.42476	97.54424	17.99143	7.777801	14.09821	92.36797	90.05207
Or	88.35627	91.81207	87.93932	0.541413	0.468869	0.566266	78.63708	88.30168	0.906259	0.466246	88.39893	91.58389	91.72696	7.922774	0.346166	0.462954	81.74966	92.17103	85.79928	0.885881	0.586611
	100	100	100	100	100	100	100	100	100	100	100	100	100	100	100	100	100	100	100	100	100
An content	1.823607	1.869888	1.268812	2.184469	2.176148	2.285314	0.478224	3.025148	2.048368	2.458996	2.563106	1.808685	0.610254	2.002075	2.236816	2.002075	1.418648	0.653558	0.721857	6.806449	9.416559

542216CII																	
Point	205 / 1.	206 / 1.	207 / 1.	218 / 1.	219 / 1.	220 / 1.	235 / 1.	236 / 1.	237 / 1.	238 / 1.	245 / 1.	246 / 1.	247 / 1.	261 / 1.	262 / 1.	270 / 1.	271 / 1.
SiO2	64.47	65.07	64.69	64.87	64.9	65.09	64.64	64.75	64.95	65.21	63.81	66.09	65.81	70.18	68.65	67.23	66.46
TiO2	0	0	0.02	0.01	0	0.02	0	0.01	0.01	0.02	0	0.01	0.02	0.01	0	0.01	0.01
Al2O3	21.59	21.65	21.84	21.59	21.88	21.84	21.91	21.93	21.55	21.98	18.19	21.04	21.13	19.9	20.41	21.22	20.92
Fe2O3	0.044452	0.096053	0.066678	0.122243	0.077791	0.11113	0.077791	0.022226	0.055565	0	0	0.066678	0.066678	0	0.005587	0	0.055565
FeO	0	0.003567	0	0	0	0	0	0	0	0.06	0.03	0	0	0.03	0.074973	0.05	0
FeOT	0.04	0.09	0.06	0.11	0.07	0.1	0.07	0.02	0.05	0.06	0.03	0.06	0.06	0.03	0.08	0.05	0.05
MnO	0	0	0.02	0	0	0	0	0	0	0.01	0	0	0	0.01	0	0	0.01
MgO	0	0.01	0	0.01	0	0	0.01	0.01	0	0	0	0	0	0	0	0	0
CaO	3.08	2.94	3.29	2.91	2.89	3.01	3.12	3	2.88	3.13	0.07	2.13	2.34	0.32	1.2	1.96	2.06
Na2O	10.05	10.08	10.03	10.23	10.24	10.36	10.08	10.12	10.2	9.98	0.79	10.63	10.53	11.46	11.21	10.65	10.7
K2O	0.06	0.05	0.07	0.06	0.07	0.08	0.05	0.03	0.05	0.06	15.12	0.07	0.09	0.34	0.24	0.09	0.11
P2O5																	
Cr2O3	0	0	0	0	0	0	0	0	0	0	0	0.02	0.01	0	0	0	0
NiO	0	0	0.01	0	0	0.01	0.01	0	0.01	0.02	0	0	0	0.01	0	0	0
ZnO																	
BaO																	
Total	99.29	99.89	100.03	99.79	100.05	100.51	99.89	99.87	99.7	100.47	98.01	100.05	99.99	102.26	101.79	101.21	100.32
Structural formula per 8 O																	
Si	2.861789	2.868756	2.8531	2.865539	2.85891	2.857465	2.853198	2.856194	2.869634	2.859312	2.997756	2.903509	2.895293	2.998076	2.956577	2.914916	2.911409
Al	1.129516	1.124943	1.135252	1.124022	1.135959	1.130001	1.13981	1.140109	1.122159	1.135886	1.007163	1.089414	1.09562	1.001941	1.03598	1.084346	1.080101
Ti	0	0	0.000663	0.000332	0	0.00066	0	0.000332	0.000332	0.000659	0	0.00033	0.000662	0.000321	0	0.000326	0.000329
Fe2+T	0.001485	0.003318	0.002213	0.004064	0.002579	0.003671	0.002584	0.000738	0.001847	0.0022	0.001179	0.002204	0.002208	0.001072	0.002881	0.001813	0.001832
Mn	0	0	0.000747	0	0	0	0	0	0	0.000371	0	0	0	0.000362	0	0	0.000371
Mg	0	0.000657	0	0.000658	0	0	0.000658	0.000657	0	0	0	0	0	0	0	0	0
Ca	0.146485	0.138874	0.155467	0.137726	0.1364	0.141578	0.147552	0.141785	0.136333	0.147046	0.003523	0.10026	0.110301	0.014647	0.055372	0.09105	0.096688
Na	0.86496	0.861635	0.857691	0.87617	0.874592	0.881813	0.862663	0.865523	0.873771	0.848453	0.071959	0.905463	0.898212	0.949214	0.936061	0.895288	0.908817
K	0.003397	0.002812	0.003938	0.003381	0.003934	0.00448	0.002815	0.001688	0.002818	0.003356	0.906123	0.003923	0.005051	0.018528	0.013185	0.004978	0.006147
P	0	0	0	0	0	0	0	0	0	0	0	0	0	0	0	0	0
Cr	0	0	0	0	0	0	0	0	0	0	0	0.000695	0.000348	0	0	0	0
Ni	0	0	0.000355	0	0	0.000353	0.000355	0	0.000355	0.000705	0	0	0	0.000344	0	0	0
Zn	0	0	0	0	0	0	0	0	0	0	0	0	0	0	0	0	0
Ba	0	0	0	0	0	0	0	0	0	0	0	0	0	0	0	0	0
Total	5.007632	5.000996	5.009426	5.011893	5.012374	5.020021	5.009636	5.007025	5.007249	4.99799	4.987704	5.005799	5.007693	4.984504	5.000057	4.992717	5.005694
An	14.43422	13.84144	15.28534	13.53872	13.43942	13.77387	14.56545	14.05209	13.45938	14.72144	0.358946	9.930225	10.88245	1.49093	5.511755	9.184772	9.557407
Ab	85.231	85.87829	84.32745	86.12893	86.17302	85.79027	85.15664	85.7806	86.26241	84.94257	7.330736	89.68123	88.61922	96.62302	93.17578	90.31309	89.83497
Or	0.334781	0.280266	0.387208	0.332355	0.387568	0.435859	0.277911	0.167305	0.278208	0.335988	92.31032	0.388548	0.498333	1.886049	1.312462	0.502136	0.60762
	100	100	100	100	100	100	100	100	100	100	100	100	100	100	100	100	100
An conten	14.48271	13.88035	15.34476	13.58387	13.49171	13.83417	14.60604	14.07564	13.49693	14.77107	4.667898	9.968959	10.93695	1.51959	5.585057	9.231125	9.615835

Appendix VII: Nepheline EMPA data for sample 542219

542219AII																						
Point	100 / 1.	101 / 1.	102 / 1.	103 / 1.	104 / 1.	112 / 1.	113 / 1.	114 / 1.	132 / 1.	133 / 1.	134 / 1.	5 / 1.	6 / 1.	7 / 1.	8 / 1.	23 / 1.	24 / 1.	25 / 1.	26 / 1.	36 / 1.	37 / 1.	38 / 1.
SiO2	44.13	43.75	43.94	43.79	44.18	43.76	43.33	43.34	43.59	43.34	43.44	43.67	43.75	44.11	43.61	43.6	43.17	43.59	43.03	43.64	43.76	43.58
TiO2	0	0.02	0.01	0	0	0	0	0	0	0.01	0.02	0	0	0	0	0.01	0.01	0.01	0	0.01	0	0.01
Al2O3	34.04	34.47	33.98	34.27	33.89	33.96	33.71	33.76	34.08	34.09	34.16	35.72	34.74	34.65	34.21	33.96	33.14	34.38	33.76	34.66	34.01	33.89
Fe2O3	0.055565	0.077791	0.033339	0.122243	0.100017	0.077791	0.077791	0.100017	0.011113	0.011113	0.011113	0.066678	0.066678	0.033339	0.011113	0.066678	0.100017	0.055565	0.033339	0.088904	0.155582	0.200034
FeO	0	0	0	0	0	0	0	0	0	0	0	0	0	0	0	0	0	0	0	0	0	0
FeOT	0.05	0.07	0.03	0.11	0.09	0.07	0.07	0.09	0.01	0.01	0.01	0.06	0.06	0.03	0.01	0.06	0.09	0.05	0.03	0.08	0.14	0.18
MnO	0.01	0	0	0	0	0.01	0	0	0	0	0	0	0.01	0	0.01	0.01	0.01	0	0	0.02	0	0.01
MgO	0	0	0	0	0	0	0	0.01	0.01	0.01	0	0	0	0.01	0.01	0	0.01	0	0	0	0	0
CaO	0.61	0.72	0.58	0.6	0.6	0.57	0.59	0.57	0.67	0.71	0.67	0.78	0.85	0.83	0.83	0.85	0.83	0.75	0.78	0.66	0.7	0.75
Na2O	16.03	15.97	15.91	15.95	16.03	15.98	16	15.93	15.98	15.79	15.87	15.32	15.86	15.7	15.69	15.85	15.86	15.71	15.86	15.74	15.88	15.75
K2O	5.78	5.87	6.06	5.91	5.89	6.28	6.22	6.34	6.22	6.26	6.31	6.01	6.01	5.9	6.16	6.02	6.15	6.09	6.24	6.14	6.05	6.16
P2O5																						
Cr2O3	0	0	0	0	0.01	0.01	0	0	0	0	0	0	0	0	0.01	0.01	0	0.01	0	0	0.01	0
NiO	0	0	0.01	0.01	0	0	0	0	0.02	0.02	0	0	0	0.02	0	0	0	0	0	0	0	0
ZnO																						
BaO																						
Total	100.65	100.87	100.52	100.64	100.69	100.64	99.92	100.04	100.58	100.24	100.48	101.56	101.28	101.25	100.54	100.37	99.27	100.59	99.7	100.95	100.55	100.33

542219DII																				
Point	205/1	206/1	207/1	208/1	224/1	225/1	226/1	227/1	241/1	242/1	243/1	244/1	267/1	268/1	269/1	270/1	283/1	284/1	285/1	286/1
SiO2	44.27	44.91	43.49	44.35	44.48	44.97	45.41	45.59	44.8	43.94	45.47	44.12	44.52	44.32	43.79	44.31	45.28	43.88	43.46	43.7
TiO2	0.01	0.01	0	0.02	0	0	0	0	0	0	0.02	0	0	0.02	0	0	0.01	0	0	0.01
Al2O3	33.22	33.43	33.28	32.88	33.01	33.47	33.73	33.08	33.58	33.03	33.27	33.18	32.82	32.67	33.24	33.04	33.54	33.64	33.44	33.31
Fe2O3	0.044452	0.11113	0.011113	0.122243	0.11113	0.100017	0.144469	0.11113	0.088904	0.088904	0.088904	0.088904	0.122243	0.166695	0.077791	0.100017	0.088904	0.033339	0.088904	0.055565
FeO	0	0	0	0	0	0	0	0	0	0	0	0	0	0	0	0	0	0	0	0
FeOT	0.04	0.1	0.01	0.11	0.1	0.09	0.13	0.1	0.08	0.08	0.08	0.08	0.11	0.15	0.07	0.09	0.08	0.03	0.08	0.05
MnO	0	0	0	0	0	0	0	0	0	0	0	0	0.02	0	0.01	0	0	0	0	0
MgO	0	0	0.01	0	0	0	0	0	0	0	0	0	0	0	0	0.01	0	0	0	0
CaO	0.66	0.64	0.73	0.67	0.67	0.68	0.68	0.7	0.7	0.66	0.63	0.57	0.7	0.69	0.72	0.71	0.73	0.71	0.69	0.73
Na2O	16.48	16.46	16	16.64	16.52	16.21	16.45	16.23	16.07	16.09	16.26	16.24	16.2	16.4	16.13	16.36	16.19	16.18	16.38	16.06
K2O	5.47	5.4	6.16	5.3	5.32	5.36	5.42	5.65	5.91	5.93	5.62	5.91	5.57	5.45	6.07	5.71	5.78	5.89	5.82	5.95
P2O5																				
Cr2O3	0	0	0	0	0	0	0	0.01	0.01	0.01	0	0.01	0	0.01	0	0	0	0	0.01	0.02
NiO	0.01	0.01	0	0.01	0	0	0.01	0.01	0	0.01	0	0	0	0.01	0	0	0.03	0	0	0
ZnO																				
BaO																				
Total	100.16	100.96	99.68	99.98	100.1	100.78	101.83	101.37	101.15	99.75	101.35	100.11	99.94	99.72	100.03	100.23	101.64	100.33	99.88	99.83

542219CII										
Point	163/1	164/1	165/1	170/1	185/1	186/1	187/1	225/1	226/1	227/1
SiO2	43.9	43.61	43.1	43.37	43.69	43.43	43.74	43.38	43.47	43.09
TiO2	0	0	0.01	0	0	0.01	0	0.02	0	0.02
Al2O3	33.39	33.52	33.66	33.43	33.57	33.43	33.36	33.35	34.05	33.71
Fe2O3	0.122243	0.100017	0.088904	0.11113	0.100017	0.11113	0.11113	0.100017	0.144469	0.100017
FeO	0	0	0	0	0	0	0	0	0	0
FeOT	0.11	0.09	0.08	0.1	0.09	0.1	0.1	0.09	0.13	0.09
MnO	0	0.02	0.01	0	0.01	0	0	0	0	0.01
MgO	0	0	0.01	0.01	0	0	0.02	0	0	0
CaO	0.74	0.73	0.75	0.47	0.65	0.66	0.66	0.62	0.56	0.59
Na2O	15.87	15.87	15.93	15.98	15.83	15.91	16.06	15.81	15.54	15.73
K2O	5.43	5.7	5.88	6.14	5.82	5.89	5.58	6.08	6	6.3
P2O5										
Cr2O3	0	0	0	0	0.01	0	0	0.01	0.01	0
NiO	0	0	0	0	0	0.01	0	0	0.01	0
ZnO										
BaO										
Total	99.44	99.54	99.43	99.5	99.67	99.44	99.52	99.36	99.77	99.54

Appendix VIII: Clinopyroxene EMPA data for sample 542219

542219AII CPX																				
Point	126 / 1 .	127 / 1 .	128 / 1 .	129 / 1 .	130 / 1 .	131 / 1 .	135 / 1 .	136 / 1 .	137 / 1 .	138 / 1 .	139 / 1 .	9 / 1 .	10 / 1 .	11 / 1 .	12 / 1 .	30 / 1 .	31 / 1 .	32 / 1 .	33 / 1 .	34 / 1 .
Mineral	cpx	cpx	cpx	cpx	cpx	cpx	cpx	cpx	cpx	cpx	cpx	cpx	cpx	cpx	cpx	cpx	cpx	cpx	cpx	cpx
SiO2	49.55	49.24	49.91	49.8	49.76	49.76	49.56	49.58	49.59	50.51	48.87	50.01	50.14	50.7	50.37	48.89	48.89	48.64	49.27	48.54
TiO2	1.54	1.55	1.34	1.36	1.38	1.42	1.66	1.62	1.65	1.23	1.62	1.36	1.5	0.93	1.04	1.47	1.63	1.48	1.26	1.2
Al2O3	5.61	5.55	5.26	5.6	5.63	5.46	4.96	4.88	4.98	5.24	5.41	5.07	4.88	5.19	5.16	5.49	5.41	4.94	5.35	5.4
Cr2O3	0	0	0.01	0	0.02	0.01	0	0	0.01	0.01	0	0.02	0.01	0	0	0	0	0	0	0
FeO	12.03	12.36	11.77	11.82	11.98	11.96	12.35	12.5	12.2	11.73	11.99	11.63	12.01	11.87	11.79	12	11.9	12.5	11.85	11.79
MnO	0.24	0.26	0.23	0.21	0.23	0.22	0.24	0.26	0.25	0.22	0.25	0.23	0.23	0.24	0.23	0.22	0.22	0.25	0.21	0.24
NiO	0.02	0	0	0	0	0.03	0	0	0	0	0	0	0	0.01	0.01	0.01	0	0	0.01	0.01
MgO	8.87	8.65	9.09	8.72	8.83	8.96	8.69	8.81	8.94	8.8	8.89	9.17	9.24	8.93	9.01	8.85	8.9	8.8	8.98	8.9
CaO	19.1	19.05	19.33	18.81	18.71	19.06	19.14	19.01	19.12	18.47	19.06	18.96	19.11	18.37	18.7	19.31	19.05	19.29	18.97	19.13
Na2O	3.42	3.3	3.35	3.44	3.53	3.38	3.35	3.35	3.35	3.79	3.39	3.45	3.4	3.84	3.72	3.25	3.37	3.29	3.45	3.36
K2O	0.01	0	0	0	0	0.01	0	0	0	0	0.01	0	0	0.01	0.01	0	0	0	0	0.01
BaO																				
SrO																				
Total reported	100.39	99.96	100.29	99.76	100.07	100.27	99.95	100.01	100.09	100	99.49	99.9	100.52	100.09	100.04	99.49	99.37	99.19	99.35	98.58
Result: cations per formula unit																				
Si	1.8363	1.8372	1.8499	1.8563	1.8478	1.8459	1.8502	1.8496	1.8464	1.8730	1.8275	1.8588	1.8552	1.8759	1.8657	1.8297	1.8303	1.8285	1.8415	1.8288
Ti	0.0429	0.0435	0.0374	0.0381	0.0385	0.0396	0.0466	0.0455	0.0462	0.0343	0.0456	0.0380	0.0417	0.0259	0.0290	0.0414	0.0459	0.0418	0.0354	0.0340
Al	0.2450	0.2440	0.2298	0.2460	0.2464	0.2387	0.2182	0.2146	0.2185	0.2290	0.2384	0.2221	0.2128	0.2263	0.2253	0.2422	0.2387	0.2189	0.2357	0.2398
Cr	0.0000	0.0000	0.0003	0.0000	0.0006	0.0003	0.0000	0.0000	0.0003	0.0003	0.0000	0.0006	0.0003	0.0000	0.0000	0.0000	0.0000	0.0000	0.0000	0.0000
Fe	0.3729	0.3857	0.3648	0.3685	0.3720	0.3710	0.3856	0.3900	0.3799	0.3638	0.3750	0.3615	0.3716	0.3673	0.3652	0.3756	0.3726	0.3930	0.3704	0.3715
Mn	0.0075	0.0082	0.0072	0.0066	0.0072	0.0069	0.0076	0.0082	0.0079	0.0069	0.0079	0.0072	0.0072	0.0075	0.0072	0.0070	0.0070	0.0080	0.0066	0.0077
Ni	0.0006	0.0000	0.0000	0.0000	0.0000	0.0009	0.0000	0.0000	0.0000	0.0000	0.0000	0.0000	0.0000	0.0003	0.0003	0.0003	0.0000	0.0000	0.0003	0.0003
Mg	0.4901	0.4811	0.5023	0.4846	0.4888	0.4955	0.4836	0.4900	0.4962	0.4865	0.4956	0.5081	0.5097	0.4926	0.4975	0.4938	0.4967	0.4932	0.5004	0.4999
Ca	0.7584	0.7616	0.7677	0.7513	0.7444	0.7576	0.7656	0.7599	0.7628	0.7338	0.7637	0.7551	0.7576	0.7283	0.7422	0.7743	0.7642	0.7770	0.7597	0.7722
Na	0.2457	0.2387	0.2407	0.2486	0.2542	0.2431	0.2425	0.2423	0.2418	0.2725	0.2458	0.2486	0.2439	0.2755	0.2672	0.2358	0.2446	0.2398	0.2500	0.2454
K	0.0005	0.0000	0.0000	0.0000	0.0000	0.0005	0.0000	0.0000	0.0000	0.0000	0.0005	0.0000	0.0000	0.0005	0.0005	0.0000	0.0000	0.0000	0.0000	0.0005
Sum of Cations	4.0000	4.0000	4.0000	4.0000	4.0000	4.0000	4.0000	4.0000	4.0000	4.0000	4.0000	4.0000	4.0000	4.0000	4.0000	4.0000	4.0000	4.0000	4.0000	4.0000
Total Charge balance	11.7574	11.7667	11.7638	11.7863	11.7655	11.7664	11.7694	11.7624	11.7622	11.7714	11.7384	11.7676	11.7630	11.7540	11.7470	11.7485	11.7466	11.7197	11.7395	11.7194
Free	0.2426	0.2333	0.2362	0.2137	0.2345	0.2336	0.2306	0.2376	0.2378	0.2286	0.2616	0.2324	0.2370	0.2460	0.2530	0.2515	0.2534	0.2803	0.2605	0.2806
Fe3	0.2426	0.2333	0.2362	0.2137	0.2345	0.2336	0.2306	0.2376	0.2378	0.2286	0.2616	0.2324	0.2370	0.2460	0.2530	0.2515	0.2534	0.2803	0.2605	0.2806
Fe2	0.1302	0.1523	0.1286	0.1548	0.1376	0.1375	0.1550	0.1524	0.1420	0.1351	0.1133	0.1291	0.1346	0.1212	0.1123	0.1241	0.1191	0.1126	0.1099	0.0909
Mg-#T	56.7913	55.5067	57.9249	56.8049	56.7826	57.1818	55.6406	55.6811	56.6398	57.2161	56.9282	58.4292	57.8318	57.2846	57.6679	56.7972	57.1404	55.6530	57.4624	57.3677
Result: components																				
En	0.2450	0.2406	0.2511	0.2423	0.2444	0.2478	0.2418	0.2450	0.2481	0.2432	0.2478	0.2541	0.2548	0.2463	0.2488	0.2469	0.2484	0.2466	0.2502	0.2499
Fs	0.0651	0.0762	0.0643	0.0774	0.0688	0.0687	0.0775	0.0762	0.0710	0.0676	0.0567	0.0646	0.0673	0.0606	0.0561	0.0620	0.0596	0.0563	0.0550	0.0454
Wo	0.3189	0.3211	0.3274	0.3229	0.3154	0.3215	0.3312	0.3275	0.3277	0.3205	0.3184	0.3259	0.3273	0.3150	0.3184	0.3227	0.3202	0.3236	0.3183	0.3175
Tschermak	0.0778	0.0758	0.0751	0.0674	0.0745	0.0746	0.0565	0.0594	0.0609	0.0581	0.0813	0.0646	0.0610	0.0723	0.0763	0.0875	0.0779	0.0879	0.0876	0.1032
Mn-Px	0.0038	0.0041	0.0036	0.0033	0.0036	0.0035	0.0038	0.0041	0.0039	0.0035	0.0040	0.0036	0.0036	0.0038	0.0036	0.0035	0.0035	0.0040	0.0033	0.0038
Ni-Px	0.0003	0.0000	0.0000	0.0000	0.0000	0.0004	0.0000	0.0000	0.0000	0.0000	0.0000	0.0000	0.0000	0.0001	0.0001	0.0002	0.0000	0.0000	0.0002	0.0002
Cr-Ts	0.0000	0.0000	0.0003	0.0000	0.0006	0.0003	0.0000	0.0000	0.0003	0.0003	0.0000	0.0006	0.0003	0.0000	0.0000	0.0000	0.0000	0.0000	0.0000	0.0000
CaTiTs	0.0429	0.0435	0.0374	0.0381	0.0385	0.0396	0.0466	0.0455	0.0462	0.0343	0.0456	0.0380	0.0417	0.0259	0.0290	0.0414	0.0459	0.0418	0.0354	0.0340
Jadeite	0.0031	0.0054	0.0045	0.0349	0.0197	0.0095	0.0119	0.0047	0.0040	0.0438	0.0000	0.0163	0.0069	0.0294	0.0142	0.0000	0.0000	0.0000	0.0000	0.0000
Acmite	0.2426	0.2333	0.2362	0.2137	0.2345	0.2336	0.2306	0.2376	0.2378	0.2286	0.2616	0.2324	0.2370	0.2460	0.2530	0.2515	0.2534	0.2803	0.2605	0.2806
Esseneite	0.0000	0.0000	0.0000	0.0000	0.0000	0.0000	0.0000	0.0000	0.0000	0.0000	0.0000	0.0000	0.0000	0.0000	0.0000	0.0000	0.0000	0.0000	0.0000	0.0000
K-Cpx	0.0005	0.0000	0.0000	0.0000	0.0000	0.0005	0.0000	0.0000	0.0000	0.0000	0.0005	0.0000	0.0000	0.0005	0.0005	0.0000	0.0000	0.0000	0.0000	0.0005
Total	1.0000	1.0000	1.0000	1.0000	1.0000	1.0000	1.0000	1.0000	1.0000	1.0000	1.0158	1.0000	1.0000	1.0000	1.0000	1.0157	1.0088	1.0405	1.0105	1.0352
Triangular Plotting Coordinates																				
En	0.3896	0.3772	0.3906	0.3771	0.3888	0.3883	0.3717	0.3777	0.3836	0.3853	0.3978	0.3941	0.3924	0.3960	0.3991	0.3909	0.3954	0.3936	0.4013	0.4078
Fs	0.1035	0.1194	0.1000	0.1204	0.1094	0.1077	0.1191	0.1175	0.1098	0.1070	0.0910	0.1002	0.1037	0.0975	0.0900	0.0982	0.0948	0.0899	0.0882	0.0741
Wo	0.5069	0.5034	0.5093	0.5025	0.5017	0.5040	0.5091	0.5048	0.5066	0.5077	0.5112	0.5057	0.5039	0.5065	0.5109	0.5109	0.5098	0.5165	0.5106	0.5181
x	0.4122	0.4285	0.4096	0.4292	0.4160	0.4154	0.4315	0.4271	0.4193	0.4167	0.4002	0.4076	0.4106	0.4050	0.3989	0.4084	0.4038	0.4020	0.3966	0.3847
y	0.5069	0.5034	0.5093	0.5025	0.5017	0.5040	0.5091	0.5048	0.5066	0.5077	0.5112	0.5057	0.5039	0.5065	0.5109	0.5109	0.5098	0.5165	0.5106	0.5181
Tschermak	0.0778	0.0758	0.0754	0.0674	0.0751	0.0749	0.0565	0.0594	0.0612	0.0584	0.0813	0.0652	0.0613	0.0723	0.0763	0.0875	0.0779	0.0879	0.0876	0.1032
Tschermak	0.1207	0.1193	0.1128	0.1056	0.1137	0.1145	0.1032	0.1049	0.1074	0.0927	0.1269	0.1032	0.1031	0.0982	0.1053	0.1289	0.1238	0.1297	0.1231	0.1372
Tschermak(%)	12.0727	11.9334	11.2767	10.5552	11.3659	11.4494	10.3159	10.4908	10.7411	9.2731	12.6902	10.3206	10.3087	9.8212	10.5296	12.8913	12.3759	12.9700	12.3069	13.7236

542219CII CPX																			
Point	1/1	157/1	158/1	159/1	168/1	169/1	177/1	178/1	199/1	200/1	201/1	218/1	219/1	220/1	234/1	235/1	236/1	244/1	246/1
Mineral	cpx	cpx	cpx	cpx	cpx	cpx	cpx	cpx	cpx	cpx	cpx	cpx	cpx	cpx	cpx	cpx	cpx	cpx	cpx
SiO2	50.59	49.68	50.91	50.62	50.68	50.81	50.24	50	48.69	49.86	50.25	50.19	50.09	50.15	50.07	49.91	50.24	50.53	50.24
TiO2	0.93	0.75	0.38	0.66	0.5	0.64	0.88	0.92	1.12	1.15	0.96	1.04	1.1	1.18	0.96	1	0.95	0.76	0.83
Al2O3	4.3	4.3	4.91	4.37	4.32	4.45	4.31	4.52	3.88	4.26	4.62	4.13	4.02	4.72	4.23	4.08	3.82	4.48	4.75
Cr2O3	0.01	0	0	0	0	0	0	0.01	0	0	0	0.01	0.01	0	0	0.01	0	0	0
FeO	11.3	11.43	11.25	11.32	11.32	11.19	11.42	11.51	12.41	12.8	11.62	12.15	12.22	11.75	12.08	12.45	12.05	11.65	11.65
MnO	0.26	0.24	0.25	0.22	0.23	0.22	0.26	0.25	0.28	0.27	0.23	0.27	0.27	0.27	0.24	0.26	0.27	0.24	0.26
NiO	0.01	0.01	0.01	0.01	0.01	0.01	0.01	0	0.01	0	0	0.02	0	0	0	0.03	0	0	0
MgO	9.67	9.75	9.49	9.73	9.67	9.68	9.64	9.57	9.61	8.84	9.2	9.39	9.13	9.07	9.25	9.28	9.52	9.38	9.35
CaO	19.63	19.69	19.38	19.54	19.06	19.18	19.54	19.62	19.1	18.91	18.65	19.25	18.89	18.91	19.04	19.03	19.32	19.04	18.99
Na2O	3.05	3.02	3.27	3.1	3.31	3.28	3.1	2.98	3.39	3.25	3.47	3.19	3.32	3.4	3.34	3.2	3.1	3.3	3.28
K2O	0	0	0.01	0	0	0	0	0	0	0	0	0	0	0	0	0	0	0.01	0
BaO																			
SrO																			
Total reported	99.75	98.87	99.86	99.57	99.1	99.46	99.4	99.38	98.49	99.34	99	99.64	99.05	99.45	99.21	99.25	99.27	99.39	99.35
Result: cations per formula unit																			
Si	1.8841	1.8647	1.8877	1.8856	1.8933	1.8918	1.8768	1.8704	1.8357	1.8741	1.8828	1.8752	1.8831	1.8742	1.8762	1.8734	1.8840	1.8868	1.8769
Ti	0.0261	0.0212	0.0106	0.0185	0.0141	0.0179	0.0247	0.0259	0.0318	0.0325	0.0271	0.0292	0.0311	0.0332	0.0271	0.0282	0.0268	0.0213	0.0233
Al	0.1887	0.1902	0.2146	0.1919	0.1902	0.1953	0.1898	0.1993	0.1724	0.1887	0.2040	0.1819	0.1781	0.2079	0.1868	0.1805	0.1688	0.1972	0.2091
Cr	0.0003	0.0000	0.0000	0.0000	0.0000	0.0000	0.0000	0.0003	0.0000	0.0000	0.0000	0.0003	0.0003	0.0000	0.0000	0.0003	0.0000	0.0000	0.0000
Fe	0.3519	0.3588	0.3489	0.3526	0.3537	0.3484	0.3568	0.3601	0.3913	0.4024	0.3641	0.3796	0.3842	0.3672	0.3785	0.3908	0.3779	0.3638	0.3640
Mn	0.0082	0.0076	0.0079	0.0069	0.0073	0.0069	0.0082	0.0079	0.0089	0.0086	0.0073	0.0085	0.0086	0.0085	0.0076	0.0083	0.0086	0.0076	0.0082
Ni	0.0003	0.0003	0.0003	0.0003	0.0003	0.0003	0.0003	0.0000	0.0003	0.0000	0.0000	0.0006	0.0000	0.0000	0.0000	0.0009	0.0000	0.0000	0.0000
Mg	0.5369	0.5456	0.5246	0.5403	0.5385	0.5373	0.5368	0.5337	0.5401	0.4953	0.5139	0.5230	0.5117	0.5053	0.5167	0.5193	0.5322	0.5221	0.5207
Ca	0.7833	0.7919	0.7700	0.7799	0.7629	0.7652	0.7821	0.7864	0.7716	0.7616	0.7487	0.7706	0.7609	0.7572	0.7644	0.7654	0.7763	0.7618	0.7601
Na	0.2202	0.2198	0.2351	0.2239	0.2397	0.2368	0.2245	0.2161	0.2478	0.2368	0.2521	0.2311	0.2420	0.2464	0.2427	0.2329	0.2254	0.2389	0.2376
K	0.0000	0.0000	0.0005	0.0000	0.0000	0.0000	0.0000	0.0000	0.0000	0.0000	0.0000	0.0000	0.0000	0.0000	0.0000	0.0000	0.0000	0.0005	0.0000
Sum of Cations	4.0000	4.0000	4.0000	4.0000	4.0000	4.0000	4.0000	4.0000	4.0000	4.0000	4.0000	4.0000	4.0000	4.0000	4.0000	4.0000	4.0000	4.0000	4.0000
Total Charge balance	11.7890	11.7422	11.7757	11.7762	11.7651	11.7780	11.7682	11.7759	11.6596	11.7651	11.7717	11.7599	11.7648	11.7763	11.7506	11.7512	11.7651	11.7741	11.7720
Free	0.2110	0.2578	0.2243	0.2238	0.2349	0.2220	0.2318	0.2241	0.3404	0.2349	0.2283	0.2401	0.2352	0.2237	0.2494	0.2488	0.2349	0.2259	0.2280
Fe3	0.2110	0.2578	0.2243	0.2238	0.2349	0.2220	0.2318	0.2241	0.3404	0.2349	0.2283	0.2401	0.2352	0.2237	0.2494	0.2488	0.2349	0.2259	0.2280
Fe2	0.1410	0.1010	0.1245	0.1289	0.1188	0.1265	0.1250	0.1360	0.0509	0.1674	0.1358	0.1395	0.1490	0.1436	0.1292	0.1421	0.1430	0.1379	0.1360
Mg-#T	60.4032	60.3267	60.0594	60.5088	60.3609	60.6616	60.0758	59.7122	57.9902	55.1791	58.5294	57.9418	57.1154	57.9127	57.7164	57.0578	58.4773	58.9366	58.8590
Result: components																			
En	0.2684	0.2728	0.2623	0.2702	0.2693	0.2687	0.2684	0.2668	0.2701	0.2477	0.2569	0.2615	0.2558	0.2527	0.2584	0.2596	0.2661	0.2611	0.2604
Fs	0.0705	0.0505	0.0623	0.0644	0.0594	0.0632	0.0625	0.0680	0.0255	0.0837	0.0679	0.0697	0.0745	0.0718	0.0646	0.0710	0.0715	0.0689	0.0680
Wo	0.3467	0.3389	0.3341	0.3420	0.3351	0.3375	0.3418	0.3413	0.3195	0.3341	0.3293	0.3375	0.3376	0.3323	0.3338	0.3335	0.3435	0.3350	0.3302
Tschermak	0.0635	0.0930	0.0911	0.0774	0.0786	0.0723	0.0738	0.0776	0.1007	0.0609	0.0631	0.0661	0.0544	0.0594	0.0697	0.0698	0.0624	0.0705	0.0765
Mn-Px	0.0041	0.0038	0.0039	0.0035	0.0036	0.0035	0.0041	0.0040	0.0045	0.0043	0.0036	0.0043	0.0043	0.0043	0.0038	0.0041	0.0043	0.0038	0.0041
Ni-Px	0.0001	0.0002	0.0001	0.0001	0.0002	0.0001	0.0002	0.0000	0.0002	0.0000	0.0000	0.0003	0.0000	0.0000	0.0000	0.0005	0.0000	0.0000	0.0000
Cr-Ts	0.0003	0.0000	0.0000	0.0000	0.0000	0.0000	0.0000	0.0003	0.0000	0.0000	0.0000	0.0003	0.0003	0.0000	0.0000	0.0003	0.0000	0.0000	0.0000
CaTiTs	0.0261	0.0212	0.0106	0.0185	0.0141	0.0179	0.0247	0.0259	0.0318	0.0325	0.0271	0.0292	0.0311	0.0332	0.0271	0.0282	0.0268	0.0213	0.0233
Jadeite	0.0093	0.0000	0.0107	0.0001	0.0049	0.0148	0.0000	0.0000	0.0000	0.0019	0.0237	0.0000	0.0068	0.0227	0.0000	0.0000	0.0000	0.0130	0.0096
Acmite	0.2110	0.2578	0.2243	0.2238	0.2349	0.2220	0.2318	0.2241	0.3404	0.2349	0.2283	0.2401	0.2352	0.2237	0.2494	0.2488	0.2349	0.2259	0.2280
Esseneite	0.0000	0.0000	0.0000	0.0000	0.0000	0.0000	0.0000	0.0000	0.0000	0.0000	0.0000	0.0000	0.0000	0.0000	0.0000	0.0000	0.0000	0.0000	0.0000
K-Cpx	0.0000	0.0000	0.0005	0.0000	0.0000	0.0000	0.0000	0.0000	0.0000	0.0000	0.0000	0.0000	0.0000	0.0000	0.0000	0.0000	0.0000	0.0005	0.0000
Total	1.0000	1.0380	1.0000	1.0000	1.0000	1.0000	1.0073	1.0079	1.0926	1.0000	1.0000	1.0091	1.0000	1.0000	1.0067	1.0159	1.0096	1.0000	1.0000
Triangular Plotting Coordinates																			
En	0.3915	0.4120	0.3982	0.3993	0.4056	0.4014	0.3990	0.3946	0.4391	0.3722	0.3928	0.3910	0.3831	0.3847	0.3934	0.3909	0.3907	0.3926	0.3954
Fs	0.1028	0.0762	0.0945	0.0952	0.0895	0.0945	0.0929	0.1006	0.0414	0.1258	0.1038	0.1043	0.1116	0.1093	0.0983	0.1069	0.1049	0.1037	0.1032
Wo	0.5057	0.5118	0.5073	0.5055	0.5049	0.5042	0.5081	0.5048	0.5195	0.5020	0.5034	0.5047	0.5054	0.5060	0.5083	0.5021	0.5044	0.5037	0.5014
x	0.4107	0.3835	0.4020	0.4018	0.3948	0.4002	0.4006	0.4076	0.3477	0.4351	0.4105	0.4118	0.4206	0.4183	0.4070	0.4134	0.4124	0.4105	0.4087
y	0.5057	0.5118	0.5073	0.5055	0.5049	0.5042	0.5081	0.5048	0.5195	0.5020	0.5034	0.5047	0.5054	0.5060	0.5083	0.5021	0.5044	0.5037	0.5014
Tschermak	0.0638	0.0930	0.0911	0.0774	0.0786	0.0723	0.0738	0.0779	0.1007	0.0609	0.0631	0.0664	0.0547	0.0594	0.0697	0.0701	0.0624	0.0705	0.0765
Tschermak	0.0899	0.1141	0.1017	0.0959	0.0927	0.0902	0.0985	0.1038	0.1325	0.0934	0.0901	0.0956	0.0858	0.0926	0.0968	0.0983	0.0892	0.0918	0.0998
Tschermak(%)	8.9879	11.4130	10.1678	9.5869	9.2657	9.0228	9.8514	10.3752	13.2488	9.3404	9.0135	9.5605	8.5795	9.2595	9.6770	9.8330	8.9192	9.1849	9.9789

542219DII CPX																				
Point	171/1	173/1	177/1	178/1	187/1	188/1	189/1	190/1	191/1	192/1	197/1	198/1	201/1	202/1	209/1	210/1	211/1	212/1	213/1	214/1
Mineral	cpx	cpx	cpx	cpx	cpx	cpx	cpx	cpx	cpx	cpx	cpx	cpx	cpx	cpx	cpx					
SiO2	50.61	50.47	50.65	50.58	50.29	50.42	50.85	50.91	51	50.3	51.16	50.59	50.99	50.47	50.48	50.56	50.11	51.3	50.78	50.68
TiO2	0.53	0.54	0.37	0.44	1.09	1	0.93	0.56	0.62	1	0.48	0.59	0.51	0.63	0.94	0.88	1.08	0.82	0.98	0.9
Al2O3	4.48	4.66	4.73	4.93	4.08	4.23	3.68	4.31	4.32	4.09	4.56	4.77	4.99	4.9	4.55	4.21	4.08	3.56	4.09	4.64
Cr2O3	0.01	0.01	0	0.01	0.01	0	0	0	0	0	0	0	0.03	0	0.01	0.02	0	0.01	0	0.01
FeO	11.39	11.52	11.38	11.38	12.13	11.63	11.37	11.22	10.91	11.2	11.45	11.48	11.27	11.44	11.63	11.8	11.93	9.79	11.37	11.88
MnO	0.23	0.23	0.24	0.25	0.27	0.24	0.25	0.24	0.24	0.24	0.23	0.23	0.23	0.25	0.24	0.27	0.23	0.17	0.24	0.24
NiO	0.01	0	0	0	0	0	0.01	0	0.02	0	0	0	0.01	0	0	0	0	0.01	0	0
MgO	9.78	9.52	9.59	9.55	9.43	9.48	9.98	9.8	10.12	9.89	9.46	9.51	9.46	9.46	9.33	9.55	9.48	10.84	9.79	9.58
CaO	19.31	19.25	19.46	19.26	19.4	19.43	19.73	19.57	19.64	19.87	19	19.28	18.83	19.23	19.32	19.53	19.39	20.37	19.49	19.24
Na2O	3.28	3.19	3.1	3.2	3.18	3.19	2.96	3.22	3.14	3.01	3.61	3.27	3.58	3.28	3.26	3.18	3.12	2.7	3.12	3.24
K2O	0	0	0	0	0	0	0.01	0.01	0.01	0	0	0.01	0	0	0	0	0.01	0	0	0
BaO																				
SrO																				
Total reported	99.63	99.39	99.52	99.6	99.88	99.62	99.77	99.84	100.02	99.6	99.95	99.73	99.9	99.66	99.76	100	99.43	99.57	99.86	100.41
Result: cations per formula unit																				
Si	1.8805	1.8831	1.8867	1.8814	1.8746	1.8809	1.8941	1.8885	1.8866	1.8749	1.8926	1.8800	1.8863	1.8768	1.8798	1.8791	1.8755	1.9056	1.8881	1.8744
Ti	0.0148	0.0152	0.0104	0.0123	0.0306	0.0281	0.0261	0.0156	0.0173	0.0280	0.0134	0.0165	0.0142	0.0176	0.0263	0.0246	0.0304	0.0229	0.0274	0.0250
Al	0.1962	0.2049	0.2077	0.2161	0.1792	0.1860	0.1616	0.1884	0.1883	0.1797	0.1988	0.2089	0.2176	0.2148	0.1997	0.1844	0.1800	0.1559	0.1792	0.2023
Cr	0.0003	0.0003	0.0000	0.0003	0.0003	0.0000	0.0000	0.0000	0.0000	0.0000	0.0000	0.0000	0.0009	0.0000	0.0003	0.0006	0.0000	0.0003	0.0000	0.0003
Fe	0.3539	0.3595	0.3545	0.3540	0.3781	0.3628	0.3542	0.3481	0.3375	0.3491	0.3542	0.3568	0.3487	0.3558	0.3622	0.3668	0.3734	0.3041	0.3536	0.3675
Mn	0.0072	0.0073	0.0076	0.0079	0.0085	0.0076	0.0079	0.0075	0.0075	0.0076	0.0072	0.0072	0.0072	0.0079	0.0076	0.0085	0.0073	0.0053	0.0076	0.0075
Ni	0.0003	0.0000	0.0000	0.0000	0.0000	0.0000	0.0003	0.0000	0.0006	0.0000	0.0000	0.0000	0.0003	0.0000	0.0000	0.0000	0.0000	0.0003	0.0000	0.0000
Mg	0.5417	0.5295	0.5326	0.5296	0.5240	0.5272	0.5542	0.5419	0.5581	0.5496	0.5217	0.5268	0.5217	0.5244	0.5179	0.5291	0.5289	0.6003	0.5427	0.5282
Ca	0.7688	0.7696	0.7767	0.7676	0.7748	0.7766	0.7874	0.7778	0.7784	0.7936	0.7531	0.7677	0.7464	0.7662	0.7709	0.7777	0.7776	0.8108	0.7765	0.7625
Na	0.2363	0.2308	0.2239	0.2308	0.2298	0.2307	0.2138	0.2316	0.2252	0.2175	0.2589	0.2356	0.2568	0.2365	0.2354	0.2292	0.2264	0.1945	0.2249	0.2323
K	0.0000	0.0000	0.0000	0.0000	0.0000	0.0000	0.0005	0.0005	0.0005	0.0000	0.0000	0.0005	0.0000	0.0000	0.0000	0.0000	0.0005	0.0000	0.0000	0.0000
Sum of Cations	4.0000	4.0000	4.0000	4.0000	4.0000	4.0000	4.0000	4.0000	4.0000	4.0000	4.0000	4.0000	4.0000	4.0000	4.0000	4.0000	4.0000	4.0000	4.0000	4.0000
Total Charge balance	11.7507	11.7709	11.7780	11.7731	11.7600	11.7733	11.7877	11.7646	11.7703	11.7680	11.7518	11.7658	11.7627	11.7672	11.7768	11.7633	11.7649	11.8188	11.7854	11.7691
Free	0.2493	0.2291	0.2220	0.2269	0.2400	0.2267	0.2123	0.2354	0.2297	0.2320	0.2482	0.2342	0.2373	0.2328	0.2232	0.2367	0.2351	0.1812	0.2146	0.2309
Fe3	0.2493	0.2291	0.2220	0.2269	0.2400	0.2267	0.2123	0.2354	0.2297	0.2320	0.2482	0.2342	0.2373	0.2328	0.2232	0.2367	0.2351	0.1812	0.2146	0.2309
Fe2	0.1047	0.1303	0.1325	0.1271	0.1381	0.1361	0.1419	0.1127	0.1078	0.1172	0.1061	0.1226	0.1114	0.1229	0.1390	0.1301	0.1383	0.1229	0.1390	0.1366
Mg-#T	60.4840	59.5652	60.0352	59.9349	58.0855	59.2345	61.0086	60.8915	62.3141	61.1514	59.5597	59.6236	59.9408	59.5807	58.8488	59.0616	58.6181	66.3728	60.5504	58.9740
Result: components																				
En	0.2709	0.2648	0.2663	0.2648	0.2620	0.2636	0.2771	0.2710	0.2790	0.2748	0.2609	0.2634	0.2609	0.2622	0.2590	0.2646	0.2645	0.3001	0.2713	0.2641
Fs	0.0523	0.0652	0.0662	0.0636	0.0691	0.0680	0.0709	0.0563	0.0539	0.0586	0.0530	0.0613	0.0557	0.0615	0.0695	0.0650	0.0692	0.0615	0.0695	0.0683
Wo	0.3320	0.3339	0.3369	0.3307	0.3400	0.3428	0.3538	0.3410	0.3411	0.3483	0.3295	0.3321	0.3234	0.3303	0.3385	0.3407	0.3417	0.3697	0.3460	0.3310
Tschermak	0.0896	0.0863	0.0925	0.0937	0.0640	0.0629	0.0538	0.0802	0.0789	0.0690	0.0807	0.0870	0.0844	0.0879	0.0673	0.0711	0.0637	0.0482	0.0570	0.0752
Mn-Px	0.0036	0.0036	0.0038	0.0039	0.0043	0.0038	0.0039	0.0038	0.0038	0.0038	0.0036	0.0036	0.0036	0.0039	0.0038	0.0042	0.0036	0.0027	0.0038	0.0038
Ni-Px	0.0001	0.0000	0.0000	0.0000	0.0000	0.0000	0.0001	0.0000	0.0003	0.0000	0.0000	0.0000	0.0001	0.0000	0.0000	0.0000	0.0000	0.0001	0.0000	0.0000
Cr-Ts	0.0003	0.0003	0.0000	0.0003	0.0003	0.0000	0.0000	0.0000	0.0000	0.0000	0.0000	0.0000	0.0009	0.0000	0.0003	0.0006	0.0000	0.0003	0.0000	0.0003
CaTiTs	0.0148	0.0152	0.0104	0.0123	0.0306	0.0281	0.0261	0.0156	0.0173	0.0280	0.0134	0.0165	0.0142	0.0176	0.0263	0.0246	0.0304	0.0229	0.0274	0.0250
Jadeite	0.0000	0.0017	0.0019	0.0039	0.0000	0.0040	0.0014	0.0000	0.0000	0.0000	0.0108	0.0014	0.0195	0.0037	0.0122	0.0000	0.0000	0.0133	0.0104	0.0015
Acmite	0.2493	0.2291	0.2220	0.2269	0.2400	0.2267	0.2123	0.2354	0.2297	0.2320	0.2482	0.2342	0.2373	0.2328	0.2232	0.2367	0.2351	0.1812	0.2146	0.2309
Esseneite	0.0000	0.0000	0.0000	0.0000	0.0000	0.0000	0.0000	0.0000	0.0000	0.0000	0.0000	0.0000	0.0000	0.0000	0.0000	0.0000	0.0000	0.0000	0.0000	0.0000
K-Cpx	0.0000	0.0000	0.0000	0.0000	0.0000	0.0000	0.0005	0.0005	0.0005	0.0000	0.0000	0.0005	0.0000	0.0000	0.0000	0.0000	0.0005	0.0000	0.0000	0.0000
Total	1.0130	1.0000	1.0000	1.0000	1.0102	1.0000	1.0000	1.0038	1.0045	1.0144	1.0000	1.0000	1.0000	1.0000	1.0000	1.0076	1.0087	1.0000	1.0000	1.0000
Triangular Plotting Coordinates																				
En	0.4134	0.3988	0.3978	0.4018	0.3904	0.3908	0.3948	0.4055	0.4139	0.4031	0.4054	0.4011	0.4076	0.4009	0.3883	0.3947	0.3916	0.4104	0.3950	0.3981
Fs	0.0799	0.0982	0.0990	0.0964	0.1029	0.1009	0.1011	0.0843	0.0800	0.0859	0.0824	0.0933	0.0870	0.0940	0.1042	0.0970	0.1024	0.0841	0.1012	0.1030
Wo	0.5067	0.5030	0.5033	0.5018	0.5066	0.5083	0.5041	0.5102	0.5061	0.5109	0.5122	0.5056	0.5054	0.5051	0.5075	0.5083	0.5060	0.5055	0.5038	0.4989
x	0.3848	0.4038	0.4048	0.4011	0.4113	0.4099	0.4078	0.3919	0.3845	0.3942	0.3909	0.3997	0.3923	0.4001	0.4133	0.4055	0.4104	0.3889	0.4077	0.4069
y	0.5067	0.5030	0.5033	0.5018	0.5066	0.5083	0.5041	0.5102	0.5061	0.5109	0.5122	0.5056	0.5054	0.5051	0.5075	0.5083	0.5060	0.5055	0.5038	0.4989
Tschermak	0.0899	0.0866	0.0925	0.0940	0.0643	0.0629	0.0538	0.0802	0.0789	0.0690	0.0807	0.0870	0.0853	0.0879	0.0676	0.0717	0.0637	0.0485	0.0570	0.0755
Tschermak	0.1047	0.1018	0.1029	0.1063	0.0949	0.0910	0.0798	0.0959	0.0962	0.0971	0.0940	0.1035	0.0995	0.1055	0.0939	0.0963	0.0941	0.0714	0.0844	0.1005
Tschermak(%)	10.4718	10.1776	10.2892	10.6266	9.4856	9.0999	7.9820	9.5871	9.6167	9.7056	9.4028	10.3519	9.9487	10.5546	9.3896	9.6275	9.4097	7.1448	8.4440	10.0535

Appendix IX: Anti-perthite EMPA data for sample 542219

	542219AII																			
Point	105 / 1.	106 / 1.	107 / 1.	109 / 1.	110 / 1.	111 / 1.	116 / 1.	117 / 1.	118 / 1.	119 / 1.	120 / 1.	121 / 1.	140 / 1.	141 / 1.	142 / 1.	1 / 1.	2 / 1.	3 / 1.	4 / 1.	15 / 1.
SiO2	64.98	65.28	65.8	64.64	66.01	65.94	64.34	66.13	66.13	65.1	64.78	65.07	65.05	64.85	66.37	64.83	64.75	66.49	66.98	64.06
TiO2	0.01	0.03	0.02	0.01	0.02	0.01	0.02	0.03	0.01	0.01	0	0.01	0.03	0.04	0.01	0.02	0.02	0.02	0.03	0.02
Al2O3	22.55	22.44	22.67	18.83	22.27	21.99	18.61	21.52	21.73	22.22	22.6	22.44	18.98	18.8	22.1	19.01	18.87	22.19	21.38	18.76
Fe2O3	0	0	0	0	0	0	0	0	0	0	0	0	#DIV/0!	0	0	0	0	0	0	0
FeO	0.03	0.03	0.04	0.03	0.04	0.07	0.05	0.04	0.03	0.02	0.01	0.02	#DIV/0!	0.03	0.04	0.01	0.02	0.06	0.04	0.04
FeOT	0.03	0.03	0.04	0.03	0.04	0.07	0.05	0.04	0.03	0.02	0.01	0.02	0	0.03	0.04	0.01	0.02	0.06	0.04	0.04
MnO	0	0	0	0.01	0	0.02	0	0.02	0	0	0.01	0.02	0	0.01	0	0	0.01	0	0	0
MgO	0	0	0.01	0	0.01	0	0.01	0	0	0.01	0	0.01	0	0	0.02	0.01	0	0	0	0.01
CaO	3.03	2.99	2.63	0.02	2.39	2.34	0	2.2	2.37	2.89	3.38	3.15	0.04	0.03	2.38	0.03	0.04	2.36	1.66	0.04
Na2O	9.59	9.57	9.53	1.83	9.67	9.6	1.36	10.44	10.07	9.67	9.67	9.68	1.48	1.72	9.98	1.45	1.8	9	9.66	1.49
K2O	0.07	0.12	0.15	13.59	0.08	0.07	14.18	0.05	0.15	0.16	0.06	0.05	14.08	13.75	0.05	13.89	13.6	0.05	0.27	13.86
P2O5																				
Cr2O3	0	0	0.01	0	0.01	0	0	0	0.01	0	0.01	0	0	0	0	0	0	0	0.01	0
NiO	0.01	0	0.01	0	0	0	0	0.01	0.01	0	0.01	0	0.02	0	0	0	0	0	0	0
ZnO																				
BaO																				
Total	100.27	100.46	100.87	98.96	100.5	100.04	98.57	100.44	100.51	100.08	100.53	100.45	99.68	99.23	100.95	99.25	99.11	100.17	100.03	98.28
Structural formula per 8 O																				
Si	2.849037	2.855973	2.861985	2.987732	2.878338	2.887286	2.992043	2.892223	2.888828	2.85994	2.838352	2.849796	2.987824	2.990213	2.883378	2.987252	2.987705	2.897566	2.92548	2.984893
Al	1.165265	1.157062	1.162125	1.025771	1.14449	1.134817	1.019983	1.109265	1.118775	1.150482	1.167061	1.158285	1.027457	1.021668	1.131571	1.032375	1.026194	1.139709	1.100574	1.03023
Ti	0.00033	0.000987	0.000654	0.000348	0.000656	0.000329	0.000699	0.000987	0.000329	0.00033	0	0.000329	0.001036	0.001387	0.000327	0.000693	0.000694	0.000655	0.000985	0.000701
Fe2+T	0.0011	0.001098	0.001455	0.00116	0.001459	0.002563	0.001945	0.001463	0.001096	0.000735	0.000366	0.000733	0	0.001157	0.001453	0.000385	0.000772	0.002187	0.001461	0.001559
Mn	0	0	0	0.000391	0	0.000742	0	0.000741	0	0	0.000371	0.000742	0	0.000391	0	0	0.000391	0	0	0
Mg	0	0	0.000648	0	0.00065	0	0.000693	0	0	0.000655	0	0.000653	0	0	0.001295	0.000687	0	0	0	0.000695
Ca	0.142338	0.140154	0.122563	0.00099	0.111658	0.109779	0	0.10309	0.110926	0.13603	0.158673	0.14781	0.001968	0.001482	0.110782	0.001481	0.001978	0.110192	0.077682	0.001997
Na	0.815243	0.811775	0.803682	0.163999	0.817539	0.815009	0.122624	0.885286	0.852909	0.823668	0.821489	0.821975	0.131801	0.15377	0.84064	0.129543	0.161035	0.760448	0.818049	0.13461
K	0.003915	0.006697	0.008323	0.801286	0.00445	0.00391	0.841184	0.00279	0.008359	0.008967	0.003354	0.002793	0.824971	0.808766	0.002771	0.816444	0.800507	0.00278	0.015043	0.823822
P	0	0	0	0	0	0	0	0	0	0	0	0	0	0	0	0	0	0	0	0
Cr	0	0	0.000344	0	0.000345	0	0	0	0.000345	0	0.000346	0	0	0	0	0	0	0	0.000345	0
Ni	0.000353	0	0.00035	0	0	0	0	0.000352	0.000351	0	0.000352	0	0.000739	0	0	0	0	0	0	0
Zn	0	0	0	0	0	0	0	0	0	0	0	0	0	0	0	0	0	0	0	0
Ba	0	0	0	0	0	0	0	0	0	0	0	0	0	0	0	0	0	0	0	0
Total	4.97758	4.973746	4.962129	4.981678	4.959584	4.954435	4.979171	4.996196	4.981917	4.980806	4.990365	4.983116	4.975797	4.978834	4.972216	4.96886	4.979275	4.913537	4.939621	4.978507
An	14.80385	14.62032	13.11438	0.102502	11.95937	11.82072	0	10.4009	11.40985	14.04305	16.13325	15.19778	0.205318	0.153741	11.60998	0.15632	0.205239	12.61616	8.529246	0.207921
Ab	84.78896	84.68107	85.99509	16.97228	87.56402	87.75827	12.72287	89.31766	87.73036	85.03129	83.52577	84.515	13.74734	15.95092	88.09962	13.67255	16.71322	87.0656	89.81905	14.01564
Or	0.40719	0.698608	0.890533	82.92522	0.476614	0.42101	87.27713	0.281439	0.859785	0.925657	0.340976	0.287215	86.04735	83.89534	0.290397	86.17113	83.08154	0.318238	1.651707	85.77644
	100	100	100	100	100	100	100	100	100	100	100	100	100	100	100	100	100	100	100	100
An conten	14.86437	14.72318	13.23222	0.600309	12.01664	11.8707	0	10.43025	11.5088	14.17425	16.18845	15.24156	1.471537	0.954637	11.6438	1.130387	1.213104	12.65644	8.67249	1.461805

Point	16 / 1.	17 / 1.	18 / 1.	19 / 1.	20 / 1.	21 / 1.	22 / 1.	27 / 1.	28 / 1.	29 / 1.	39 / 1.	41 / 1.	51 / 1.	52 / 1.	54 / 1.	55 / 1.	56 / 1.	57 / 1.	74 / 1.	75 / 1.	76 / 1.
SiO2	64.36	66.33	66.26	65.37	64.98	65.01	64.8	64.61	64.55	64.84	64.69	65.11	65.67	65.5	65.2	65.33	64.7	65.19	64.17	66.23	65.82
TiO2	0.02	0.01	0.01	0.01	0.02	0.01	0.01	0	0.03	0.01	0.02	0	0.02	0.02	0.02	0.02	0.01	0	0.01	0.03	0.02
Al2O3	18.81	21.91	21.66	21.99	22.44	22.3	22.17	22.27	22.15	22.29	22.45	22.59	21.13	20.95	22.09	22.33	22.16	21.93	18.66	21.28	21.43
Fe2O3	0	0	0	0	0	0	0	0	0	0	0	#DIV/0!	0	0	0	0	0.014089	0	0	0	0
FeO	0.09	0.07	0.1	0.13	0.04	0.1	0.09	0.08	0.09	0.07	0.04	#DIV/0!	0.04	0.02	0.03	0.05	0.107322	0.05	0.05	0.07	0.04
FeOT	0.09	0.07	0.1	0.13	0.04	0.1	0.09	0.08	0.09	0.07	0.04	0	0.04	0.02	0.03	0.05	0.12	0.05	0.05	0.07	0.04
MnO	0.01	0	0	0	0	0	0.01	0	0	0	0	0	0	0	0	0.01	0.01	0.01	0	0	0.01
MgO	0	0	0.01	0	0.01	0	0	0	0.01	0.01	0	0	0	0	0	0	0	0	0	0.01	0
CaO	0.01	2.38	2.29	2.94	3.25	3.19	3.02	3.07	3.06	2.99	3.27	3.22	1.93	1.64	2.76	3.02	3.21	2.81	0.03	1.87	2.23
Na2O	1.53	9.81	9.94	9.83	9.77	9.78	9.8	9.53	9.64	9.4	9.5	9.15	8.14	7.06	9.4	9.66	9.81	9.65	1.07	9.24	9.77
K2O	13.89	0.06	0.09	0.18	0.07	0.12	0.15	0.22	0.14	0.22	0.22	0.17	2.21	4.46	0.09	0.12	0.16	0.12	14.82	1.41	0.25
P2O5																					
Cr2O3	0	0	0	0	0.01	0	0	0	0	0.01	0.02	0	0	0.01	0	0	0.01	0	0.02	0	0
NiO	0.02	0	0	0.01	0	0	0.01	0	0	0.01	0.01	0	0	0	0	0	0	0	0.01	0.02	0
ZnO																					
BaO																					
Total	98.74	100.57	100.36	100.46	100.59	100.51	100.06	99.78	99.67	99.85	100.22	100.24	99.14	99.66	99.59	100.54	100.19	99.76	98.84	100.16	99.57
Structural formula per 8 O																					
Si	2.985558	2.89073	2.895459	2.86488	2.845016	2.849477	2.852546	2.85056	2.851355	2.855588	2.843242	2.852808	2.916603	2.918543	2.871698	2.857612	2.84766	2.871141	2.985709	2.910002	2.899278
Al	1.02839	1.125381	1.115537	1.135829	1.157944	1.151992	1.150225	1.158005	1.153157	1.15697	1.162928	1.166543	1.106037	1.100192	1.146691	1.151169	1.149511	1.13834	1.023262	1.10197	1.112535
Ti	0.000698	0.000328	0.000329	0.00033	0.000659	0.00033	0.000331	0	0.000997	0.000331	0.000661	0	0.000668	0.00067	0.000662	0.000658	0.000331	0	0.00035	0.000991	0.000663
Fe2+T	0.003491	0.002551	0.003654	0.004765	0.001465	0.003666	0.003313	0.002952	0.003325	0.002578	0.00147	0	0.001486	0.000745	0.001105	0.001829	0.004417	0.001842	0.001946	0.002572	0.001474
Mn	0.000393	0	0	0	0	0	0.000373	0	0	0	0	0	0	0	0	0.00037	0.000373	0.000373	0	0	0.000373
Mg	0	0	0.000651	0	0.000653	0	0	0	0.000658	0.000656	0	0	0	0	0	0	0	0	0	0.000655	0
Ca	0.000497	0.111131	0.107217	0.13805	0.152458	0.149809	0.142438	0.145121	0.144823	0.141086	0.153988	0.151162	0.091839	0.078294	0.130245	0.141533	0.151374	0.132599	0.001496	0.088032	0.105244
Na	0.13761	0.828927	0.842175	0.835279	0.829372	0.831139	0.836438	0.815217	0.825624	0.802658	0.809562	0.777313	0.700946	0.609929	0.802729	0.819253	0.837149	0.824045	0.096527	0.787156	0.834404
K	0.821939	0.003336	0.005017	0.010063	0.00391	0.00671	0.008423	0.012382	0.007889	0.01236	0.012335	0.009502	0.125208	0.253506	0.005057	0.006696	0.008983	0.006742	0.879613	0.079029	0.014048
P	0	0	0	0	0	0	0	0	0	0	0	0	0	0	0	0	0	0	0	0	0
Cr	0	0	0	0	0.000346	0	0	0	0	0.000348	0.000695	0	0	0.000352	0	0	0.000348	0	0.000736	0	0
Ni	0.000746	0	0	0.000352	0	0	0.000354	0	0	0.000354	0.000353	0	0	0	0	0	0	0	0.000374	0.000707	0
Zn	0	0	0	0	0	0	0	0	0	0	0	0	0	0	0	0	0	0	0	0	0
Ba	0	0	0	0	0	0	0	0	0	0	0	0	0	0	0	0	0	0	0	0	0
Total	4.979324	4.962384	4.97004	4.989547	4.991822	4.993122	4.994441	4.984237	4.987827	4.97293	4.985234	4.957328	4.942787	4.962232	4.958187	4.97912	5.000146	4.975082	4.990012	4.971114	4.968018
An	0.05177	11.77992	11.23384	14.03815	15.46633	15.16808	14.42703	14.91909	14.80301	14.75638	15.77928	16.11573	10.00436	8.313881	13.88495	14.62905	15.17521	13.76388	0.152975	9.225596	11.0354
Ab	14.33371	87.8665	88.2405	84.93855	84.13705	84.15258	84.71981	83.80802	84.39064	83.95091	82.95677	82.87127	76.35637	64.76695	85.57598	84.67887	83.92423	85.53631	9.873524	82.49234	87.49164
Or	85.61452	0.353577	0.525657	1.023297	0.396615	0.679341	0.853155	1.272897	0.806349	1.292701	1.263947	1.013001	13.63927	26.91917	0.539069	0.692081	0.900568	0.699814	89.9735	8.282067	1.472957
	100	100	100	100	100	100	100	100	100	100	100	100	100	100	100	100	100	100	100	100	100
An conten	0.359877	11.82172	11.2932	14.18329	15.52792	15.27182	14.55118	15.11144	14.92334	14.94964	15.98128	16.28065	11.58439	11.37628	13.96021	14.731	15.31311	13.86088	1.525708	10.05866	11.20038

542219CII																
Point	206/1	207/1	208/1	209/1	214/1	215/1	216/1	217/1	228/1	229/1	230/1	231/1	240/1	241/1	242/1	243/1
SiO2	64.11	64.33	65.79	66.02	64.32	64.27	65.74	65.44	63.95	63.77	65.72	65.33	64.04	64.26	65.84	65.19
TiO2	0.02	0.03	0.02	0.03	0.02	0.02	0	0	0.01	0.02	0.01	0	0.02	0.03	0.02	0.01
Al2O3	18.39	18.57	21	21.01	18.5	18.41	21.19	21.19	18.41	18.35	21.37	21.28	18.51	18.44	21.6	21.35
Fe2O3	0	0	0	0	0	0	0	0	0	0	0	0	0	0.044452	0	0
FeO	0.03	0.03	0.05	0.07	0.05	0.03	0.07	0.08	0.03	0.04	0.04	0.06	0.03	0	0.08	0.05
FeOT	0.03	0.03	0.05	0.07	0.05	0.03	0.07	0.08	0.03	0.04	0.04	0.06	0.03	0.04	0.08	0.05
MnO	0	0	0.01	0.01	0	0	0	0	0.01	0.01	0	0.01	0	0	0	0.01
MgO	0	0	0	0	0.01	0	0.01	0.01	0	0	0	0	0	0.01	0.01	0
CaO	0.02	0.03	2.1	1.94	0.03	0.02	2.18	2.13	0.08	0.02	2.22	2.2	0.04	0.06	2.39	2.38
Na2O	1.33	1.54	10.44	10.4	1.27	1.25	10.43	10.06	0.88	1.06	10.26	10.05	1.55	2.32	10.01	10.24
K2O	14.64	14.18	0.07	0.16	14.51	14.75	0.05	0.17	14.72	14.8	0.14	0.17	13.99	13.21	0.11	0.09
P2O5																
Cr2O3	0	0	0	0.01	0	0	0	0	0	0	0.02	0	0	0	0	0
NiO	0	0	0.01	0.01	0.02	0	0	0	0.01	0.01	0	0.01	0	0.03	0	0
ZnO																
BaO																
Total	98.54	98.71	99.49	99.66	98.73	98.75	99.67	99.08	98.1	98.08	99.78	99.11	98.18	98.4	100.06	99.32
Structural formula per 8 O																
Si	2.991691	2.989851	2.904487	2.908726	2.992209	2.993082	2.897735	2.899325	2.994778	2.991276	2.893466	2.894624	2.990304	2.989252	2.889099	2.885729
Al	1.011422	1.017203	1.092669	1.09097	1.014325	1.010471	1.100828	1.106482	1.016103	1.014462	1.108881	1.111247	1.018662	1.010979	1.117085	1.113864
Ti	0.000702	0.001049	0.000664	0.000994	0.0007	0.0007	0	0	0.000352	0.000705	0.000331	0	0.000702	0.001049	0.00066	0.000333
Fe2+T	0.001171	0.001166	0.001846	0.002579	0.001945	0.001168	0.00258	0.002964	0.001175	0.001569	0.001473	0.002223	0.001172	0.001556	0.002936	0.001851
Mn	0	0	0.000374	0.000373	0	0	0	0	0.000397	0.000397	0	0.000375	0	0	0	0.000375
Mg	0	0	0	0	0.000693	0	0.000657	0.00066	0	0	0	0	0	0.000693	0.000654	0
Ca	0.001	0.001494	0.099332	0.091578	0.001495	0.000998	0.102955	0.10111	0.004014	0.001005	0.104721	0.104439	0.002001	0.00299	0.112365	0.112879
Na	0.120335	0.138774	0.893635	0.888404	0.114551	0.112868	0.891381	0.864175	0.079902	0.096404	0.875827	0.863367	0.140328	0.209247	0.851641	0.87887
K	0.871485	0.840699	0.003942	0.008992	0.861076	0.876255	0.002811	0.009608	0.879346	0.885584	0.007863	0.009609	0.833316	0.783885	0.006157	0.005082
P	0	0	0	0	0	0	0	0	0	0	0	0	0	0	0	0
Cr	0	0	0	0.000348	0	0	0	0	0	0	0.000696	0	0	0	0	0
Ni	0	0	0.000355	0.000354	0.000748	0	0	0	0.000377	0.000377	0	0.000356	0	0.001122	0	0
Zn	0	0	0	0	0	0	0	0	0	0	0	0	0	0	0	0
Ba	0	0	0	0	0	0	0	0	0	0	0	0	0	0	0	0
Total	4.997806	4.990235	4.997303	4.993319	4.987743	4.995543	4.998947	4.984325	4.976443	4.991781	4.993259	4.986241	4.986485	5.000776	4.980598	4.998982
An	0.100719	0.152288	9.964018	9.259876	0.153031	0.100789	10.32494	10.3714	0.416707	0.102254	10.59492	10.68524	0.205113	0.300207	11.58208	11.32378
Ab	12.12054	14.14662	89.64054	89.83086	11.72332	11.39941	89.39311	88.64306	8.294922	9.807207	88.60959	88.3317	14.38314	21.00616	87.78325	88.1664
Or	87.77874	85.70109	0.395439	0.909264	88.12364	88.4998	0.281947	0.985539	91.28837	90.09054	0.795499	0.983054	85.41175	78.69363	0.63467	0.509828
	100	100	100	100	100	100	100	100	100	100	100	100	100	100	100	100
An conter	0.82413	1.065029	10.00358	9.344845	1.288535	0.876412	10.35413	10.47464	4.783342	1.031883	10.67987	10.79133	1.406015	1.409002	11.65606	11.3818

542219DII																				
DataSet	179/1	180/1	181/1	194/1	195/1	196/1	219/1	220/1	221/1	222/1	223/1	236/1	237/1	238/1	239/1	240/1	248/1	249/1	250/1	258/1
SiO2	65.32	65.45	64.93	64.4	65.6	64.97	64.79	65.28	65.46	65.28	65.61	65.18	65.06	66.07	65.3	64.8	66.21	66.13	70.36	64
TiO2	0.01	0.01	0	0.02	0.01	0.02	0	0.02	0	0.02	0.01	0	0	0	0	0.01	0	0	0	0.01
Al2O3	21.19	21.67	21.03	21.74	21.64	21.59	21.41	21.49	21.06	21.26	21.07	21.43	21.83	21.81	21.34	21.78	20.94	20.91	20.55	18.08
Fe2O3	0.044452	0.017014	0.055565	0.077791	0.166695	0.11113	0.033339	0.044452	0.088904	0.088904	0.077791	0.088904	0.077791	0	0.066678	0.077791	0.066678	0.066678	0	0
FeO	0	0.05469	0	0	0	0	0	0	0	0	0	0	0	0.08	0	0	0	0	0.06	0.05
FeOT	0.04	0.07	0.05	0.07	0.15	0.1	0.03	0.04	0.08	0.08	0.07	0.08	0.07	0.08	0.06	0.07	0.06	0.06	0.06	0.05
MnO	0.01	0	0.01	0.01	0	0	0	0	0.01	0	0	0	0.01	0	0	0	0	0.01	0.01	0.01
MgO	0	0.01	0.03	0	0.01	0	0	0.01	0	0.01	0	0	0	0	0	0	0.01	0	0.01	0
CaO	2.8	2.95	2.92	3.28	2.78	3.11	2.87	2.97	2.74	2.69	2.55	2.8	2.93	2.79	2.73	3.1	2.23	2.11	0.81	0.03
Na2O	10.21	10.11	10.23	9.98	10.53	10.01	10.24	10.13	10.24	10.23	10.33	10.25	10.3	10.07	10.32	10.09	10.59	10.63	11.58	1.21
K2O	0.09	0.09	0.09	0.08	0.24	0.07	0.07	0.13	0.13	0.11	0.1	0.09	0.05	0.16	0.05	0.09	0.1	0.13	0.05	14.59
P2O5																				
Cr2O3	0	0.02	0	0	0.01	0	0.01	0	0	0	0.01	0.01	0.01	0	0	0	0	0	0	0
NiO	0	0.01	0.01	0.01	0	0	0	0	0	0	0.01	0	0	0.01	0.01	0.01	0	0	0	0
ZnO																				
BaO																				
Total	99.67	100.39	99.3	99.59	100.97	99.87	99.42	100.07	99.72	99.68	99.76	99.84	100.26	100.99	99.81	99.95	100.14	99.98	103.43	97.98
Structural formula per 8 O																				
Si	2.885262	2.871414	2.88186	2.853045	2.868327	2.866804	2.87136	2.873944	2.890506	2.883289	2.89393	2.875825	2.860599	2.878462	2.88068	2.858619	2.906756	2.907874	2.97428	3.002239
Al	1.103138	1.120482	1.100085	1.135121	1.115172	1.122787	1.118294	1.11505	1.096014	1.106703	1.095323	1.114371	1.131244	1.11988	1.109522	1.132397	1.083481	1.083654	1.023829	0.999593
Ti	0.000332	0.00033	0	0.000666	0.000329	0.000664	0	0.000662	0	0.000664	0.000332	0	0	0	0	0.000332	0	0	0	0.000353
Fe2+T	0.001478	0.002568	0.001856	0.002593	0.005485	0.00369	0.001112	0.001473	0.002954	0.002955	0.002582	0.002952	0.002574	0.002915	0.002214	0.002582	0.002203	0.002206	0.002121	0.001962
Mn	0.000374	0	0.000376	0.000375	0	0	0	0	0.000374	0	0	0	0.000372	0	0	0	0	0.000372	0.000358	0.000397
Mg	0	0.000654	0.001985	0	0.000652	0	0	0.000656	0	0.000658	0	0	0	0	0	0	0.000654	0	0.00063	0
Ca	0.132513	0.138666	0.138858	0.155689	0.130236	0.14703	0.136277	0.140093	0.129631	0.127298	0.120509	0.132363	0.138029	0.130233	0.129034	0.146522	0.104894	0.099408	0.036686	0.001508
Na	0.87441	0.859978	0.880345	0.857242	0.892695	0.856385	0.879893	0.864684	0.876694	0.87606	0.883422	0.876843	0.878072	0.85062	0.882697	0.863023	0.901428	0.906276	0.949106	0.110053
K	0.005071	0.005037	0.005096	0.004521	0.013386	0.00394	0.003957	0.007301	0.007323	0.006198	0.005627	0.005065	0.002804	0.008892	0.002814	0.005065	0.0056	0.007292	0.002696	0.873069
P	0	0	0	0	0	0	0	0	0	0	0	0	0	0	0	0	0	0	0	0
Cr	0	0.000694	0	0	0.000346	0	0.00035	0	0	0	0.000349	0.000349	0.000348	0	0	0	0	0	0	0
Ni	0	0.000353	0.000357	0.000356	0	0	0	0	0	0	0.000355	0	0	0.00035	0.000355	0.000355	0	0	0	0
Zn	0	0	0	0	0	0	0	0	0	0	0	0	0	0	0	0	0	0	0	0
Ba	0	0	0	0	0	0	0	0	0	0	0	0	0	0	0	0	0	0	0	0
Total	5.002577	5.000176	5.010818	5.009609	5.026627	5.001301	5.011243	5.003862	5.003495	5.003824	5.002427	5.007769	5.014043	4.991354	5.007315	5.008895	5.005017	5.007083	4.989706	4.989173
An	13.09425	13.81573	13.55641	15.30185	12.56718	14.59566	13.35883	13.8421	12.78859	12.60931	11.93681	13.05007	13.54683	13.15825	12.71846	14.44125	10.36583	9.813451	3.711341	0.153135
Ab	86.40464	85.68243	85.94612	84.2538	86.14109	85.0132	86.25324	85.43654	86.489	86.77679	87.50586	86.45051	86.17793	85.94333	87.00421	85.05957	89.08074	89.46669	96.0159	11.17707
Or	0.501109	0.501835	0.497475	0.444352	1.291728	0.391136	0.387928	0.721366	0.722408	0.613901	0.557333	0.499418	0.275237	0.898423	0.277337	0.499175	0.553434	0.719862	0.272761	88.6698
	100	100	100	100	100	100	100	100	100	100	100	100	100	100	100	100	100	100	100	100
An content	13.1602	13.88541	13.62419	15.37015	12.73164	14.65298	13.41086	13.94267	12.88165	12.6872	12.00371	13.11557	13.58422	13.27754	12.75383	14.5137	10.42351	9.884606	3.721491	1.351566

DataSet	259/1	260/1	261/1	262/1	263/1	264/1	265/1	266/1	279/1	280/1	281/1	282/1	295/1	296/1	297/1	298/1
SiO2	64.07	64.09	68.36	71.37	66.77	65.16	64.58	64.92	65.62	64.33	64.67	65.28	65.51	64.21	64.79	64.94
TiO2	0	0.02	0	0	0	0	0.01	0.01	0.01	0.01	0.01	0.01	0	0.02	0	0
Al2O3	18.13	18.05	21.33	20.4	21.09	21.17	21.71	21.68	21.4	21.88	21.53	21.96	21.48	21.66	21.6	21.77
Fe2O3	0	0	0	0	0	0.077791	0.033339	0.033339	0	0.066678	0.133356	0.022226	0.100017	0.133356	0.088904	0.11113
FeO	0.03	0.03	0.05	0.01	0.05	0	0	0	0.07	0	0	0	0	0	0	0
FeOT	0.03	0.03	0.05	0.01	0.05	0.07	0.03	0.03	0.07	0.06	0.12	0.02	0.09	0.12	0.08	0.1
MnO	0	0	0	0	0	0.01	0	0	0	0	0.01	0	0.01	0	0	0.01
MgO	0	0.01	0.01	0	0.01	0	0.01	0	0	0	0	0.01	0	0.01	0	0
CaO	0.04	0.02	1.04	0.36	2.28	2.66	3.13	3.1	2.57	3.15	3.16	3.23	2.8	3.4	3.12	2.58
Na2O	1.21	1.13	11.14	11.35	10.5	10.24	9.96	10.02	10.29	10.01	10.05	10.13	10.33	9.82	9.99	10.31
K2O	14.73	14.59	0.22	0.28	0.14	0.09	0.05	0.05	0.04	0.08	0.1	0.1	0.12	0.07	0.1	0.11
P2O5																
Cr2O3	0	0	0	0	0	0	0	0	0	0	0	0.02	0	0	0	0.01
NiO	0	0	0	0	0.01	0.01	0.01	0.01	0.02	0	0	0.01	0	0	0	0
ZnO																
BaO																
Total	98.21	97.94	102.15	103.77	100.85	99.41	99.49	99.82	100.02	99.52	99.65	100.77	100.34	99.31	99.68	99.83
Structural formula per 8 O																
Si	3.000452	3.005695	2.93171	2.999048	2.909361	2.885494	2.85998	2.864917	2.885716	2.850617	2.862795	2.856802	2.876898	2.85275	2.864845	2.865529
Al	1.000667	0.997681	1.078126	1.010317	1.08306	1.104892	1.133142	1.127593	1.109151	1.1427	1.123288	1.13264	1.111759	1.134173	1.125658	1.132167
Ti	0	0.000705	0	0	0	0	0.000333	0.000332	0.000331	0.000333	0.000333	0.000329	0	0.000668	0	0
Fe2+T	0.001175	0.001177	0.001793	0.000351	0.001822	0.002592	0.001111	0.001107	0.002574	0.002223	0.004443	0.000732	0.003305	0.004459	0.002958	0.00369
Mn	0	0	0	0	0	0.000375	0	0	0	0	0.000375	0	0.000372	0	0	0.000374
Mg	0	0.000699	0.000639	0	0.000649	0	0.00066	0	0	0	0	0.000652	0	0.000662	0	0
Ca	0.002007	0.001005	0.047787	0.016208	0.106442	0.126207	0.148515	0.146574	0.121091	0.149554	0.149877	0.151448	0.131746	0.161846	0.147812	0.121976
Na	0.109867	0.10275	0.926305	0.924727	0.887065	0.879203	0.855213	0.857337	0.87737	0.860022	0.862588	0.859527	0.879563	0.845907	0.856463	0.882066
K	0.87996	0.872847	0.012036	0.015009	0.007782	0.005084	0.002825	0.002815	0.002244	0.004522	0.005647	0.005582	0.006722	0.003967	0.005641	0.006192
P	0	0	0	0	0	0	0	0	0	0	0	0	0	0	0	0
Cr	0	0	0	0	0	0	0	0	0	0	0	0.000692	0	0	0	0.000349
Ni	0	0	0	0	0.00035	0.000356	0.000356	0.000355	0.000707	0	0	0.000352	0	0	0	0
Zn	0	0	0	0	0	0	0	0	0	0	0	0	0	0	0	0
Ba	0	0	0	0	0	0	0	0	0	0	0	0	0	0	0	0
Total	4.994128	4.982558	4.998397	4.965661	4.996532	5.004203	5.002135	5.00103	4.999185	5.009972	5.009346	5.008757	5.010366	5.004432	5.003377	5.012342
An	0.202355	0.102903	4.845963	1.695504	10.63048	12.4896	14.75482	14.55947	12.10057	14.74747	14.72109	14.89813	12.94121	15.99709	14.63605	12.07401
Ab	11.07716	10.52121	93.93354	96.73442	88.59235	87.00728	84.96455	85.16094	87.6752	84.80661	84.72426	84.55271	86.39845	83.61078	84.80543	87.31309
Or	88.72048	89.37589	1.220495	1.570078	0.777165	0.503125	0.280625	0.279589	0.224233	0.445927	0.554651	0.549156	0.660336	0.392127	0.558517	0.612902
	100	100	100	100	100	100	100	100	100	100	100	100	100	100	100	100
An content	1.794006	0.968581	4.905838	1.72255	10.71375	12.55275	14.79634	14.60029	12.12776	14.81352	14.8032	14.9804	13.02723	16.06006	14.71826	12.14847

	ppm					Ratios													U-Pb discordance	
Name	U	Th	^{206}Pb	$^{206}Pb_c$(%)	206/204	$^{207}Pb/^{206}Pb^*$	1SE	$^{208}Pb/^{206}Pb$	1SE	$^{207}Pb/^{235}U^*$	2SE	$^{206}Pb/^{238}U^*$	2SE	Rho	$^{208}Pb/^{232}Th^*$	1SE	$^{232}Th/^{238}U$	1SE	Central (%)	Minimum rim (%)
525964_XX1_CORE-01	40	15.9	15.1	.	1065	0.19505	0.00229	0.11237	0.01341	12.61246	0.85998	0.46898	0.03002	0.939	0.13089	0.0051	0.40263	0.04355	-13.22	-2.21
525964_XX1_CORE-02	35	13.3	13	.	4354	0.19471	0.00233	0.10772	0.01315	12.44452	0.86234	0.46355	0.03014	0.939	0.13069	0.00483	0.38207	0.04267	-14.11	-3.03
525964_XX1_RIM-03	24	16.1	8.6	.	982	0.19672	0.0024	0.17376	0.02108	12.20717	0.84976	0.45006	0.02934	0.936	0.11466	0.00455	0.68204	0.07496	-17.23	-6.55
525964_XX2_CORE-01	45	30.2	17.2	.	2588	0.19467	0.00234	0.18479	0.02205	12.6286	0.8945	0.4705	0.03134	0.941	0.12986	0.00498	0.66951	0.07227	-12.82	-1.28
525964_XX2_CORE-02	53	31.4	18.4	.	4177	0.19423	0.00236	0.15533	0.01787	11.42394	0.78884	0.42659	0.02758	0.936	0.11143	0.00419	0.59464	0.06171	-20.82	-10.64
525964_XX2_RIM-03	43	19.4	16.2	.	4458	0.1928	0.00236	0.12346	0.01413	12.21056	0.86892	0.45934	0.03068	0.939	0.12609	0.00488	0.44976	0.04607	-14.28	-2.85
525964_XX3_CORE-01	48	27.9	18.2	.	1425	0.19791	0.00286	0.16336	0.01971	12.66948	0.92238	0.4643	0.03102	0.918	0.13054	0.00534	0.58104	0.06301	-14.98	-3.7
525964_XX3_CORE-02	21	17.9	8	.	299	0.20565	0.00286	0.24571	0.03023	13.15719	0.97578	0.46403	0.0319	0.927	0.13556	0.00622	0.84107	0.09156	-17.31	-6.19
525964_XX4_CORE-01	48	23.6	18.1	.	29145	0.19144	0.00241	0.1403	0.0174	12.5245	0.92198	0.4745	0.03282	0.94	0.13323	0.00538	0.49967	0.05599	-10.99	.
525964_XX5_CORE-01	31	13.2	11.4	.	1920	0.1911	0.00258	0.1147	0.01452	11.90612	0.92978	0.45186	0.03312	0.938	0.12242	0.00531	0.42335	0.04789	-15.13	-2.61
525964_XX5_CORE-02	32	11.8	11.3	.	2025	0.19117	0.0026	0.10343	0.01297	11.72347	0.92342	0.44476	0.03288	0.939	0.12152	0.00528	0.37857	0.04226	-16.49	-4.06
525964_XX5_CORE-03	33	12.9	11.7	.	3867	0.19114	0.00262	0.10673	0.01363	11.6618	0.92084	0.4425	0.03278	0.938	0.1184	0.00515	0.39889	0.04557	-16.9	-4.5
525964_XX6_CORE-01	41	14.3	15.2	.	2223	0.19547	0.0027	0.09801	0.01206	12.43266	0.9849	0.4613	0.03424	0.937	0.12758	0.00556	0.35436	0.03859	-14.77	-2.14
525964_XX6_CORE-02	35	10.5	12.8	.	2298	0.19577	0.00274	0.07874	0.00954	12.10609	0.96924	0.44849	0.03364	0.937	0.11807	0.0052	0.29909	0.03182	-17.23	-4.83
525964_XX6_CORE-03	24	6.1	8.7	.	1688	0.19631	0.00278	0.06803	0.00835	11.98418	0.96714	0.44275	0.03346	0.936	0.11949	0.00545	0.25208	0.0271	-18.45	-6.14
525964_XX7_CORE-01	27	14	9.8	.	2212	0.1982	0.00285	0.12452	0.01563	12.21767	1.00592	0.44707	0.0345	0.937	0.10648	0.00495	0.52282	0.05752	-18.23	-5.65
525964_XX7_CORE-02	43	19.8	15.8	.	3027	0.19659	0.00283	0.11688	0.01464	12.25204	1.01666	0.452	0.03518	0.938	0.11433	0.00539	0.46211	0.05051	-16.84	-3.9
525964_XX7_RIM-03	46	23.2	17.3	.	4033	0.19562	0.00284	0.13543	0.01678	12.4023	1.03544	0.45981	0.03598	0.937	0.12399	0.00573	0.50223	0.05429	-15.1	-1.78

	ppm					Ratios													U-Pb discordance	
Name	U	Th	^{206}Pb	$^{206}Pb_c$(%)	206/204	$^{207}Pb/^{206}Pb^*$	1SE	$^{208}Pb/^{206}Pb$	1SE	$^{207}Pb/^{235}U^*$	2SE	$^{206}Pb/^{238}U^*$	2SE	Rho	$^{208}Pb/^{232}Th^*$	1SE	$^{232}Th/^{238}U$	1SE	Central (%)	Minimum rim (%)
525969_XX1_CORE-01	39	25.6	14.3	.	1189	0.19264	0.00171	0.18525	0.02107	12.29206	0.66144	0.46279	0.0235	0.944	0.12839	0.00367	0.66774	0.07152	-13.59	-4.95
525969_XX1_CORE-02	50	40.3	18.5	.	1160	0.19168	0.00179	0.22739	0.02588	12.25696	0.65914	0.46378	0.02338	0.938	0.1289	0.00366	0.81813	0.0878	-13.09	-4.43
525969_XX2_CORE-01	32	16.8	10.8	.	618	0.19599	0.00179	0.16179	0.0186	11.53168	0.63846	0.42673	0.0223	0.944	0.12887	0.00364	0.53576	0.05804	-21.31	-13.25
525969_XX2_CORE-02	26	13.6	9.3	.	1139	0.19509	0.00176	0.14923	0.01704	12.1367	0.66388	0.45119	0.0233	0.944	0.12617	0.0038	0.53365	0.05713	-16.53	-8.07
525969_XX2_CORE-03	24	13.6	8.5	.	1383	0.19423	0.00178	0.16042	0.01821	11.88718	0.64602	0.44387	0.02272	0.942	0.12374	0.00368	0.57541	0.0613	-17.62	-9.33
525969_XX3_CORE-01	20	6.7	6.8	.	1048	0.1956	0.00183	0.10031	0.02055	11.6456	0.62956	0.4318	0.0219	0.938	0.12928	0.00575	0.33502	0.06644	-20.26	-12.33
525969_XX3_CORE-02	11	3.9	3.7	.	557	0.19633	0.00188	0.09705	0.01284	11.27571	0.61934	0.41655	0.02144	0.937	0.1129	0.00395	0.35807	0.04476	-23.28	-15.54
525969_XX4_CORE-01	32	24.5	11.3	.	1178	0.19664	0.00185	0.21499	0.02422	11.88092	0.65354	0.4382	0.02264	0.94	0.12194	0.00354	0.77263	0.08169	-19.39	-11.23
525969_XX4_CORE-02	26	19	9.3	.	1554	0.19577	0.00187	0.20843	0.02405	12.14395	0.68146	0.4499	0.02374	0.94	0.12552	0.00379	0.74708	0.08082	-16.97	-8.37
525969_XX4_CORE-03	22	11.1	8	.	3460	0.19664	0.00188	0.14009	0.01602	12.13212	0.68594	0.44748	0.0238	0.941	0.12532	0.00389	0.50021	0.05343	-17.68	-9.1
525969_XX5_CORE-01	55	15.8	20.8	.	1467	0.19037	0.00193	0.07854	0.009	12.19797	0.7215	0.46471	0.02582	0.939	0.12713	0.00402	0.28711	0.03061	-12.47	-2.81
525969_XX5_CORE-02	54	16.5	20.5	.	1165	0.19074	0.00195	0.08665	0.01025	12.34878	0.7447	0.46954	0.02664	0.941	0.1324	0.00444	0.30729	0.03375	-11.69	-1.74
525969_XX5_CORE-03	54	18.2	20.4	.	2464	0.19017	0.00195	0.09345	0.01097	12.3218	0.74274	0.46993	0.02664	0.94	0.1294	0.00426	0.33936	0.03701	-11.42	-1.44
525969_XX6_CORE-01	38	35	14.2	.	5131	0.19135	0.00199	0.25387	0.02934	12.17441	0.74088	0.46144	0.0264	0.94	0.12679	0.00416	0.92395	0.09893	-13.42	-3.58
525969_XX6_CORE-02	38	35.1	14.2	.	1320	0.1931	0.00203	0.25307	0.02925	12.22319	0.74948	0.4591	0.02646	0.94	0.12598	0.00418	0.92227	0.09861	-14.42	-4.66
525969_XX6_CORE-03	38	35.3	14.2	.	1457	0.19297	0.00204	0.25525	0.02974	12.25181	0.75834	0.46048	0.02678	0.94	0.12674	0.00421	0.92737	0.09998	-14.13	-4.23
525969_XX7_CORE-01	60	67.6	21.9	.	3211	0.19077	0.00203	0.31428	0.03657	12.0152	0.7421	0.4568	0.02648	0.939	0.12562	0.00416	1.14285	0.12312	-14.09	-4.18
525969_XX7_CORE-02	58	65.5	21.6	.	3487	0.19086	0.00205	0.31672	0.03721	12.275	0.7732	0.46644	0.02762	0.94	0.12908	0.00439	1.14453	0.12417	-12.31	-1.98
525969_XX7_CORE-03	55	53.1	20.5	.	3040	0.19028	0.00206	0.26527	0.03092	12.14837	0.77504	0.46305	0.0278	0.941	0.12626	0.00432	0.97283	0.10439	-12.75	-2.32

	ppm					Ratios													U-Pb discordance	
Name	U	Th	^{206}Pb	$^{206}Pb_c$(%)	206/204	$^{207}Pb/^{206}Pb^*$	1SE	$^{208}Pb/^{206}Pb$	1SE	$^{207}Pb/^{235}U^*$	2SE	$^{206}Pb/^{238}U^*$	2SE	Rho	$^{208}Pb/^{232}Th^*$	1SE	$^{232}Th/^{238}U$	1SE	Central (%)	Minimum rim (%)
525971_XX1_CORE-01	29	18.2	10.2	.	2934	0.19549	0.00238	0.18354	0.02059	11.79935	0.87188	0.43775	0.03054	0.944	0.12546	0.00489	0.6404	0.06354	-19.13	-7.92
525971_XX1_CORE-02	32	20.4	11.3	.	2065	0.19599	0.00242	0.18632	0.02095	11.82306	0.88668	0.43751	0.03098	0.944	0.12575	0.0049	0.64822	0.06441	-19.33	-7.97
525971_XX1_RIM-03	29	18.3	10.2	.	383	0.2039	0.00275	0.19843	0.02222	12.17587	0.91804	0.4331	0.03048	0.934	0.13461	0.00561	0.63842	0.06243	-22.36	-11.63
525971_XX3_CORE-01	51	32.8	18.5	.	5618	0.19365	0.00244	0.18141	0.02022	11.78741	0.89476	0.44147	0.03162	0.943	0.12336	0.00492	0.64922	0.06346	-17.88	-6.13
525971_XX3_RIM-03	35	21.9	12.4	.	4405	0.19416	0.00247	0.17841	0.01998	11.69268	0.89806	0.43678	0.03164	0.943	0.12243	0.00497	0.63651	0.06231	-18.91	-7.17
525971_XX4_CORE-01	25	16.2	9	.	270	0.20927	0.0021	0.21476	0.02945	12.72735	0.50368	0.44109	0.01504	0.862	0.14704	0.0036	0.64425	0.08623	-22.35	-17.25
525971_XX5_CORE-01	43	33.3	15.5	.	2512	0.19551	0.00173	0.21607	0.03004	12.00364	0.46242	0.44529	0.01524	0.888	0.12286	0.00304	0.78313	0.10631	-17.74	-12.23
525971_XX5_CORE-02	37	26.6	13.1	.	2568	0.19566	0.00176	0.20076	0.02743	11.75944	0.4622	0.43589	0.01524	0.889	0.12097	0.00311	0.72338	0.09623	-19.53	-14.02
525971_XX9_CORE-01	50	106.5	19.6	.	2055	0.18583	0.00175	0.69732	0.09749	12.42966	0.55414	0.48512	0.0196	0.907	0.15699	0.00438	2.15482	0.29196	-6.98	.
525971_XX10_CORE-01	38	37.6	14.6	.	5642	0.18671	0.00193	0.30146	0.0413	12.10889	0.50572	0.47037	0.01708	0.87	0.1419	0.00379	0.99931	0.13306	-10.12	-3.59
525971_XX10_RIM-02	25	15	9.5	.	4599	0.18624	0.0027	0.17775	0.02456	11.8946	0.5316	0.4632	0.01576	0.761	0.13634	0.00465	0.60389	0.0802	-11.33	-5.1
525971_XX11_CORE-01	24	13.9	9.2	.	1236	0.18666	0.00198	0.15476	0.02142	11.94308	0.55054	0.46406	0.019	0.888	0.12362	0.00386	0.58094	0.07745	-11.31	-4.04
525971_XX12_CORE-01	45	31	17.7	.	3053	0.1864	0.002	0.19864	0.02764	12.20689	0.56622	0.47495	0.01954	0.887	0.13626	0.0043	0.69238	0.09275	-9.14	-1.65
525971_XX13_CORE-01	72	49.5	29.1	.	2882	0.18517	0.00202	0.19989	0.02818	12.4602	0.60462	0.48803	0.02114	0.893	0.14148	0.00461	0.68952	0.09339	-6.17	.
525971_XX13_RIM-02	54	40.8	22.4	.	204	0.20886	0.00265	0.2709	0.03837	14.36266	0.37134	0.49875	0.01124	0.872	0.17801	0.0076	0.75901	0.10108	-12.08	-4.41
525971_XX14_CORE-01	37	22.8	14.5	.	3141	0.18655	0.00209	0.17607	0.02462	12.04572	0.5752	0.46831	0.01976	0.883	0.13359	0.0044	0.61723	0.08284	-10.46	-2.88
525971_XX14_CORE-02	38	23.3	14.7	.	3595	0.18636	0.0021	0.17695	0.02477	12.08353	0.5884	0.47025	0.0203	0.886	0.1333	0.00452	0.62423	0.0837	-10.02	-2.23
525971_XX15_CORE-01	28	15.2	10.3	.	2124	0.1888	0.0022	0.16002	0.02234	11.6206	0.58018	0.44641	0.01972	0.885	0.12936	0.00444	0.55219	0.07371	-15.4	-7.93
525971_XX16_CORE-01	36	26	14.3	.	1447	0.18863	0.00219	0.21151	0.02987	12.31512	0.6311	0.47351	0.02162	0.891	0.13841	0.0049	0.72357	0.09752	-10.21	-2.01
525971_XX16_CORE-02	32	21.3	12.4	.	952	0.19859	0.00277	0.21408	0.03015	12.89729	0.68338	0.47103	0.02122	0.85	0.14811	0.00528	0.68086	0.09151	-13.96	-6.28
525971_XX16_RIM-03	51	38.7	19.9	.	30265	0.18849	0.00224	0.22657	0.03237	12.14164	0.64188	0.46719	0.02206	0.893	0.13928	0.00514	0.75994	0.10333	-11.36	-2.98

	ppm					Ratios														U-Pb discordance	
Name	U	Th	^{206}Pb	$^{206}Pb_c$(%)	206/204	$^{207}Pb/^{206}Pb^*$	1SE	$^{208}Pb/^{206}Pb$	1SE	$^{207}Pb/^{235}U^*$	2SE	$^{206}Pb/^{238}U^*$	2SE	Rho	$^{208}Pb/^{232}Th^*$	1SE	$^{232}Th/^{238}U$	1SE	Central (%)	Minimum rim (%)
525972_XX1_CORE-01	60	90.5	24.4	.	425	0.19992	0.00187	0.4918	0.09513	13.00735	0.57748	0.47188	0.019	0.907	0.15324	0.00325	1.51445	0.28957	-14.22	-7.51
525972_XX1_CORE-02	52	80	21.2	.	364	0.19954	0.00166	0.52811	0.10216	13.14123	0.57928	0.47765	0.0195	0.926	0.16181	0.00282	1.55898	0.29866	-13.05	-6.17
525972_XX1_CORE-03	50	96.9	20.2	.	2184	0.19045	0.00146	0.55738	0.10696	12.23941	0.549	0.4661	0.01964	0.939	0.13365	0.00257	1.94383	0.36888	-12.24	-4.97
525972_XX2_CORE-01	61	78.8	25.1	.	246	0.19704	0.0016	1.11879	0.22125	13.18799	0.6176	0.48543	0.02132	0.938	0.41425	0.008	1.31102	0.25641	-10.83	-3.21
525972_XX2_CORE-02	62	61.8	24.5	.	865	0.18832	0.00147	0.53316	0.10357	11.84416	0.54032	0.45615	0.01954	0.939	0.24376	0.00695	0.9977	0.1905	-13.4	-6.07
525972_XX4_CORE-01	79	36.4	32	.	2319	0.18174	0.00181	0.13704	0.02663	11.80955	0.672	0.47129	0.02512	0.937	0.13871	0.0033	0.46564	0.08894	-8.1	.
525972_XX4_CORE-02	128	92.2	54.1	.	2972	0.18001	0.00181	0.22774	0.04745	12.09337	0.68402	0.48724	0.02576	0.935	0.15348	0.00444	0.72298	0.14794	-4.3	.
525972_XX4_RIM-03	21	88.2	8.4	.	1432	0.19077	0.00196	1.22888	0.23826	12.26268	0.70642	0.4662	0.02508	0.934	0.13429	0.00331	4.26607	0.81235	-12.33	-2.96
525972_XX5_CORE-01	93	384.1	39.3	.	4046	0.18782	0.00198	1.23727	0.24277	12.7508	0.7755	0.49238	0.0281	0.938	0.14568	0.00382	4.18186	0.80439	-6.33	.
525972_XX5_CORE-02	107	448.3	45	.	25649	0.18668	0.00199	1.22732	0.23953	12.5537	0.76056	0.48772	0.02766	0.936	0.14148	0.00366	4.23081	0.80958	-6.8	.
525972_XX5_RIM-03	70	305.8	29.4	.	7465	0.18802	0.00203	1.28567	0.25026	12.54152	0.77022	0.48377	0.0278	0.936	0.14153	0.00377	4.3947	0.83793	-8.04	.
525972_XX6_CORE-01	110	1974.9	48.5	.	1992	0.18822	0.0021	5.3677	1.05839	13.22834	0.85294	0.50973	0.03084	0.938	0.1519	0.0042	18.0123	3.47402	-3.18	.
525972_XX6_CORE-02	86	1367.2	37.8	.	407	0.19787	0.0023	4.8488	0.96678	14.00387	0.9176	0.5133	0.03146	0.935	0.15482	0.00431	16.0757	3.13539	-6	.
525972_XX7_CORE-01	57	49	20.9	.	925	0.1898	0.0014	0.25814	0.02653	12.63064	0.54282	0.48265	0.01948	0.939	0.14412	0.00299	0.8645	0.08524	-8.89	-1.67
525972_XX7_CORE-02	52	41.3	19.3	.	563	0.19224	0.0014	0.24947	0.02594	12.98732	0.56462	0.48997	0.02006	0.942	0.15318	0.00327	0.79792	0.07956	-8.38	-1.04
525972_XX7_CORE-03	53	43.7	19.5	.	729	0.19094	0.00141	0.25485	0.02624	12.82563	0.55296	0.48718	0.01974	0.94	0.14899	0.00315	0.83334	0.08226	-8.44	-1.17
525972_XX9_CORE-01	37	378.7	13.1	.	1920	0.19369	0.00146	3.06723	0.31652	12.35788	0.55808	0.46273	0.0197	0.942	0.13833	0.00314	10.26028	1.00958	-13.94	-6.79
525972_XX9_CORE-02	35	377.3	12.6	.	734	0.19448	0.00149	3.23506	0.33688	12.66785	0.58746	0.47243	0.02068	0.944	0.14123	0.00329	10.82125	1.07248	-12.4	-4.91
525972_XX9_RIM-03	12	92.7	4.3	.	427	0.19728	0.00164	2.27552	0.23356	12.50912	0.56374	0.45987	0.01928	0.93	0.1363	0.00302	7.6776	0.75247	-15.6	-8.72
525972_XX10_CORE-01	68	467	26.5	.	636	0.19685	0.00169	2.11324	0.2346	13.97021	0.64028	0.5147	0.02186	0.927	0.15632	0.00349	6.95832	0.74214	-5.39	.
525972_XX10_CORE-02	44	263	16.1	.	784	0.19393	0.00156	1.79078	0.18835	12.95831	0.60918	0.48461	0.0214	0.939	0.1427	0.00338	6.08165	0.60859	-9.95	-2.18
525972_XX10_RIM-03	26	50.2	8.9	.	1879	0.19158	0.00147	0.5734	0.05831	11.92862	0.53568	0.45158	0.01906	0.94	0.13168	0.00299	1.96647	0.19045	-15.34	-8.33
525972_XX11_CORE-02	51	38.3	18.2	.	3863	0.18869	0.00148	0.21673	0.02245	12.05105	0.55988	0.4632	0.02026	0.942	0.13333	0.0031	0.75294	0.0742	-12.18	-4.6
525972_XX11_CORE-01	49	42.5	16.9	.	2842	0.18996	0.00147	0.25068	0.02577	11.74616	0.54406	0.44846	0.01958	0.943	0.12882	0.00301	0.87269	0.08525	-15.4	-8.13
525972_XX11_CORE-03	29	34.4	10.7	.	1780	0.19241	0.00155	0.34316	0.03563	12.88398	0.60314	0.48564	0.02134	0.939	0.13827	0.0032	1.20525	0.11909	-9.24	-1.42
525972_XX12_CORE-01	36	357.6	12.9	.	3676	0.19108	0.00151	2.96077	0.30842	12.31383	0.57952	0.46739	0.02072	0.942	0.1374	0.00326	10.07162	0.99687	-12.21	-4.56
525972_XX12_CORE-02	50	564.9	18.3	.	2898	0.19003	0.00151	3.32668	0.34887	12.41511	0.59952	0.47382	0.02162	0.945	0.13903	0.00339	11.33759	1.12722	-10.64	-2.61
525972_XX12_CORE-03	56	664.8	21.1	.	7657	0.18941	0.0015	3.53349	0.37144	12.76798	0.61468	0.4889	0.02222	0.944	0.14469	0.00353	11.93904	1.19014	-7.57	.
525972_XX13_CORE-01	49	414.4	18.1	.	728	0.19397	0.00168	2.53314	0.26506	12.79238	0.65264	0.47831	0.02294	0.94	0.14114	0.00364	8.58431	0.8458	-11.14	-2.78
525972_XX13_CORE-02	63	535.5	25.2	.	280	0.20522	0.00184	2.61129	0.30592	14.58028	0.78502	0.51529	0.02616	0.943	0.15804	0.00437	8.5139	0.94488	-8.04	.
525972_XX13_RIM-03	63	36.3	23.1	.	1885	0.18886	0.00164	0.16902	0.01778	12.20933	0.63356	0.46886	0.02292	0.942	0.13697	0.00361	0.57858	0.05721	-11.17	-2.57
525972_XX14_CORE-01	21	56.6	7.2	.	1681	0.19344	0.00176	0.78736	0.0817	11.85286	0.61992	0.4444	0.0218	0.938	0.12725	0.00337	2.74972	0.26752	-17.27	-9.29
525972_XX14_CORE-02	22	51.9	7.6	.	1662	0.192	0.00171	0.69093	0.07202	11.81463	0.62284	0.4463	0.02214	0.941	0.1286	0.00344	2.39774	0.23413	-16.46	-8.29
525972_XX14_RIM-03	55	196.1	19.4	.	3021	0.19069	0.00169	1.02055	0.10767	11.88159	0.6329	0.45189	0.0227	0.943	0.12767	0.00348	3.61235	0.35679	-14.99	-6.56
525972_XX15_CORE-01	56	612.5	20.6	.	2233	0.19074	0.00171	3.19649	0.33917	12.3146	0.66348	0.46824	0.02378	0.943	0.13628	0.00374	10.98306	1.0907	-11.94	-3.09
525972_XX15_CORE-02	75	934.8	28.5	.	9003	0.18889	0.0017	3.69068	0.40173	12.62078	0.6991	0.4846	0.02538	0.945	0.14277	0.00404	12.52728	1.2752	-8.2	.
525972_XX15_CORE-03	72	895.3	27.3	.	5070	0.18854	0.00171	3.67109	0.40026	12.64305	0.70612	0.48634	0.02568	0.946	0.14215	0.00406	12.56036	1.27927	-7.74	.
525972_XX16_RIM-03	52	38.2	18.8	.	2210	0.18605	0.00184	0.20595	0.02193	11.69995	0.69012	0.45609	0.02534	0.942	0.12632	0.00385	0.74359	0.07302	-12.62	-2.9
525972_XX17_CORE-01	93	344.7	35	.	5138	0.18669	0.00187	1.04581	0.11325	12.16372	0.73264	0.47255	0.02684	0.943	0.13269	0.00412	3.72432	0.37162	-9.7	.
525972_XX17_CORE-02	130	547.9	52.3	.	9460	0.18447	0.00185	1.22916	0.13875	12.96786	0.7971	0.50986	0.02962	0.945	0.14709	0.00468	4.26072	0.44455	-1.69	.
525972_XX17_CORE-03	134	553	54.2	.	1337	0.18569	0.00188	1.20241	0.13874	13.07578	0.82282	0.51071	0.03042	0.947	0.14794	0.00487	4.15081	0.44208	-2.02	.
525972_XX18_CORE-01	152	673.2	59.3	.	9054	0.18364	0.00188	1.25428	0.13941	12.45067	0.77724	0.49172	0.029	0.945	0.13816	0.00449	4.46402	0.45584	-4.87	.
525972_XX18_CORE-02	178	845.8	74.9	.	1980	0.18452	0.00192	1.40796	0.1632	13.50992	0.84308	0.53101	0.03124	0.943	0.15582	0.00495	4.79812	0.51589	2.36	.
525972_XX18_RIM-03	30	40.1	11.3	.	1334	0.18936	0.00198	0.4005	0.04524	12.28454	0.78126	0.47051	0.02826	0.945	0.14056	0.00494	1.3406	0.13816	-11.03	-0.37
525972_XX19_CORE-01	82	50.7	31.1	.	6940	0.18917	0.002	0.17521	0.01853	12.41369	0.79692	0.47593	0.02884	0.944	0.13325	0.00443	0.62578	0.05989	-9.94	.
525972_XX19_RIM-02	34	65.6	12.3	.	1693	0.19274	0.00208	0.57188	0.06318	12.1144	0.77272	0.45586	0.02736	0.941	0.13248	0.00444	1.96781	0.19855	-14.91	-4.78
525972_XX19_RIM-03	22	11.2	8	.	2366	0.19317	0.00209	0.14378	0.01547	11.85859	0.75952	0.44523	0.02684	0.941	0.12703	0.00421	0.5039	0.04928	-17.03	-7.11

	ppm					Ratios														U-Pb discordance	
Name	U	Th	^{206}Pb	$^{206}Pb_c$(%)	206/204	$^{207}Pb/^{206}Pb^*$	1SE	$^{208}Pb/^{206}Pb$	1SE	$^{207}Pb/^{235}U^*$	2SE	$^{206}Pb/^{238}U^*$	2SE	Rho	$^{208}Pb/^{232}Th^*$	1SE	$^{232}Th/^{238}U$	1SE	Central (%)	Minimum rim (%)
542206_XX1-01	63	73.9	24.7	.	2656	0.18959	0.00089	0.3385	0.04118	12.25266	0.332	0.46872	0.01192	0.938	0.13375	0.00137	1.18619	0.14299	-11.45	-7.07
542206_XX1_CORE-01	63	73.9	24.7	.	2656	0.18959	0.00089	0.3385	0.04118	12.25266	0.332	0.46872	0.01192	0.938	0.13375	0.00137	1.18619	0.14299	-11.45	-7.07
542206_XX1_CORE-02	60	71.1	24	.	3658	0.18938	0.00091	0.33781	0.04117	12.35938	0.3375	0.47333	0.0121	0.937	0.13497	0.00141	1.18466	0.14304	-10.51	-6.05
542206_XX1_RIM-03	32	21.1	12.5	.	1689	0.19158	0.00094	0.19289	0.02365	12.19988	0.33244	0.46186	0.01174	0.932	0.13429	0.00147	0.66342	0.08058	-13.41	-9.14
542206_XX2_CORE-01	54	60.9	21.7	.	904	0.19191	0.00098	0.33078	0.04045	12.69966	0.3703	0.47994	0.01312	0.937	0.13912	0.00158	1.1411	0.13805	-10.14	-5.38
542206_XX2_CORE-02	55	62.6	21.9	.	2719	0.18763	0.00094	0.32466	0.0395	12.2357	0.33792	0.47297	0.01218	0.932	0.13373	0.00144	1.14823	0.13836	-9.96	-5.43
542206_XX2_CORE-03	52	61.7	21.2	.	406	0.19814	0.0011	0.34525	0.04253	13.24703	0.39184	0.48489	0.0133	0.927	0.1405	0.00165	1.19152	0.14519	-11.29	-6.61
542206_XX3_CORE-01	42	33.2	16.5	.	1468	0.19115	0.00099	0.23155	0.0283	12.48384	0.36782	0.47366	0.01308	0.937	0.13619	0.00156	0.80532	0.09738	-11.06	-6.29
542206_XX3_CORE-02	42	33.4	16.6	.	2314	0.18947	0.00099	0.23074	0.0282	12.37745	0.36124	0.47378	0.01292	0.934	0.13548	0.00156	0.80694	0.09756	-10.45	-5.69
542206_XX3_CORE-03	42	33.6	16.7	.	3064	0.19017	0.00099	0.22945	0.02806	12.36043	0.36286	0.47141	0.01294	0.935	0.13465	0.00157	0.80335	0.09715	-11.14	-6.39
542206_XX4_CORE-02	40	31.7	15.8	.	801	0.19399	0.00116	0.23924	0.02983	12.57821	0.44156	0.47027	0.01552	0.94	0.13966	0.00213	0.8056	0.09882	-12.63	-7.04
542206_XX4_CORE-03	36	28.6	14.2	.	23371	0.19268	0.00115	0.23276	0.02925	12.34567	0.43364	0.46471	0.01536	0.941	0.13479	0.00196	0.80247	0.09928	-13.24	-7.67
542206_XX5_CORE-01	42	32.4	16.6	.	3937	0.19146	0.00112	0.22179	0.02751	12.14407	0.42946	0.46002	0.01536	0.944	0.13256	0.00194	0.76969	0.09393	-13.72	-8.11
542206_XX5_CORE-02	41	31.2	16.2	.	1474	0.19304	0.00114	0.22602	0.02813	12.3997	0.44684	0.46586	0.01586	0.945	0.13694	0.00205	0.76894	0.0941	-13.15	-7.4
542206_XX5_CORE-03	42	31.8	16.3	.	1555	0.19137	0.00113	0.222	0.02751	12.13532	0.43676	0.45992	0.01562	0.944	0.13273	0.00199	0.76922	0.09373	-13.71	-7.99
542206_XX6_CORE-01	47	44.5	18.7	.	313	0.20338	0.00133	0.26641	0.03316	13.08021	0.48292	0.46645	0.0161	0.935	0.13064	0.00201	0.95117	0.11634	-16.23	-10.7
542206_XX6_CORE-02	49	39.2	19.5	.	2627	0.19103	0.00116	0.2314	0.02878	12.29269	0.45638	0.4667	0.01638	0.945	0.13437	0.00209	0.80373	0.09819	-12.32	-6.32
542206_XX6_CORE-03	52	42.6	20.2	.	80800	0.19062	0.00116	0.23237	0.02878	11.91577	0.43972	0.45337	0.0158	0.944	0.12862	0.00198	0.81911	0.09963	-14.69	-8.89
542206_XX7_CORE-01	25	13.9	9.5	.	2633	0.1908	0.00138	0.16214	0.01999	11.82102	0.4743	0.44934	0.01682	0.933	0.13061	0.00214	0.55778	0.06734	-15.51	-9.31
542206_XX7_CORE-02	24	13.7	9.3	.	1834	0.19409	0.00147	0.16551	0.02032	12.21439	0.48134	0.45641	0.01662	0.924	0.13201	0.00208	0.57222	0.06891	-15.24	-9.23
542206_XX7_CORE-03	23	12.8	8.8	.	1283	0.1936	0.00144	0.16375	0.02026	12.09271	0.48906	0.45302	0.01702	0.929	0.13242	0.00221	0.5602	0.06785	-15.72	-9.54
542206_XX8_CORE-01	41	32.5	16.1	.	2318	0.1929	0.00144	0.22963	0.02833	12.25146	0.50586	0.46062	0.01772	0.932	0.1332	0.00219	0.7941	0.0959	-14.08	-7.62
542206_XX8_CORE-02	42	32.6	16.2	.	1375	0.193	0.00148	0.22947	0.02838	12.22683	0.51818	0.45948	0.01814	0.932	0.13386	0.00225	0.78766	0.09525	-14.32	-7.7
542206_XX8_CORE-03	42	33.2	16.4	.	2758	0.1922	0.00148	0.22812	0.02815	12.13183	0.51016	0.45779	0.0179	0.93	0.13172	0.00218	0.79279	0.09569	-14.38	-7.82
542206_XX9_CORE-01	77	60.4	30.9	.	1165	0.19182	0.00146	0.22407	0.02787	12.57486	0.54392	0.47546	0.01924	0.936	0.13446	0.0024	0.79234	0.0962	-10.94	-3.88
542206_XX9_CORE-02	78	59.9	31.4	.	7019	0.18886	0.00147	0.22074	0.02741	12.42235	0.5398	0.47705	0.01936	0.934	0.13572	0.00236	0.77589	0.09408	-9.62	-2.39
542206_XX9_CORE-03	80	57.4	32	.	5762	0.1888	0.00148	0.20627	0.02559	12.34334	0.53632	0.47418	0.0192	0.932	0.13456	0.00232	0.72685	0.08808	-10.14	-2.96
542206_XX10_CORE-01	30	19	10.9	.	1219	0.1938	0.00134	0.18648	0.01732	12.09449	0.3546	0.45261	0.0117	0.881	0.13154	0.00156	0.64165	0.05852	-15.86	-11.61
542206_XX10_CORE-02	29	18.9	10.8	.	1091	0.19391	0.00137	0.19385	0.01806	12.20883	0.3617	0.45663	0.0119	0.879	0.13561	0.00162	0.65274	0.0597	-15.15	-10.83
542206_XX10_CORE-03	29	19.7	10.8	.	851	0.19399	0.00137	0.19892	0.01847	12.16456	0.3575	0.4548	0.01174	0.878	0.13442	0.0017	0.67305	0.06129	-15.51	-11.25
542206_XX10A_CORE-(	55	56.1	20.7	.	3282	0.19162	0.00138	0.29475	0.02742	12.22106	0.372	0.46255	0.0124	0.881	0.13324	0.00166	1.02324	0.09332	-13.3	-8.74
542206_XX10A_CORE-(	55	50.2	20.7	.	2413	0.19017	0.00134	0.26498	0.02468	12.15025	0.36442	0.46339	0.01226	0.883	0.13353	0.00163	0.91956	0.08402	-12.65	-8.1
542206_XX10A_CORE-(	63	57.5	23.9	.	1572	0.19022	0.00135	0.26582	0.02475	12.32419	0.37592	0.4699	0.01268	0.884	0.13555	0.00168	0.92152	0.08412	-11.44	-6.74
542206_XX11_CORE-01	23	14.9	8.3	.	1259	0.19347	0.00141	0.19194	0.01788	12.05452	0.36528	0.4519	0.01202	0.877	0.13122	0.00168	0.66101	0.06035	-15.88	-11.51
542206_XX11_CORE-02	23	15.1	8.2	.	808	0.19338	0.00141	0.19092	0.01771	11.86773	0.35716	0.4451	0.0117	0.874	0.12787	0.00158	0.66458	0.06048	-17.12	-12.85
542206_XX11_CORE-03	22	14.6	8.2	.	817	0.19258	0.00141	0.19023	0.01762	11.93801	0.3649	0.44959	0.01206	0.878	0.13055	0.00163	0.65511	0.05948	-16.03	-11.62
542206_XX12_CORE-01	38	39.6	14.1	.	1034	0.19058	0.0015	0.30624	0.04088	12.20879	0.40694	0.46462	0.01364	0.881	0.13476	0.00192	1.05585	0.13929	-12.56	-7.5
542206_XX12_CORE-02	36	36.5	13.4	.	2297	0.19085	0.00152	0.29579	0.03098	12.10233	0.3939	0.45992	0.01306	0.873	0.13262	0.00179	1.02574	0.10553	-13.53	-8.69
542206_XX12_RIM-03	26	18.3	9.7	.	1521	0.19174	0.00154	0.20231	0.01879	12.03091	0.39316	0.45509	0.01296	0.872	0.13074	0.00173	0.70417	0.06397	-14.73	-9.95
542206_XX13_CORE-01	67	82.4	25.3	.	4261	0.19016	0.00154	0.3578	0.03354	12.26277	0.42406	0.46771	0.0143	0.884	0.13424	0.00189	1.24662	0.11394	-11.83	-6.52
542206_XX13_CORE-02	63	80	24.2	.	4363	0.18951	0.00153	0.36157	0.03394	12.28453	0.43134	0.47014	0.01466	0.888	0.13384	0.00193	1.2701	0.11613	-11.15	-5.68
542206_XX13_CORE-03	62	78	23.9	.	6699	0.18954	0.00154	0.36149	0.03418	12.35447	0.43658	0.47273	0.01484	0.888	0.13544	0.002	1.26176	0.11618	-10.68	-5.14
542206_XX14_CORE-01	141	329.3	55.8	.	7539	0.1862	0.00154	0.66592	0.0633	12.5491	0.4624	0.48881	0.0161	0.894	0.13794	0.00209	2.35977	0.218	-6.41	-0.28
542206_XX14_CORE-02	82	126.9	31.8	.	4729	0.18771	0.00155	0.44276	0.04195	12.40833	0.44396	0.47942	0.0152	0.887	0.1356	0.00203	1.56536	0.14432	-8.76	-3.02
542206_XX14_RIM-03	27	17.8	10.2	.	1715	0.1907	0.00162	0.18771	0.01757	12.1011	0.42054	0.46023	0.01394	0.872	0.13119	0.00193	0.6585	0.06006	-13.42	-8.24
542206_XX15_CORE-01	84	67	32.6	.	4066	0.18843	0.0016	0.22783	0.02158	12.38876	0.4588	0.47685	0.0157	0.889	0.13545	0.00206	0.8021	0.07382	-9.5	-3.6
542206_XX15_CORE-02	85	67.7	32.9	.	18922	0.18739	0.00159	0.22768	0.02154	12.34305	0.4482	0.47773	0.01534	0.884	0.13488	0.00203	0.8064	0.07419	-8.96	-3.16
542206_XX15_CORE-03	77	59.8	29.8	.	5894	0.18869	0.00163	0.22288	0.02111	12.3639	0.46422	0.47522	0.01584	0.887	0.13511	0.00212	0.78397	0.07205	-9.91	-3.96
542206_XX16_CORE-01	38	31.5	14.3	.	2722	0.191	0.00181	0.23908	0.0226	12.17276	0.48394	0.46222	0.01616	0.88	0.13234	0.00216	0.83503	0.07638	-13.15	-7.14
542206_XX16_CORE-02	38	31.2	14.4	.	2967	0.18997	0.00181	0.23472	0.02211	12.01858	0.47586	0.45884	0.01592	0.876	0.13099	0.00214	0.82217	0.07493	-13.44	-7.49
542206_XX16_RIM-03	31	21.9	11.4	.	1908	0.19062	0.00184	0.20892	0.0214	11.93852	0.48534	0.45423	0.01624	0.88	0.13137	0.00226	0.72235	0.07178	-14.53	-8.47
542206_XX17_CORE-01	51	45.7	19.2	.	4560	0.1903	0.00187	0.26056	0.02463	12.18224	0.49514	0.46429	0.0165	0.875	0.13308	0.00219	0.90901	0.08304	-12.53	-6.35
542206_XX17_CORE-02	42	35.2	16	.	2383	0.19027	0.00189	0.24111	0.02274	12.18413	0.49614	0.46443	0.01652	0.873	0.13284	0.00222	0.84297	0.0768	-12.49	-6.31
542206_XX18_CORE-01	59	60.1	22.6	.	3654	0.19009	0.0019	0.29345	0.02778	12.20363	0.51598	0.46563	0.01734	0.881	0.13364	0.00236	1.02245	0.09316	-12.2	-5.71
542206_XX18_CORE-02	50	43.8	18.7	.	4099	0.19002	0.00192	0.25381	0.02397	12.05317	0.50126	0.46005	0.01672	0.874	0.13157	0.00224	0.8875	0.08083	-13.23	-6.96
542206_XX18_CORE-03	49	43.3	18.5	.	3381	0.19017	0.00193	0.25572	0.02429	12.13793	0.51062	0.46292	0.01704	0.875	0.13242	0.0023	0.89401	0.08185	-12.74	-6.36
542206_XX19_CORE-01	29	20.9	10.7	.	670	0.19684	0.00205	0.20123	0.01947	12.39995	0.53064	0.45688	0.01708	0.874	0.12526	0.00227	0.73396	0.0684	-16.01	-9.84
542206_XX19_CORE-02	32	20.4	11.8	.	3649	0.19185	0.00202	0.1864	0.01789	11.97021	0.51656	0.45251	0.01706	0.873	0.13029	0.00227	0.64739	0.05987	-15.25	-8.92
542206_XX19_CORE-03	35	23.3	13.1	.	2234	0.19135	0.00202	0.1928	0.01838	11.98565	0.52054	0.4543	0.01724	0.874	0.13148	0.00236	0.66617	0.06108	-14.75	-8.33
542206_XX20_CORE-01	29	19.2	10.6	.	6149	0.19165	0.00224	0.19365	0.01843	11.82407	0.55228	0.44746	0.01808	0.865	0.12914	0.00249	0.67095	0.06104	-16.14	-9.38
542206_XX20_CORE-02	51	51.3	19.3	.	6204	0.18945	0.00218	0.28414	0.02831	11.97842	0.56928	0.45858	0.01908	0.875	0.12945	0.00256	1.00661	0.09604	-13.32	-6.11

	ppm					Ratios														U-Pb discordance	
Name	U	Th	^{206}Pb	$^{206}Pb_c$(%)	206/204	$^{207}Pb/^{206}Pb^*$	1SE	$^{208}Pb/^{206}Pb$	1SE	$^{207}Pb/^{235}U^*$	2SE	$^{206}Pb/^{238}U^*$	2SE	Rho	$^{208}Pb/^{232}Th^*$	1SE	$^{232}Th/^{238}U$	1SE	Central (%)	Minimum rim (%)
542204_XX1_CORE-01	26	20.3	9.5	.	1121	0.19685	0.00231	0.22875	0.04084	12.00355	0.62036	0.44225	0.02038	0.891	0.13053	0.00254	0.77502	0.13639	-18.71	-11.33
542204_XX1_CORE-02	17	10.5	6.1	.	637	0.19679	0.00242	0.18066	0.03134	11.90121	0.63632	0.43863	0.02082	0.888	0.12732	0.00253	0.62239	0.10622	-19.35	-11.8
542204_XX1_CORE-03	22	16.3	8	.	1378	0.19503	0.00243	0.22045	0.03816	11.98073	0.66012	0.44553	0.0219	0.892	0.13086	0.0027	0.75054	0.12767	-17.55	-9.53
542204_XX1_CORE-04	25	10.7	8.9	.	740	0.19644	0.0025	0.12429	0.02256	11.79128	0.65536	0.43535	0.0215	0.889	0.12569	0.00261	0.43049	0.07688	-19.85	-12.02
542204_XX1_CORE-05	30	12.9	11	.	1707	0.19409	0.00252	0.12452	0.02228	11.82661	0.66716	0.44193	0.02214	0.888	0.12888	0.00274	0.42698	0.07509	-17.93	-9.76
542204_XX2_CORE-01	7	4	2.6	.	293	0.1999	0.00277	0.15516	0.02703	11.84857	0.70842	0.42989	0.02276	0.886	0.12153	0.00297	0.54888	0.09356	-21.85	-13.68
542204_XX2_CORE-02	6	2.8	2.2	.	355	0.19956	0.00284	0.13766	0.0241	11.6862	0.7249	0.42472	0.0234	0.888	0.12799	0.00354	0.45679	0.07795	-22.69	-14.27
542204_XX2_CORE-03	6	3	2.2	.	628	0.20271	0.00316	0.14238	0.02506	11.91128	0.7739	0.42616	0.02428	0.877	0.1261	0.00386	0.48115	0.08227	-23.29	-14.66
542204_XX2_CORE-04	9	5.6	3	.	382	0.20148	0.00303	0.19182	0.03361	11.72212	0.7613	0.42195	0.02428	0.886	0.12231	0.00303	0.66175	0.11318	-23.72	-15.05
542204_XX3_CORE-02	6	2.9	2.1	.	203	0.19412	0.00124	0.14589	0.01965	11.86391	0.34066	0.44325	0.0114	0.896	0.12709	0.00237	0.50879	0.06756	-17.7	-13.58
542204_XX3_CORE-04	6	3.4	2.3	.	357	0.20122	0.00121	0.16649	0.02247	12.56352	0.36268	0.45284	0.01188	0.909	0.13737	0.00248	0.54884	0.07307	-18.06	-13.93
542204_XX3_CORE-05	8	4.2	2.7	.	557	0.19688	0.001	0.16531	0.0225	10.74712	0.35776	0.3959	0.01256	0.953	0.12859	0.00206	0.50897	0.06833	-27.24	-22.8
542204_XX4_CORE-01	24	14.1	9.2	.	490	0.19943	0.00153	0.18585	0.02489	12.75382	0.36434	0.46383	0.01118	0.844	0.14615	0.00277	0.58984	0.07786	-15.53	-11.56
542204_XX5_CORE-01	30	13.9	11.1	.	854	0.19163	0.00088	0.13109	0.01828	11.98904	0.33404	0.45376	0.01194	0.944	0.12692	0.00182	0.4687	0.06473	-14.95	-10.62
542204_XX5_CORE-02	27	12.6	10.2	.	895	0.19106	0.00086	0.13548	0.01835	12.1168	0.34514	0.45997	0.01242	0.949	0.13111	0.00197	0.4753	0.06367	-13.59	-9.07
542204_XX5_CORE-03	19	8.4	7.3	.	870	0.19324	0.00094	0.12733	0.01718	12.2635	0.3587	0.46027	0.0127	0.943	0.1319	0.0022	0.4443	0.05917	-14.25	-9.68
542204_XX6_CORE-01	20	8.1	7.5	.	2439	0.19005	0.001	0.11853	0.01631	12.20802	0.38994	0.46588	0.01406	0.944	0.13349	0.00236	0.41366	0.05609	-12.14	-6.98
542204_XX6_CORE-02	27	15.8	9.9	.	754	0.18641	0.00101	0.17731	0.02442	11.34076	0.41924	0.44124	0.0156	0.956	0.13474	0.00259	0.58066	0.07851	-15.59	-9.73
542204_XX6_CORE-03	35	19	11.9	.	248	0.19534	0.00167	0.19766	0.0294	11.24744	0.4904	0.4176	0.01674	0.92	0.15203	0.00263	0.54294	0.07946	-22.81	-16.76
542204_XX7_CORE-01	10	6	3.9	.	555	0.1949	0.00113	0.16261	0.02193	12.1683	0.41794	0.45282	0.01464	0.941	0.12663	0.00234	0.58148	0.07711	-16.16	-10.92
542204_XX7_CORE-02	17	8	6.4	.	576	0.19275	0.00109	0.13462	0.01825	11.99231	0.4037	0.45123	0.0143	0.941	0.12997	0.0025	0.46737	0.06227	-15.78	-10.6
542204_XX8_CORE-01	27	20.2	10.1	.	602	0.19542	0.00113	0.22927	0.03139	12.12927	0.44566	0.45015	0.0157	0.949	0.139	0.00276	0.74251	0.09975	-16.82	-11.21
542204_XX8_CORE-02	29	25.4	10.5	.	747	0.19592	0.00122	0.2724	0.0385	12.15808	0.4715	0.45008	0.01654	0.947	0.13749	0.00272	0.89172	0.12373	-16.99	-11.08
542204_XX9_CORE-01	29	16.8	11.2	.	1699	0.19362	0.00118	0.17818	0.02431	12.5424	0.46798	0.46983	0.01658	0.945	0.1431	0.00306	0.585	0.07815	-12.6	-6.61
542204_XX9_CORE-02	29	21.4	11.4	.	2998	0.19339	0.00119	0.2122	0.02882	12.72051	0.48162	0.47706	0.01708	0.945	0.13684	0.00276	0.73977	0.09848	-11.17	-5
542204_XX9_CORE-03	67	58.4	25.4	.	3930	0.19097	0.00117	0.24782	0.03366	12.14104	0.44534	0.46109	0.01594	0.942	0.1299	0.00256	0.87965	0.11722	-13.36	-7.51

	ppm					Ratios														U-Pb discordance	
Name	U	Th	^{206}Pb	$^{206}Pb_c$(%)	206/204	$^{207}Pb/^{206}Pb^*$	1SE	$^{208}Pb/^{206}Pb^*$	1SE	$^{207}Pb/^{235}U^*$	2SE	$^{206}Pb/^{238}U^*$	2SE	Rho	$^{208}Pb/^{232}Th^*$	1SE	$^{232}Th/^{238}U$	1SE	Central (%)	Minimum rim (%)
542229_XX1_CORE-01	32	55.6	10	.	239	0.1972	0.00266	0.50886	0.071	9.90177	0.55948	0.36417	0.01808	0.879	0.10724	0.00437	1.7281	0.22657	-33.14	-26.56
542229_XX1_CORE-02	31	48.7	9.5	.	244	0.1993	0.00274	0.46502	0.06486	9.99157	0.57214	0.36361	0.01826	0.877	0.10621	0.00439	1.59194	0.20826	-33.75	-27.18
542229_XX1_CORE-03	42	91	13	.	318	0.19529	0.00268	0.61573	0.08573	9.75016	0.55554	0.36209	0.01808	0.876	0.1027	0.00428	2.17083	0.28322	-33.06	-26.4
542229_XX2_CORE-01	20	29.3	6	.	155	0.20395	0.00284	0.45122	0.0629	10.19448	0.59026	0.36252	0.0184	0.877	0.10825	0.00459	1.51103	0.19695	-35.03	-28.55
542229_XX2_CORE-02	13	16.8	3.8	.	99	0.21562	0.00306	0.42251	0.05902	10.61241	0.63416	0.35697	0.01876	0.88	0.11232	0.00485	1.34276	0.17485	-38.44	-32.2
542229_XX2_CORE-03	14	18	4.1	.	121	0.21077	0.00305	0.41726	0.05843	10.19985	0.61618	0.35097	0.01862	0.878	0.11026	0.00484	1.32819	0.17307	-38.52	-32.18
542229_XX3_CORE-01	66	143.7	20.9	.	548	0.19229	0.00276	0.61608	0.08674	9.81717	0.5928	0.37027	0.01968	0.88	0.10393	0.0046	2.19487	0.2875	-30.77	-23.39
542229_XX3_CORE-02	67	153.7	21.5	.	537	0.19134	0.00277	0.64064	0.0903	9.82934	0.59384	0.37257	0.01976	0.878	0.1037	0.00465	2.30173	0.3015	-30.09	-22.64
542229_XX4_CORE-01	28	42.2	8.8	.	218	0.20092	0.00295	0.43801	0.06172	10.09178	0.62642	0.36429	0.01992	0.881	0.10638	0.00486	1.49986	0.19566	-34.01	-26.88
542229_XX4_CORE-02	14	12.4	4.4	.	115	0.217	0.00326	0.29299	0.04148	10.89133	0.6901	0.36402	0.0203	0.88	0.12044	0.00564	0.88555	0.11572	-37.5	-30.78
542229_XX4_CORE-03	21	30.3	6.7	.	96	0.22773	0.00358	0.45356	0.06411	11.34746	0.72384	0.36139	0.02006	0.87	0.11517	0.00543	1.42324	0.1855	-39.93	-33.58
542229_XX5_CORE-01	35	65.8	10	.	290	0.20088	0.00166	0.58247	0.06174	9.94951	0.45764	0.35923	0.01542	0.933	0.10937	0.00258	1.9131	0.19338	-34.92	-29.51
542229_XX5_CORE-02	26	48.2	7.5	.	149	0.21595	0.00287	0.59463	0.06329	10.74763	0.53416	0.36096	0.01516	0.845	0.11362	0.00286	1.88908	0.19128	-37.82	-32.79
542229_XX6_CORE-01	13	20	3.8	.	96	0.22658	0.00197	0.53465	0.05925	11.81126	0.55346	0.37807	0.01646	0.929	0.12631	0.00313	1.60024	0.1693	-36.94	-31.82
542229_XX7_CORE-01	39	105.2	10.9	.	280	0.19626	0.00164	0.80693	0.08561	9.38824	0.4449	0.34694	0.01538	0.936	0.10295	0.00251	2.71945	0.27424	-36.09	-30.55
542229_XX7_CORE-02	56	178.6	15.9	.	458	0.19298	0.0016	0.93307	0.0996	9.3249	0.44614	0.35046	0.01574	0.938	0.1024	0.00251	3.19355	0.32391	-34.64	-28.88
542229_XX7_CORE-03	57	165.7	16.4	.	435	0.19319	0.00159	0.85717	0.09211	9.54104	0.45076	0.35819	0.01586	0.937	0.10434	0.00255	2.94264	0.30099	-33.26	-27.46
542229_XX8_CORE-01	47	89.2	13.6	.	341	0.19857	0.00166	0.5728	0.06107	9.90788	0.47402	0.36188	0.01622	0.937	0.1075	0.00264	1.92821	0.19534	-33.9	-28.14
542229_XX8_CORE-02	53	138.2	15.6	.	449	0.19549	0.00167	0.7768	0.08312	9.88431	0.47002	0.3667	0.01626	0.933	0.10762	0.00263	2.64676	0.26936	-32.26	-26.38
542229_XX8_CORE-03	54	128.4	15.9	.	417	0.19603	0.00164	0.70044	0.07499	9.8649	0.4685	0.36499	0.01622	0.936	0.10697	0.00264	2.38992	0.24325	-32.71	-26.87

Appendix XI: Nepheline EMPA data for sample 542205

SAMPLE NO.	**Lithology**	**DESCRIPTIONS**
525964	KSPAR-NEPH-BT pegmatite	Alteration to clay minerals present throughout the sample. Biotite (<5%) associated either opaque's (10%). Coarse Nep (35%) and felspar (50%).
525969	KSPAR-NEPH-BT pegmatite (ultra-coarse)	Biotite (10%) associated with the opaque's. Some alteration of minerals to clay is present throughout the sample. Sample is very coarse minerals occurring together in a pocket like fashion. Nepheline (20%), Feldspar and Plagioclase (50%) and 10% opaque's. Contact appears to be one giant nepheline crystal in contact with feldspar plagioclase and calcite. crystal does have some small veinlets can't really identify the minerals.
525971	ijolite	> 70% nepheline, 20 % clinopyroxene, 9% biotite and 1% calcite.
525972	carbonatite-breccia	Coarse grained calcite towards the top of the thin section, while medium grained to the bottom, some nepheline clasts seen approx. 1-4mm in diameter. Possibly some feldspar clasts as well, 1-4mm. Flow textures present, matrix appears to flow around the clasts. Some Biotite and aegerine-augite present approx. 5% each. Large clasts approx. 1.5-2cm appears to be made up of fine-grained calcite crystals and are surround by biotite and clinopyroxene.

525974	melteigite	More nepheline still appears intercumulus approx. 60-65% clinopyroxene, 24% nepheline, 1% biotite. Crystals of clinopyroxene and biotite entrained in nepheline crystals
525978	melteigite-dyke (in TTG)	More urtitic than ijolitic sample has around 50%nep, 30% clinopyroxene, 20% biotite. Also appears to be some plagioclase in the sample possibly some feldspar.
525980	grey syenitic gneiss	70 % feldspar with >5% nepheline and
525981	grey syenitic gneiss	Green clinopyroxene seen occurring with a yellow brown mineral (not biotite)?? Is this titanite??Possible just more clinopyroxene? Majority of sample (>60%) appears to be felspar, microcline, orthoclase and plagioclase.
525982	ijolite	Approx. 10% biotite and 10% CPX, with 30% nepheline and 45% feldspar. <5% calcite. Alteration to clay minerals present.
525983	NEPH-BT pegmatite	Don't see much biotite appears to be pegmatitic nepheline (40%) and feldspar (60%).
525984	melteigite-dyke (in ijolite)	nepheline (intercumulus, late stage nepheline) surrounded by green pyroxene (aegerine) (p3 and 4) smaller crystals of what appears to be clinopyroxene are present in the nepheline crystals (p1 and 2) - crystals show aegerine green colour and have incline extinction. Sample has > 70% crystals. Brown platy biotite. p5 and 6

		show intercumulus nepheline with green clinopyroxene and biotite.
525986	melteigite-dyke (in ijolite)	60% clinopyroxene and 30% nep, <1% calcite and 9% biotite.
525987	melteigite	Goes from >75%cpx to approx. 65%cpx then to approx. 60% clinopyroxene. Throughout the sample approx. 1% biotite.
525988	urtite	Approximately 75 % nepheline with 10% clinopyroxene and 5% biotite and 10% feldspar
542203	melteigite (medium-grained, massive- no banding)	approx. 40 % nep, 40% clinopyroxene and 10% biotite. Clinopyroxene crystal with twinning? Nepheline appears to be intercumulus. Biotite impeding growth of CPX most likely formed first P3 and 4.
542204	melteigite (banded)	Transition from finer nepheline to a coarser nepheline. The coarser material appears to contain approx. 75% clinopyroxene and 25% nep. The finer material appears to be <1% biotite with 50% nepheline and 50% clinopyroxene towards the end of the thin section. The contact is sharp not gradational across the contact 40% nepheline with 5%bio, 50% clinopyroxene and possibly some feldspar. Veinlet of clinopyroxene cutting across the sample.

542205	banded ijolite transition to melteigite (banded)	Ijolite section of the sample contains coarse nepheline >70% with approx. 10% clinopyroxene and 5% biotite and 2% calcite. Dark alteration also present. Change from ijolite to melteigite section of the sample appears to gradational. Approx. 50% clinopyroxene and <30%neph, 10% biotite. The "bottom" of sample ijolitic /urtitic to melteigite possibly urtite.
542206	KSPAR-NEPH-BT-PX pegmatite	Possibly Large feldspar grain (2cm). Fine grained matrix if calcite. Biotite associated with the magnetite. Some fairly large nepheline grains (1mm-6mm) present confirmed with interference figure. Very little aegerine present.
542208	melteigite (medium-grained, massive, rare NEPH-macrocrysts)	approx. 50% clinopyroxene, 10 % biotite, 5 % calcite and 30% nepheline. Go over sample again.
542209	melteigite (with NEPH+KSPAR liquid segregations)	Top of sample is coarse ijolite while the bottom is more medium grained- fine grained melteigite
542210	syenitic gneiss	Clinopyroxene present approx. 10%. Rest of the sample appears to be felspar (>70%), however there does appear to be another mineral possibly nepheline at 5%. Calcite also present towards the bottom of the thin section. Alteration to clay minerals present throughout the sample.
542212	ijolite	Approx. 10% biotite and 10% clinopyroxene, with 30% nepheline and

		45% feldspar. <5% calcite. Alteration to clay minerals present.
542214	ijolite	Approx. 5% biotite and 15% clinopyroxene, with 30% nepheline and 45% feldspar. <5% calcite.
542215	ultramafic inclusions in ijolite	Outer part of sample appears to be 50% nepheline, 25% clinopyroxene, 20% biotite and 5% calcite. The inner mafic intrusion appears to be 75% clinopyroxene, 15% biotite and 10% nepheline, <1% calcite.
542216	layering in ijolite-melteigite-foyaite	Gradational change from ijolite to melteigite. Top part of this section contains approx. >70% nepheline with 15% clinopyroxene, 10% bio and <5% calcite. "Bottom" of sample contains 75% clinopyroxene with > 25% nep and 5% biotite.
542219	contact between syenitic gneiss, melteigite-layer and massive ijolite	Sharp contact between a syenitic gneiss and a melteigite, which is in sharp contact with a ijolite. All rock types appear to be coarse grained, the syenitic gneiss has 10% clinopyroxene, 10%nepheline and 75% feldspar with 5% biotite and calcite
542220	contact between syenitic gneiss, melteigite-layer and massive ijolite	Contact between ijolite and melteigite. Ijolite section -approx. 70% nepheline with 5% biotite, 10% clinopyroxene and >5% calcite possibly some feldspar. The melteigite section there is <2%neph sample appears to be 80% clinopyroxene and 20% biotite.

542221	melt-pools and felsic segregations in melteigite	Gradational change going from <5% nepheline in the sample at the bottom of the thin section to little/no nepheline and then approx. 10-15% nepheline at the top of the thin section. <2% calcite.
542222	contact between ijolite (NEPH-poor) and urtite (NEPH-rich)	> 70% nepheline therefore it is a ijolite, approx. 10% clinopyroxene, clinopyroxene is altering to a dark mineral that not easily identifiable, cloudiness appears in some places? Calcite present approx. 5% and 5% biotite. Across the contact 35% nepheline and 35% green clinopyroxene. 5% calcite and 5% biotite possible some felspar.
542224	ijolite	Alteration to clay minerals present in the sample. Would say it seems more like urtite than ijolite looking at the thin section as only approx. 40% nepheline is present along with 40% green clinopyroxene, 10 % biotite and < 2% calcite, possibly some feldspar.
542225	ultramafic (pyroxenite/melteigite)	Sample contains 60% green clinopyroxene, 20% biotite, < 10% feldspar and nepheline (some plagioclase seen) and <5% calcite. Minerals are aligned possibly showing a flow texture?
542223	grey syenitic gneiss	Green pyroxene present approx. 20%. Rest of the sample appears to be felspar (>60%), however there does appear to be another mineral (uniaxial negative interreference figure- nepheline?). Calcite also present towards the bottom

		of the thin section. Alteration to clay minerals present throughout the sample.
542226	"sheared" ijolite (remobilized crystal-mush)	A: Sample generally fairly coarse however there appears to be a veinlet containing smaller crystals cutting across the sample. Sample is approx. 70% nepheline with 10% clinopyroxene, 5% biotite 15% feldspar, <2% calcite. At the veinlet there is a concentration of biotite crystals.
542227	mica pyroxenite	542227A: < 10% nepheline in the sample >65% of the sample appears to be green clinopyroxene. 20% biotite and < 5% calcite.
542228	ijolite (fine-grained, quenched)	Too much clinopyroxene and biotite, approx. 50% and 10% respectively. Plagioclase also present in the sample (P2) approx. 15%. Nepheline approx. 23% and some calcite present <2%. Possibly some zircon present in the sample??
542229	carbonatite-breccia dyke	Fine grained calcite matrix, calcite crystals appear to flow around the larger grains. Rounded grains of nepheline present in the sample as well as clinopyroxene and feldspar grains. Lots of alteration to clay present throughout the sample. Biotite appears to occur only within the nepheline and clinopyroxene clasts.

542230	carbonate-phase as part of KSPAR-BT pegmatite	99% calcite, 1 crystal of biotite. Some alteration to clay present in the sample.
542231	ijolite (coarse-grained)	Seems more like urtite only appears to be approximately 45% nepheline and 50% green clinopyroxene with 2% biotite, 1% calcite and 1%opaqs
542232	carbonatite vein	100% calcite some alteration to clay is present in the sample.
542249	carbonatite dyke	Garnet 20% with possible rims secondary reaction- in fractures. May have polycrystalline garnet??? Some garnets may contain zircon. Aegerine-augite 10% rim around "garnet". 70% of sample is calcite.
542262	carbonatite dyke (in altered TTG country-rock)	practically 100% calcite but abbot 1% clinopyroxene seen and some brown mineral P1-4.
542263	carbonatite dyke in TTG	Lots of calcite altered to clay. Some biotite approx. 5%